Higgs collider phenomenology: important backgrounds, naturalness probes and the electroweak phase transition.

A Dissertation presented

by

Harikrishnan Ramani

to

The Graduate School

in Partial Fulfillment of the

Requirements

for the Degree of

Doctor of Philosophy

in

Physics and Astronomy

Stony Brook University

August 2017

Harikrishnan Ramani

2017

Stony Brook University

The Graduate School

Harikrishnan Ramani

We, the dissertation committee for the above candidate for the

Doctor of Philosophy degree, hereby recommend

acceptance of this dissertation

Patrick Meade - Dissertation Advisor
Associate Professor, Department of Physics and Astronomy

George Sterman - Chairperson of Defense
Distinguished Professor, Department of Physics and Astronomy

Dmitri Tsybychev - Committee Member
Associate Professor, Department of Physics and Astronomy

Eder Izaguirre - Outside Member
Assistant Physicist, Department of Physics, Brookhaven National Laboratory

This dissertation is accepted by the Graduate School

Charles Taber
Dean of the Graduate School

Abstract of the Dissertation

Higgs collider phenomenology: important backgrounds, naturalness probes and the electroweak phase transition.

by

Harikrishnan Ramani

Doctor of Philosophy

in

Physics and Astronomy

Stony Brook University

2017

The Higgs boson discovered in 2012, might be the portal to new physics. With the Higgs as the common theme we present the following research arcs.

In order to study the Higgs, it is important to have a very good handle on Standard model(SM) backgrounds. One such background process is SM WW production, which reported routine 3 sigma excesses in early run 1 of the LHC. However, experiments use Parton Showers for theoretical prediction and this might be inadequate for exclusive cross-sections. We show that taking into account higher order Sudakov logarithms through transverse momentum and jet-veto resummation predicts a larger cross-section than parton showers and reduces the theory-experiment disagreement.

Next, improvements are suggested to the state-of-the-art finite temperature field theory calculations that can predict the nature of the electroweak phase transitions in beyond-the-standard model scenarios. We find that relaxing the high-temperature approximation and resumming logs of temperature to super-daisy order can have significant changes in the order of the phase transition. This in turn can have important consequences for the possibility of creating the baryon anti-baryon asymmetry across this phase transition. Our improved calculation in general predicts weaker phase transitions, and hence smaller baryon-anti baryon asymmetry. This strengthens the case for building future colliders in the form of a no-lose theorem; absence of deviation from the Standard model in Higgs precision physics can falsify the possibility of Electroweak Baryogenesis.

Finally, we present another consequence of Higgs precision studies, constraining new physics invented to ameliorate the hierarchy problem. These theories generically predict top partners at the electroweak scale, which are connected with the top quark through a symmetry. However these top partners have not been detected at colliders making the electroweak scale severely fine-tuned. We find that generically, top-partner mass limits will reach a TeV just from Higgs precision at future colliders.

Dedication Page

To my grandfather, who taught me to ask questions.

Contents

List of Figures

List of Tables

Preface

"A scientific man ought to have no wishes, no affections, - a mere heart of stone."—Charles Darwin

Acknowledgements

I would like to start by acknowledging my advisor Dr. Patrick Meade, for mentoring me through my thesis, for the many illuminating discussions some of which would never make it to written verse. From him, I learnt to pose physics problems that are interesting and more importantly learnt a bevy of tools to attack them. I also learnt the importance of putting one's own work through intense scrutiny and taking pride in academic credibility.

I would also like to thank the professors at Stony Brook for the remarkable quality of graduate level courses, especially Dr. Peter van Nieuwenhuizen for countless personal sessions that even spilled into weekends. I would also like to acknowledge Dr. Robert Shrock, Dr. Rouven Essig and Dr. Sasha Abanov for memorable courses, and Dr. Rouven Essig for always being available for discussions and for agreeing to be my academic referee. Many thanks to Dr. George Sterman for among other things, providing an incredible work environment at the Yang Institute of Theoretical physics and for supporting me for travel to various workshops and conferences and for the graduate Quantum Field Theory course. I would like to thank Dr. Sally Dawson at the Brookhaven National Lab for collaboration and agreeing to be my academic referee. It would be remiss to not mention Ms. Elizabeth Gasparino and Ms. Helen Carrano, secretaries at the YITP who have attended to my administrative requests sometimes at very short notice. I would also like to thank various collaborators and officemates who have played a big part in my graduate studies through regular discussions; Dr. Yi-Ming Zhong, Dr. Andrea Massari, Dr. Michael Spillane and Dr. Tyler Corbett. I would also like to acknowledge the postdocs at the YITP I have had the pleasure to collaborate with, Dr. Samuel Mcdermott and Dr. David Curtin. Finally I would like to thank my defense committee members Dr. Dmitri Tsybychev and Dr. Eder Izaguirre.

My interest in physics was cultivated by strong influences during my high-school years, from Mr. Ananthan, Mr. Ravi Shankar and Mr. Sadagoppan Rajesh to whom I shall forever be grateful. This was further nurtured by a strong undergraduate program in theoretical physics in the Chennai

Mathematical Institute, and I would like to thank Dr.K.Narayan for his continued interest in my academic success.

On the personal front, I would like to thank my grandfather, Dr. K.V.Natarajan, for the first scientific discussions I had when I was a mere kindergartener. I still reminisce those countless occasions of banter during my childhood that I believe went a long way in me obsessing about physics. I would also like to thank my other grandparents who have played a pivotal role during my childhood, for all the moral stories and for raising my parents through adversity. Any of this would be impossible without my mother Gita Ramani and my father Ramani Natarajan, who has repeatedly put my academic requirements over their bare necessities. I also need to thank them for being role-models to look up-to and for their clarity in decision making. I need to acknowledge my parents and sister Gayathri Ramani, for also supporting me on this very non-traditional career choice, which has led to many frustrations and long absences from home.

I would also like to thank Anirudh Ramkumar and Karthikeyan Harith for a decade long friendship that has traversed many continents. I would also like to thank my many friends I made during my graduate studies: Mehdi Namazi, Oumarou Njoya, Hualong Gervais, Moshe Kellerstein, Karen Chen and Jean Paul Nery.

List of Publications

This thesis is based on the following original publications in refereed journals.

1. S. Dawson, P. Jaiswal, Y. Li, H. Ramani and M. Zeng, Phys. Rev. D **94**, no. 11, 114014 (2016) doi:10.1103/PhysRevD.94.114014 [arXiv:1606.01034 [hep-ph]].
2. P. Jaiswal, P. Meade and H. Ramani, Phys. Rev. D **93**, no. 9, 093007 (2016) doi:10.1103/PhysRevD.93.093007 [arXiv:1509.07118 [hep-ph]].
3. H. Ramani, PoS DIS **2015**, 118 (2015).
4. P. Meade, H. Ramani and M. Zeng, Phys. Rev. D **90**, no. 11, 114006 (2014) doi:10.1103/PhysRevD.90.114006 [arXiv:1407.4481 [hep-ph]].

Furthermore, the following are included in this thesis, on the arxiv and currently under peer review.

1. R. Essig, P. Meade, H. Ramani, Y. Zhong arXiv:1707.03399 [hep-ph].
2. D. Curtin, P. Meade and H. Ramani, arXiv:1612.00466 [hep-ph].

Finally, the following results were not included in this thesis.

1. S. D. McDermott, P. Meade and H. Ramani, Phys. Lett. B **755**, 353 (2016) doi:10.1016/j.physletb.2016.02.033 [arXiv:1512.05326 [hep-ph]].
2. S. D. McDermott, H. H. Patel and H. Ramani, arXiv:1705.00619 [hep-ph].

Chapter 1

Introduction

The Standard Model of particle physics is a remarkable human achievement. It has survived intense scrutiny for three decades, and with the discovery of the Higgs boson the existence of all its postulated particles have been confirmed. As much as it is celebrated, we have long known that it is by no means a complete theory; there are some experimental observations it does not explain. There are also issues of aesthetics. It is replete with extremely small and large numbers and chance cancellations that seem to beg for a more complete theory. Many of the Standard Model's inadequacies and pressing questions might very well be answered by utilizing the Higgs boson as a portal to new physics. In this thesis, I present a myriad of research arcs tied together by a common theme: the Higgs boson.

1.1 Standard Model of Particle Physics

The Standard Model (SM) of particle physics as it stands today catalogues all known elementary particles into symmetries and describes the interactions among them. The Gauge symmetries $SU(3)_{\text{color}}\times SU(2)_{\text{EW}}\times U(1)_{\text{Y}}$ define the SM model with particles arranged under different representations of these gauge groups. The Standard Model consists of matter particles, the fermions which transform under the SU(2) gauge group as fundamental or singlets based on their chirality . They are broadly divided into quarks, which are also fundamentals of $SU(3)_{\text{color}}$, and leptons, which are singlets under this transformation. Regardless, both quarks and leptons occur in three copies called generations. They interact with each other based on their charges, which are mediated by force carriers; the vector gauge bosons that transform as adjoints under the corresponding gauge groups. Finally there is one scalar field, the Higgs, which transforms as a fundamental only under the SU(2)×U(1) gauge group. It obtains a vacuum expectation value (vev), which breaks the SU(2)×U(1) symmetry to a U(1) symmetry [9]. Through symmetry breaking, it also supplies mass to the gauge bosons corresponding to the broken symmetries as well as to the fermions. Additionally, all these particles couple to gravity through the stress-energy tensor. Gravity is extremely weak compared to the other SM forces. As a result, it is often justifiably omitted when talking about testing the SM in the laboratory. On large length scales, when quantum effects are unimportant, gravity is adequately described by general relativity. However, a complete quantum theory of gravity has remained elusive.

The Standard Model was itself deciphered in gradual steps over multiple decades, with the complete theory finalized only in the late 1970s. At this time, the model still required experimental confirmation of a few postulated particles. The existence of these particles were subsequently verified, with the last discovery, of the Higgs as recent as 2012 [10, 11]. Over the last three decades, many other Standard Model predictions have also been put to the test. This has been accomplished primarily through high-energy collisions and other terrestrial experiments, and comparing observations with SM predictions. These endeavors have produced no deviations from the SM thus far. However, more recently, there have been some cosmological observations that cannot be explained adequately by the SM. Also, as briefly mentioned earlier, there are numerous issues of coincidences and disparities, which warrant explanation. One way to solve these shortcomings is to engage in 'Beyond the Standard Model' (BSM) model building. We now list some of these outstanding problems and outline proposed solutions with references for further reading.

1.2 Problems from Astronomical / Cosmological Observations

The Horizon problem [12]

The Standard Model of cosmology is based on a singularity, the Big Bang, and then a period of sustained cosmic expansion continuing to this day. Observation of the homogeneous and isotropic universe around us appears to indicate causal contact sometime in our history. However, current estimates of the age of the universe seem to be orders of magnitude smaller than the time needed for our entire observable universe to have been causally connected sometime in our past. This is called the horizon problem. The horizon problem is solved by positing that an inflaton field that led to a period of exponential accelerated cosmic expansion. This would make the causally connected patch much larger, explaining the isotropy and homogeneity we observe today.

Dark Energy [12]

The isotropy and homogeneity of the observable universe is described by the Friedman-Robertson-Walker (FRW) metric. Using the Einstein equation, we can relate this metric to the energy density of our universe. Information about cosmic expansion can then accurately describe the energy budget of our universe today, as well as that of our past just a few seconds after the Big Bang when our universe was very young. A remarkable consequence of this exercise is that over two-thirds of our universe is made up of not radiation or cold matter but vacuum energy, called "Dark Energy". From dimensional grounds, the sum of the zero-point energies would estimate Dark Energy to be around the Planck scale. However, its cosmological measurement is 120 orders of magnitude smaller. Currently, the only satisfactory explanation for this is Weinberg's anthropic principle [13], which shows that larger values of Dark Energy would prevent formation of structure.

Dark Matter [14]

Dark Matter (DM) was first detected using rotation curves of galaxies that predicted more matter in these galaxies than was visible. Precision cosmology has also returned overwhelming evidence that only a quarter of the cold matter that makes up our universe is actually SM-like. This is irrefutable proof that new physics exists. *A priori*, no interaction with the SM is required for DM excepting gravity. However, many models of DM have been proposed that would couple weakly to the SM. These models are motivated by the observation that DM models that have weak-scale interactions with the SM and have weak-scale masses miraculously predict DM density that matches observation (WIMP miracle). Moreover, many theories written to explain other problems, like Super Symmetry (SUSY), contain new weak scale stable particles that fit this bill. These models also have falsifiability in the near future through direct and indirect detection experiments. Furthermore, it would also be an improbable coincidence if DM and SM, which interact only through gravitation, have similar densities today. However, a series of collider and dedicated DM detection experiments have returned null results. This has led to an expansion of the radius around the WIMP-miracle lamppost. We now have a burgeoning field with clever model building predicting the correct DM density as well as new generation experiments to probe lower DM masses. However, it remains possible that DM interacts with us only gravitationally, and the coincidence in the energy densities is due to other reasons.

Neutrino Mass [15]

The SM does not contain a right-handed neutrino; as a result, the Higgs vev does not supply it with mass. However, the discovery of solar neutrino oscillations directly contradicts the possibility of massless neutrinos. Subsequent experiments have confirmed that at least two neutrinos are massive as well as extremely small (sub eV splitting), several orders of magnitude smaller than all other SM particles. All of these findings require BSM explanation. The see-saw mechanism explains this through the observation that a matrix with electroweak-scale entries can have an eigenvalue much heavier, compensated by another eigenvalue much lighter than the electroweak scale. This results in neutrinos that are very light, with another set of very heavy neutrinos much above the electroweak scale.

Baryogenesis [16]

This is dealt with in detail in this thesis, and outlined in a subsequent Section.

1.3 Small or Arbitrary parameter problems

Strong CP problem [17]

Charge Parity (CP) violation has been established as a property of the Weak interactions of the Standard Model. However there is one other CP violating term that obeys gauge symmetry in the QCD sector with an associated dimensionless angle θ_{QCD}. Yet the upper limits on the measured neutron dipole moment sets a limit twelve orders of magnitude smaller than what would arise from $\theta_{\text{QCD}} \sim 1$. This is the strong CP problem. The most accepted solution involves introducing new pseudo-scalar particles called axions, which have not been discovered yet.

Grand Unification [18]

The gauge couplings in the SM are arbitrary parameters determined by experiment. The SU(2)xU(1) gauge couplings are relatively small compared to the SU(3) coupling. Furthermore, quarks carry SU(3) charge in addition to SU(2)xU(1) charges, while leptons carry only the latter. It would be desirable to discover an underlying principle explaining these quirks. Grand Unified Theories (GUTs) do this by expanding the SM gauge group to a larger gauge group, such that the quarks and leptons fit in a unified manner as representations of this larger gauge group. Additionally, the larger gauge group has one coupling and gets spontaneously broken at $\sim 10^{15}$ GeV scale to the SM gauge group through another Higgs mechanism. Running to lower electroweak-scale energies naturally produces the different gauge couplings we observe. Unification of the quarks and leptons is typically accompanied by predictions of baryon-number violation that in turn predict proton decay. Non-observation of proton decay has placed a severe strain on vanilla GUT theories.

The Electroweak Scale Hierarchy Problem [19]

This is dealt with in detail in this thesis, and outlined in the next Section.

The next two sections are devoted to more thoroughly exploring two of the problems with the SM, which will be discussed in-depth in this thesis.

1.4 The Hierarchy Problem

First, we examine the Hierarchy Problem. The Hierarchy problem can be understood by analyzing the disparity in mass scales in the SM.

Gravity, previously discussed in brief, has a natural mass scale set by the Newton constant G, at 10^{19} GeV, called the Planck scale. This sets a natural mass scale against which all other mass scales can be compared. Quantum Chromodynamics (SU(3)$_{\text{color}}$) has a Landau pole at around $\Lambda_{\text{QCD}} \sim$ 200 MeV where its coupling becomes non-perturbative; this sets another mass scale. Particles with color, the quarks and gluons, condense into color-neutral composites with masses around Λ_{QCD}. However, this scale is dynamically generated, allowing the large discrepancy between it and the Planck scale to be considered natural. Interestingly, some of these composite particles, the pions, are pseudo-Goldstone bosons under an approximate symmetry. This protects them from acquiring Λ_{QCD} scale mass. As a result, the pions are an order of magnitude lighter (100 MeV). This is an example of the 't Hooft symmetry principle: "a quantity in nature should be small only if the underlying theory becomes more symmetric as that quantity tends to zero".

Nevertheless, there is one other fundamental mass scale in the SM set by the Higgs mass. This sets the scale of the Higgs expectation value and the mass scale of electroweak gauge bosons. Thus, all these particles have a mass of around a hundred GeV. This is called the electroweak scale. However, the Higgs is a fundamental scalar in the SM. As such, the smallness of its mass is not protected by a symmetry. This is unlike fermions and Gauge bosons which when massless obey Chiral and Gauge symmetry. New physics at any high scale coupled to the SM would supply radiative corrections making it natural for the Higgs to live at that high scale. It then becomes reasonable to expect the electroweak scale to be at the Planck scale. Yet, it is actually 16 orders of magnitude lower. This does not necessarily invalidate the SM. The Higgs mass counter-term fixed by the experimental determination of the Higgs mass must be subtracted from the natural high scale to get to the electroweak scale. However, it is baffling that the Planck scale and the counter-term, both large numbers, conspire to cancel to many orders of magnitude to leave us with an arbitrary new small scale: the electroweak scale. Thus, the Hierarchy problem is a problem of incredible fine-tuning. It seems to suggest that there exists an as-yet unobserved symmetry protecting the Higgs mass.

One such symmetry is Super-Symmetry (SUSY), a space-time symmetry relating every SM particle to a hypothetical super partner with opposite statistics. Thus, the Higgs has a super partner called the Higgsino, and their properties are closely related due to SUSY. Since the Higgsino is a fermion, it is protected by chiral symmetry. In turn, so is the Higgs. SUSY thus elegantly solves the Hierarchy problem.

A second possible solution to the Hierarchy problem is inspired by the trick that makes pions much lighter than Λ_{QCD}. Little Higgs and Composite Higgs theories propose that the Higgs is actually a pseudo-Nambu Goldstone boson of some spontaneously broken UV symmetry. Unlike SUSY, these theories only postpone the Hierarchy problem. A UV-completion is required to explain a second hierarchy problem between the afore-mentioned symmetry breaking scale and the

Planck scale.

Both these theories in their natural form predict new particles around the electroweak scale and can be directly produced at colliders. Furthermore, they also indirectly affect precision standard model measurements, specifically Higgs precision measurements due to the central role the Higgs plays in the Hierarchy problem. These properties can be exploited to falsify these theories at colliders past, present and future. We discuss this in further detail at the end of this Chapter and in further Sections.

It is important to note that there are fermion masses ranging from 173 GeV (top quark) to electrons (500 keV), all of which acquire masses from the Higgs vev. While troubling, the six orders of magnitude between these two scales is small compared to the sixteen orders of magnitude Hierarchy problem in the electroweak sector. Also, fermion masses are protected by chiral symmetry. Hence, these mass parameters are considered technically natural.

1.5 Baryogenesis

It is an established fact that there exists a local excess of particles over anti-particles around us. Our very existence attests to this fact. If particles and anti-particles were equally dense locally, they would annihilate each other leaving us with photons and no possibility of complex structure. Astronomical observations suggest that this excess is present at very large length scales as well. This is referred to as the Baryon-Anti-Baryon asymmetry, otherwise known as the Baryon asymmetry.

Any primordial asymmetry is washed out by inflation. Thus, starting from symmetric initial conditions, we require a mechanism that produces the Baryon asymmetry. This is called Baryogenesis. A theory of particle physics that allows for Baryogenesis should have certain symmetries broken, enumerated as the Sakharov conditions. These are

- Baryon number violation. This is a straightforward condition: we need ΔB processes to generate a Baryon asymmetry.
- C and CP violation. For every $\Delta B = +1$ process, its C and CP conjugate are both $\Delta B = -1$ processes. Thus, we need these symmetries to be violated in order to have preferential

Baryon production.

- We require out-of-equilibrium conditions in order to have a preferential time direction. This would allow the Baryon number violating processes to generate the asymmetry.

The SM does not contain any Baryon number violating processes at tree level. However, there are non-perturbative processes: the electroweak sphalerons that violate Baryon number. C is maximally violated in the electroweak sector, and the mass matrices of quarks provide CP violation. There is also an electroweak phase transition in the early universe that could provide for in-equilibrium conditions for successful Electroweak Baryogenesis. In practice, however, the CP violation in the SM is not enough to generate the amount of Baryon asymmetry we observe today. Even if we remedied this by increasing the CP asymmetry through new physics, there is another problem: the order of the electroweak phase transition.

Any discussion of this order requires exploration of the electroweak phase transition itself. The electroweak scale masses of the W and Z bosons demonstrate that the Electroweak symmetry is spontaneously broken today. This symmetry breaking is achieved by the Higgs doublet obtaining a vacuum expectation value due to a negative mass. However in the very early universe, large temperatures supply positive corrections to the Higgs mass (also called a thermal mass). This stabilizes the Higgs field at the origin of field space, rendering the electroweak symmetry exact. As the universe expands, it cools, and at some temperature T_c it can no longer stabilize the vev at the origin. Slightly below this temperature, the universe transitions from an Electroweak Symmetry restored phase to a symmetry-broken phase . This is the electroweak phase transition.

It is important to note that non-perturbative sphaleron processes are turned off for large gauge boson masses, and hence absent today. However, these processes are thought to have been active in the early universe, leading to the washing out of any Baryon asymmetry produced. For this reason, it would be impossible to generate a Baryon asymmetry in the SM prior to the electroweak phase transition.

With the Higgs vev as the order parameter, we can now seek the order of the phase transition. If the phase-transition were second order, then there would be no discontinuity in the order parameter. When the phase transition is complete, the vev is non-zero yet very small. However, there are still active sphaleron processes that will wash out any Baryon asymmetry created across the phase transition. In a first order phase transition, there is tunneling from the symmetry-restored vacuum to a sufficiently large symmetry broken vacuum where the sphaleron processes are turned off. As a result, the Baryon asymmetry generated during the phase transition remains as the universe cools.

The discovery of the 125 GeV Higgs fixes all the parameters needed to calculate the finite temperature potential and the order of the phase transition in the SM. It results in a second order phase transition providing another bottleneck for electroweak baryogenesis.

This can be remedied by introducing new physics coupled to the Higgs that could strengthen the order of the phase transition to strongly first order. However, this would result in modification in Higgs precision measurements at colliders that could be studied to falsify these theories.

Thus far, we have enumerated various problems of the SM and discussed certain BSM solutions. These solutions are typically accompanied by other predictions, which can be confirmed or falsified at colliders. Next, we shall briefly discuss state-of the art collider physics as well as future proposals.

1.6 Colliders: Past, Current and Future State of Experiments

As particle physics reached the threshold of Electroweak particle discovery, there was a new barrier to circumvent. Heavy degrees of freedom needed to be produced, and this could only be accomplished by accelerating known particles to very high energies. This idea is the foundation for collider building: accelerate charged particles in electromagnetic fields, collide them, and observe hints of new particles. Through persistent experimental effort and theoretical intuition, the SM was verified over several colliders, each probing higher energies than the previous. The same strategy is now used for probing BSM physics.

Recent colliders that have completed their physics runs are the LEP, an electron-positron collider, and the Tevatron, a proton-anti-proton collider. These colliders were built to discover the predicted particles of the SM. There were also high hopes that they would produce particles from well-motivated theories like SUSY. However, while ruling out the possibility of a light Higgs boson [20], they also discovered no new physics.

The Large Hadron Collider (LHC) was built at this juncture. Its original proposal to run at 14 TeV was meant to confirm the existence of a SM Higgs boson. Pending discovery of the Higgs, it was also hoped that the collider would shed light on the Higgs couplings to the rest of the SM as well as precision Electroweak processes, placing the SM under even tighter scrutiny. Finally, it was hoped to discover predictions of theories such as SUSY, Randall-Sundrum models [21], and DM candidates.

The LHC started its physics runs in 2010. Ever since, we have accumulated data at a breakneck rate, first at 7 TeV and 8 TeV center of mass energy, and more recently from the 13 TeV version. The Higgs was finally discovered in 2012 with a mass of 125 GeV. However, the LHC has not discovered any sign of new physics. All the Higgs couplings with SM particles seem to match SM predictions. Mass limits on Super-partners have now been pushed to above a TeV. The LHC will continue to run, with hopes that it will eventually accumulate 3000 fb^{-1} of data. This would greatly reduce statistical error in many experimental measurements. Among other things, this will "begin" the era of precision Higgs physics and as discussed earlier, several BSM models have irreducible deviations from SM Higgs properties.

Several ideas for future colliders have been proposed that would improve our understanding of particle physics. Most of these are e^+e^- machines geared towards improving Higgs precision studies. They include the International Linear Collider (ILC) [22], Compact Linear Collider (CLIC) [23], Circular Electron Positron Collider (CEPC) [6], and the Future Circular collider (FCC-ee) [24]. These colliders would operate just above the threshold of a Higgs in association with one or two of the other weak scale particles. They could improve precision constraints on Higgs coupling to other SM particles by an order of magnitude. Finally, a 100 TeV proton-proton collider has also been proposed. One obvious advantage it would have over the e^+e^- machines is the increased center of mass energy, which would increase the accessibility of TeV scale physics. A 100 TeV collider [1] could also shed light on the tri-Higgs coupling to 10$\%$ accuracy, which would be impossible to achieve at an electron-positron collider. Currently, these collider proposals are at early stages of development, and it remains to be seen if they achieve fruition.

1.7 Outline of Thesis

The beginning of this work has sought to introduce the SM, its problems and possible solutions. It has also emphasized the study of Higgs precision physics at colliders.

However, in order to adequately study the Higgs, it is also important to have a working understanding of SM backgrounds. One such background process, SM WW production, reported 3 sigma excesses in early Run 1 of the LHC. This led to excitement for the possibility of elusive new physics. However before embarking on enumerating new physics scenarios that would fit this excess, it was important to check the robustness of the theory - experiment disagreement.

It is important to mention that the SM WW process suffers from its own dominant background, from top physics. In order to suppress this and improve the signal-background ratio, jets with transverse momentum higher than 25 GeV are vetoed. Introduction of this new scale spoils perturbation theory that is usually adequate to predict inclusive cross-sections. This break-down of perturbation theory is remedied by resummation; systematically taking into account the leading terms from every order. For most cross-sections, this effect is captured by parton showers incorporated in MonteCarlo simulations which resum at the lowest possible order.

In Chapter 2, we perform transverse momentum resummation at higher order, since transverse momentum and the jet p_T are related variables. This leads to changes in the shape of cross-sections and a reweighting method is prescribed to improve accuracy of MonteCarlo simulations. In Chapter 3, the interplay between jet-veto and transverse momentum resummation is analyzed, providing credence to capturing jet effects through transverse momentum. Chapter 4 deals with jet-veto resummation to an even higher order, and the same cross-section is estimated to hitherto unattained accuracy. A common result from all these Chapters suggest a significant change in the theoretically computed jet-veto cross-section from MonteCarlo predictions, resulting in better experiment-theory agreement.

Next, in Chapter 5, we study an important consequence of precision Higgs studies: understanding the nature of the electroweak phase transition. The phase transition takes place in the early universe where finite temperature effects are important and depend on the details of the Finite temperature Higgs potential. These effects cannot be recreated directly in a lab and need to be studied indirectly through the fact that all finite-temperature effects can be estimated by the zero-temperature Lagrangian. Thus deviations in finite temperature from SM cosmology, are tied to deviations in zero-temperature Higgs precision. In order to compete with increasing zero-temperature Higgs precision, improvements are carried out to state-of-the-art finite temperature field theory by relaxing certain approximations. Consequences to the interplay between precision Higgs measurements and the possibility of a first-order phase transition are reexamined.

Finally, in Chapter 6, we present another implication of Higgs precision studies. Top partners predicted by theories that solve the Hierarchy problem while making minimal assumptions on the rest of the new physics particle spectrum still require them to be coupled to the Higgs boson. Thus electroweak scale top partners as required by notions of naturalness imply that they affect Higgs precision. Limits on top partner masses are set from this principle. Ways to hide top partners from Higgs precision measurements are described as well as ways to circumvent them.

Overall, this thesis seeks to highlight various facets of studying the Higgs boson, from SM backgrounds to consequences of Higgs precision to well-motived new physics.

Chapter 2

Transverse momentum resummation effects in W^+W^- measurements

2.1 Introduction

The Standard Model (SM) of particle physics has been tested at a new energy frontier by the Large Hadron Collider (LHC). SM cross sections were measured at both 7 and 8 TeV, and the SM has passed with flying colors in almost every channel. Nevertheless there has been one channel that is consistently off at the LHC for both the ATLAS and CMS experiments, the W^+W^- cross section measured in the fully leptonic final state. This state is naively one of the most straightforward channels to measure both theoretically and experimentally as it is an electroweak final state with two hard leptons. However, at 7 and 8 TeV ATLAS [25, 26] and CMS[27, 28] have measured a discrepancy with the SM NLO calculation [29, 30] of $\mathcal{O}(20\%)$ and this extends to differential measurements not just simply an overall rescaling.

This discrepancy is particularly compelling for a number of reasons. First and foremost, one of the most important channels for the Higgs is the W^+W^- decay channel of which SM W^+W^- is the largest background. Since this channel doesn't have a particular kinematic feature akin to bumps in the $\gamma\gamma$ or ZZ channels, it is important to understand the shape of the SM background quite well. CMS [31] and ATLAS[32] use data driven techniques to extrapolate and find the signal strength of the Higgs. While these data driven techniques are validated in many ways, it's often times difficult to find perfectly orthogonal control regions and correlations may arise at higher order in theoretical calculations or because of new physics contributions. Given the shape differences observed, whether or not this is due to an insufficient SM calculation or new physics, it is important to understand that there could possibly be effects which alter the signal strength of the Higgs when the SM W^+W^- channel is understood better [33].

Another compelling reason for understanding the discrepancy is the possibility of new sub TeV scale physics. The dilepton + MET final state is an important background to many searches, but even more so, the large $\mathcal{O}$(pb) discrepancy currently observed still allows for the possibility of new $\mathcal{O}(100)$ GeV particles. While models of this naively would have been ruled out by previous colliders, or other searches at the LHC, in fact it turns out that there could be numerous possibilities for physics at the EW scale. These include Charginos[34], Sleptons[35], Stops[36, 37, 38] or even more exotic possibilities[39]. Remarkably, as first shown in[34], not only could new physics be present at the EW scale, it in fact can *improve* the fit to data compared to the SM significantly, because it preferentially fills in gaps in the differential distributions when new physics is at the EW scale. In particular the possibility of particles responsible for naturalness in SUSY being at the weak scale and realizing a solution of the hierarchy problem makes this particularly compelling given all the negative results in other channels.

Finally, It is particularly interesting simply from the point of QCD and the SM to understand why the W^+W^- channel has a persistently discrepant experimental result compared to SM predictions when other similar uncolored final states e.g. ZZ and WZ seem to agree quite well with experiment. There are potential theoretical reasons within the SM that could explain the difference compared to experiment and to other EW channels. One of the first points that could be addressed in the context of the W^+W^- measurement is whether or not the fixed order calculation was sufficient to describe the data. Currently the W^+W^- channel is formally known at NLO, and this is implemented in various NLO MC generators employed by ATLAS and CMS in their analyses. However, partial NNLO results are also incorporated, since $gg \to W^+W^-$ via a quark loop is included through the generator gg2VV[40, 41]. The merging of NLO WW and WWj predictions have been investigated in [42, 43, 44], while approximate calculations for higher order corrections to $gg \to W^+W^-$ are performed in [45]. Theoretically the full NNLO calculation of W^+W^- production turns out to be quite difficult, but within the past year there has been a great deal of progress; the complete NNLO calculation for ZZ total cross section has recently been completed[46]. The results of[46] are interesting, given that compared to NLO, the NNLO effect can be sizable $\mathcal{O}(10\%)$. However, when examined closely, if the full NNLO results are compared to the NLO + $gg \to ZZ$ the difference is less than $\mathcal{O}(5\%)$. Given this result for ZZ, unless there were large differences from a channel with very similar contributions, it would be highly unlikely that the full NNLO result could explain the discrepancies in the W^+W^- result.

There can be effects beyond the fixed order calculation that matter as well. As with any calculation there are additional logarithms that arise whenever there is an extra scale in the problem, for instance threshold resummation logs, or logs of the transverse momentum of the system compared to the hard scale of the system. These logarithms can either change the overall cross section as in the case of threshold resummation, or the shape of the p_T distribution in p_T resummation. In [47] the threshold resummation effects were calculated to approximate NNLL accuracy for W^+W^- production, and the effects were found to be small for the overall cross section of $\mathcal{O}(.5 - 3\%)$ compared to NLO (the NNLO calculation would largely include these logs and thus these effects shouldn't be taken independently in magnitude). Another contribution which primarily effects the overall cross section, comes from π^2 resummation[48, 49, 50]. This has yet to be computed for W^+W^- , however it would affect other EW channels similarly, so the W^+W^- channel shouldn't be singled out and it clearly doesn't explain a discrepancy of $\mathcal{O}(20\%)$ as measured in that channel.

While the aforementioned effects primarily affect total cross-section, there are avenues that change the shape in a differential direction while keeping the total cross section constant. One such effect is p_T resummation first calculated for W^+W^- in[51, 52]. An interesting difference that arises with p_T resummation, compared to threshold resummation, is the interplay between the effects of resummation and the way the cross section is measured for W^+W^- . Given that p_T resummation changes the shape of the p_T distribution, and the p_T distribution would be a delta function at 0 at the Born level, QCD effects are crucial for getting this distribution correct. These effects are normally sufficiently accounted for by using a Parton Shower (matched to LO or NLO fixed order) which only approaches NLL accuracy. However, in the W^+W^- channel compared to the $W^{\pm}Z$ and ZZ channels there is an additional jet veto requirement for the measurement. This requirement arises because there is an overwhelming background to W^+W^- coming from $t\bar{t}$ production and decay. The most straightforward way to reduce the $t\bar{t}$ background is to veto on extra jets to isolate the W^+W^- contribution. Given this jet veto, and the correlation between jet veto efficiency and the p_T shape of the W^+W^- system, there is an added sensitivity to the jet veto and the shape of the p_T distribution that other channels typically don't have. There is precedent for turning to p_T resummation rather than using a parton shower alone when shape differences are important, e.g. the W mass measurement at the D0[53].

In this paper we will examine the detailed effects of p_T resummation at approximate NNLL accuracy when combined with how the experimental measurements are performed. Typically the comparison between p_T resummed processes e.g. Drell-Yan or ZZ is done at the unfolded level experimentally. However, the extrapolation from the fiducial cross section to the inclusive cross section can be the source of the discrepancy and a new analysis has to be carefully performed to understand the W^+W^- channel. The difficulty in doing this of course is that in the context of p_T resummation, all radiation is inclusively summed without reference to a jet algorithm, and there is no jet-veto that can be explicitly performed. In light of this, we undertake a procedure similar to what is done for Higgs production predictions at the LHC using HqT[54] to predict the transverse momentum distribution of the Higgs. We investigate the effects of taking NLO + parton shower generated events for W^+W^- , reweighting them with the NNLL resummed p_T distribution before cuts, and then applying the cuts to find the fiducial cross section, and how the total cross section should be interpreted. We find that this leads to $\mathcal{O}(3-7\%)$ changes in the total cross section, for central choices of scales, which reduces the discrepancy. Additionally, we find that differential distributions are improved.

A jet veto introduces an additional scale and thus logs related to this scale. Such logs are not identical to the logs accounted for by p_T resummation. A program of jet veto resummation [55, 56, 57, 58, 59, 60, 61, 62] would in principle be required to isolate these effects. These logs are clearly not taken account in our calculation explicitly due to the fact that there are no jets in our resummation calculation. Nevertheless, as mentioned earlier, the probability of an event passing the jet veto and the transverse momentum of the W^+W^- system is strongly correlated, therefore in the process of reweighting the parton showered events and using a jet algorithm, there is a large overlap between the logs accounted for in jet veto resummation, and the logs accounted for in our procedure. This correlation was observed for instance in [55], where for Higgs and Drell-Yan the effects of reweighting the p_T distribution agreed very well with the jet-veto efficiency coming from a jet veto resummation calculation. Given that Higgs production is dominated by gluon initial states, we expect the agreement between reweighting and jet-veto resummation to be even better for W^+W^- . An additional motivation for performing p_T resummation and reweighting is that we can perform detector simulations on the fully exclusive events, and predict differential observables. In particular, the p_T distribution of the W^+W^- system, which ATLAS has shown at 7 and 8 TeV, has had a shape discrepancy which we find is in better agreement when performing p_T resummation. In the context of a jet veto resummation calculation alone it is impossible to predict this shape without resorting to a reweighting procedure as well. Nevertheless, it would be interesting to understand the interplay of jet veto and p_T resummation effects even further which we leave to future work.

The rest of the paper is structured as follows. In Section 2.2, we outline our methodology and calculation of the NNLL resummed W^+W^- p_T distribution. In Section 2.4 we explicitly describe our reweighting procedure, and demonstrate the effects on the total cross section at various energies from different NLO generators and parton showers. Finally, in Section 3.6, we discuss the implications of these results both for scale choices used in resummation and the associated errors as well as how to test these effects in other channels. In particular, given the similarity in scales of W^+W^- , $W^\pm Z$ and ZZ processes, and the fact that resummation does not differentiate with respect to the hard matrix element, if resummation effects are responsible for even part of the discrepancy as currently measured there are distinct predictions in other channels.

2.2 W^+W^- transverse momentum resummation

The resummation method

For hadron collider production of electroweak bosons with invariant mass M and transverse momentum p_T, the fixed-order perturbative expansion acquires powers of large logarithms, $\alpha_s^n \log^m (M/p_T)$, with $m \leq 2n-1$, which can be resummed to all orders [63, 64, 65, 66, 67, 68, 69, 70, 71, 72]. We implement the method of Refs. [73, 74] to calculate the WW transverse momentum distribution at partial NNLL+LO.[1] Some aspects of the method are outlined below. The factorized cross section is

$$\frac{d\sigma^{WW}}{dp_T^2}(p_T, M, s) = \sum_{a,b} \int_0^1 dx_1 \int_0^1 dx_2\, f_{a/h_1}\left(x_1, \mu_F^2\right) f_{b/h_2}\left(x_2, \mu_F^2\right) \frac{d\hat{\sigma}_{ab}^{WW}}{dp_T^2}\left(p_T, M, \hat{s}, \alpha_s\left(\mu_R^2\right), \mu_R^2, \mu_F^2\right), \tag{2.2.1}$$

where f_{a/h_1} and f_{b/h_2} are the parton distribution functions for the parton species a and b in the two colliding hadrons, $\hat{s} = sx_1x_2$ is the partonic center of mass energy, and $d\hat{\sigma}_{ab}^{WW}/dp_T^2$ is the partonic cross section. The partonic cross section will be the sum of a resummed part and a finite part; the finite part matches resummation with fixed order calculations. In our case, we will give approximate NNLL+LO results which effectively include the exact LO results at $O\left(\alpha_s\left(\mu_R^2\right)\right)$, plus approximate NNLL resummation correction terms at $O\left(\alpha_s^n\left(\mu_R^2\right)\right)$, $2 \leq n \leq \infty$.

The quantity that is resummed directly is actually the double transform of the partonic cross section,

$$\mathcal{W}_{ab,N}^{WW}\left(b, M; \alpha_s\left(\mu_R^2\right), \mu_R^2, \mu_F^2\right), \tag{2.2.2}$$

where b, the impact parameter, is the Fourier transform moment with respect to p_T, while N is the Mellin transform moment with respect to $z = M/\hat{s}$. To invert the Mellin transform, we use the standard formula

$$\mathcal{W}_{ab}^{WW}\left(b, M, \hat{s} = M^2/z; \alpha_s\left(\mu_R^2\right), \mu_R^2, \mu_F^2\right) = \int_{c-i\infty}^{c+i\infty} \frac{dz}{2\pi i}\, z^{-N} \mathcal{W}_{ab,N}^{WW}\left(b, M, \alpha_s\left(\mu_R^2\right), \mu_R^2, \mu_F^2\right) \tag{2.2.3}$$

---

[1] In our convention, LO p_T distribution is at the same α_s order as the NLO total cross section.

where c, a positive number, is the intercept between the integration contour and the real axis. In numerical implementations, the contour is deformed to the left on both the upper and lower complex planes, leaving the integral invariant but improving numerical convergence. To perform the convolution in Eq. Eq. (**??**), we fit the parton distribution functions with simple analytic functions [75] to obtain analytical Mellin transforms. We multiply the Mellin transform of the parton distribution functions with the Mellin transform of the partonic cross section, before we actually invert the transform. The error associated with fitting is less than 10^{-3}.

To invert the Fourier transform in Eq. Eq. (**??**), we use

$$\begin{aligned} \frac{d\hat{\sigma}_{ab}^{WW}}{dp_T^2}\left(p_T, M, \hat{s}, \alpha_s\left(\mu_R^2\right), \mu_R^2, \mu_F^2\right) &= \frac{M^2}{\hat{s}} \int \frac{d^2\mathbf{b}}{4\pi} e^{i\mathbf{b}\cdot p_T}\, \mathcal{W}_{ab}^{WW}\left(b, M, \hat{s}, \alpha_s\left(\mu_R^2\right), \mu_R^2, \mu_F^2\right) \\ &= \frac{M^2}{\hat{s}} \int \frac{d^2\mathbf{b}}{4\pi} \frac{b}{2} J_0\left(b p_T\right) \mathcal{W}_{ab}^{WW}\left(b, M, \hat{s}, \alpha_s\left(\mu_R^2\right), \mu_R^2, \mu_F^2\right). \end{aligned} \tag{2.2.4}$$

The double transform in Eq. Eq. (**??**) contains large logarithms of the form $\sim \log(M\, b)$ which correspond to $\sim \log\left(M/p_T\right)$ before the Fourier transform. Ignoring the finite term from matching to fixed-order results, the large logarithms are resummed to all order by exponentiation (omitting summation over flavor indices, which is needed when multiple parton flavors mix under DGLAP evolution) [73],

$$\begin{aligned} \mathcal{W}_{ab,\,N}^{WW}\left(b, M; \alpha_s\left(\mu_R^2\right), \mu_R^2, \mu_F^2\right) = \mathcal{H}_N^{WW}&\left(M, \alpha_s\left(\mu_R^2\right); M^2/\mu_F^2, M^2/Q^2\right) \\ &\times \exp\left\{\mathcal{G}_N\left(\alpha_s\left(\mu_R^2\right), L; M^2/\mu_R^2, M^2/Q^2\right)\right\}, \end{aligned} \tag{2.2.5}$$

where the $\mathcal{H}_{NN}^{WW}$ function is only sensitive to physics at the scale comparable with M and hence does not depend on b. On the other hand, the function $\mathcal{G}_N$ is sensitive to physics at the scale of $1/b \sim p_T$, and is exponentiated to all orders in α_s. The quantity L is defined as

$$L \equiv \ln \frac{Q^2 b^2}{b_0^2}, \quad b_0 \equiv 2e^{-\gamma_E} \approx 1.12, \tag{2.2.6}$$

where Q, termed the resummation scale, is chosen to be comparable in magnitude to the hard scale of the process. It is an inherent ambiguity in resummation calculations, in addition to the usual μ_R and μ_F ambiguities for fixed order calculations.

The exponent in Eq. Eq. (**??**) can be expanded in successive logarithmic orders [73, 76]

$$\begin{aligned}\mathcal{G}_N\left(\alpha_s, L; M^2/\mu_R^2, M^2/Q^2\right) = {} & L g^{(1)}\left(\alpha_s L\right) + g_N^{(2)}\left(\alpha_s L; M^2/\mu_R^2, M^2/Q^2\right) \\ & + \frac{\alpha_s}{\pi} g_N^{(3)}\left(\alpha_s L; M^2/\mu_R^2, M^2/Q^2\right) \\ & + \sum_{n=4}^{+\infty}\left(\frac{\alpha_s}{\pi}\right)^{n-2} g_N^{(n)}\left(\alpha_s L; M^2/\mu_R^2, M^2/Q^2\right). \qquad (2.2.7)\end{aligned}$$

This expansion makes sense if we regard $\alpha_s L$ as of order unity. The $g^{(1)}$ term is the leading logarithmic (LL) term, while $g^{(2)}$ and $g^{(3)}$ are the NLL and NNLL terms, and so on. The variation of Q shuffles terms between the fixed order and resummed terms and can give an estimate for as yet uncomputed higher Logs.

An alternative representation [73, 72] of Eq. Eq. (**??**) is (for illustration, we give the expression that is valid when there is a single parton flavor)

$$\mathcal{G}_N\left(\alpha_s, L; M^2/\mu_R^2, M^2/Q^2\right) = -\int_{b_0^2/b^2}^{Q^2} \frac{dq^2}{q^2}\left[A(\alpha_s(q^2)) \ln\frac{M^2}{q^2} + \tilde{B}_N(\alpha_s(q^2))\right], \qquad (2.2.8)$$

$$\tilde{B}_N(\alpha_s) \stackrel{\text{def}}{=} B(\alpha_s) + 2\beta(\alpha_s)\frac{d\ln C_N(\alpha_s)}{d\ln\alpha_s} + 2\gamma_N(\alpha_s), \qquad (2.2.9)$$

where $A(\alpha_s)$ and $B(\alpha_s)$ come from the Sudakov form factor, while $C_N(\alpha_s)$ is related to the perturbative generation of transverse momentum dependent parton distributions from collinear parton distributions, and $\gamma_N(\alpha_s)$ is the moment-space expression for the DGLAP splitting kernel. We include $A(\alpha_s)$ to α_s^3 order, $B(\alpha_s)$ to α_s^2 order, the DGLAP splitting kernel γ_N to α_s^2 order (i.e. NLO), and the $C_N(\alpha_s)$ coefficient to α_s order. Most of the above ingredients are available in [73, 72], except the α_s^3 order piece of $A(\alpha_s)$ which is calculated in [77]. We re-used part of the QCD-Pegasus code [78] to calculate the NLO DGLAP splitting kernel in complex moment space. The spin-averaged one-loop virtual correction to $q\bar{q} \to W^+W^-$, computed in [29], is absorbed into the order α_s flavor-diagonal part of the C_N function. We also do not have the full two-loop virtual corrections to the $q\bar{q} \to W^+W^-$ amplitude. Therefore, our results have approximate NNLL accuracy.

To ensure that the resummed and matched prediction preserves the NLO total cross section, in Eq. Eq. (**??**) we shift L from the definition Eq. Eq. (**??**) to the modified value $\ln\left(Q^2 b^2/b_0^2 + 1\right)$, which imposes $G_N = 0$ when $b = 0$. This shift does not affect the low p_T region to leading power in p_T/M.

2.3 Numerical results

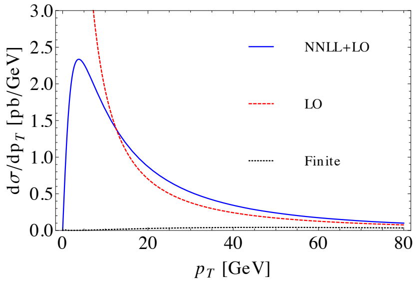

Figure 2.1: Plot of resummed, finite (matching) and fixed-order W^+W^- transverse momentum distributions from 8 TeV proton collisions. Note that the LO p_T distribution has the same α_s order as the NLO total cross section.

The full details about the underlying resummation formalism, in particular the diagonalization of the DGLAP splitting kernel in the multi-flavor case, and the matching to fixed-order calculations, are covered in [73, 74] and will not be repeated here. We now go on to present numerical results. To make sure our numerical implementation is correct, we have reproduced the Z-boson resummed transverse momentum distribution in [74], including effects of varying the resummation scale Q.

We use the MSTW 2008 NLO parton distribution functions [79]. The central scales we use are $\mu_R = \mu_F = 2m_W$, $Q = m_W$. In fig. 2.1, we plot the resummed, fixed-order, and finite part of the W^+W^- transverse momentum distribution using central scales for 8 TeV pp collisions to make it easier for future studies to compare results directly. We can see that resummation cures the $p_T \to 0$ divergence of the LO distribution and generates substantial corrections. The total cross section obtained from integrating our p_T distribution agrees with exact fixed order results to better than 0.5%, which is a consistency check for our numerical accuracy.

To assess perturbative scale uncertainties, we simultaneously vary μ_R and μ_F up and down by

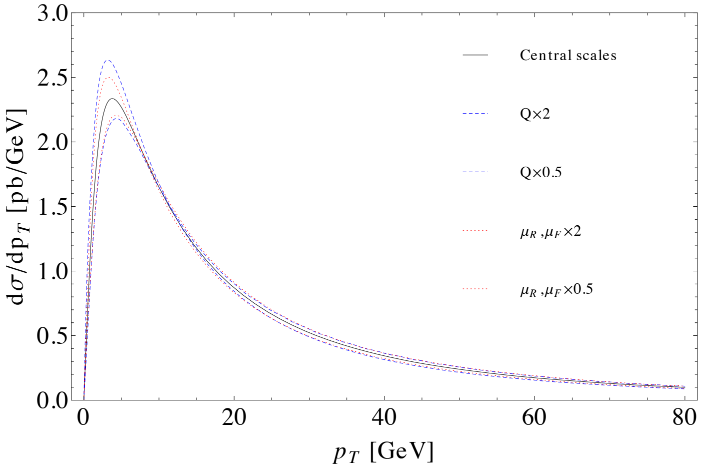

Figure 2.2: Plot of renormalization, factorization and resummation scale variations of the W^+W^- transverse momentum distribution for 8 TeV collisions.

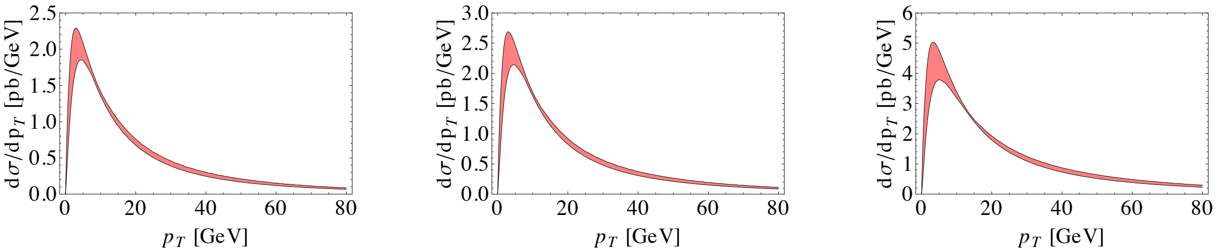

Figure 2.3: NNLO+LO predictions, with error bands, for the W^+W^- transverse momentum distribution for 7,8 and 14 TeV collisions.

a factor of 2, and separately vary Q up and down by a factor of 2. The resulting variations in the transverse momentum distributions are plotted in Fig. 2.2 for 8 TeV collisions. We can see that the largest scale uncertainties result from varying the resummation scale Q. By adding μ_R & μ_F variations and Q variations in quadrature[2], we produce the distribution with error bands, for 7, 8 and 14 TeV, shown in Fig. 2.3. if The combined scale uncertainty at the peak of the distribution is around $\pm 10\%$ for each collision energy.

We now briefly mention non-perturbative effects. In Eq. Eq. (**??**) $\mathcal{W}_{ab}^{WW}$ in fact becomes

---

[2] For example, if the simultaneous variation of μ_R & μ_F up and down by a factor of 2 produces a variation of $+a_1\,/-b_1$, and similarly the Q variation produces a variation of $+a_2\,/-b_2$, we take the combined scale uncertainty to be $+\sqrt{a_1^2+a_2^2}\,/-\sqrt{b_1^2+b_2^2}$. This procedure for combining uncertainties is used throughout.

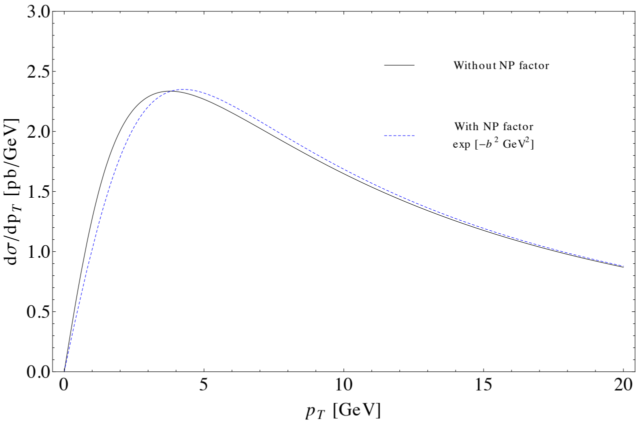

Figure 2.4: NNLL+LO prediction for the WW transverse momentum distribution at 8 TeV, with and without the non-perturbative Gaussian smearing factor $\exp\left[-1\,\mathrm{GeV}^2\,b^2\right]$.

singular at large b due to the divergence of the QCD running coupling below the scale Λ_{QCD}. This is a non-perturbative issue and becomes important at low p_T. Many prescriptions for regulating the non-perturbative singularity exists, such as the b^* model [67, 71] and the minimal prescription [80]. We adopt a simple cutoff at $b = 2\mathrm{GeV}^{-1}$ for the choice of resummation scale $Q = 2m_W$ and $b = 4\mathrm{GeV}^{-1}$ for $Q = m_W$ and $Q = m_W/2$, and give results both with and without an additional non-perturbative Gaussian smearing factor of $\exp\left[-g_{NP}^2\,\mathrm{GeV}^2\,b^2\right]$ with $g_{NP} = 1$. The W^+W^- fiducial cross sections after reweighting parton shower events, only differ by about 1% with and without the Gaussian smearing factor, much smaller than the perturbative scale uncertainties we will encounter. In Fig. 2.4 we compare the predicted WW transverse momentum distribution with and without the Gaussian smearing factor. The smearing causes the peak to shift by about 0.5 GeV to larger p_T.

There are of course uncertainties not directly related to our calculation, for instance using different PDF sets can have a few percent effect as demonstrated in [26]. Since the PDF uncertainties affect both the resummed result and the parton shower result, we expect the effect to largely cancel in the reweighting factor.

Finally, we compare our p_T distribution at 8 TeV with the SCET-based resummation calculation by [52] in Fig. 2.5. The results are in good agreement, but our results show a larger error band because we varied both μ_R (with μ_F locked to be equal to μ_R) and the resummation scale Q, the latter of which indicates ambiguities in splitting contributions into the resummed part and the finite part, while the calculation by [52] only considers the variation of one scale.

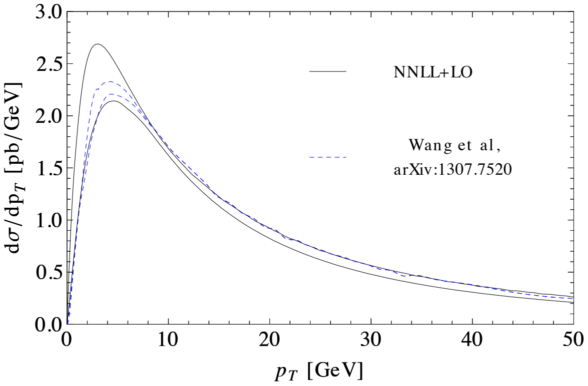

Figure 2.5: Comparision of our resummed WW p_T distribution with a SCET-based resummation calculation, with error bands shown for both.

2.4 Transverse Momentum Reweighting and Fiducial Cross Sections

The transverse momentum resummation shown in Section 2.2 systematically improves our understanding of the p_T distribution of the diboson system. However, the W^+W^- p_T distribution as measured by the LHC experiments is not the same as the distribution that is calculated in Section 2.2. This is because the detector only measures a certain fiducial region of phase space, there are additional cuts put on the physics objects to reduce backgrounds, and finally there are detector effects which smear the p_T distribution compared to the theoretical prediction. In very clean channels such as Drell-Yan or ZZ production, these effects can be unfolded more easily, and an unambiguous prediction for the p_T of the system can be compared to theoretical predictions. For W^+W^- the effects are more difficult to unfold and as of yet a full analysis has yet to be compared to the experimental results for the W^+W^- diboson system's p_T . In fact, only ATLAS has released a distribution, the vector sum of the p_T of the leptons and MET, directly correlated to the p_T of the diboson system.

In order to compare to data, we must implement the same cuts that the experiments perform. Immediately this runs into potential problems as the distributions predicted in Section 2.2 are fully inclusive, and even at the leptonic level there are cuts that restrict the distributions to a fiducial phase space. To circumvent these difficulties we implement a reweighting procedure on generated events for the p_T of the system prior to cuts, and then perform the analysis cuts to find the effects of p_T resummation. This of course isn't a perfect matching of the effects of resummation and data, but without unfolded distributions this is the closest possible comparison that can be made at this point. This procedure is akin to that used for predicting the Higgs signal at the LHC, where the transverse momentum resummed shape, taken from HqT for instance[81], is used to reweight the MC simulated events.

It is possible that a comparison between reweighted events after experimental cuts and the original Monte Carlo events *could* predict the same cross section. The formalism we use by definition does not change the total inclusive cross section. However, if the reweighted distributions that have a different shape are also cut on, then this will effect the total measured cross section. This happens because the cuts change the fiducial cross section and hence the inferred total cross section once the acceptances and efficiencies are unfolded. As we will show, there isn't a direct cut on the reweighted p_T distribution, but the jet veto cut is highly correlated with it and significantly effects the extrapolated total cross section. Additionally, the cause of the correlation will also reflect that different underlying Monte Carlo generators and parton showers will have different size effects when extrapolating to the total cross section. These differences are demonstrated in Figure 2.6 where the p_T distributions predicted by resummation are compared to various Monte Carlos (POWHEG BOX[82, 83, 84], MadGraph/aMC@NLO and matched Madgraph 0j+1j[85]) in combination with different parton showers from Herwig++[86] and Pythia8[87]. MSTW2008 NLO pdf sets were used for all NLO event generations to be consistent with resummation and CTEQ6 LO pdf[88] was used for the Madgraph 0+1j analysis.

Since the resummation procedure predicts $p_{T_{WW}}$ shape, we reweight with respect to truth level events i.e. $p_{T_{WW}}$ just after the shower but before detector simulation. To perform the reweighting procedure, resummed theory curves from Section 2.2 and MC events are binned into 0.5 GeV bins

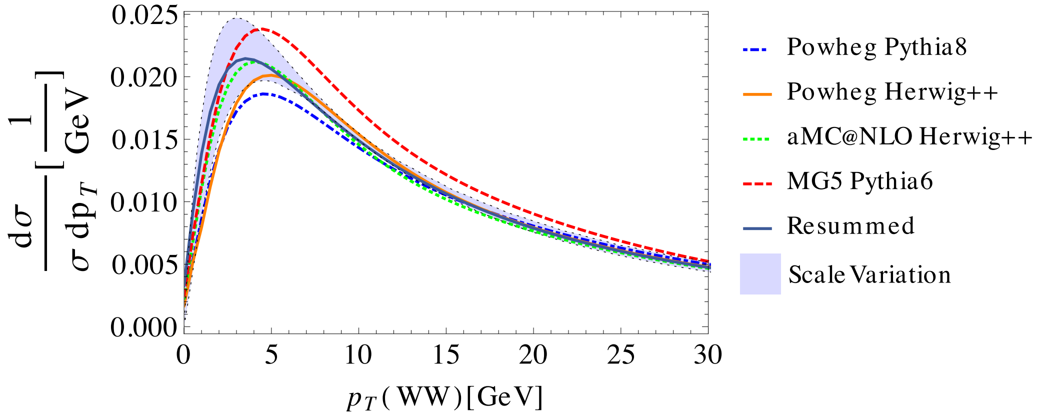

Figure 2.6: Plot of Resummation predicted and MC+shower predictions for W^+W^- transverse momentum distributions at 8 TeV. The shaded region represents the scale Q variation by a factor of 2 relative to the central scale choice $Q = m_W$ for the resummation prediction.

along $p_{T_{WW}}$. A reweighting factor is then computed

$$F[p_T] = \frac{\text{Resummed bin}[p_T]}{\text{MC bin}[p_T]}. \tag{2.4.1}$$

To approximate detector effects MC events are then smeared using Delphes[89] for a fast detector simulation[1]. Finally, once detector level events are produced we apply the cuts performed by the LHC experiments. An example of the cuts implemented by the ATLAS measurement at 7 TeV is reproduced below in Table 2.1. The cuts from CMS are quite similar, the jet veto as we will show turns out to be the most important effect, and CMS has a jet veto of 30 GeV compared to 25 GeV for ATLAS. We comment on this slight difference in Section 3.6, however, since CMS hasn't produced a plot of the p_T of the W^+W^- system similar to ATLAS, we adopt the ATLAS cuts when demonstrating the effects of using the p_T resummed reweighted distributions. Pythia8 was

---

[1] The detector simulation is important to match data, as the p_T distribution of the diboson system predicted by MC@NLO[90] shown by ATLAS can not be matched without additional smearing of the MET. We demonstrated this with both PGS and Delphes. In the end however, this smearing does not effect the resummation reweighting effects shown here, because the underlying MC events and resummed reweighted events are affected in the same way. We have demonstrated this explicitly by changing the MET resolution by a factor of 2 each way, which simply shifts the peak of the p_T distribution.

used with default tuning and since all our results are shape dependent, the reweighting procedure should be performed again using our resummation-theory curves when using a non-default Pythia8 tuning.

Exactly two oppositely-sign leptons, $p_T > 20\mathrm{GeV}, \mathrm{p}_{\mathrm{T}_{\mathrm{leading}}} > 25\mathrm{GeV}$
$m_{ll'} > 15, 15, 10\mathrm{GeV}$ (ee,$\mu\mu$,$e\mu$)
$\lvert m_{ll'} - m_Z \rvert > 15, 15, 0\mathrm{GeV}$ (ee,$\mu\mu$,$e\mu$)
$E^{\mathrm{miss}}_{T,\mathrm{Rel}} > 45, 45, 25\mathrm{GeV}$(ee,$\mu\mu$,$e\mu$)
Jet Veto $25\mathrm{GeV}$
$p_{T\,ll'} > 30\mathrm{GeV}$

Table 2.1: ATLAS cut flow for 7 TeV analysis[25]

2.5 Reweighting Results

We perform the reweighting as described above using a central scale $Q = m_W$ as well as varying the resummation scale Q up and down by a factor of 2 while keeping μ_R and μ_F fixed. We define the percentage difference caused by reweighting as

$$\text{percentage difference} = \frac{(\text{events}_{\text{res}} - \text{events}_{\text{MC}}) \cdot 100}{\text{events}_{\text{MC}}} \tag{2.5.2}$$

where

- events_{MC} is events predicted by the MC before reweighting
- events_{res} is events after reweighting the MC events.

with a positive percentage difference implying an increase in the theoretical prediction on σ_{Fid}. To demonstrate the effects of other scale variations on σ_{Fid} we also varied μ_R and μ_F as well as the non-perturbative factor discussed in Section 2.2 and report the percentage differences compared to Powheg +Pythia8 (8 TeV) as an example in Table 2.2.

Scale Choice	% difference	% difference with $g_{\text{NP}} = 1$
Central ± Combined error	$6.5^{+5.0}_{-3.0}$	$6.4^{+5.0}_{-3.0}$
Central scales, $Q = m_W$, $\mu_R = \mu_F = 2m_W$	6.5	6.4
$Q = 2\times$central	5.0	4.8
$Q = 0.5\times$central	10.8	10.6
$\mu_R = \mu_F = 0.5\times$central	3.9	3.8
$\mu_R = \mu_F = 2\times$central	9.2	9.0

Table 2.2: Percentage differences of reweighted theory predictions compared to Powheg+Pythia8 at 8 TeV for σ_{Fid} and various choices of scale. The 2nd column does not include the Gaussian smearing factor for non-perturbative effects, while the 3rd column includes a non-zero non-perturbative factor $g_{NP} = 1$ typical for quark dominated initial states.

We find that as observed in Section 2.2, the Q variation leads to a larger percentage difference than the μ_F or μ_R scale variation. The non-perturbative factor g_{NP} shifts the peak of the underlying p_T distributions slightly, but in the end has a minimal effect on the cross section. We show the effects of reweighting on MC generators and parton showers in Tables 2.3, 2.4, 2.5 for 7,8 and 14 TeV respectively.

MC + Parton Shower	Corrections (%)
Powheg+Pythia8	$6.4^{+4.7}_{-2.8}$
Powheg+Herwig++	$3.8^{+4.5}_{-2.6}$
aMC@NLO+Herwig++	$3.3^{+5.0}_{-3.0}$

Table 2.3: Percentage differences for σ_{Fid} of reweighted theory predictions compared to MCs+Parton Showers at 7 TeV.

MC + Parton Shower	Corrections (%)
Powheg+Pythia8	$6.5^{+5.0}_{-3.0}$
Powheg+Herwig++	$3.8^{+4.3}_{-2.5}$
aMC@NLO+Herwig++	$3.1^{+5.0}_{-3.0}$
MADGRAPH LO+Pythia6	$-9.6^{+4.4}_{-2.7}$

Table 2.4: Percentage differences for σ_{Fid} of reweighted theory predictions compared to MCs+Parton Showers at 8 TeV.

MC + Parton Shower	Corrections (%)
Powheg+Pythia8	$7.0^{+6.4}_{-5.1}$
Powheg+Herwig++	$4.4^{+5.9}_{-4.7}$
aMC@NLO+Herwig++	$4.2^{+6.5}_{-5.2}$

Table 2.5: Percentage differences for σ_{Fid} of reweighted theory predictions compared to MCs+Parton Showers at 14 TeV.

To demonstrate the effects on differential distributions, we use the ATLAS cutflows and show the predictions of p_T resummation for the 7 TeV ATLAS study[25] compared to the original MC@NLO+Herwig++ results used by ATLAS. In Figure 2.7, we plot the four distributions shown in [25]. As can be seen in Figure 2.7, p_T reweighting can improve the differential distributions somewhat, but is not capable of explaining the full discrepancy using a central choice of scales. With further statistics at the next run it would be useful for the experiments to start to quantify these shape discrepancies rather than simply reporting the total cross section.

To demonstrate the effects at 8 TeV we show the distribution most affected, $p_T(ll + E_T^{\text{miss}})$, in Figure 2.8 using the same cutflows and different generators. This distribution is directly correlated with the p_T of the diboson system predicted by resummation, and shows the variation compared to MC generators + parton showers. The largest discrepancy compared to MC comes from the use of Powheg+Pythia8, while both Powheg and aMC@NLO are in much better agreement when

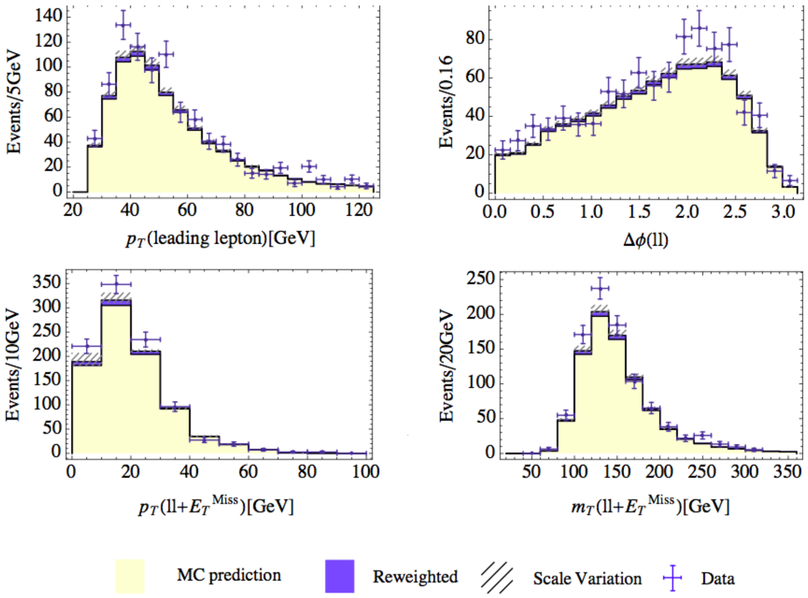

Figure 2.7: aMC@NLO+Herwig++ observables histogrammed for W^+W^- transverse momentum distribution for 7 TeV collisions and including the reweighting correction.

Herwig++ is used as the parton shower. However, this does not mean the effects of the parton shower are the sole cause of the discrepancy. In the fractional difference shown in Figure 2.8, we see the roughly the same shape dependence for both Powheg curves, but the overall magnitude is reduced for Powheg+Herwig++ compared to Powheg+Pythia8.

2.6 Jet Veto

As we have shown thus far, even though the inclusive total cross-sections are the same by design, there are appreciable corrections to the fiducial cross section after reweighting. This means that some of the cuts are well correlated with the p_{TWW} variable and seem to preferentially select the low p_{TWW} region where the resummation curve dominates all the MCs except Madgraph LO. The percentage change due to reweighting at each cut level was analyzed, and as an example the effects of reweighting at each state in the cut flow is shown for Powheg-Pythia8 at 8 TeV in Table 2.6. The jet veto stage is the largest contributor to the reweighting excess. To explicitly check this, the order of the jet veto and p_{Tll} cuts was reversed and the biggest jump was found to still be the jet veto

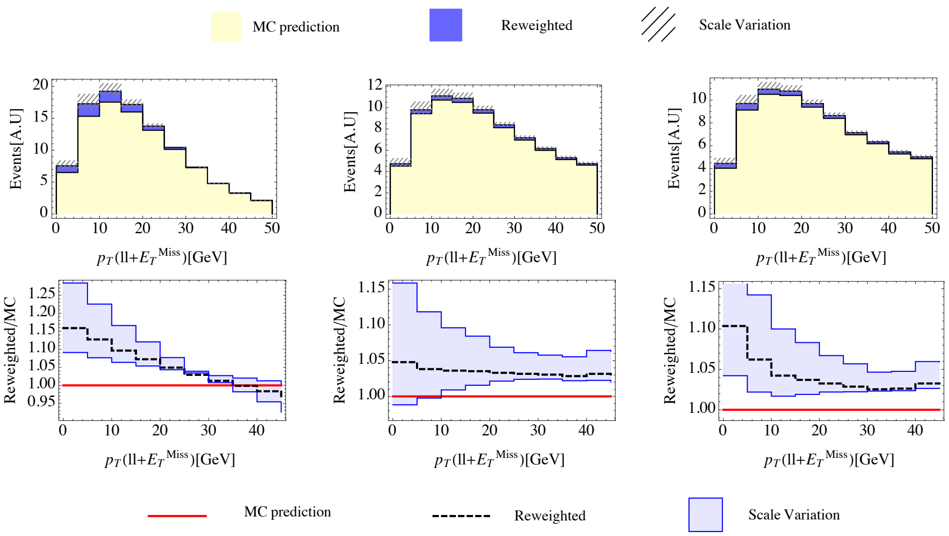

Figure 2.8: The top row shows the reweighting correction for left (Powheg+Pythia8), center (aMC@NLO+Herwig++), right (Powheg+Herwig++) to the $p_T(ll+E_T^{\text{miss}})$ observable. The bottom row has bin-by-bin percentage difference in events between reweighting and the MC + PS.

cut. In Figure 2.9 we show the correlation between 0 jet events and > 0 jet events as a function of $p_T(ll+E_T^{\text{miss}})$ before the jet veto is applied. Note that in Figure 2.9, 0-jet events primarily comprise the low p_T of the diboson system, and as such a jet veto implies that the fiducial cross section will become more sensitive to the shape given by p_T resummation. This clearly points to the Jet Veto cut as the major contributor to changes in the fiducial cross section from p_T resummation reweighting. If the jet veto were increased this result would still hold, however the 0-jet cross section would then be integrated over a larger range of p_T for the diboson, and thus there would be a smaller effect on the fiducial cross section. In particular, if the jet veto were dropped entirely this would be equivalent to integrating over the entire diboson p_T which by definition would not change the measured cross section.

Cut	% difference
Exactly two oppositely-sign leptons, $p_T > 20\text{GeV}, \mathrm{p}_{\mathrm{T}_{\text{leading}}} > 25\text{GeV}$	1.36
$m_{ll'}$ cuts	1.16
$E_{T,\text{Rel}}^{\text{miss}}$	0.83
Jet Veto	9.72
$p_{T ll'}$	10.75

Table 2.6: Percentage increase due to Resummation-Reweighting ($Q = \frac{m_W}{2}$, $\mu_R = \mu_F = 2m_W$) compared to Powheg-Pythia8 at 8 TeV for each cut stage in the cutflows listed from Table 2.1. All percentages are cumulative showing that the jet-veto is the largest effect.

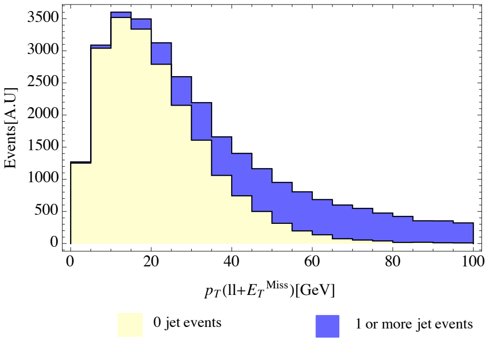

Figure 2.9: Events before the Jet veto. The number of 0 jet events or events with 1 or more jets is shown as a function of the p_T of the diboson system. Since 1 or more jet - events are vetoed, this sculpts the p_T -shape.

2.7 Discussion

As we have shown, p_T resummation, when used to reweight NLO MC distributions, can have a sizable effect on the predicted fiducial and the inferred total cross sections. The general trend in comparison with Monte Carlo generators and parton showers is to increase the predicted cross section $\sim 3 - 7\%$ and thus decrease the observed discrepancy compared to ATLAS and CMS. Our change in the predicted cross section and differential distributions depends on the choice of resummation scale for the W^+W^- final state whose uncertainty is not accounted for in fixed order+parton shower calculations. At large p_T the fixed order calculation is valid , while at small to moderate p_T the resummation calculation is most reliable. This scale in practice is analogous to the Matrix Element-Parton Shower matching scale when implementing matching procedures between the two. As discussed in Section 2.2, the resummation scale should be similar to the other hard scales in the problem. We have chosen the simple scale choice, analogous to what is done for Drell-Yan[91, 74], of $\sim M/2$, which for the W^+W^- process we have approximated as the fixed scale $Q = M_W$. We have demonstrated that the variation in this scale actually can imply quite a deal of uncertainty. For instance at 8 TeV using Powheg+Pythia8, by varying Q by a factor of 2 each we introduce a variation on the measured cross section $\sim \pm 3\%$.

Given that there is no a priori correct choice of the scale Q, a question naturally arises whether one can simply choose a scale to match the experimental data presented thus far. It is important to note that the measurements presented thus far have used *different* event generators and parton showers. For instance the preliminary result at 8 TeV by CMS[28] used Madraph LO + Pythia6 whereas the ATLAS full luminosity result [26] used Powheg + Pythia8. As shown in Table 2.4, the excess shown by CMS should be even *larger* based on our results while the ATLAS discrepancy should be reduced as mentioned above. Therefore even if a single scale was chosen for the results thus far, it wouldn't imply that it could put both experiments results into better agreement with the SM. However, if a consistent choice of generator was implemented we could in principle address the question of choosing a scale that was best for this process.

If one chooses a best fit scale Q to fit the experimental discrepancy in W^+W^- data there are potential implications elsewhere. Given that the premise behind resummation is that it should be approximately factorized from the hard process, if the initial partons for two processes are the same and there are no colored particles that are exclusively identified in the final state, the effects of resummation should be universal for different processes with similar scales. Thus, if there is a “correct" choice of scale for the W^+W^- process, then this choice of scale should be implemented for $W^\pm Z$ and ZZ diboson process as well, because of the similar hard scales in these diboson systems. The $W^\pm Z$ and ZZ process are experimentally even easier channels, especially the ZZ channel where the p_T of the ZZ system can be reconstructed with less uncertainty. The drawback of course is the reduced number of events in these channels, but nevertheless statistics are starting to approach the point where a useful comparison can be made e.g. the recent CMS 8 TeV measurement [28]. The ZZ cross section and p_T distribution [92] are in remarkable agreement with the SM and as such if there were a large change in the p_T distribution caused by the use of the best-fit W^+W^- scale Q then it would cause the agreement with the SM of ZZ to become worse. However, we note that the change from p_T resummation in the W^+W^- process is mostly due to the imposition of a jet-veto which the ZZ channel does not have. We find that choosing a scale that fits the W^+W^- discrepancy and naively calculating the inclusive change for ZZ causes a disagreement with data in all p_T bins. Further study of course is warranted, and a simultaneous fit should be employed to understand the agreement between the SM and measured diboson processes. This of course brings up a more general point that in analyzing the agreement between the SM and LHC data, similar theoretical methods should be employed and not just a choice of what fits best for a given process. The understanding of the different choices made by experiments contains important theoretical information about the SM and in the worst case scenario new physics could be inadvertently missed from being discovered.

Another important lesson reemphasized by this study is the need for further theoretical investigations of jet vetos. As we have shown p_T resummation causes a sizable effect on the total cross section because of the interplay between the jet veto and the p_T distribution. Clearly the correlation demonstrated in Section 2.4, especially Fig. 2.9, shows that the effects calculated in jet-veto resummation should be well approximated by the method employed here, similar to what was shown in [55]. Of course there are additional logs related to the jet veto which cannot be systematically improved upon within p_T resummation. However, the distributions shown in Figures 2.7 and 2.8 can't be reproduced in jet veto resummation alone, whereas our methods can. It would be interesting to further investigate the interplay of these two types of resummation and the reweighting of parton showered events for more processes.

Another interesting question associated with the jet veto is how the LHC experiments can test the effects of the jet veto on the W^+W^- cross section measurement. The jet veto is a necessary evil in the context of measuring W^+W^- without being overwhelmed by $t\bar{t}$. However, if the jet veto were weakened significantly, then the effects demonstrated in this note would disappear both in the context of p_T resummation and jet veto resummation. If the jet-veto were varied, this could be compared to definitive predictions for the cross section as a function of the jet veto. To alleviate the issue of the $t\bar{t}$ background, we suggest that the experiments separately implement a b-jet veto and a light jet veto, of which the light jet veto should be varied to study its effects.

In this paper we haven't explicitly demonstrated the effects of resummation on the contribution of $gg \to W^+W^-$ to the W^+W^- cross section. This contribution is a small fraction of the total cross section, and as such even though resummation effects will modify its shape as well, it won't change our conclusions. However, it is important to note that the peak of the p_T spectrum for $gg \to W^+W^-$ should be at approximately 10 GeV high than for quark initiated W^+W^- , as is generic for gg initiated processes, in e.g. [73]). For a sufficiently precise measurement of the p_T distribution it would be necessary to have the shape of this distribution correct as well. A more interesting direction is the implications of understanding the correct shape of the SM W^+W^- production background for the extraction of the Higgs signal in the $H \to W^+W^-$ decay channel. Given that the W^+W^- background is extracted via data-driven methods, it is important that the shape of the distributions of the W^+W^- background is known when extrapolating from control to signal regions. While the p_T of the W^+W^- system isn't a variable used for the signal/control regions, as shown in our results for the reweighted kinematic distributions at 7 TeV there is a non negligible effect on the shape of relevant variables. Future investigation is needed to study the effects of resummation on the measured signal strength of the Higgs in the W^+W^- channel.

There are other avenues for future study, for instance investigating simultaneous resummation of W^+W^- p_T with other observables, such as rapidity, to determine if any of the other cuts put on the fiducial phase space could alter the extraction of a total cross section. Regardless of future direction, this work has clearly demonstrated the importance of p_T resummation when combined with fiducial phase space cuts. Similar to how the p_T distribution of the Higgs signal is reweighted to make precise predictions for Higgs physics, it is important to use the correct p_T shape when considering processes where the W^+W^- signal is either being measured or is an important background. To help facilitate future studies we plan to distribute the underlying p_T resummed distributions used in this study to any group interested in using them via a website.

Chapter 3

Precision diboson measurements and the interplay of pT and jet-veto resummations

3.1 Introduction

Run I of the LHC was an overwhelming success, the Higgs discovery[10] completed the Standard Model (SM) of particle physics. However, it also explicitly brought to the fore the question of naturalness in the SM. In particular, the lack of any sign of physics beyond the SM (BSM) at Run 1 leaves a number of questions for the prospects of discovery at Run 2 given the impressive exclusions at high masses. Nevertheless, the LHC has also brought about a new opportunity for precision measurements at the electroweak (EW) scale and the opportunity to test the SM in ways that were essentially inaccessible before. New precision measurements are crucial both for understanding the properties of the Higgs better, as well as for searching for new physics at the EW scale where the phase space of new physics would strongly overlap with the SM.

At Run 1 of the LHC the energy and luminosity were sufficient to start probing certain EW processes with unprecedented statistics, e.g. diboson production. Probing diboson production is important for a number of reasons within the SM, as it is the main background for several of the most important Higgs search channels, and it can test the EW gauge structure of the SM. Historically it is also useful for looking for deviations from the SM for instance in aTGCs(anomalous triple gauge couplings) and aQGCs(anomalous quartic gauge couplings) which can be related to a whole host of EW precision tests (EWPT). Diboson production is also an important background for almost any model of new physics that has new EW charged particles or modifies and extends the EW gauge/Higgs structure of the SM in any way. Given the ubiquitous importance of diboson production, it is necessary to improve both the theoretical and experimental understanding of the many channels within the SM.

In most diboson channels at run 1 and especially at run 2 there will be sufficient statistics such that all productions modes can be observed in leptonic final states making for relatively clean measurements. In fact almost all measurements of the total inclusive cross section at run 1 agreed very well with the NLO QCD predictions. However, there is far more information that can be gleaned from diboson channels than their overall rate alone. Given that the production of a diboson pair is an uncolored final state, the QCD corrections to diboson production will have very similar predictions that roughly depend on the mass scale and the particles in the initial state production e.g. $q\bar{q}$ or gg. For instance the transverse momentum distribution of the W^+W^- , ZZ and $W^\pm Z$ channels all should be very similar and correlating between various channels can be a test of QCD. This is similar to the program carried out at lower energies where Drell-Yan production and single $W^\pm$ productions can be correlated and predictions can be made that allow one to extract important EW measurements such as the $W^\pm$ mass. Understanding diboson production in differential shape directions can test QCD, but it can also then be applied to searches/exclusions of new physics models as has been demonstrated in the W^+W^- channel [35, 37] and applying similar methods to the $t\bar{t}$ channel in [93]. In this paper we begin to suggest a program of measurements and correlations amongst EW diboson channels motivated by current higher order QCD calculations [94, 95, 96]. This program can be straightforwardly extended to processes beyond diboson production, but we focus on diboson production in this paper because of an anomaly that persisted from the Run 1 of the LHC.

At run 1 of the LHC almost all the diboson channels agreed with the SM NLO QCD predictions except for the W^+W^- (ATLAS and CMS) and $W^\pm\gamma$(CMS only) and $W^\pm Z$(CMS only) channels. The W^+W^- channel is particularly interesting because it consistently reported discrepancies with theoretical predictions both at 7 and 8 TeV, and both in ATLAS [25, 26] and CMS[27, 28]. Importantly the excesses reported were not only in the overall rate but there were also shape discrepancies in many differential directions. Many attempts to explain the excess were put forward using both BSM physics[34, 35, 36, 37, 38, 39, 97, 98], as well as higher order QCD corrections to the SM process. The W^+W^- channel is currently unique amongst the diboson channels as it employs a jet veto of 25 GeV (30 GeV) for ATLAS (CMS) to reduce the $t\bar{t}$ background. This implies that not only fixed order QCD corrections are important, but there can also be large logarithms that need to be resummed as well. The introduction of the jet veto is of course not the only reason that large logs may appear and need to be resummed, in certain differential directions it is crucial to include resummation to predict the shape accurately[1].

Given the presence of the jet veto for the W^+W^- channel it makes sense to perform jet-veto resummation to resum logs of the form $\ln{(p_T^{\text{veto}}/M)}$, where M is the scale of the hard interaction, and see the effects on the W^+W^- cross section. This was carried out in [99] where it was shown that it does improve the agreement between the measured cross section and theoretical prediction. However, using jet-veto resummation alone does not directly make predictions for other differential directions. To describe other differential directions one must employ a reweighting of MC events, which we explore in this paper, or a joint resummation. These are both interesting and compelling avenues to pursue, because as stated earlier the experimental W^+W^- measurements had shape discrepancies and not solely rate discrepancies.

One interesting differential direction reported by ATLAS was $p_T(\ell^+\ell^- + \text{MET})$ which had a shape discrepancy particularly at low values of this variable where there were an excess of events [2] . What makes the $p_T(\ell^+\ell^- + \text{MET})$ distribution particularly interesting is that it is essentially a proxy for the p_T^{WW} given that it was measured in the fully leptonic channel. It is well known to accurately predict the p_T shape for EW final states at low p_T, p_T resummation must be used to go beyond fixed order calculations or MC parton shower predictions. While naively p_T resummation will not change the overall inclusive cross section at all [73], there is a strong correlation between the p_T^{veto} and p_T^{WW} when a jet veto is imposed. For instance at NLO, the jet recoiling off the di-

---

[1] There are also threshold logarithms associated with soft-gluon emissions. Threshold resummation and approximate NNLO results for W^+W^- production were presented in [47].

[2] CMS has not released a distribution of this,but it would be very useful if they did.

boson pair has equal but opposite transverse momentum. However, with p_T resummation alone there are no jets, and hence this correlation can only be extended and observed by employing a reweighting procedure for instance as used in [53, 54]. This was done for the W^+W^- channel in [100] and it was shown by reweighting with respect to the resummed p_T^{WW}, there were effects on the fiducial cross section which improved the agreement with the experimental data. Subsequently, the full luminosity 8 TeV analysis by CMS[101] employed the p_T-resummation curves reweighting from [100] as well as the full NNLO cross-section[94] and found good agreement between experiment and theory. Whereas the reweighting from NNLO is an overall normalization, the reweighting from p_T-resummation is a shape effect.

Because of the strong correlation between p_T^{veto} and p_T^{WW} it should be expected that the jet-veto resummation [99] and the p_T resummation calculations [100] should give similar results. In [55] this was shown to be the case for Drell-Yan and Higgs production, with discrepancies occurring at higher orders because the correlation between p_T^{veto} and p_T^{WW} is weakened and depends on jet clustering effects. Nevertheless a naive reading of [99] and [100] seemed to imply that there was a larger discrepancy between these methods than would be expected. In fact this led to further paper on QCD effects in these channels trying to explain the experimental discrepancy[102] and automate jet-veto resummation[103]. Given the success of [101] it is important to further study how well p_T resummation captures the jet veto logs in the W^+W^- process.

In this paper we show that [99] and [100] agree quite well when carefully compared using the same experimental variable [3]. We additionally investigate more generally the comparison between jet veto and p_T resummation with the same scale choices and parameters to understand their correlation and interplay. While this is useful for making predictions for jet-vetoed cross sections, it doesn't address other differential directions in particular why there are shape discrepancies in the fiducial cross section as well for W^+W^- . To investigate this we propose a new method to use Jet-Veto resummation to reweight MC samples to obtain a more accurate prediction of differential cross sections with a jet veto. We then study how well the predictions of this method compares with p_T resummation. The dependence of the agreement between these resummation reweight-

---

[3] The main naive discrepancy is due to how [99] presented the effects of resumming additional π^2's but there is no inherent discrepancy when making predictions for the fiducial cross section that ATLAS or CMS would measure.

ing methods for different jet radius is studied in detail for $R = 0.4, 0.5$ and for a large radius $R = 1$ where correlations are expected to be stronger. We also investigate the contributions from non-perturbative (NP) effects such as hadronization and Multi-Parton Interactions(MPI).

Based on this study the results can be extended to a better understanding of other diboson channels as well. For instance, while there has been extensive work on NP effects and scale choices for single vector boson processes, at the LHC this may now be carried out across even more channels. The detailed understanding of the W^+W^- channel, which has high statistics but additional jet-veto complication, could then be used in conjunction with other diboson processes which are more rare but do not have a jet veto. Fitting across various channels at the high luminosity LHC could shed light on optimal resummation scale choices and modeling non perturbative factors as well as allowing for new opportunities to test QCD and search for new physics. In particular the fact that at run 1 diboson channels other than W^+W^- seemed to agree well with only NLO MC predictions, whereas W^+W^- required NNLO+NNLL QCD calculations to be accurately described could provide a window into understanding how well the SM actually describes the data when theoretical predictions are *uniformly* applied. The rest of the paper is organized as follows. In section 2, we briefly review Jet veto and p_T resummation theory. In section 3, we introduce our new method to reweight using jet veto resummation and reweighting using p_T resummation is reviewed. In section 4 we demonstrate the correlation of these methods and their dependence on other variables. Finally we discuss future work and how best to integrate these techniques into a larger program for the next runs of the LHC.

3.2 Jet-Veto and p_T Resummation Theory

In this section, we briefly review the relevant resummations of large logarithms in non-inclusive measurements that arise at higher orders in perturbation theory. In particular, we are interested in resummation of logarithms that arise in the presence of a jet-veto or in the measurement of p_T distributions of WW, as well as the correlations between the two. In either case, the presence of large logarithms is a consequence of the presence of multiple scales in the problem. Besides the scale of the hard interaction M, non-inclusive measurements introduce additional scales, p_T^{veto} for jet-veto measurement and p_T^{WW} for p_T distribution measurement, leading to logarithms of the form $\alpha_s^n \log^m(p_T/M)$ and $\alpha_s^n \log^m(p_T^{\text{veto}}/M)$ respectively at higher orders with $m \leq 2n$.

We now briefly describe resummation of large logarithms as implemented in this paper. The resummation of logarithms from jet-vetos can be done directly in QCD [55], but it naturally can also be expressed in soft-collinear effective theory (SCET) [57]. For the W^+W^- process we employ the SCET calculation as described in [99]. The EFT is matched to the full theory of QCD at a hard scale $\mu_h \sim 2m_W$ [4]. Using the power counting parameter $\lambda = p_T^{\text{veto}}/M$, the matching coefficient is renormalization-group (RG) evolved to a soft-scale, $\mu_f \sim p_T^{\text{veto}}$ characterizing the initial-state radiation (ISR). The RG evolution of the matching coefficient resums large logarithms of the form $\log \lambda$. The factorized jet-veto cross-section in SCET can be parametrically written as

$$\frac{\mathrm{d}\sigma(p_T^{\text{veto}})}{\mathrm{d}M} \sim H(\mu) Z_S(\mu, \nu, \bar{\nu}) B(\mu, \nu) \bar{B}(\mu, \bar{\nu}) \tag{3.2.1}$$

where, $M = M_{WW}$, the *hard* function H is the square of the matching coefficient, B and $\bar{B}$ are the collinear and anti-collinear *beam*-functions which describe ISR in the presence of jet-veto, and Z_S is a renormalization constant for the product of beam functions, also referred to as *soft*-function in the literature. The beam functions have additional (rapidity) divergences which are not regulated by dimensional regularization and need additional regulators. Associated with these additional regulators are the renormalization scales ν and $\bar{\nu}$ as well as corresponding RG equations [105]. After implementing RG evolution in the μ–ν space, the product of beam functions and soft-function in the factorized cross-section takes the form :

$$Z_S(\mu, \nu, \bar{\nu}) B(\mu, \nu) \bar{B}(\mu, \bar{\nu}) = \left(\frac{\mu^2}{M^2}\right)^{g(\mu)} \hat{Z}_S \hat{B} \hat{\bar{B}}(\mu) \tag{3.2.2}$$

where the expressions for g, $\hat{Z}_S$, $\hat{B}$ and $\hat{\bar{B}}$ as well as the procedure for estimating the scale uncertainties can be found in [105]. The beam functions develop dependence on the jet-clustering parameter R at $\mathcal{O}(\alpha_s^2)$, which can lead to substantial scale uncertainties for small R due to presence of $\log R$ terms which are not resummed in the current implementation.

---

[4] Ref. [99] employed the choice $\mu_h \sim M$ to minimize logarithms of the form $\log(\mu_h/M)$. Further, the default choice of the hard matching scale in [99] was chosen to be $\mu_h^2 = -M^2$ to resum π^2 terms (see [104] for further discussion). However, in order to facilitate comparison with [100], the default matching scale in this paper is chosen to be $\mu_h = 2m_W$.

To resum logarithims of the form $\log(p_T/M)$ we use the formalism of [73] which was implemented for the W^+W^- channel LHC measurements in [100]. The resummed partonic cross section takes the form

$$\frac{d\hat{\sigma}_{ab}^{WW}}{dp_T^2}\left(p_T, M, \hat{s}, \alpha_s\left(\mu_R^2\right), \mu_R^2, \mu_F^2\right) = \frac{M^2}{\hat{s}}\int \frac{d^2\mathbf{b}}{4\pi} e^{i\mathbf{b}\cdot p_T}\, \mathcal{W}_{ab}^{WW}\left(b, M, \hat{s}, \alpha_s\left(\mu_R^2\right), \mu_R^2, \mu_F^2\right). \tag{3.2.3}$$

where $\mathcal{W}_{ab}^{WW}$ is the resummed cross section in impact parameter space (b-space). The resummation is more easily performed after doing a further Mellin transformation which demonstrates the typical exponentiated structure

$$\mathcal{W}_{ab,N}^{WW}(b, M, \mu_F^2, \mu_R^2) = \mathcal{H}_N^{WW}(M, \mu_F^2, Q)\exp\left\{\mathcal{G}_N(L, \mu_R^2, Q)\right\}, \tag{3.2.4}$$

where N is the moment of the Mellin transform with respect to $z = M/\hat{s}$, $\mathcal{H}_N^{WW}$ is the hard function, and $\mathcal{G}_N$ depends on physics at scales of $\sim p_T$. We have introduced the new scale Q that accounts for the uncertainty associated with matching to the hard process and separating it into the various pieces, and finally $L = \log Q^2 b^2/b_0^2$ with b_0 a fixed constant of $\mathcal{O}(1)$. In understanding the uncertainties associated with the resummed calculation we vary μ_F, μ_R and Q, where Q is expected to be similar to M but below it. NP effects can be systematically included to p_T resummation, however, for the distributions discussed in this paper the effects are small and the interested reader can find more details in [100].

In both [99] and [100] the resummation was carried out to order NNLL+NLO which matched to NLO fixed order cross-section rather than NNLO, given that the full NNLO cross section was not yet available. With the calculation of the NNLO cross section for W^+W^- production[94], it is possible to extend this analysis to NNLL+NNLO. This was performed for p_T resummation in [106]. However work on similar next order analysis for jet veto resummation is still ongoing [1]. In order to compare resummations at the same order we use NNLL+NLO for both resummations in this paper.

The correlations between jet-veto and p_T resummation are most evident when one looks at large logarithms at *fixed order* in perturbation theory. To study the correlation, we focus on the leading-jet p_T which can be described by $\mathrm{d}\sigma(p_T^{\text{veto}})/\mathrm{d}\ln p_T^{\text{veto}}$. At $\mathcal{O}(\alpha_s)$, leading-jet p_T is exactly balanced by the p_T of the WW system and therefore, $\mathrm{d}\sigma(p_T^{\text{veto}})/\mathrm{d}\ln p_T^{\text{veto}} = \mathrm{d}\sigma(p_T)/\mathrm{d}\ln p_T$. At $\mathcal{O}(\alpha_s^2)$, situation is complicated by the fact that more than one emission is allowed and the leading-jet p_T is no longer equal to the p_T of the WW system. Nevertheless, given the similarity in structure of IR singularities, we expect correlations among the two observables. Indeed at $\mathcal{O}(\alpha_s^2)$, the logarithmic singularities in the difference $\mathrm{d}\sigma(p_T^{\text{veto}})/\mathrm{d}\ln p_T^{\text{veto}} - \mathrm{d}\sigma(p_T)/\mathrm{d}\ln p_T$ evaluated at $p_T = p_T^{\text{veto}}$ arise entirely from jet-clustering effects [56]. Although this does not constitute a rigorous proof, it lends credence to the p_T reweighting technique as a means of estimating jet-veto efficiency.

Finally, we comment on underlying events (UE) or soft-physics, which is known to effect non-inclusive observables, such as p_T distributions or jet-multiplicity. Some sources of soft-physics can be captured perturbatively via resummation, however NP effects such as hadronization (characterized by scale $\Lambda \lesssim$ GeV), although not calculable in perturbation theory, appear as power suppressed terms $\mathcal{O}(\Lambda/p_T^{\text{veto}})$ in SCET when the beam functions are operator product expanded on to parton distribution functions (PDFs). Following [107], we parametrize NP effects for the jet-veto calculation by substituting $g(\mu)$ in Eq 3.2.2 with

$$g(\mu) \to g(\mu) - \frac{1}{2}\frac{\Lambda}{p_T^{\text{veto}}}. \tag{3.2.5}$$

3.3 Reweighting MC events and Applications

Each of the resummation methods outlined in the previous sections makes an accurate prediction for a unique differential variable. For transverse momentum resummation it is the transverse-momentum of the diboson, while for jet veto resummation, it is the cross section of the zero-jet bin. Both methods are more accurate for their corresponding differential observables than combining a fixed order calculation with a parton shower, however inherently they are inclusive with respect to other observables. As a result it is impossible to get a fully differential cross section solely from either of these resummation schemes. Theoretically this is fine, but the most important question is how to compare to experimental results. To do so would require the unfolding of experimental events to make a prediction for a theoretical observable. This leaves the results susceptible to inherent biases in the original events used to simulate the results which are then inverted to define an unfolding for experimental results. A much more straightforward procedure is simply to provide experiments with MC events that they can pass through their own detector simulations and compare directly to data. This is impossible with just the results of the resummation calculations, however a theoretical solution that avoids unfolding data is to reweight monte carlo events. Reweighting techniques have been used in multiple experiments, and have been used both for reweighting to theoretical calculations as well as reweighting distributions based on experimental data. For the purposes of this paper reweighting simply amounts to the following. Given a particular differential direction denoted by ξ predicted from resummation, the resummed distribution is binned and a reweighting function is defined by

$$\mathrm{F}[\xi] = \frac{\text{Resummed bin}[\xi]}{\text{MC bin}[\xi]}. \tag{3.3.1}$$

In this section we describe reweighting methods for each resummation calculation. For p_T reweighting we employ a technique similar to that used in HqT [54] and in [100] where the underlying MC events are reweighted by the p_T of the diboson predicted from p_T resummation. This was employed by CMS for the 8 TeV W^+W^- measurement[108] using the results of [100] and good agreement was found for the cross section measurements. ATLAS has not employed such a method, but it would be interesting to see given that ATLAS has consistently released the distribution of $p_T(\ell^+\ell^- + \mathrm{MET})$ which is the p_T of the diboson system up to the contribution to MET from the resolution of QCD objects.

For jet-veto reweighting it is a more subtle question of how to reweight events. At its core, jet-veto resummation only gives one number, the 0-jet bin cross section. There was an attempt in [103] to construct an automated jet veto resummation procedure that reweights madgraph events at LO or NLO. Unfortunately, this doesn't solve the problem of interfacing with experimental results as only the LO version produces events. In this case distributions determined by QCD corrections may be inherently incorrect, e.g. the p_T of the diboson system will have a pole at p_T =0. More generally, given the predicted 0-jet bin and the overall inclusive cross section, it is always possible to construct a crude two-bin reweighting function simply based on whether or not there is a reconstructed MC jet above or below a jet veto scale which can be applied to events simulated at LO or NLO and interfaced with a parton shower. The data-driven normalization applied to the WW background for Higgs studies, roughly corresponds to such a crude two-bin reweighting, and hence studying its effects on other differential shapes acquires importance. However, in predicting differential shapes, for instance for the W^+W^- measurement (or W^+W^- background to $H \to W^+W^-$), in the fiducial cross section a reweighting function constructed this way would simply be an overall K-factor since all MC events in the 0-jet bin would be weighted the same as they would all pass the jet-veto. As a result, the predictions for the shape of the fiducial cross section will by definition only be as good as the underlying Monte Carlo prediction.

A potentially more interesting possibility is to use the calculation of the jet-vetoed cross section from resummation to construct a continuous distribution for $\frac{d\sigma}{dp_T^j}$ where p_T^j is the p_T of the leading jet in the event. However, depending on exactly how this is implemented there are issues with the size of the errors and the correlation to p_T^{WW}. Going to lower p_T^j quickly leads to poor convergence of perturbation theory and eventually non-perturbative corrections take over. In Fig. 3.1, $\frac{d\sigma}{dp_T^j}$ is plotted as a function of p_T^j by differentially binning the jet-veto cross-section $\sigma(p_T^{\text{veto}})$ (see Section 3.2) with respect to p_T^{veto}. To estimate the effects of NP corrections, we have also implemented $\Lambda = 500$ MeV in Eq 3.2.5[5]. The relative scale uncertainty in $\frac{d\sigma}{dp_T^j}$, δ for each bin is estimated by the corresponding scale uncertainty in the jet-veto cross-section. The relative scale uncertainties normalized with respect to $\Lambda = 0$ central values are also in Fig 3.1. Given the large errors at low p_T^j, reweighting at low p_T^j is not advisable. Even if one is able to reduce scale uncertainties by going to high orders and further, devise methods to systematically quantify the NP corrections, there is still the problem of poor correlation between p_T^j and p_T^{WW} at low p_T. This is quantified in Figure 3.2 where we plot the difference between p_T^j and p_T^{WW} as a percentage of p_T^{WW} for a Powheg Monte Carlo WW sample showered with Pythia8,

$$\rho(p_T) = \frac{\langle |p_T^j(p_T) - p_T| \rangle}{p_T} \tag{3.3.2}$$

where p_T refers to p_T^{WW}. For the above reasons we conclude that the naive two-bin reweighting

---

[5] In [103] a similar uncertainty was estimated and they further attempted to quantify this effect by turning on/off hadronization in Pythia, resulting in a fit of $\Lambda = 240$ MeV. Given the inherent uncertainty associated with how the many contributions to soft physics are taken into account in Pythia we use $\Lambda = 500$ MeV simply as an example as the ultimate uncertainty may be even larger.

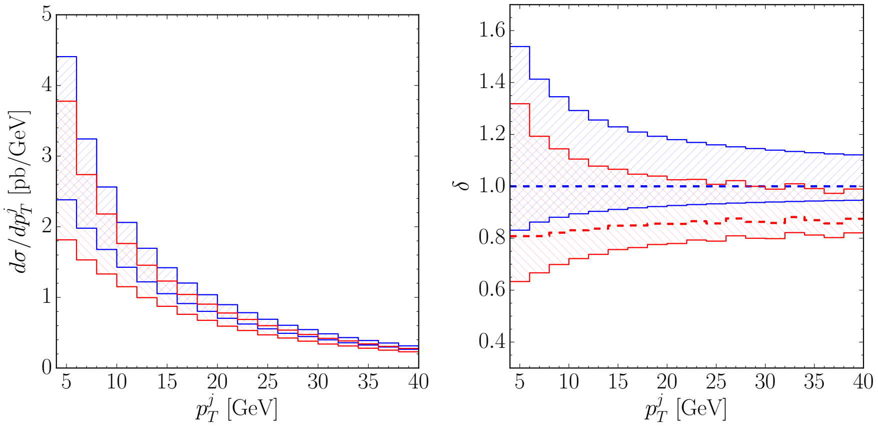

(a)

▨ Λ_{NP}=0 MeV ▧ Λ_{NP}=500 MeV

(b)

Figure 3.1: For $\sqrt{s} = 8$ TeV and $R = 0.4$ anti-k$_T$ jet algorithm, in the left hand panel $d\sigma/dp_T^j$ is plotted. For the distribution shown in blue, errors come from scale variations without NP factors, in red $\Lambda_{NP} = 500\,\mathrm{MeV}$ uncertainties are included. In the right hand panel, the fractional uncertainty of $d\sigma/dp_T^j$ from scale variation relative to the central scale choice is shown with and without NP uncertainties.

method is the safest way forward if reweighting with jet-veto resummation has to be employed and we use only this method in the next section.

Both p_T and jet-veto reweighting methods have their own advantages and disadvantages. In p_T reweighting, all jet dependent effects are inherited completely from the underlying MC given that p_T resummation sums over all gluons and is fully inclusive. This makes it impossible to estimate systematics on the jet-vetoed cross section from a purely theoretical viewpoint alone. However, as we will show we find good agreement for the jet-veto efficiency between p_T reweighting and the jet-veto resummation calculation. The jet-veto reweighting method gives the most theoretically under control calculation of the jet-veto efficiency, but all differential quantities including the p_T of the system will be essentially the same as for the MC as we show in the next section. Therefore without joint resummation, we will show that p_T reweighting gives the best overall pre-

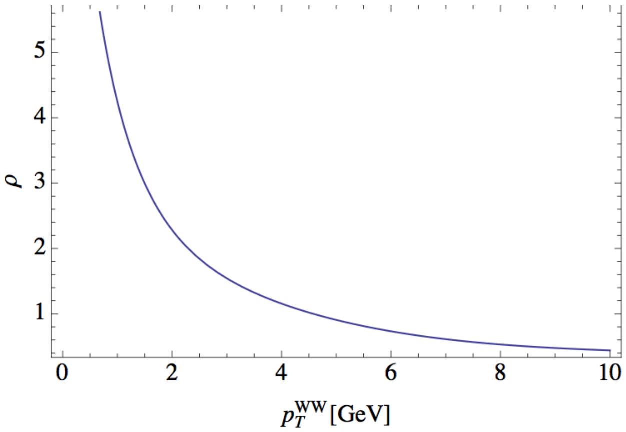

Figure 3.2: correlation variable ρ as a function of p_T^{WW}

dictions of rate and shape in this channel. This is important since the ATLAS measurements of the p_T of the diboson system in the fiducial region disagree with the NLO+parton shower predictions, and jet-veto reweighting would predict the same distribution as the MC.

3.4 Results and Comparison

The `Powheg+Pythia` events for the process $pp \to W^+W^-$ at NLO are reweighted using two procedures, utilizing two different resummations, as described in the previous section. These are then used to calculate jet-veto efficiency and the p_T shape of the WW system in the zero-jet bin. We have consistently used the `MSTW2008nlo` PDF sets in both the resummation calculations and MC simulations. Earlier efforts at addressing these procedures separately Ref. [99],[100] employed different scale choices. In this paper, we choose the same hard scale of $2M_W$ to compare both procedures. We also turn off π^2 contributions that affect the overall cross-section. However, there are still additional scale choices that must be made independently because of the different formalisms for the calculations, that we now list and we describe their impact on the uncertainty. For p_T resummation the renormalization (hard scale) and factorization scales are taken to be $\mu_R = \mu_F = 2M_W$, and there is an additional resummation scale Q whose central scale is chosen to be Q= M_W. For jet-veto resummation, the central values for the hard scale and the factorization scale are chosen to be $2M_W$ and p_T^{veto} respectively. To capture scale variations, we vary the hard scale and factorization scale by a factor of 2 and $\frac{1}{2}$ around their respective central values and add the resulting errors in quadrature. Additionally, there are scale uncertainties associated with rapidity divergences in SCET for which we follow the prescription outlined in [105]. For p_T resummation, based on the nature of the calculation we vary μ_F and μ_R in a correlated way by a factor of 2 around the central scale, and separately vary the resummation scale by the same factors and then add the resulting errors in quadrature. We have used the anti-k$_T$ jet algorithm for jet-clustering in `Pythia` and the same algorithm is employed in the jet-veto resummation calculations. The analyses were performed both at 8 TeV as well as 13 TeV. These results are plotted in Figure 3.3 and the central values of the jet veto efficiencies relevant to ATLAS and CMS with their corresponding 1σ errors are given in Table 3.1. The left plots show jet-veto efficiency ϵ, the fraction of events passing the jet veto, predictions directly from resummation (blue) as well as that obtained from p_T reweighting (red). This is to be compared with jet-veto efficiencies from `Powheg` (black), which predicts a slighty lower efficiency. The two resummation methods however agree within 1σ error bars at both 8 TeV and 13 TeV. This demonstrates that the existing procedure to use p_T resummation to estimate the jet-veto cross-section is reliable. On the other hand, the p_T shape of the W^+W^- system in the zero-jet bin, shown on the right hand side of Figure 3.3, as predicted by our jet-veto resummation reweighting retains the peak position of the underlying `Pythia` sample while p_T resummation predicts a softer p_T shape[6].

3.5 Jet Definitions and other QCD effects

The jet-veto resummation calculation contains dependence on the jet-algorithm through R-dependent terms, which for small R are dominated by $\log R$ terms arising from collinear splitting. As shown in Figure 3.4, the agreement between jet veto and p_T resummation is better for large R. This is expected since, for larger R, more of the hadronic activity is captured as a single jet and hence the

---

[6] It should be noted that $p_T(\ell\ell + \text{MET})$ is the actual measurable quantity that corresponds to the p_T^{WW} shape and this suffers from significant MET smearing.

	Jet Veto Efficiency	
p_T^{veto}	25 GeV	30 GeV
8 TeV p_T resummation	$0.71^{+0.03}_{-0.02}$	$0.76^{+0.03}_{-0.02}$
8 TeV Jet-veto resummation	$0.73^{+0.09}_{-0.05}$	$0.78^{+0.09}_{-0.05}$
13 TeV p_T resummation	$0.66^{+0.04}_{-0.03}$	$0.71^{+0.03}_{-0.03}$
13 TeV Jet-veto resummation	$0.65^{+0.07}_{-0.03}$	$0.70^{+0.07}_{-0.03}$

Table 3.1: Jet Veto Efficiency at 8 and 13 TeV for $R = 0.4$

correlation between the leading jet momentum and W^+W^- momentum is higher. While moving to $R \sim 1$ reduces the scale uncertainty in jet-veto resummation, due to better control of $\log R$ terms in perturbation theory, MPI effects can be quite large for large R making the choice $R \sim 1$ far from ideal as we discuss below.

While the p_T reweighting technique, which is inclusive in hadronic activity, is robust against MPI and NP effects such as hadronization, the same is not true for jet-p_T reweighting technique. The p_T distribution of a colorless-final state, such as W^+W^- , will be practically unaffected by MPI since the soft-radiation associated with MPI is mostly isotropic. On the other hand, observables involving jets in the final state, such as jet-veto efficiencies, will be strongly effected by MPI. Jets with large R contain more soft-radiation and therefore are prone to larger MPI effects. We confirm this effect, that while turning off MPI does not affect the p_T^{WW} shape, it does have an effect on jet-veto efficiency especially for large R as shown in Fig 3.5. To avoid such contamination, we recommend that LHC experiments continue to choose $R \sim 0.4$ in the W^+W^- channel thereby minimizing dependence on MPI modeling. Further, for the case of jet-vetoes, MPI effects will be more pronounced for small p_T^{veto} where the soft-radiation starts competing with the *true partonic* jet p_T. In order to minimize the impact of NP effects on jet p_T reweighting, a large underflow bin in jet-p_T was chosen. With this choice of underflow bin, the p_T shapes are fairly independent of whether MPI and hadronization effects in `Pythia` are included or not, as long as the jet radius parameter R is not too large[7].

---

[7] By default, we have turned on MPI and hadronization effects in `Pythia`.

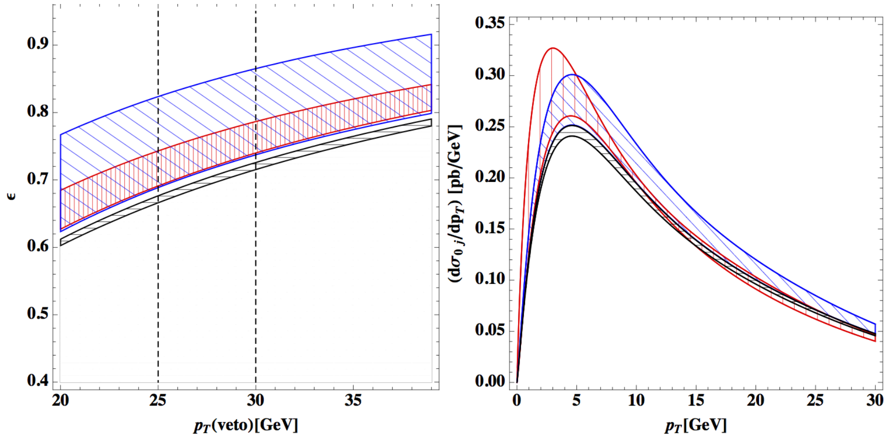

(a) 8 TeV

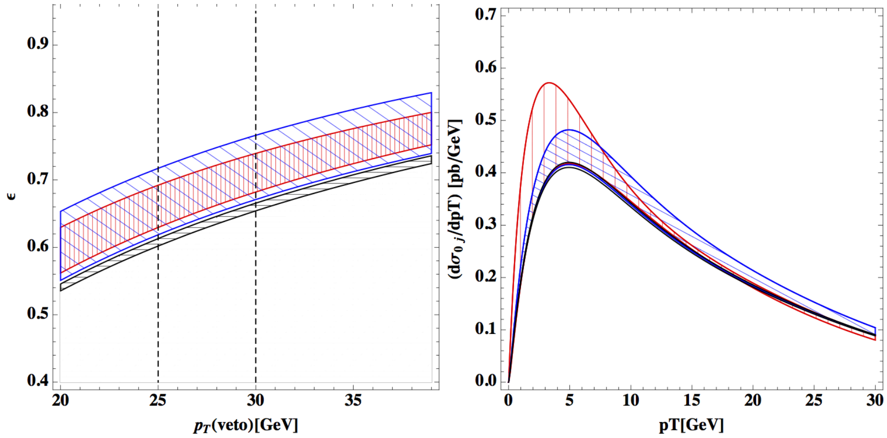

(b) 13 TeV

▧ JetVetoResummation ▥ $\mathrm{p_T}$Resummation ▤ PowhegPythia

Figure 3.3: Comparison of jet-veto efficiency and p_T^{WW} in the zero jet bin, from jet veto resummation and pT resummation for R=0.4 at 8 TeV (top) and 13 TeV (bottom).

3.6 Discussion

In this paper we have explored the agreement of different resummation procedures for predicting both the W^+W^- fiducial cross section with a jet veto as well as the differential cross section with respect to the diboson p_T. Prior to this paper there was some confusion surrounding the different resummation methods and whether they led to different conclusions [103]. The reflection of this is most clearly represented in the most recent ATLAS and CMS measurements, where CMS chose to

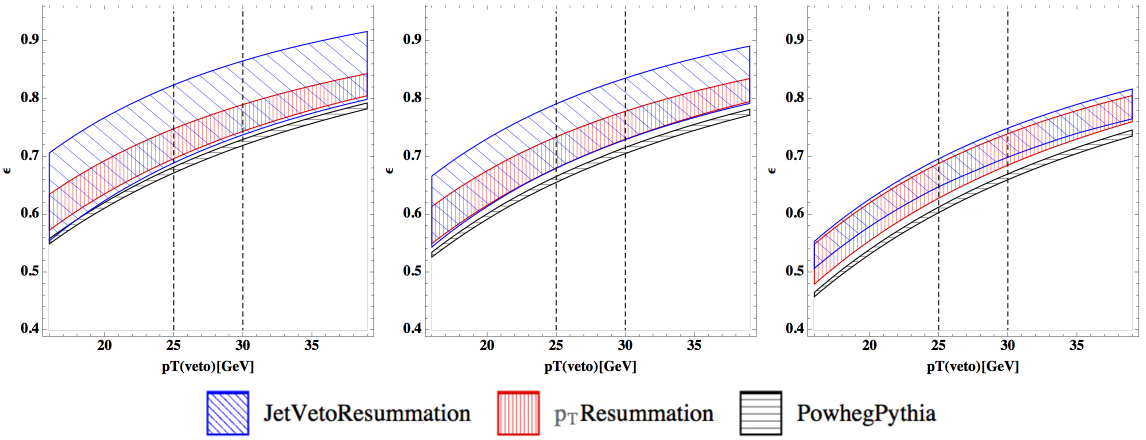

Figure 3.4: Comparison of jet veto efficiencies for 8 TeV for R=0.4, 0.5 and 1.

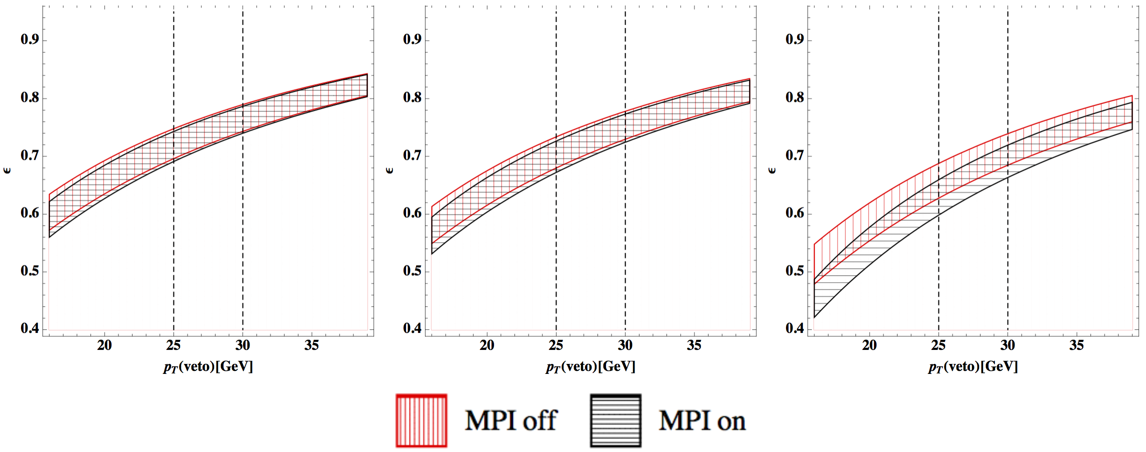

Figure 3.5: Comparison of jet veto efficiencies for 8 TeV using pT reweighting method with MPI off vs on for R =0.4, 0.5 and 1.

use the resummation improved theory predictions and found agreement with the SM while ATLAS did not and has a discrepancy which persists. Nevertheless, in this paper we have shown that when comparing jet veto efficiencies directly, without modifying the inclusive cross section, the methods of [100] and [99] agree very well. In particular, we have identified that the predictions at both Run 1 and Run 2 of the LHC should agree within perturbative uncertainties for each method, as well as with any reasonable choices of jet definitions or variation of non-perturbative sources of error. Therefore regardless of the method, ATLAS and CMS should use some form of resummation when comparing to theoretical predictions to describe the W^+W^- fiducial cross section with a jet veto.

In addition to the results for the jet vetoed cross section, we have also implemented a reweighting procedure based upon jet-veto resummation so that differential predictions can be compared between the two methods. For instance since p_T resummation by construction best predicts the p_T distribution of the diboson system, it's useful to compare the predictions from the jet-veto reweighted method as shown in Figure 3.3. The increase at low p_T compared to `Powheg-Pythia` is noticeable for both methods which would for instance bring the ATLAS experimental data for $p_T(\ell^+\ell^- + \mathrm{MET})$ into better agreement, however, there are still noticeable differences. In particular, p_T resummation predicts a p_T distribution that peaks at lower p_T than the jet-veto reweighting procedure and the MC prediction. To compare these methods further there are both experimental and theoretical opportunities and challenges. In measuring the p_T of the system of the system experimentally for the W^+W^- channel there inherently will be smearing due to the MET resolution.

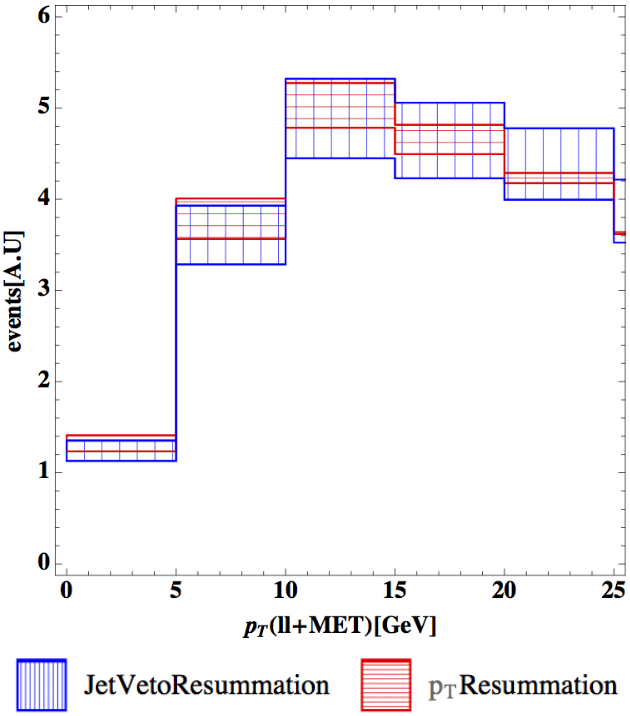

Figure 3.6: The $p_T(\ell^+\ell^- + \mathrm{MET})$ distribution after a parametrized smearing of MET.

We demonstrate this in Figure 3.6 by applying a MET smearing[8] to the predictions for the

---

[8] We find smearing parameters for MET parallel and perpendicular to p_T^{WW} by fitting to the p_T $(\ell^+\ell^- + \mathrm{MET})$

$p_T(\ell^+\ell^- + \mathrm{MET})$ distribution from both p_T and jet-veto resummation. Unfortunately even though at truth level there are theoretically different distributions, the difference are washed out in a channel such as W^+W^-. Nevertheless, it is important to note that the resummation calculations reviewed in this paper are essentially universal for all diboson processes. Therefore, with the high luminosity run of the LHC it should be possible to disentangle these effects and ultimately provide a robust test of whether QCD can successfully describe these important proves of the EW structure of the SM. In addition, it would be useful to find new variables in MET dominated channels that remove the sensitivity to the MET uncertainty and allow for further quantitative tests of QCD predicted by resummation.

Theoretically without relying on reweighting, the only way to advance further in the directions we have explored is to go to a joint resummation formalism such as in [109]. While this program is and should be carried out, much information can be gained by comparing across channels with and without jet-vetoes to better choose scales and NP factors in p_T resummation. At this point, with the lessons learned from comparing individual resummation methods we recommend that experimentalists implement p_T resummation reweighting for all diboson channels. This should be extended not only to the SM measurements but to background processes as well, for instance for $h \to W^+W^-$. A final theoretical error in jet-vetoed processes can be formed from jet-vetoed cross sections, but in practice at this point p_T resummation is most useful to reweight events and better to directly compare with experimental data.

As we have demonstrated, we have entered into a qualitatively new era at the LHC where we now have an example of the need for NNLL resummation in addition to NNLO fixed order calculations to describe the data. To go further will require both theoretical and experimental efforts. It is important that a program be developed that cuts across various SM channels and provides a comprehensive test of how well the SM describes LHC data. While we have shown that higher order QCD corrections can ameliorate the most discrepant SM measurement from Run 1 of the LHC, it is important to note that none of these effects were included in other SM channels. In particular, the stunning agreement with the SM in almost all channels compared to NLO MC

---

plot in [26].

results and inclusive cross sections should now be interpreted as a systematic discrepancy in almost all diboson channels other than W^+W^-. It is important to investigate this further, and we hope with a concerted theoretical and experimental effort at Run 2, we will see whether the SM triumphs at the EW scale or we will have our first hints of new physics emerging.

Chapter 4

Resummation of jet veto logarithms at N^{3}LL$_a$ + NNLO for W^+W^- production at the LHC

4.1 Introduction

Run 1 of the LHC saw unprecedented reach in the energy frontier. This resulted in the Higgs discovery and also opened up opportunities for electroweak precision measurements. While precision electroweak processes are important in their own right, they also serve as the largest backgrounds to the important Higgs decays. Thus it is imperative to confirm electroweak predictions.

The 7 and 8 TeV run, while confirming the Higgs prediction, provided little evidence in terms of physics beyond the standard model (BSM), with most electroweak channels agreeing exactly with the Standard Model predictions. At this juncture a 3σ excess was reported by both ATLAS and CMS [25, 26, 110, 111] and this led to speculation about the existence of new physics [35, 34, 39, 36, 38, 37].

The WW channel is interesting in its own right because it tests the structure of the three gauge boson vertex and is a significant background for many BSM searches. The $h \to W^+W^-$ signal also has the SM W^+W^- production as an irreducible background, making it crucial to understand electroweak W^+W^- production accurately[94, 112, 113, 29, 114, 47].

It is interesting to note that the W^+W^- channel has a large top quark background. In order to tame this background, events containing jets with transverse momentum above 25 (30) GeV for ATLAS(CMS) are vetoed. This jet veto cut necessary to obtain the fiducial cross section is unique to the W^+W^- channel among electroweak processes. The presence of a new scale (the jet-veto scale) disparate from the typical energy scale $\sim 2m_W$ introduces large logarithms in perturbation theory. These effects can be large and increase the theoretical prediction for the fiducial cross section compared with NLO parton shower predictions[100, 99, 102, 103, 115]. This effect along with the NNLO fixed order calculation [94] created better agreement with experimental results and indeed this was confirmed by CMS [108]. These developments are summarized in [116]. The full 8 TeV ATLAS analysis, however, still reports a small excess [117].

The availability of two-loop matrix elements for W^+W^- production [95, 118] has made possible NNLO predictions for the W^+W^- production total cross section [94] and differential distributions [112]. Furthermore, it is possible to extend both transverse momentum [106] to NNLL +NNLO (equivalent to NNLL'+NNLO or N^{3}LL$_a$+NNLO in our log-counting convention) and jet-veto resummation calculations to N^{3}LL$_a$+NNLO. The latter is carried out in this paper using soft collinear effective theory [119, 120, 121, 122, 123, 124, 125]. This leads to more precise results with smaller scale uncertainties, which could result in better tests of experiment-theory agreement.

The paper is organized as follows. In Section 4.2 we review the implementation of differential NNLO diboson production in Sherpa [126], and in Section 4.3 the SCET formalism for jet veto resummation. In Section 4.4 we present numerical results followed by concluding remarks.

4.2 fixed order

We make NNLO predictions for on-shell W^+W^- production with arbitrary cuts, using an implementation of q_T subtraction [127, 113] in Sherpa [126] with matrix element generators AMEGIC++ [128] and Comix [129]. We use the SCET transverse momentum factorization formalism [77], with the 2-loop transverse parton distribution functions calculated in [130], to predict the NNLO cross section below a given q_T^{cut} for the W^+W^- pair momentum. This is implemented as a K factor multiplying the Born cross section in Sherpa. The NNLO cross section above the q_T cut corresponds to an NLO cross section for W^+W^-j production [131, 132, 133], obtained using Sherpa's built-in NLO capability based on Catani-Seymour dipole subtraction [134] and the OpenLoops implementation [135] of one-loop virtual matrix elements (a customized version with $n_f = 4$ flavors is used). We extract the two-loop virtual correction from the public code `qqvvamp` [95] for diboson production, together with appropriate coupling factors specific to the W^+W^- process. In Ref. [95], Eq. (6.2)-(6.5) defines the IR-divergent, UV renormalized amplitude in the standard $\overline{\text{MS}}$ scheme at the renormalization scale $\mu_r = m_{WW}$,

$$\Omega(\epsilon) = \Omega^{(0)} + \left(\frac{\alpha_s}{2\pi}\right)\Omega^{(1)} + \left(\frac{\alpha_s}{2\pi}\right)^2\Omega^{(2)}. \tag{4.2.1}$$

Eq. (6.6) of Ref. [95] defines the IR-finite amplitude in the scheme of [136], and can be re-written as

$$\Omega^{\text{finite}} = \Omega(\epsilon) \cdot I(\epsilon), \tag{4.2.2}$$

where

$$I(\epsilon) = 1 - \left(\frac{\alpha_s}{2\pi}\right) I_1(\epsilon) - \left(\frac{\alpha_s}{2\pi}\right)^2 I_2(\epsilon). \tag{4.2.3}$$

Several checks are performed to confirm the validity of our extraction of virtual amplitudes from the `qqvvamp` library. First, when only Drell-Yan type diagrams are taken into account by the code, we reproduce the well-known 1-loop and 2-loop hard functions for the Drell-Yan process [137, 113]. Second, we are able to reproduce known 1- and 2-loop diphoton production virtual corrections [138] from `qqvvamp`, by setting the outgoing boson mass close to zero. Third, the one-loop W^+W^- virtual correction extracted from the library agrees with the known results in [29].

We adopt the $n_f = 4$ scheme in both the fixed order and resummed calculations, to avoid complications from top resonances. In the $n_f = 5$ scheme, effects from the top resonance first enter the W^+W^- rate at NLO[94]. We use MSTW 2008 NNLO $n_f = 4$ parton distributions [139]. To speed up the numerical evaluation, we fit the 2-loop virtual correction for both d-type and u-type quarks, as a function of the pair invariant mass m_{WW} and the polar angle θ. We use cubic interpolation on a two-dimensional grid of size 34×89, achieving an accuracy of 10^{-4} in almost all phase space points. We use the physical constants $G_F = 1.1663787 \times 10^{-5}$ GeV^{-2}, $m_W = 80.399$ GeV, and $m_Z = 91.1876$ GeV.

Though we will present cross sections with kinematic cuts in latter parts of the paper, we first check that the total cross section from our implementation reproduces known results, at the renormalization scale and factorization scale $\mu_r = \mu_f = m_W$. For the 13 TeV $pp \to W^+W^-$ total cross section, we obtain (118.4 ± 0.4) pb with $q_T^{\mathrm{cut}} = m_{WW}/200$ and 46 million integration points, or (118.8 ± 0.8) pb with $q_T^{\mathrm{cut}} = m_{WW}/2000$ and 342 million integration points, demonstrating excellent q_T^{cut} independence through one order of magnitude. Both of the above results agree with the known NNLO results in [94] within statistical errors. For the rest of this paper, we will use $q_T^{\mathrm{cut}} = m_{WW}/200$, and omit the uncertainty from q_T^{cut} dependence, estimated to be around 0.34% from the two numbers above. For 8 TeV, we obtain (59.94 ± 0.16) pb with $q_T^{\mathrm{cut}} = m_{WW}/200$, again in close agreement with Ref. [94]. For the purpose of comparison, these results include the gg box diagram (without the small interference effect from Higgs intermediate states), which contributes 3.9 pb at 13 TeV and 1.5 pb at 8 TeV.

4.3 Jet veto resummation

We study the process $q\bar{q}(gg) \to W^+W^- + X$ where X are hadronic jets satisfying the jet-veto condition, $p_T^{\text{jet}} < p_T^{\text{veto}}$. The core Born process $q\bar{q} \to W^+W^-$ starts at $\mathcal{O}(\alpha_s^0)$, while the core Born process $gg \to W^+W^-$ is loop-induced and starts at $\mathcal{O}(\alpha_s^2)$. Notice that the resummed corrections to $q\bar{q} \to W^+W^-$ also include gg initial state contributions, in e.g. the $\mathcal{O}(\alpha_s^2)$ order double-real part, but this is distinct from the loop-induced $gg \to W^+W^-$ which may be considered as a separate process. Due to the presence of multiple scales, large logarithms of the form $\alpha_s^n \ln^m \lambda$ $(m \leq 2n)$ arise at higher orders in perturbation theory, with $\lambda \equiv \left(\frac{p_T^{\text{veto}}}{m_{WW}}\right) \ll 1$ being the ratio of two scales. Methods for resumming these large logarithms are developed in Refs. [55, 56, 57, 58, 59, 60, 61]. We employ SCET formalism with λ as the power-counting parameter of the effective theory. While we work at leading order in SCET, the expansion in α_s in the context of resummation has differing conventions in the literature that we wish to clarify. Counting large logarithms $\log \lambda \sim \alpha_s^{-1}$, we define N^{n+1}LL resummation as the expansion in α_s up to and including $\mathcal{O}(\alpha_s^n)$ terms.

Using the SCET formalism with an analytic regulator to deal with rapidity divergences, the jet-veto cross-section factorizes as [60, 105],

$$\begin{aligned}\frac{d\sigma}{dm_{WW}\,dy\,d\cos\theta} = &\sum_{i,j=q,\bar{q},g} \mathcal{H}_{ij}(m_{WW},\mu_f,\mu_h,\cos\theta)\\ &\times \mathcal{B}_i(\xi,p_T^{\text{veto}},\mu_f,\nu_B,R)\,\mathcal{B}_j(\bar{\xi},p_T^{\text{veto}},\mu_f,\bar{\nu}_B,R)\\ &\times \left(\frac{\nu_S\bar{\nu}_S}{\nu_B\bar{\nu}_B}\right)^{g(\mu_f)} \mathcal{S}(p_T^{\text{veto}},\mu_f,\nu_S,\bar{\nu}_S,R)\,, \end{aligned} \tag{4.3.4}$$

where $\mathcal{H}$, $\mathcal{B}$ and $\mathcal{S}$ are the hard, beam and soft functions, respectively, R is the jet radius and first enters at two-loops, and $\nu_S,\bar{\nu}_S,\nu_B,\bar{\nu}_B$ are rapidity renormalization scales. The function $g(\mu_f)$ is defined in Eq. 4.3.26. In principle, the beam function could depend on an independent scale, μ_b, but we always take $\mu_b = \mu_f$. We ignore factorization-violating effects which start at $\mathcal{O}(\alpha_s^4)$ [140, 141, 142].

4.3.1 Hard function

The hard function $\mathcal{H}$ is roughly speaking the square of the SCET Wilson coefficient C which is obtained by matching SCET to QCD at a hard scale, $\mu_h \sim m_{WW}$, and then by renormalization group (RG) evolving down to the factorization scale, $\mu_f \sim p_T^{\text{veto}}$.

For the NLL+LO resummation of $gg \to W^+W^-$, we only need the LO hard function, which may be easily extracted from the Born-level distributions generated by Sherpa. For the rest of this subsection, we will focus on the 2-loop hard function for $q\bar{q} \to W^+W^-$, needed for N^{3}LL resummation.

The SCET hard matching coefficient C is given by,

$$C = \Omega(\epsilon)/\Omega_{sc}(\epsilon) = \Omega(\epsilon)\cdot I^{\text{SCET}}(\epsilon), \tag{4.3.5}$$

where,

$$I^{\text{SCET}}(\epsilon) = 1 - \left(\frac{\alpha_s}{2\pi}\right) I_1^{\text{SCET}}(\epsilon) - \left(\frac{\alpha_s}{2\pi}\right)^2 I_2^{\text{SCET}}(\epsilon). \tag{4.3.6}$$

In Eq. Eq. (**??**), Ω is the full QCD amplitude defined in Eq. Eq. (**??**), and Ω_{sc} is the amplitude obtained from the SCET Lagrangian by setting the hard matching coefficient to 1. For massless parton scattering, Ω_{sc} is a dimensionless integral at every non-zero loop order, and contains pure IR poles after $\overline{\mathrm{MS}}$ UV subtraction (here "pure poles" means there are no ϵ-independent constant terms).

In other words, the main difference between the definition of the SCET hard function and the IR subtraction scheme used in `qqvvamp` is the fact that SCET uses pure poles for subtraction. The amplitude Ω^{finite} from `qqvvamp` can be squared and converted into the SCET hard function $\mathcal{H}$ at the central hard scale $\mu_h = m_{WW}$ by using the relation,

$$\begin{aligned}\tilde{\mathcal{H}}(\mu_h = m_{WW}) &= \left|\Omega^{\text{SCET}}\right|^2 \\ &= \left|\Omega^{\text{finite}}\right|^2 \left[1 + \left(\frac{\alpha_s}{2\pi}\right) \hat{I}_1(\epsilon) + \left(\frac{\alpha_s}{2\pi}\right)^2 \hat{I}_2(\epsilon)\right],\end{aligned} \tag{4.3.7}$$

where,

$$\begin{aligned}\hat{I}_1 &= \frac{\pi^2 C_F}{6}, \\ \hat{I}_2 &= \frac{1}{72} C_F \left(\pi^4 C_F + 36\delta_{q_T}^{(1)} + 12\pi^2 K + 48\beta_0 C_F \zeta_3\right),\end{aligned} \tag{4.3.8}$$

and $\delta_{q_T}^{(1)}$ and K are defined in Eq. (6.11) of Ref. [95]. Once we have the 1-loop and 2-loop hard function $\tilde{\mathcal{H}}$ at the scale m_{WW}, we use SCET RG running to restore the full dependence on the scale μ_h. Writing

$$\mathcal{H} = \mathcal{H}^{(0)} + \mathcal{H}^{(1)} a_s + \mathcal{H}^{(2)} a_s^2, \tag{4.3.9}$$

where $a_s = \alpha_s/(4\pi)$, and

$$L_h = \log \frac{\mu_h}{m_{WW}}, \tag{4.3.10}$$

the μ_h dependence of $\mathcal{H}^{(2)}$ is

$$\begin{aligned}\mathcal{H}^{(2)}(\mu_h) = \mathcal{H}^{(2)}(m_{WW}) &+ 2\mathcal{H}^{(1)}(m_{WW})\gamma_0 L + 2\gamma_1 L \\ &- 2\Gamma_1 L^2 - 2\mathcal{H}^{(1)}(m_{WW})\Gamma_0 L^2 + 2\gamma_0^2 L^2 \\ &- 4\Gamma_0\gamma_0 L^3 + 2\Gamma_0^2 L^4 + 2\beta_0 \left(\mathcal{H}^{(1)}(m_{WW}) L + \gamma_0 L^2 - \frac{2}{3}\Gamma_0 L^3\right),\end{aligned} \tag{4.3.11}$$

where Γ_n and γ_n are the perturbative expansions of the cusp and non-cusp part of the anomalous dimension for the Drell-Yan like hard function, found in e.g. [143].

The SCET Wilson coefficients C satisfy the RG equation,

$$\mu\frac{\mathrm{d}C(\mu)}{\mathrm{d}\mu} = \left(\Gamma_i^{\text{cusp}}\log\left(\frac{-m_{WW}^2 - i\epsilon}{\mu_h^2}\right) + 2\gamma_i\right)C(\mu)\,, \tag{4.3.12}$$

where γ and Γ^{cusp} are the anomalous and cusp-anomalous dimensions, respectively, with $i = F$ for a $q\bar{q}$ initiated process, while $i = A$ for a gg initiated-process. For brevity, we have suppressed Lorentz indices as well as external particle momentum dependence in the Wilson coefficients. N^{3}LL accuracy requires 3-loop anomalous dimensions which are known and 4-loop cusp anomalous dimensions for which we use the Pade approximation. Up to 3-loops, the gluon anomalous dimensions can be obtained from the quark anomalous dimensions by replacing C_F with C_A.

The solution to the RG evolution of the SCET Wilson coefficients can be written as [143],

$$C(\mu) = \mathcal{U}(\mu,\mu_h)C(\mu_h)\,, \tag{4.3.13}$$

where the evolution function $\mathcal{U}$ is given by,

$$\begin{aligned}\mathcal{U}(\mu,\mu_h) \;&= \exp\;\Big[2S(\mu,\mu_h) - 2a_\gamma(\mu,\mu_h)\\ &\qquad -a_\Gamma(\mu,\mu_h)\log\left(\frac{-m_{WW}^2 - i\epsilon}{\mu_h^2}\right)\Big]\end{aligned} \tag{4.3.14}$$

and expressions for S, a_γ and a_Γ can be found in Ref. [143].

Using Eq.Eq. (**??**), we get the following result for the resummed hard function

$$\mathcal{H}(\mu,\mu_h) = |\mathcal{U}(\mu,\mu_h)|^2\,\tilde{\mathcal{H}}(\mu_h) \tag{4.3.15}$$

4.3.2 Beam function

The beam functions, at lowest order are simply the PDFs, $\mathcal{B}_i = \phi_i$, while at higher orders the PDFs are convoluted with kernels as follows,

$$\mathcal{B}_i(\xi, p_T^{\text{veto}}, \mu, R) = \int_\xi^1 \frac{dz}{z}\sum_k I_{i\leftarrow k}(z, p_T^{\text{veto}}, \mu, R)\phi_k(\frac{\xi}{z}, \mu)\,. \tag{4.3.16}$$

Expanding the kernels in α_s, we have

$$I_{i\leftarrow k}(z, p_T^{\text{veto}}, \mu, R) = \hat{I}_{qi}^{(0)} + a_s\hat{I}_{qi}^{(1)} + a_s^2\hat{I}_{qi}^{(2)} + \cdots \tag{4.3.17}$$

where $a_s \equiv \alpha_s(\mu)/(4\pi)$. The kernels $\hat{I}$ are in general functions of $\{z, \mu, p_T^{\text{veto}}, R\}$. The $\mathcal{O}(\alpha_s)$ kernels are

$$\begin{aligned}
\hat{I}_{qq}^{(1)} = &- \left[\left(\frac{d_1}{2} + \gamma_0 \right) L_\perp + \Gamma_0 \frac{L_\perp^2}{4} \right] \delta(1-z) \\
&- \mathcal{P}_{qq}^{(1)} \frac{L_\perp}{2} + \mathcal{R}_{qq}^{(1)}(z), \qquad (4.3.18) \\
\hat{I}_{qg}^{(1)} = &-\mathcal{P}_{qg}^{(1)} \frac{L_\perp}{2} + \mathcal{R}_{qg}^{(1)}(z), \qquad (4.3.19)
\end{aligned}$$

where we define $L_\perp = 2\log(\mu/p_T^{\text{veto}})$, γ_n and Γ_n denote the non-cusp and cusp anomalous dimensions for the hard function at order n, and $\mathcal{P}_{ij}^{(n)}$ denotes the DGLAP splitting kernel at order n. The non-logarithmic terms in the above equations, denoted by $\mathcal{R}_{ij}^{(n)}$, can be deduced from Ref. [77], and are given by

$$\begin{aligned}
\mathcal{R}_{qq}^{(1)}(z) &= C_F \left[2(1-z) - \frac{\pi^2}{6} \delta\left(1-z\right) \right], \\
\mathcal{R}_{qg}^{(1)}(z) &= 4T_F z(1-z). \qquad (4.3.20)
\end{aligned}$$

In addition, we include approximate NNLO kernels by solving RG evolution equations to obtain the terms that depend on $L_\perp$.[1]. Here, $d_1 = 0$ while d_2 depends on the jet radius R and can be found in Ref. [61]. The N^{3}LL ingredient d_3 also depends on R. The leading $\log R$ terms in d_3 are known and can be extracted from [145, 146]. We include these terms in our numerical results.

The result for $\hat{I}_{qq}^{(2)}$, describing the quark beam function corresponding to the quark PDF of the

---

[1] Approximate NNLO beam functions have been previously obtained in a different rapidity regularization scheme in Ref. [144].

same flavor, is

$$
\begin{aligned}
\hat{I}_{qq}^{(2)} &= \frac{(\Gamma_0)^2}{2}\left(\frac{L_\perp}{2}\right)^4 \\
&+ \left[(d_1 - \frac{4}{3}\beta_0 + 2\gamma_0)\delta(1-z)\mathcal{P}_{qq}^{(1)}(z)\right]\Gamma_0\left(\frac{L_\perp}{2}\right)^3 \\
&+ \Bigg\{ \left[\frac{d_1}{2}(d_1 + 4\gamma_0) - 2\beta_0(d_1+\gamma_0) + 2\gamma_0^2 - \Gamma_1\right] \\
&\times \delta(1-z) - \Gamma_0\mathcal{R}_{qq}^{(1)}(z) + (d_1 - \beta_0 + 2\gamma_0)\mathcal{P}_{qq}^{(1)}(z) \\
&+ \frac{\mathcal{P}_{qq}^{(1)}(z)\otimes\mathcal{P}_{qq}^{(1)}(z)}{2} + \frac{\mathcal{P}_{qg}^{(1)}(z)\otimes\mathcal{P}_{gq}^{(1)}(z)}{2}\Bigg\}\left(\frac{L_\perp}{2}\right)^2 \\
&+ \Bigg\{ -(d_2 + 2\gamma_1)\delta(1-z) - (d_1 - 2\beta_0 + 2\gamma_0)\mathcal{R}_{qq}^{(1)} \\
&- \mathcal{P}_{qq}^{(2)}(z) - \mathcal{R}_{qq}^{(1)}(z)\otimes\mathcal{P}_{qq}^{(1)}(z) \\
&- \mathcal{R}_{qg}^{(1)}(z)\otimes\mathcal{P}_{gq}^{(1)}(z)\Bigg\}\left(\frac{L_\perp}{2}\right)^1 + \mathcal{R}_{qq}^{(2)}(z)\left(\frac{L_\perp}{2}\right)^0 ,
\end{aligned}
\tag{4.3.21}
$$

where,

$$
f(z,\dots)\otimes g(\xi,\dots) = \int_\xi^1 \frac{\mathrm{d}z}{z} f(z,\dots)g(\xi/z,\dots)\,. \tag{4.3.22}
$$

The result for $\hat{I}_{qg}^{(2)}$, describing the quark/anti-quark beam function involving the gluon PDF, is

$$
\begin{aligned}
\hat{I}_{qg}^{(2)} &= \Gamma_0\mathcal{P}_{qg}^{(1)}(z)\left(\frac{L_\perp}{2}\right)^3 \\
&+ \Bigg\{ -\Gamma_0\mathcal{R}_{qg}^{(1)}(z) + (d_1 - \beta_0 + 2\gamma_0)\mathcal{P}_{qg}^{(1)}(z) \\
&+ \frac{\mathcal{P}_{qq}^{(1)}(z)\otimes\mathcal{P}_{qg}^{(1)}(z)}{2} + \frac{\mathcal{P}_{qg}^{(1)}(z)\otimes\mathcal{P}_{gg}^{(1)}(z)}{2}\Bigg\}\left(\frac{L_\perp}{2}\right)^2 \\
&+ \Bigg\{ -(d_1 - 2\beta_0 + 2\gamma_0)\mathcal{R}_{qg}^{(1)}(z) - \mathcal{P}_{qg}^{(2)}(z) \\
&- \mathcal{R}_{qq}^{(1)}(z)\otimes\mathcal{P}_{qg}^{(1)}(z) - \mathcal{R}_{qg}^{(1)}(z)\otimes\mathcal{P}_{gg}^{(1)}(z)\Bigg\}\left(\frac{L_\perp}{2}\right)^1 \\
&+ \mathcal{R}_{qg}^{(2)}(z)\left(\frac{L_\perp}{2}\right)^0 .
\end{aligned}
\tag{4.3.23}
$$

Finally, the result for $\hat{I}^{(2)}_{qq'}$, describing the quark beam function corresponding to the PDF of an anti-quark or a quark of a different flavor, is

$$\begin{aligned}\hat{I}^{(2)}_{qq'} &= \left\{\frac{\mathcal{P}^{(1)}_{qg}(z)\otimes\mathcal{P}^{(1)}_{gq'}(z)}{2}\right\}\left(\frac{L_\perp}{2}\right)^2\\ &\quad+\left\{-\mathcal{P}^{(2)}_{qq'}(z)-\mathcal{R}^{(1)}_{qg}(z)\otimes\mathcal{P}^{(1)}_{gq'}(z)\right\}\left(\frac{L_\perp}{2}\right)^1\\ &\quad+\mathcal{R}^{(2)}_{qq'}(z)\left(\frac{L_\perp}{2}\right)^0 .\end{aligned} \tag{4.3.24}$$

The coefficients of $(L_\perp/2)^0$ in the above three equations are unknown, and are set to zero in our calculation. Due to the missing non-logarithmic contributions in the beam functions, we can not claim full N^{3}LL accuracy. We term our resummation with approximate two-loop beam functions as partial N^{3}LL, abbreviated as N^{3}LL$_p$.

4.3.3 Rapidity Renormalization Group

We adopt a regularization scheme for rapidity divergences where the soft-function $\mathcal{S} = 1$ to all orders in perturbation theory. In the language of the rapidity renormalization group [147, 148], the factor $(\nu_S\bar{\nu}_S/\nu_B\bar{\nu}_B)^{g(\mu)}$ in Eq. Eq. (2.2.1) is the result of the RG evolution of the rapidity scale ν between soft modes ($\nu_S \sim \bar{\nu}_S \sim \mu_f$) and collinear modes ($\nu_B \sim \bar{\nu}_B \sim m_{WW}$). Suppressing the p_T^{veto}, R and ξ dependence of the beam functions for brevity, the rapidity scale variation around their central values at the boundaries of the rapidity RG can be summarized as [105],

$$\begin{aligned}&\left(\frac{\nu_S\bar{\nu}_S}{\nu_B\bar{\nu}_B}\right)^{g(\mu_f)}\mathcal{B}_i(\mu_f,\nu_B)\,\mathcal{B}_j(\mu_f,\bar{\nu}_B)\\ &=\left(r\frac{\mu_f^2}{m_{WW}^2}\right)^{g(\mu_f)}\left[r^{-g(\mu_f)}\mathcal{B}_i(\mu_f)\,\mathcal{B}_j(\mu_f)\right]_{\mathcal{O}(\alpha_s^n)}\end{aligned} \tag{4.3.25}$$

where $1/2 < r < 2$ contributes to the rapidity scale uncertainty. The quantity inside the square bracket is expanded to $\mathcal{O}(\alpha_s^n)$ for N^{n+1}LL resummation while $g(\mu_f)$ outside the square bracket must be evaluated to $\mathcal{O}(\alpha_s^{n+1})$. For the central scale $r = 1$, Eq. Eq. (**??**) reduces to a form given in Ref. [60] where the factor $(\mu_f^2/m_{WW}^2)^{g(\mu_f)}$ has been termed the 'collinear anomaly'.

Writing $g(\mu)$ as a polynomial in $L_\perp \equiv 2\log(\mu/p_T^{\text{veto}})$,

$$g(\mu) \equiv \sum_{p=0}^{\infty} g^{(p)} L_\perp^p \,, \tag{4.3.26}$$

the perturbative expansions for $g^{(p)}$ are given by [105],

$$\begin{aligned}
g^{(0)} &= a_s d_1 + a_s^2 d_2 + a_s^3 d_3 \\
g^{(1)} &= a_s \Gamma_0 + a_s^2(\beta_0 d_1 + \Gamma_1) + a_s^3(2\beta_0 d_2 + \beta_1 d_1 + \Gamma_2) \\
g^{(2)} &= a_s^2 \frac{\beta_0 \Gamma_0}{2} + a_s^3(\beta_0^2 d_1 + \frac{\beta_1 \Gamma_0}{2} + \beta_0 \Gamma_1) \\
g^{(3)} &= a_s^3 \frac{\beta_0^2 \Gamma_0}{3}
\end{aligned} \tag{4.3.27}$$

where Γ_n and β_n denote the cusp anomalous dimension and the QCD beta function at order n.

The jet-veto resummed result can be combined with the fixed order result,

$$\sigma^{\text{matched}}_{\text{N}^3\text{LL}_p+\text{NNLO}} = \sigma^{\text{res}}_{\text{N}^3\text{LL}_p} + \sigma_{\text{NNLO}} - \sigma^{\text{res}}_{\text{N}^3\text{LL}_p}|_{\text{exp.}} \,, \tag{4.3.28}$$

and $\sigma^{\text{res}}|_{\text{exp.}}$ is the resummed result expanded up to $\mathcal{O}(\alpha_s^2)$. For the loop-induced gg contribution, we only match to LO, in which case the matching is trivial. These results can be directly compared with experiment for a given jet veto cut.

4.4 Results

Applying the formalism described in the above sections, we compute fixed-order and resummed W^+W^- cross section under a jet veto.

We present the fixed order NLO and NNLO cross sections with a jet veto at 13 TeV for two different central scale choices in Tab. 4.1. Our default choice in the remainder of this section is $\mu_f = \mu_r = p_T^{\text{veto}}$, which is convenient because we match resummation and fixed order results at the central scale $\mu_f = p_T^{\text{veto}}$. We see, however, that if we had chosen a larger scale, say $\mu_f = \mu_r = 2m_W$, the fixed order results would not be much changed. We will comment on the smallness of the scale dependence later. The scale uncertainties in the NLO and NNLO results are obtained by simultaneously varying μ_r and μ_f up and down by a factor of 2 around the central value p_T^{veto}.

	ATLAS	CMS
NLO ($\mu_f = \mu_r = p_T^{\text{veto}}$)	71.18 ± 2.17	74.68 ± 0.77
NLO ($\mu_f = \mu_r = 2m_W$)	72.82 ± 1.69	77.26 ± 1.30
NNLO ($\mu_f = \mu_r = p_T^{\text{veto}}$)	70.01 ± 1.09	73.46 ± 0.16
NNLO ($\mu_f = \mu_r = 2m_W$)	69.68 ± 0.88	74.89 ± 0.79

Table 4.1: Fixed order 13 TeV jet veto cross-sections for two disparate factorization/beam function central scale choices (p_T^{veto} and $2m_W$) for the ATLAS configuration $p_T^{\text{veto}} = 25$ GeV and R=0.4 and CMS configuration $p_T^{\text{veto}} = 30$ GeV and R=0.5 for on-shell W^+W^- production. The scale variations are symmetrized, i.e. they are averages over the absolute values of the fluctuations at twice the central scale and half the central scale. All cross section numbers are listed in pb. These numbers do not include the gg initial state.

The central hard scale is taken to be $\mu_h^2 = m_{WW}^2$ for the resummation of $q\bar{q} \to W^+W^-$, but the time-like scale choice $\mu_h^2 = -m_{WW}^2$ is used for the loop-induced gg channel to resum the π^2 terms that give large corrections to the LO hard function. The central factorization and beam function scales are $\mu_f = \mu_b = p_T^{\text{veto}}$, and the rapidity scale variation factor r defined in Ref. [105] is centered at 1. We vary these scales up and down by a factor of 2 in order to estimate uncertainties from as yet uncomputed higher order contributions. As an example, the cross sections with these scale variations are tabulated in Table 4.2 for $q\bar{q}$ processes with the CMS jet veto cut ($p_T^{\text{veto}} = 30$ GeV, $R = 0.5$) at 13 TeV.[2]

The rapidity scale variation at N^{3}LL$_p$+NNLO is artificially small at the central μ_b, as shown in the last column of the 2nd-to-last row in Table 4.2, due to the lack of non-logarithmic terms in our approximate NNLO beam functions. We therefore estimate the rapidity scale variation fixing μ_h at the central scale, but μ_b at half the central scale.

The scale uncertainties from μ_h, μ_b and r variations are symmetrized for simplicity (i.e. we do not give asymmetric error bars), and added in quadrature to obtain the combined uncertainty. Due to the Monte Carlo integration used to compute the fixed order NNLO cross section, we also have

---

[2] The qualitative features of this table also hold true at 8 TeV and for the ATLAS jet veto cuts at both 8 and 13 TeV.

$\{\mu_h/m_{WW}, \mu_b/p_T^{\text{veto}}, r\}$	NNLL+NLO	N^{3}LL$_p$+NNLO
$\sigma\{1,1,1\}$	67.49	71.18
$\Delta\sigma\{1,(2,\frac{1}{2}),1\}$	0.93	1.58
$\Delta\sigma\{(2,\frac{1}{2}),1,1\}$	1.92	0.84
$\Delta\sigma\{1,1,(2,\frac{1}{2})\}$	1.31	0.04
$\Delta\sigma\{1,\frac{1}{2},(2,\frac{1}{2})\}$	1.83	0.79

Table 4.2: 8 and 13 TeV scale variations for the CMS configuration $p_T^{\text{veto}} = 30$ GeV and R=0.5 for on-shell W^+W^- production. The scale variations are symmetrized, i.e. they are averages over the absolute values of the fluctuations at twice the central scale and half the central scale. All cross section numbers are listed in pb. These numbers do not include the gg initial state.

an additional statistical error. However it is small compared to the combined scale variations. We present the final results most relevant to the experiments, R=0.4, $p_T^{\text{veto}} = 25$ GeV for ATLAS in Table 4.3 and R=0.5, $p_T^{\text{veto}} = 30$ GeV for CMS in Table 4.4 with the theoretical error bars. The information from these two tables is also summarized in the plot, Figure 4.1. We note the effects of the π^2 resummation by presenting our final results both with and without this resummation (the last 2 lines in Tabs. 4.3, and 4.4). This effect can be seen to be small.

Going to one higher order, i.e. NNLL+NLO → N^{3}LL$_p$ +NNLO, has an appreciable effect on the jet veto cross section prediction, due to both the higher accuracy in the resummation and the matching to higher fixed order calculations. We observe that there is a reduction in scale uncertainties. We also present the corresponding fixed order results in order to illustrate the effects of resummation. One notices that the scale dependence of the corresponding fixed order calculations are much smaller than those of the resummed results, and in fact much smaller (as a percentage) than the uncertainties in the W^+W^- total cross section reported in Ref. [94]. This is because of the under-estimation of the scale dependence due to an accidental cancellation, as observed in Ref. [60].

Finally we compare the total $q\bar{q}$+gg cross-section under a jet-veto with full luminosity Run-1 experimental results from the LHC. For CMS, the unfolded result, available in Table 6 of [101], is

Order	8 TeV	13 TeV
NLO	38.68 ± 0.26	71.18 ± 2.17
NNLL+NLO	35.70 ± 1.73	62.88 ± 3.01
NNLO ($\mu = p_T^{\text{veto}}$)	$38.53 \pm 0.09 \pm 0.09$	$70.01 \pm 1.04 \pm 0.34$
N^{3}LL$_p$+NNLO	$37.36 \pm 1.46 \pm 0.09$	$65.60 \pm 2.61 \pm 0.34$
gg NLL	0.35 ± 0.11	0.80 ± 0.12
gg NLL (with π^2)	0.57 ± 0.21	1.31 ± 0.43
Total N^{3}LL$_p$+NNLO +gg NLL	37.45 ± 1.47	66.40 ± 2.63
Total N^{3}LL$_p$+NNLO +gg NLL (with π^2)	37.93 ± 1.48	66.91 ± 2.67

Table 4.3: 8 and 13 TeV Jet veto cross sections for the ATLAS configuration $p_T^{\text{veto}} = 25$ GeV and R=0.4 for on-shell W^+W^- production. All cross section numbers are listed in pb. The first error bar following each number denotes the scale uncertainty, while the 2nd error bar, if present, denotes the statistical error from Monte Carlo integration in the implementation of NNLO in Sherpa with the q_T subtraction cutoff $M_{WW}/200$.

44.0 ± 0.7(stat)± 2.5(exp)± 1.4(theo)± 1.1(lumi), in picobarns. This is in good agreement with our theoretical prediction of (40.66 ± 1.16) pb. For ATLAS, our theoretical prediction is (37.93 ± 1.48) pb, which may be compared with experimental data once an unfolded jet vetoed cross section is produced by ATLAS.

Order	8 TeV	13 TeV
NLO	41.50 ± 0.12	74.68 ± 0.77
NNLL+NLO	37.90 ± 1.50	67.49 ± 2.81
NNLO ($\mu = p_T^{\mathrm{veto}}$)	$41.20 \pm 0.03 \pm 0.09$	$73.46 \pm 0.19 \pm 0.18$
$\mathrm{N^3LL_a}$+NNLO	$39.95 \pm 1.13 \pm 0.09$	$71.13 \pm 1.96 \pm 0.18$
gg NLL	0.43 ± 0.37	1.01 ± 0.29
gg NLL (with π^2)	0.71 ± 0.25	1.65 ± 0.54
Total $\mathrm{N^3LL}_p$+NNLO +gg NLL	40.38 ± 1.19	71.42 ± 1.99
Total $\mathrm{N^3LL}_p$+NNLO +gg NLL (with π^2)	40.66 ± 1.16	72.78 ± 2.04

Table 4.4: Same as Table 4.3 , but for the CMS configuration $p_T^{\mathrm{veto}} = 30$ GeV and R=0.5 for on-shell W^+W^- production. All cross section numbers are listed in pb.

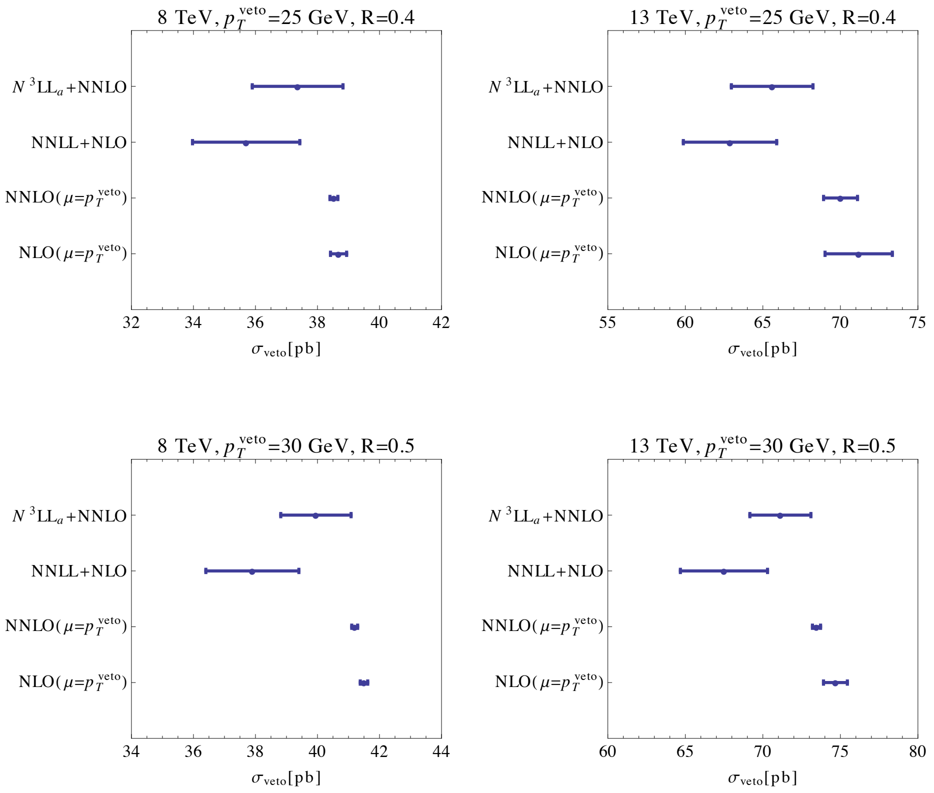

Figure 4.1: Summary of jet veto resummation results for $q\bar{q} \to W^+W^-$. We include results at 8 TeV and 13 TeV, under ATLAS or CMS jet veto cuts.

Chapter 5

Thermal Resummation and Phase Transitions

5.1 Introduction

Thermal phase transitions are ubiquitous phenomena in nature, but in fundamental physics they are difficult to study, and very few are known. In the SM there are phase transitions associated with QCD and the EW symmetry. The QCD phase transition can be studied directly in heavy ion collisions, with rapid progress over the last decade [149]. However, the EW phase transition (EWPT) is far out of reach of direct testability. Going beyond the Standard Model (BSM), the nature of the EW phase transition could change, and there could be additional phase transitions unrelated to the EWPT but still screened from us by the CMB. Nevertheless, even without direct measurements of the EWPT in the near future these phenomena can be indirectly studied, with profound consequences for our understanding of the early universe. The EWPT and other phase transitions can have correlated signals detectable at current and future colliders, and in the burgeoning field of gravitational wave astronomy. Therefore, it is important to have as much control of the underlying Finite-Temperature Quantum Field Theory (FTQFT) calculations as possible, so that potential signals are reliably understood and predicted. This is the aim of this paper, and we will introduce new methods in FTQFT to capture the effects of BSM physics on phase transitions.

While our results will be general, we single out the EWPT for special study given its possible deep connection to another fundamental question in particle physics.

One of the most profound mysteries in particle physics is our mere existence, and that of all baryons in the universe. A dynamical explanation for our universe containing an excess of matter over antimatter requires BSM physics. At some time in the history of the primordial plasma, after reheating but before Big Bang Nucleosynthesis ($T \sim \mathrm{GeV}$), a mechanism of *baryogenesis* has to create the observed baryon asymmetry [150, 151] of

$$\eta = \frac{n_B - n_{\overline{B}}}{n_\gamma} \sim 10^{-9} \ . \tag{5.1.1}$$

This requires the three Sakharov conditions [152] to be satisfied: baryon number (B) violation, CP violation, and a sufficiently sharp departure from thermal equilibrium.

Electroweak Baryogenesis [153, 154, 155, 156, 157, 158, 159] is a very appealing possibility, since all involved processes must occur near the weak scale, making it in principle testable. (See [160, 161, 16, 162, 163, 164] for reviews.) In the SM, high temperature effects stabilize the Higgs field at the origin, restoring electroweak symmetry [165, 166]. In this high-temperature unbroken phase, the SM in fact contains a $(B+L)$-violating process in the form of nonperturbative sphaleron transitions, which can convert a chiral asymmetry into a baryon asymmetry. The EWPT from the unbroken to the broken phase at $T \sim 100\mathrm{GeV}$ provides, in principle, a departure from thermal equilibrium. In the presence of sufficient CP-violation in the plasma, a baryon excess can be generated

EWBG cannot function within the SM alone. There is insufficient CP-violation (see for example [16]), and the EWPT is not first order for $m_h \gtrsim 70\mathrm{GeV}$ [167, 168]. Additional BSM physics is required to generate a strong phase transition (PT) and supply additional CP-violating interactions in the plasma.

Many theories have been proposed to fulfill these requirements of EWBG, including extensions of the scalar sector with additional singlets [169, 170, 171, 172, 173, 174, 175, 176, 177, 178, 179, 180, 181, 182] (which can be embedded in supersymmetric models [183, 184, 185, 186, 187, 188, 189]), two-Higgs doublet models [190, 191], triplet extensions [192, 193, 194], and the well-known Light-Stop Scenario in the MSSM [195, 196, 197, 198, 199, 200, 201, 202, 203, 204, 205] which is now excluded [206, 207, 208, 209]. To determine whether a particular, complete model can successfully account for the observed baryon asymmetry, the temperature-dependent Higgs potential and the resulting nature of the phase transition have to be carefully calculated to determine the sphaleron energy as well as the bubble nucleation rate and profile. This information serves as an input to solve a set of plasma transport equations, which determine the generated baryon asymmetry of the universe (BAU). The full calculation is very intricate, with many unresolved theoretical challenges (see e.g. [200, 210, 211, 212, 213, 214, 215, 216, 202, 217, 218, 201, 219, 220, 221, 222, 223, 224]).

The sectors of a theory which generate the strong phase transition, and generate baryon number via CP-violating interactions in the plasma, do not have to be connected (though they can be). Since one of the most appealing features of EWBG is its testability, it makes sense to consider these two conditions and their signatures separately. The ultimate aim is a model-independent understanding of the collider, low-energy, and cosmological signatures predicted by all the various incarnations of EWBG.

We will focus on the strong electroweak phase transition. If it is first order, there is a critical temperature T_c where the Higgs potential has two degenerate minima $h = 0$ and v_c, separated by an energy barrier. As the temperature decreases, the minimum away from the origin becomes the true vacuum, the Higgs field tunnels to the broken phase, and bubbles of true vacuum expand to fill the universe. A necessary condition for avoiding baryon washout is that v_c is sufficiently large to suppress sphalerons. Specifically, a BSM theory which realizes EWBG has to satisfy

$$\frac{v_c}{T_c} > 0.6 - 1.6 \; . \tag{5.1.2}$$

In most cases we will adopt the lower value of 0.6 as our cutoff [225] to be as inclusive as possible (though it is sometimes instructive to examine the parameter space that survives the more standard $v_c/T_c > 1$ criterion.) This is a useful way of checking whether a given BSM scenario is a viable candidate for EWBG, as well as determining the correlated signatures we could measure today.

Computing this ratio seems like a straightforward exercise, and a standard recipe has been adopted in the literature for computing the EWPT in BSM models (see e.g. [163] for a review). This involves constructing the one-loop effective Higgs potential at finite temperature by using a well-known generalization of the standard Coleman-Weinberg potential; possibly including a selection of the most important higher-loop effects and/or RG-improvements; and resumming an important set of contributions called hard thermal loops.

We carefully review this calculation in Section 5.2. Our focus is the resummation of hard thermal loops. The standard procedure, which we call *Truncated Full Dressing* (TFD), involves a very simple computation of thermal masses $\Pi_i \sim T^2$ for particles i in the plasma, to leading order in the high-temperature approximation, and inserting them back into the effective potential [226, 227, 228].

Various extensions of this simple recipe, to include higher-order corrections in temperature or coupling, have been explored roughly twenty years ago in the context of ϕ^4 theories [229, 230, 231, 232, 233, 234]. However, possibly because the consensus on the (most) correct generalization seemed unclear, and the involved calculations seemed onerous to perform for every BSM theory, these improvements have not found wide application in the study of the EWPT in general BSM scenarios.

We revisit these issues in a modern light, with a focus on the study of general BSM effects which can induce a strong EWPT. A simple and easily implementable extension of the TFD calculation is urgently required for two reasons: to correctly determine the phenomenology of EWBG, and to understand Effective Field Theory (EFT) at finite temperature.

Since the high-temperature expansion of Π_i is truncated at the leading term, it is only accurate to $\mathcal{O}(m/T)$. This can easily be $\sim 40\%$ at $T = T_c$, and vary with the Higgs field since its VEV determines particle masses. While this does not directly translate to a corresponding error on the full effective potential, an important class of (particularly testable) EWBG theories generates a strong EWPT via a partial cancellation between Π_i and tree-level parameters. In this case, accurate determination of the thermal masses, and their h-dependence, is clearly necessary to have confidence in the results of the phase transition computation, and hence the observables correlated with EWBG.

Effective Field Theories (EFTs) are a powerful tool to parameterize general new physics effects at zero temperature as a set of non-renormalizable operators involving SM fields. To understand the signatures of EWBG in a model-independent fashion, one would like to extend such an EFT analysis to finite temperature. Early attempts like [235, 236, 237, 238] suggested that a $|H|^6$

operator could induce a strong EWPT in correlation with sizable deviations in the cubic Higgs self-coupling, which could be detected with the next generation of future lepton [239, 240] and 100 TeV [241, 1, 242] colliders, or even the HL-LHC [243, 244, 245, 246, 247, 248]. Unfortunately, EFTs at finite Temperature are very poorly understood. For example, the effects of a particle with a mass of 300 GeV are quite well described in an EFT framework for collider experiments with $\sqrt{s} = 100\text{GeV}$, but it seems doubtful that this is the case for temperatures of $T = 100\text{GeV}$, since thermal fluctuations can excite modes somewhat heavier than T. Without understanding these effects in detail, we cannot know the EFT's radius of convergence in field space or temperature, and hence know whether its predictions regarding the EWPT can be trusted. The authors of [249] investigated the validity of finite temperature EFT by comparing it to a singlet scalar model in the TFD prescription. Since the assumptions of the high-temperature approximation ($T \gg m$) for Π_i in TFD are fundamentally incompatible with the assumptions of an finite-temperature EFT analysis ($T \ll m$), careful study of these decoupling effects during a phase transition, and EFT matching at finite temperature, requires a more complete treatment of thermal masses.

In this work, we develop a consistent, easily implementable procedure for the numerical computation and resummation of thermal masses in general BSM theories, beyond leading order in temperature and coupling.

We examine two competing approaches which were proposed in the context of ϕ^4 theories: *Full Dressing* (FD) [229, 230, 231] and *Partial Dressing* (PD) [232]. We verified the claims of [232] that PD avoids the problem of miscounting diagrams beyond one-loop order [233, 234], and that it generalizes beyond $\mathcal{O}(T^2)$. We therefore focus on PD. We review its formal underpinnings in Section 5.3 and outline how to generalize it to BSM theories, in general without relying on the high-temperature approximation.

Applying the PD procedure beyond the high-temperature approximation requires numerically solving a type of finite-temperature gap equation. We outline the implementation of this calculation in Section 5.4 in the context of a specific BSM benchmark model. Computing the strength of the EWPT with PD is extremely numerically intensive, necessitating the use of a custom-built `c++` code. This allows us to study the importance of resummed finite-temperature effects for the phase transition, but is impractical for future BSM studies. We show it is possible to modify PD by extending the gap equation and implementing certain approximations. This greatly increases numerical reliability, while reducing CPU cost by several orders of magnitude. We call this updated resummation procedure *Optimized Partial Dressing* (OPD) and show it is equivalent to PD for BSM studies of the EWPT.

OPD is only slightly more CPU-intensive than the standard TFD calculation used in most studies of the EWPT to date, and very easy to implement in Mathematica. We hope that this calculation, which is explained in Section 5.4 and summarized in the form of an instruction manual in Appendix A, will be useful in the future study of the EWPT for BSM theories.

The BSM model we use to develop and evaluate the PD and OPD resummation schemes is the SM with N_S added singlets transforming under an unbroken $O(N_S)$ symmetry in our vacuum (or $\mathbb{Z}_2$ if $N_S = 1$) and coupling to the SM via a quartic Higgs portal $\lambda_{HS}|H|^2 S_i^2$ without Higgs mixing. This benchmark model serves as a useful "worst-case scenario" for the collider phenomenology of EWBG, since it can produce a strong EWPT in a variety of ways which are representative of more complete theories, while generating the minimal set of collider signatures consistent with EWBG. The authors of [2] studied this scenario with $N_S = 1$ using the TFD calculation, making progress towards a "phenomenological no-lose theorem for EWBG" by showing that the future 100 TeV and lepton colliders could probe its EWBG-compatible parameter space completely. We update and generalize this phenomenological analysis for $N_S \geq 1$ in the PD scheme. As shown in Section 5.5, the "no-lose theorem" is strengthened, with EWPTs caused by larger numbers of scalars being easier to detect at colliders.

Phenomenologically, the main lessons of the updated PD calculation are that the detailed correlations between a strong EWPT and collider observables can be significantly shifted, especially in more complete theories of EWBG than our SM + $N_S \times S$ benchmark model. Furthermore, two-step transitions are more prevalent than suggested by earlier TFD calculations. This raises the exciting prospect of discovering the traces of a strong two-step transition with gravitational wave observations [250, 251]. Finally, unlike (O)PD, the TFD calculation overestimates the reliability of the finite-temperature EWPT calculation, underlining the importance of tracking error terms when computing the strength of the PT.

This paper is structured as follows. The standard TFD calculation of the EWPT is pedagogically reviewed in Section 5.2. Section 5.3 lays the formal groundwork of the PD scheme, while the implementation of the full calculation and its extension to the OPD scheme is described in Section 5.4. The differences in physical predictions between the standard TFD and the new (O)PD calculation are explored in Section 5.5. We conclude in Section 5.6, and provide an instruction manual for easy implementation of the OPD calculation for the EWPT in Appendix A.

5.2 Review: Calculating the Electroweak Phase Transition

We now review the standard computation of the finite-temperature Higgs potential in BSM theories (see e.g. [163]). We call the leading-order thermal mass resummation [226, 227, 228] TFD, to contrast with the PD procedure which we review and develop further in Sections 5.3 and 5.4. This will make plain some important shortcomings of TFD.

As a BSM benchmark, we consider the SM with N_S added real SM-singlet scalar fields S_i obeying an $O(N_S)$ symmetry (or $\mathbb{Z}_2$ if $N_S = 1$). We are also interested in regions of parameter space where this symmetry is unbroken in the zero-temperature vacuum of our universe today (i.e. $\langle S_i \rangle = 0$). This forbids Higgs-Singlet mixing, which significantly simplifies several formal aspects of thermal mass resummation. Unmixed singlet extensions also represent a useful "phenomenological nightmare scenario" for EWBG [2] with minimal experimental signatures. We show in Section 5.5 that this model can nonetheless be completely probed by the next generation of colliders.

5.2.1 Tree-level Potential

The tree-level scalar potential is

$$V_0 = -\mu^2 |H|^2 + \lambda |H|^4 + \frac{1}{2}\mu_S^2 (S_i S_i) + \frac{1}{4}\lambda_S (S_i S_i)^2 + \lambda_{HS} |H|^2 (S_i S_i). \tag{5.2.3}$$

We focus on the real h component of the SM Higgs doublet $H = (G^+, (h + iG^0)/\sqrt{2})$ which acquires a VEV during EWSB. Without loss of generality, we also assume that any excursion in S-field-space occurs along the S_0 direction. Therefore, the relevant part of the tree-level potential is

$$V_0 = -\frac{1}{2}\mu^2 h^2 + \frac{1}{4}\lambda h^4 + \frac{1}{2}\mu_S^2 S_0^2 + \frac{1}{4}\lambda_S S_0^4 + \frac{1}{2}\lambda_{HS} h^2 S_0^2 \; . \tag{5.2.4}$$

(Of course, Eq. (5.2.3) determines the form of the scalar masses $m^2_{G^+}(h, S_0), m^2_{S_i}(h, S_0), \ldots$ which determine the form of one-loop contributions as outlined below.) Our aim is to obtain the effective potential $V_{\text{eff}}(h, S, T)$ at one-loop order.

5.2.2 Coleman Weinberg Potential

At zero-temperature, the one-loop effective potential can be written as

$$V_{\text{eff}}^{T=0}(h, S) = V_0 + \sum_i V^i_{\text{CW}}(m^2_i(h, S)) \tag{5.2.5}$$

The Coleman-Weinberg potential is the zero-momentum piece of the zero-temperature effective action, and is a sum of 1PI one-loop diagrams with arbitrary numbers of external h and S_0 fields and particles $i = \{t, W, Z, h, G^\pm, G^0, S_0, S_k, \ldots\}$ running in the loop (where $k > 0$). Note that we are working in Landau gauge to avoid ghost-compensating terms, which requires including the Goldstone contributions separately, in addition to the massive W, Z bosons. (We discuss issues of gauge invariance in Section 5.2.6.)

The dependence of the i^{th} particle tree-level mass $m^2_i = m^2_i(h, S)$ on the VEVs of h and S determines V_{CW}. Summing over all contributions gives [252]:

$$V^i_{CW} = \frac{1}{2} \int \frac{d^4k}{(2\pi)^4} \log[k^2_E + m^2_i(h, S)] \tag{5.2.6}$$

where e.g. $m_h(h, S_0) = -\mu^2 + 3\lambda h^2 + \lambda_{HS} S^2_0$ and k_E is the euclidian momentum of particle i in the loop. We adopt the dimensional regularization scheme and $\overline{\text{MS}}$ renormalization scheme, with the usual $\epsilon = 2 - \frac{D}{2}$. This makes one-loop matching more onerous than the on-shell renormalization scheme, but allows for the potential to be RG-improved more easily. The result is

$$V^i_{CW} = \frac{m^4_i(h, S)}{64\pi^2} \left(-\epsilon - \gamma_E + \log 4\pi + \log \frac{m^2_i(h, S)}{\mu^2_R} \right) \tag{5.2.7}$$

(Hereafter we drop the explicit h, S dependence of the masses for brevity.) μ_R is the renormalization scale, and variation of physical observables after matching with different values of μ_R is a common way of assessing the uncertainty of our results due to the finite one-loop perturbative expansion. Adding counterterms and removing divergences yields the familiar expression

$$V^i_{CW} = (-1)^F g_i \frac{m^4_i}{64\pi^2} \left(\log \left[\frac{m^2_i}{\mu^2_R} \right] - c_i \right), \tag{5.2.8}$$

where $F = 1(0)$ for fermions (bosons), $c_i = \frac{3}{2}(\frac{5}{2})$ for scalars/fermions (vectors), and g_i is the number of degrees of freedom associated with the particle i.

5.2.3 Finite Temperature

Finite-temperature quantum field theory (FTQFT) enables the computation of observables, like scalar field vacuum expectation values, in the background of a thermal bath. The corresponding Greens functions can be computed by compactifying time along the imaginary direction, for details see e.g. [163]. To get an intuitive idea of finite-temperature effects on the one-loop effective potential, it is useful to consider integrals of the form

$$\int \frac{dk_0}{2\pi} f(k_0) \tag{5.2.9}$$

where k_0 is the time-like component of the loop momentum. This can be evaluated in FTQFT as

$$\int \frac{dk_0}{2\pi} f(k_0) \to T \sum_{n=-\infty}^{\infty} f(k_0 = i\omega_n) \ , \tag{5.2.10}$$

where $\omega_n = 2n\pi T$ and $(2n+1)\pi T$ are the Matsubara frequencies for bosons and fermions, respectively. Eq. (5.2.10) can be written in the instructive form:

$$\int \frac{dk_0}{2\pi} f(k_0) \to \int_{-i\infty}^{i\infty} \frac{dz}{4\pi i} \left[f(z) + f(-z)\right] \ + \ \eta \int_C \frac{dz}{2\pi i} n(z) \left[f(z) + f(-z)\right] \ , \tag{5.2.11}$$

where $\eta = \pm 1$ for bosons/fermions and $n(z) = (e^{z/T} - \eta)^{-1}$ are the standard Fermi-Dirac/Bose-Einstein distribution functions, for a particular choice of contour C. The first term, which is $n(z)$ independent, is simply the usual zero-temperature loop integral, while the second term is the new contribution from thermal loops in the plasma. This makes effects like thermal decoupling very apparent – if the particle mass is much larger than the temperature, its contribution to the second loop integral will vanish as $n(z) \to 0$.

Applying this formalism to the one-loop effective potential at finite temperature generalizes Eq. (5.2.5):

$$V_{\text{eff}}^{T>0}(h, S, T) = V_0 + \sum_i \left[V_{\text{CW}}^i(m_i^2(h, S)) + V_{\text{th}}^i(m_i^2(h, S), T)\right] \ , \tag{5.2.12}$$

where the second term is the usual Coleman-Weinberg potential, and the third term is the one-loop thermal potential

$$V_{\rm th}^{i}(m_i^2(h,S),T) = (-1)^F g_i \frac{T^4}{2\pi^2} J_{\rm B/F}\left(\frac{m_i^2(h,S)}{T^2}\right) \tag{5.2.13}$$

with thermal functions

$$J_{\rm B/F}(y^2) = \int_0^\infty dx\, x^2\, \log\left[1 \mp \exp(-\sqrt{x^2+y^2})\right] \tag{5.2.14}$$

which vanish as $T \to 0$. Note that y^2 can be negative. The thermal functions have very useful closed forms in the high-temperature limit,

$$\begin{aligned} J_B(y^2) &\approx J_B^{\rm high-T}(y^2) = -\frac{\pi^4}{45} + \frac{\pi^2}{12}y^2 - \frac{\pi}{6}y^3 - \frac{1}{32}y^4 \log\left(\frac{y^2}{a_b}\right) \\ J_F(y^2) &\approx J_F^{\rm high-T}(y^2) = \frac{7\pi^4}{360} - \frac{\pi^2}{24}y^2 - \frac{1}{32}y^4 \log\left(\frac{y^2}{a_f}\right) \qquad \text{for } |y^2| \ll 1\ , \end{aligned} \tag{5.2.15}$$

where $a_b = \pi^2 \exp(3/2 - 2\gamma_E)$ and $a_f = 16\pi^2 \exp(3/2 - 2\gamma_E)$. This high-$T$ expansion includes more terms, but they do not significantly increase the radius of convergence. With the log term included, this approximation for both the potential and its derivatives is accurate to better than $\sim 10\%$ even for $m \sim (1-3) \times T$ (depending on the function and order of derivative), but breaks down completely beyond that. The low-temperature limit ($|y^2| \gg 1$) also has a useful expansion in terms of modified Bessel functions of the second kind:

$$\begin{aligned} J_B(y^2) &= \tilde{J}_B^{(m)}(y^2) = -\sum_{n=1}^{m} \frac{1}{n^2} y^2 K_2(y\, n) \\ J_F(y^2) &= \tilde{J}_F^{(m)}(y^2) = -\sum_{n=1}^{m} \frac{(-1)^n}{n^2} y^2 K_2(y\, n) \qquad \text{for } |y^2| \gg 1\ . \end{aligned} \tag{5.2.16}$$

This expansion can be truncated at a few terms, $m = 2$ or 3, and yield very good accuracy, but convergence for smaller $|y^2|$ is improved by including more terms.

For negative m_i^2, the effective potential (both zero- and finite-temperature) includes imaginary contributions, which were discussed in [237]. These are related to decay widths of modes expanded around unstable regions of field space, and do not affect the computation of the phase transition. Therefore, we always analyze only the real part of the effective potential.

5.2.4 Resummation of the Thermal Mass: Truncated Full Dressing (TFD)

The effective potential defined in Eq. (5.2.12) can be evaluated at different temperatures to find v_c and T_c. The high-temperature expansion of J_B already reveals how one particular BSM effect could induce a strong EWPT. If a light boson is added to the plasma with $m_i^2 \sim h^2$, then the $-y^3$ term in J_B will generate a negative cubic term $-h^3$ in the effective potential, which can generate an energy barrier between two degenerate vacua. However, the calculation of the effective finite-temperature potential is still incomplete. There is a very well-known problem which must be addressed in order to obtain a trustworthy calculation [226, 227, 228].

This can be anticipated from the fact that a symmetry, which is broken at zero temperature, is restored at high-temperature. Thermal loop effects overpower a temperature-independent tree-level potential. This signals a breakdown of fixed-order perturbation theory, which arises because in FTQFT a massive scalar theory has not one but two scales: μ and T. Large ratios of T/μ have to be resummed.

To begin discussing thermal mass resummation, let us first consider not our BSM benchmark model but a much simpler ϕ^4 theory with quartic coupling λ and N scalar fields which obey a global $O(N)$ symmetry:

$$V_0 = -\frac{1}{2}\mu^2\phi_i\phi_i + \frac{1}{4}\lambda(\phi_i\phi_i)^2 \, . \tag{5.2.17}$$

(In fact, if we were to ignore fermions and gauge bosons, and set $\lambda = \lambda_{HS} = \lambda_S$, our BSM benchmark model would reduce to this case with $N = N_S + 4$.)

In FTQFT, the leading order high temperature behavior for diagrams with external scalar lines is directly related to the 0-temperature superficial degree of divergence d. Diagrams which have $d > 0$ have a T^d high temperature behavior. For $d \leq 0$, there is a linear T dependence. Appropriate factors of the coupling λ, N and the tree level mass parameter μ can be added from vertex counting and dimensional grounds. Therefore, the one-loop scalar mass correction shown in Fig. 5.1 (a) scales as $\sim N\lambda T^2$ to leading order in temperature, which is the "hard thermal loop". The phase transition occurs around the temperature where this thermal mass cancels the tree-level mass at the origin:

$$\mu^2 \sim N\lambda T^2 \qquad \Rightarrow \qquad \alpha \,\equiv\, N\lambda\frac{T^2}{\mu^2} \,\sim\, 1 \tag{5.2.18}$$

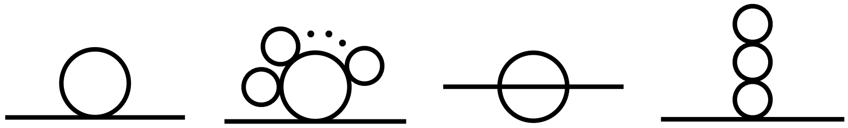
(a) (b) (c) (d)

Figure 5.1: Various scalar mass contributions in ϕ^4 theory: (a) one-loop mass correction, which is quadratically divergent at zero temperature, (b) higher-loop daisy contributions which are leading order in T and N at high temperature, (c) the two-loop “lollipop” contribution which is subleading in T and N to the two-loop daisy, (d) the three-loop superdaisy contribution, which is subleading in T but of equal order in N to the three-loop daisy.

At n-loop order, the leading contribution in temperature to the thermal mass is given by daisy diagrams shown in Fig. 5.1 (b):

$$\delta m^2_{\text{n-loop daisy}} \sim N^n \frac{\lambda^n T^{2n-1}}{\mu^{2n-3}} \quad , \quad n \geq 2 \tag{5.2.19}$$

The ratio of the n to the $n+1$ loop daisy contribution scales as

$$\frac{\delta m^2_n}{\delta m^2_{n-1}} \sim \alpha \tag{5.2.20}$$

which is not parametrically small during the phase transition, causing the perturbative expansion to break down. This can also be understood as an IR divergent contribution (in the high T limit) to the zero mode propagator.

To make the expansion more reliable, it is necessary to resum the the thermal mass by replacing the tree-level $m^2_{\text{tree}}(\phi)$ in Eq. (5.2.12) by $m^2(\phi) = m^2_{\text{tree}}(\phi) + \Pi(\phi, T)$, where in the standard method, Π is taken to be the leading contribution in temperature to the one-loop thermal mass. For scalars this can be obtained by differentiating V_{th} with respect to ϕ:

$$\Pi \sim \lambda T^2 + \ldots \tag{5.2.21}$$

The ellipses represent subleading contributions in both the high-temperature expansion and coupling order, which are neglected.

This substitution automatically includes daisy contributions to all orders in the effective potential. The largest contributions which are not included are the two-loop “lollipop” diagrams shown in Fig. 5.1 (c), scaling as $\lambda^2 T^2 N$, and the three-loop superdaisy shown in Fig. 5.1 (d), scaling as $\lambda^3 T^4 N^3/\mu^2$. Reliability of the perturbative expansion with the above thermal mass substitution requires

$$\lambda \ll 1, \quad \beta \equiv \frac{\lambda T N}{\mu} \ll 1\,. \tag{5.2.22}$$

These are obtained by requiring the ratio of the one-loop thermal mass to the sunset and the ratio of the two-loop daisy to the three-loop daisy to be small.

To illustrate how this resummation procedure is implemented in most BSM calculations, let us again turn to our $SM + N_S \times S$ benchmark model. The "dressed" effective potential is given by

$$V_{\text{eff}}^{\text{dressed}}(h,S,T) = V_0 + \sum_i \left[V_{\text{CW}}^i(m_i^2(h,S)+\Pi_i) + V_{\text{th}}^i(m_i^2(h,S)+\Pi_i,T)\right]\,, \tag{5.2.23}$$

where

$$\begin{aligned}\Pi_h(0) = \Pi_G(0) &= T^2\left(\frac{3}{16}g^2 + \frac{1}{16}g'^2 + \frac{1}{4}\lambda_t^2 + \frac{1}{2}\lambda + \frac{N_S}{12}\lambda_{HS}\right) \\ \Pi_S(0) &= T^2\left(\frac{1}{3}\lambda_{HS} + \frac{N_S+2}{12}\lambda_S\right) \\ \Pi_{GB}^L(0) &= \frac{11}{6}T^2\,\text{diag}(g^2,g^2,g^2,g'^2)\end{aligned} \tag{5.2.24}$$

and Π_{GB}^L is added only to the longitudinal gauge boson masses squared in the gauge basis, which are then diagonalized. Gauge symmetry suppresses thermal contributions to the transverse mode [230]. Note that fermions do not receive large thermal masses due to chiral symmetry protection. Furthermore, there are no zero modes $\omega_n = (2n+1)\pi T$, and as a result no IR divergences appear in the fermion propagator.

As we explain in Section 5.3, substituting $m_{\text{tree}}^2 + \Pi$ directly into the effective potential is called *Full Dressing* (FD). Since the thermal mass Π is explicitly evaluated only to leading order in the high-temperature expansion, we refer to this resummation procedure as *Truncated Full Dressing* (TFD). TFD is the standard approach for BSM calculations of the EW phase transition.

If V_{th}^i is expanded using the high-Temperature approximation of Eq. (5.2.15), the field dependent terms in logs cancel cancel between V_{CW}^i and V_{th}^i. The y^2 term gives an overall contribution proportional to $T^2\Pi_i$, which is field-independent when using only the leading-order contribution to Π_i in temperature. This just leaves the y^3 term, which can be captured by adding V^i_{ring}:

$$V_{\text{eff}}^{\text{dressed}}(h,S,T) = V_0 + \sum_i \left[V^i_{\text{CW}}(m_i^2(h,S)) + V^i_{\text{th}}(m_i^2(h,S),T) + V^i_{\text{ring}}(m_i^2(h,S),T)\right] \ , \tag{5.2.25}$$

where

$$V^i_{\text{ring}}(m_i^2(h,S),T) = -\frac{g_i T}{12\pi}\left(\left[m_i^2(h,S)+\Pi_i\right]^{3/2} - \left[m_i^2(h,S)\right]^{3/2}\right) \ . \tag{5.2.26}$$

Adding V^i_{ring} amounts to resumming the IR-divergent contributions to the Matsubara zero mode propagator. It is tantamount to performing the $m_i^2 \to m_i^2 + \Pi_i$ replacement in the full effective potential, under the assumption that only the thermal mass of the zero mode matters, which is equivalent to making a high-Temperature approximation.

This is the version of the finite-temperature effective potential used in most BSM calculations. In some cases, Eq. (5.2.25) is used but with the full finite-temperature V^i_{th} instead of the high-T expansion. This is more accurate when m_i is comparable to the temperature, but in that case the assumptions that justify using V_{ring} are explicitly violated, and Eq. (5.2.23) is the more consistent choice. In practice, there is not much numerical difference between these two recipes. As we discuss in Section 5.2.6, all of these TFD calculations have problems arising from using only the leading-order contribution of Π_i in temperature.

5.2.5 Types of Electroweak Phase Transitions

It is well-known that in the SM for $m_h \gtrsim 70\text{GeV}$, the EWPT is not first-order [167, 168]. To make the PT first order, new physics effects have to be added to the SM to generate an energy barrier between two degenerate vacua at $T = T_c$. These BSM scenarios can be broadly classified into a few classes (see also [253, 1]) based on the origin of the barrier between the two degenerate vacua. These are phase transitions driven by thermal effects, tree-level renormalizable effects, loop effects at zero-temperature and non-renormalizable operators. Note that our simple BSM benchmark model realizes the first three of these mechanisms. Rigorous study of the fourth mechanism will require the updated thermal resummation procedure we present in this paper.

PT driven by BSM Thermal Effects

It is possible that BSM bosonic degrees of freedom are present in the plasma. If they have the right mass and coupling to the SM Higgs, they can generate an energy barrier to make the PT strongly first order. Schematically, this can be understood as follows. If the boson(s) have tree-level mass $m_i^2 = \mu_S^2 + \lambda_{HS} h^2$, the effective potential of Eq. (5.2.25) contains a term of the form

$$-\frac{T}{12\pi}\left[\mu_S^2 + \lambda_{HS} h^2 + \Pi_S\right]^{3/2} \tag{5.2.27}$$

If this term is dominated by the h-dependent piece at $T = T_c$, the resulting $\sim -\lambda_{HS} h^3 T$ negative cubic term can generate an energy barrier between two degenerate minima and catalyze a strong first order PT.

In order for this cubic term to be manifest, it is required that $\mu_S^2 + \Pi_S \ll \lambda_{HS} v_c^2$. In the SM the W and Z bosons generate a cubic term, but their contribution is too small to make the SM EWPT first order. This can be enhanced in BSM scenarios by a partial cancellation between the new boson's thermal mass and a negative bare mass at $T = T_c$.

This scenario was long regarded as one of the most promising avenues for EWBG, because light stops in supersymmetry could serve as these new bosonic degrees of freedom (DOF) [195, 196, 197, 198, 199, 200, 201, 202, 203, 204, 205]. Higgs coupling measurements have since excluded that possibility for the MSSM [206, 207] and general models with colored scalars [208, 209]. Other scenarios, including the SM + $N_S \times S$ benchmark model we explore here, can easily realize this possibility [208, 209].

The mass of these light BSM bosonic DOF cannot significantly exceed $T_c \sim \mathcal{O}(100\text{GeV})$ to ensure their thermal contributions are unsuppressed. This makes such EWBG scenarios prime candidates for discovery at the LHC, and possibly future colliders. It is therefore of paramount importance to robustly correlate the predicted collider signatures with the regions of parameter space which allow for a strong phase transition.

This mechanism relies on a partial cancellation between a zero-temperature mass and a thermal mass. However, in the standard calculation, the thermal mass is computed only to leading order in the high-T expansion. This is troubling, since (a) even within the high-T expansion, subleading terms in the expansion can change the thermal mass by $\mathcal{O}(40\%)$ or more [254], and (b) the thermal mass should decrease for nonzero Higgs expectation values, since the bosons become heavier as $h \to v_c$ and partially decouple from the plasma. This can affect the electroweak phase transition, and the corresponding predictions for collider observables from a strong EWPT. Addressing this issue will be one of the major goals of our work.

PT driven by tree-level renormalizable effects

It is possible to add new scalars to the SM Higgs potential, see e.g. [169, 182, 179, 255]. In that case, the tree-level structure of the vacuum can be modified. For example, it is possible for the universe to first transition to a nonzero VEV of an additional singlet, only to transition to another vacuum with a nonzero Higgs VEV at a lower temperature. It is also possible for the Higgs to mix with new DOF (i.e. both the Higgs and the new DOF acquire VEVs in our vacuum). In that case, the tree-level potential can have a barrier between the origin and the EWSB minimum, resulting in a strong one-step phase transition at finite temperature.

These tree-driven one- or two-step PTs can easily be very strongly first order, but can also cause runaway bubbles, which are incompatible with sufficient BAU generation [256]. On the other hand, the strong nature of these PTs might make them discoverable by future gravitational wave observations [251]. It is therefore important to understand which regions of parameter space are associated with these types of phase transitions.

An intriguing version of the two-step EWBG scenario is possible when a triplet scalar is added to the SM [192, 193, 194]. In that case, the baryon asymmetry can be created in the first transition to the triplet-VEV-phase, and preserved in the second transition to the doublet-VEV phase which the universe inhabits at zero temperature.

PT driven by loop effects at zero temperature

New degrees of freedom with sizable couplings to the Higgs can generate non-analytical contributions to V_{CW} at zero temperature which "lift" the local $h = v$ minimum to a higher potential relative to the origin, compared to the SM. With this shallower potential well, SM Z and W boson thermal contributions can be strong enough to generate a cubic potential term at finite temperature, resulting in a strong PT. This was recently discussed in the context of future collider signatures by [2], and we will generalize their phenomenological results in this paper.

PT driven by non-renormalizable operators

The previous two phase transition classes are primarily associated with the zero-temperature effects of BSM degrees of freedom on the Higgs potential. If these states are sufficiently heavy, it might be reasonable to parametrize some of their effect in an EFT framework by adding a set or non-renormalizable operators to the SM Higgs potential. This was used to correlate Higgs self-coupling deviations with a strong EWPT [235, 236, 237].

While EFT analyses are useful for analyzing broad classes of new physics effects, their construction and validity at finite temperature is not well-understood.[1] At zero-temperature experiments, like mono-energetic collisions with energy E, the effects of perturbatively coupled particle with mass m can be well described by an EFT if $m/E > 1$. This is not the case in a plasma, where the heavy state can be directly excited even if m/T is larger than unity, generating sizable thermal loop contributions. Furthermore, EFTs are problematic when studying phase transitions, since the spectrum which is integrated out changes between the two vacua. Finally, the agreement between a full theory including heavy states and an EFT description cannot presently be studied reliably. This is because in the TFD thermal mass resummation procedure, the effects of new particles in the full theory on light scalar thermal masses never decouples since $\Pi \sim T^2$ is independent of contributing particle masses. The non-decoupling of high mass DOFs in the full theory calculation is clearly unphysical, preventing us from understanding the EFT's radius of convergence in field space and temperature. This provides another strong motivation for treating thermal masses more carefully.

---

[1] The authors of [257] studied the agreement between a singlet extension of the SM and the corresponding EFT, but since TFD was used decoupling effects could not be correctly modeled.

5.2.6 Problems with the standard one-loop TFD calculation of the phase transition

There are a few ways in which the standard calculation with TFD thermal mass resummation, as outlined above, is incomplete and can be extended.

1. *Resumming Goldstones:* At zero temperature, SM Goldstone contributions must be resummed to eliminate the unphysical divergence in the derivatives of V_{CW} when their masses at tree-level are zero [258, 259]. The numerical effects of the Goldstone contributions, once resummed, are small, so we can deal with this by not including Goldstones in the loop calculations of certain couplings. In the $\overline{\text{MS}}$ scheme this is not a (numerical) problem as long as the tree-level Higgs VEV is somewhat shifted from the loop-level Higgs VEV.

2. *Gauge dependence:* Since the potential is derived from the gauge-dependent 1PI effective action, v_c is not a gauge-independent quantity. In the standard Landau-gauge-fixed calculation, we compute v_c/T_c as a proxy for the sphaleron energy in the broken phase (which is gauge independent), and the requirement that $v_c/T_c > 0.6$ is understood to be an approximate minimal necessary condition for EWBG to be plausible.

   A fully gauge-independent calculation of T_c and the sphaleron energy would make the calculation more reliable. This problem was considered by the authors of [225] in the high-temperature approximation. The gauge dependent potential without any thermal mass resummation is

$$V_{\text{eff}}^{T>0}(h,S,T;\xi) = V_0 + \sum_i \left[V_{\text{CW}}^i(m_i^2(h,S;\xi)) + V_{\text{th}}^i(m_i^2(h,S;\xi),T)\right] \ , \qquad (5.2.28)$$

   where ξ is the gauge parameter. Consider the gauge dependence of the third term V_{th}^i:

$$V_{\text{th}}^i = \frac{T^4}{2\pi^2}\Big[\sum_{\text{scalar},i} J_B\left(\frac{m_i^2(h,S;\xi)}{T^2}\right) + 3\sum_{\text{gauge},a} J_B\left(\frac{m_a^2(h)}{T^2}\right) - \sum_{\text{gauge},a} J_B\left(\frac{\xi m_a^2(h)}{T^2}\right)\Big] \ , \qquad (5.2.29)$$

   where $m_i^2(h;\xi) = m_i^2(h) + \xi m_a^2$, and we have dropped fermion contributions which do not contain any gauge dependence. In the high-temperature expansion and for small ξ, the

ξ-dependent contribution of DOF i charged under the gauge symmetry is

$$V^i_{\rm th}[\xi] = \frac{T}{2\pi^2}(m_i^3(h;\xi) - \xi m_a^3(h)) + \frac{m_i^4(h;\xi) - \xi m_a^4(h)}{64\pi^2}\log\frac{\mu_R^2}{T^2}\,. \tag{5.2.30}$$

Note that the $\mathcal{O}(T^2)$ term, and hence the dominant contribution to the thermal mass, is gauge-independent. This means that T_c only has a small gauge dependence, confirmed by [225] for small values of ξ. Furthermore, for singlet extensions the new contributions to the potential which drive the strong phase transition are by definition gauge-independent. Therefore we do not deal with the issue of gauge dependence here and proceed with the standard Landau gauge-fixed calculation. Certainly, further work is needed to construct a fully gauge-independent general calculation of the strength of the electroweak phase transition, and to understand how sensitive the results of a gauge-fixed calculation are to the choice of gauge parameter.

3. *RG-improvement:* the convergence of the one-loop effective potential can be improved by using running couplings with 2-loop RGEs. This is independent of other improvements to the calculation and is most important when the theory contains sizable mass hierarchies. We will not discuss it further here.

4. *Higher-loop corrections:* it is possible to evaluate higher-loop contributions to the zero- and finite-temperature effective potential, such as the 2-loop lollipop that is not included via thermal mass resummation. Alternatively, estimates of these contributions can be used to determine whether the one-loop expansion is reliable. In our BSM calculations we will carefully do the latter, using high-T approximations for the relevant diagrams.

5. *Consistent Thermal Mass Resummation:* In the standard Truncated Full Dressing calculation outlined above, the effective finite-temperature Higgs potential is computed by inserting the truncated thermal masses $\Pi_i \sim T^2$ into the one-loop potential as shown in Eq. (5.2.23). This is also called "resumming hard thermal loops", since it amounts to resumming only the contribution to the Matsubara zero mode propagator. This is indeed correct, if those contributions dominate the sum of diagrams, which is the case in the extreme limit of the high-temperature approximation.

> Early calculations that used this approximation [226, 227, 228, 260] were interested mainly in the restoration of electroweak symmetry at high temperature. Determining T_c with reasonable accuracy only requires considering the origin of the Higgs potential where the top and gauge boson masses are entirely dominated by thermal effects. In this case, the truncated high-T expansion for Π_i is justified, though there are significant deviations which arise from subleading terms in the high-temperature expansion even at the origin.
>
> However, when studying the strong first-order phase transition and computing v_c, we have to deal with finite excursions in field space which by definition are comparable to the temperature. For $h \sim T$, masses which depend on the Higgs VEV due to a Higgs coupling strong enough to influence the PT cease to be small at tree-level compared to thermal effects, and should start decoupling smoothly from the plasma. The resulting h-dependence of $\Pi_i(h, T)$ is therefore important. This is especially the case when the strong phase transition is driven by light bosons in the plasma, and therefore reliant on the partial cancellation between a zero-temperature mass and a thermal mass correction. Obtaining correct collider predictions of a strong EWPT requires going beyond the TFD scheme.
>
> As mentioned previously, the high-T thermal mass resummation is also incompatible with any EFT framework of computing the electroweak phase transition, since in this approximation the contribution of heavy degrees of freedom to thermal masses does not decouple. This confounds efforts to find a consistent EFT description of theories at finite temperature. Since EFTs are such a powerful tool for understanding generic new physics effects at zero temperature, rigorously generalizing their use to finite temperature is highly motivated.

We will concentrate on ameliorating the problems associated with TFD thermal mass resummation. Some of the necessary components exist in the literature. It is understood that a full finite-temperature determination of the thermal mass can give significantly different answers from the high-T expansion for the thermal mass [254]. This was partially explored, to subleading order in the high-T-expansion, for ϕ^4 theories [229, 230, 231, 233, 234, 232], but never in a full BSM calculation, without high-temperature approximations.

We will perform a consistent (to superdaisy order) finite-temperature thermal mass computation by numerically solving the associated gap equation and resumming its contributions in such a way as to avoid miscounting important higher-loop contributions. Since we are interested in the effect of adding new BSM scalars to the SM in order to generate a strong EWPT, we will be performing this procedure in the scalar sector only. We now explain this in the next section.

5.3 Formal aspects of finite-temperature mass resummation

As outlined above, in a large class of BSM models a strong EWPT is generated due to new weak-scale bosonic states with large couplings to the Higgs. A near-cancellation between the new boson's zero-temperature mass and thermal mass can generate a cubic term in the Higgs potential, which generates the required energy barrier between two degenerate minima $h = 0, v_c$ at $T = T_c$. To more accurately study the phase transition (and correlated experimental predictions) in this class of theories, we would like to be able to compute the thermal masses Π_i of scalars i beyond the hard thermal loop approximation used in TFD. In other words, rather than resumming only the lowest-order thermal mass in the high-temperature expansion, $\Pi_i \sim T^2$, we aim to compute and resum the full field- and temperature-dependent thermal mass $\delta m_i(h, T)$, with individual contributions to δm_i accurately vanishing as degrees of freedom decouple from the plasma. We also aim to formulate this computation in such a way that it can be easily adapted for other BSM calculations, and the study of Effective Field Theories at finite Temperature.

A straightforward generalization of the TFD calculation might be formulated as follows. The finite-temperature scalar thermal masses can be obtained by solving a one-loop gap equation of the form

$$\delta m_i^2 = \sum_j \partial_i^2 (V_{\text{CW}}^j + V_{\text{th}}^j) \, , \tag{5.3.31}$$

where ∂_i represents the derivative with respect to the scalar i. The hard thermal loop result $\delta m_i^2 \sim T^2$ is the solution at leading order in large T/m. To obtain the finite-temperature thermal mass, we can simply keep additional orders of the high-T expansion, or indeed use the full finite-temperature thermal potential of Eqns. (5.2.13, 5.2.14) in the above gap equation. In the latter case, the equation must be solved numerically. Once a solution for $\delta m_i^2(h,T)$ is obtained, we can obtain the improved one-loop potential by substituting $m_i^2 \to m_i^2 + \delta m_i^2$ in $V_{\text{CW}} + V_{\text{th}}$ as in Eq. (5.2.23).

Solving this gap equation, and substituting the resulting mass correction into the effective potential itself, is called *Full Dressing* [229, 230, 231]. This procedure is physically intuitive, but it is not consistent. Two-loop daisy diagrams, which can be important at $T = T_c$, are miscounted [233, 234].

An alternative construction involves substituting $m_i^2 \to m_i^2 + \delta m_i^2$ in the first derivative of the effective potential. This tadpole resummation, called *Partial Dressing*, was outlined for ϕ^4 theories in [232]. The authors claim that PD correctly counts daisy and superdaisy diagrams to higher order than FD.

There appears to be some confusion in the literature as to whether FD or PD is correct [229, 230, 231, 232, 233, 234], but we have repeated the calculations of [232], and confirm their conclusions. Partial Dressing (a) consistently resums the most dominant contributions in the high-temperature limit, where resummation is important for the convergence of the perturbative finite-temperature potential, (b) works to higher order in the high-temperature expansion, including the important log term, to correctly model decoupling of modes from the plasma, and (c) is easily adaptable to general BSM calculations. We review the important features of PD below and then outline how to generalize this procedure to numerically solve for the thermal mass at finite temperature.

5.3.1 Tadpole resummation in ϕ^4 theories

To explore the correct resummation procedure we first study a ϕ^4 theory with N real scalars obeying an $O(N)$ symmetry. This can then be generalized to the BSM theories of interest for EWBG. The tree-level potential is

$$V_0 = -\frac{1}{2}\mu^2 \phi_i \phi_i + \frac{1}{4}\lambda(\phi_i\phi_i)^2 \, . \tag{5.3.32}$$

Without loss of generality, assume that all excursions in field space are along the ϕ_0 direction.

Resummation of the thermal mass is required when high-temperature effects cause the fixed-order perturbation expansion to break down. We are therefore justified in using the high-T expan-

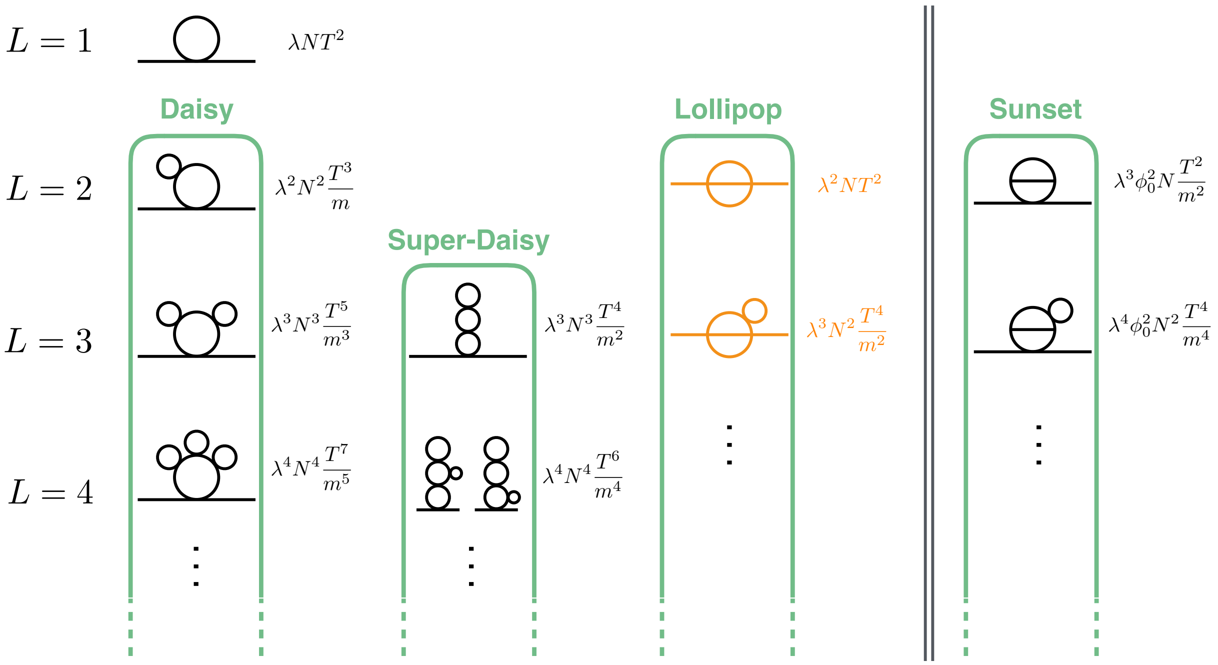

Figure 5.2: Complete set of 1- and 2- loop contributions to the scalar mass, as well as the most important higher loop contributions, in ϕ^4 theory. The scaling of each diagram in the high-temperature approximation is indicated, omitting symmetry- and loop-factors. Diagrams to the right of the vertical double-lines only contribute away from the origin when $\langle \phi \rangle = \phi_0 > 0$. We do not show contributions which trivially descend from e.g. loop-corrected quartic couplings. Lollipop diagrams (in orange) are not automatically included in the resummed one-loop potential.

sion to study the details of the thermal mass resummation procedure and ensure diagrams are not miscounted. Conversely, when $T \sim m$, there is no mismatch of scales to produce large ratios that have to be resummed. In this limit, the thermal mass will be less important, but should decouple accurately, and the resummed calculation should approach the fixed-order calculation. We now review how the PD procedure outlined in [232] achieves both of these objectives.

Partial Dressing Results for $N = 1$

We start by summarizing the main result of [232], which studied the $N = 1$ ϕ^4 theory in the high-temperature expansion. The first derivative of the one-loop effective potential $V_1 = V_{\text{CW}} +$

$V_{\rm th}$, see Eqns (5.2.8), (5.2.13) and (5.2.15), without any thermal mass resummation, is

$$\frac{\partial V_1}{\partial \phi} \;=\; V_1' \;=\; (6\lambda\phi)\left[\frac{T^2}{24} - \frac{Tm}{8\pi} - \frac{m^2 L}{32\pi^2}\right] \tag{5.3.33}$$

where $L = \ln\frac{\mu_R^2}{T^2} - 3.9076$ and the log-term arises from a cancellation between the zero- and finite-temperature potential. The tree-level scalar mass is $m^2 = -\mu^2 + \frac{\lambda}{2}\phi^2$. Differentiating this once again will yield the one-loop thermal mass shown in Fig. 5.2, as well as an electron-self-energy-type diagram for $\phi \neq 0$ that descends from loop corrections to the quartic coupling. During the phase transition, $\alpha \equiv N\lambda T^2/m^2 \approx 1$, requiring daisies to be resummed. This is evident in Fig. 5.2 from the fact that subsequent terms in each family of diagrams (Daisy, Super-Daisy, Lollipop and Sunset) is related to the previous one by a factor of α.

The second derivative of the one-loop potential defines a *gap equation*, which symbolically can be represented as

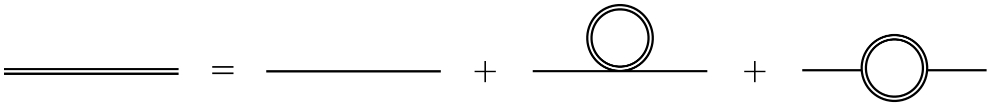

where double-lines represent improved propagators with the resummed mass M, while single-lines are un-improved propagators with the tree-level mass m. Algebraically, this gap equation is obtained by substituting M^2 into the second derivative of the one-loop effective potential:

$$\begin{aligned} M^2 &= m^2 + V_1''|_{m^2\to M^2} \\ \Rightarrow \quad M^2 &= m^2 + \frac{\lambda T^2}{4} - \frac{3\lambda T M}{4\pi} - \frac{3\lambda M^2 L}{16\pi^2} - \zeta\left[\frac{9\lambda^2\phi^2 T}{4\pi M} + \frac{9\lambda^2\phi^2}{8\pi^2}\right] \end{aligned} \tag{5.3.34}$$

where we have inserted a factor $\zeta = 1$ for reasons which will be made clear below. The PD procedure involves resumming these mass corrections by substituting $m^2 \to M^2$ in the first derivative of the potential Eq. (5.3.33) rather than the potential itself. The potential is then obtained by integrating with respect to ϕ:

$$V_1^{pd} \equiv \int d\phi\; V_1'|_{m^2\to M^2(\zeta=1)}\,. \tag{5.3.35}$$

By expanding the above in large T, one can show that V_1^{pd} correctly includes all daisy and superdaisy contributions shown (in the form of mass contributions) in Fig. 5.2, to both leading, subleading and log-order in temperature.

This partial dressing procedure does make one counting mistake, which is that all the sunset diagrams in Fig. 5.2, starting at 2-loop order and nonzero for $\phi \neq 0$, are included with an overall multiplicative pre-factor of $3/2$. This can be fixed by changing ζ in the gap equation (5.3.34) from 1 to $2/3$, resulting in the one-loop effective potential

$$V_1^{pd_{2/3}} \equiv \int d\phi \; V_1'|_{m^2 \to M^2(\zeta=2/3)} \tag{5.3.36}$$

Finally, non-daisy type diagrams, most importantly the two-loop lollipop in Fig. 5.2 and its daisy-dressed descendants, are by definition not included in this one-loop resummed potential. However, in the high-temperature limit they can be easily included by adding the explicit expression for the lollipoop loop tadpole (one external ϕ line, hence the name),

$$V_2' \supset V_\ell' \; = \; (6\lambda\phi)\frac{\lambda T^2}{32\pi^2}\left[\log\frac{m^2}{T\mu_R} + 1.65\right] \tag{5.3.37}$$

with the same $m^2 \to M^2(\zeta = 2/3)$ substitution:

$$V_1^{pd_{2/3}+\ell} \equiv \int d\phi \, [V_1' + V_\ell']_{m^2 \to M^2(\zeta=2/3)} \tag{5.3.38}$$

($\zeta = 1$ can also be used, in which case 2-loop sunsets are not corrected.) This effective potential includes all daisy, superdaisy, sunset and lollipop contributions correctly, and is therefore correct to three-loop superdaisy order.

Comparing resummation schemes

We have verified that the above results generalize to $O(N)$ ϕ^4 theories, with $N > 1$. As mentioned above, at temperatures near the phase transition the parameter $\alpha \equiv N\lambda T^2/m^2$ is ≈ 1, necessitating resummation. To compare different resummation approaches, let us first define which parameters are required to be small for the improved perturbative expansion to converge. Zero-temperature perturbation theory requires

$$N\lambda \; \ll \; 1 \tag{5.3.39}$$

(where the above equation, and other inequalities of its type, typically contain loop- and symmetry-factors which we usually suppress). Satisfying Eq. (5.3.39) means that during the phase transition, in regions of field space where $\alpha \approx 1$, the high-temperature expansion (whether in T/m or T/M) is usually valid. In order for the series of high-temperature contributions to converge, the parameter β must also be small:

$$\beta \equiv N\lambda \frac{T}{m} = \alpha\sqrt{N\lambda} \ll 1 \tag{5.3.40}$$

An easy way to see this is to examine Fig. 5.2. Let us call the mass contribution of the one-loop $\sim T^2$ diagram δm_1, and the total contributions of the daisy, super-daisy, lollipop and suset family of diagrams $\delta m_D^2, \delta m_{SD}^2, \delta m_{LL}^2, \delta m_{SS}^2$ respectively. After resummation in α, we obtain[2]

$$\delta m_1^2 \sim \lambda N T^2 \qquad \delta m_D^2 \sim \lambda^2 N^2 \tfrac{T^3}{m} \qquad \delta m_{SD}^2 \sim \lambda^3 N^3 \tfrac{T^4}{m^2}$$

$$\delta m_{LL}^2 \sim \lambda^2 T^2 N \qquad \delta m_{SS}^2 \sim \lambda^3 \phi_0^2 N \tfrac{T^2}{m^2}$$

Making use of $\alpha \approx 1$, these contributions arrange themselves in order of size:

$$\frac{\delta m_D^2}{\delta m_1^2} \sim \frac{\delta m_{SD}^2}{\delta m_D^2} \sim \alpha \frac{m}{T} = \beta \tag{5.3.41}$$

$$\frac{\delta m_{LL}^2}{\delta m_D^2} \sim \frac{1}{N}\frac{m}{T} = \frac{1}{\alpha}\frac{1}{N}\beta \tag{5.3.42}$$

$$\frac{\delta m_{SS}^2}{m_D^2} \sim \frac{\alpha}{N^2}\frac{\phi_0^2}{T^2}\frac{m}{T} = \frac{\phi_0^2}{T^2}\frac{1}{N^2}\beta \tag{5.3.43}$$

Clearly β is the relevant expansion parameter which has to be small for the series to converge. Furthermore, in terms of β, both the lollipop and sunset diagrams are of the same order as the superdaisy family, but with additional suppression factors of $1/N$.[3] (In our regime of interest, ϕ_0 is usually not much larger than T, so the sunsets are subdominant or at most comparable to the lollipop and superdaisy.)

We can now carefully compare different resummation approaches. The partial dressing procedure, with the lollipop correction and the additional sunset contribution, is accurate to $\mathcal{O}(\beta^2)$.

---

[2] Note that in the individual diagrams of Fig. 5.2, the un-improved tree-level mass m is used in the propagator. The entire e.g. lollipop series can be obtained by evaluating the leading diagram with the daisy-improved mass M.

[3] Due to the different symmetry factors of the lowest-order superdaisy and lollipop diagrams, the corresponding N-suppression is not numerically significant for $N \lesssim 10$.

Since tree- and loop-contributions are of similar size near the phase transition we compare all subleading contributions to the unimproved one-loop thermal mass δm_1^2. Relative to δm_1^2, the size of neglected zero-temperature contributions and non-daisy contributions at three-loop order are

$$(N\lambda)^2 \text{ and } \beta^3 \sim (N\lambda)^{3/2} , \tag{5.3.44}$$

respectively.

The alternative *Full Dressing* procedure [229, 230, 231] involves solving the same gap equation as for partial dressing, but substituting $m^2 \to M^2$ in the potential V_1 instead of its first derivative. This essentially dresses up both the propagator and the cubic coupling in the potential.[4]

The authors of [232] demonstrate that FD miscounts daisies and super-daisies (starting at the 2-loop level), does not include sunset contributions, and includes lollipop contributions but with a wrong prefactor and without the log-dependence of Eq. (5.3.37), which arises from neglecting internal loop momenta (as expected in a resummation procedure which does not explicitly calculate multi-loop diagrams). We have confirmed their results. Therefore, ignoring the incorrect accounting of the lollipop which vanishes at the origin, the error terms of a PD calculation are

$$(N\lambda)^2 \text{ and } \beta \sim (N\lambda)^{1/2} , \tag{5.3.45}$$

The standard BSM calculation is even worse, since TFD only uses the leading-order thermal mass, leading to possible error terms

$$(N\lambda)^2 \;\; , \;\; \beta \sim (N\lambda)^{1/2} \text{ and } \frac{m}{T} . \tag{5.3.46}$$

The advantages of partial dressing, compared to the truncated (or un-truncated) full dressing procedure, are clear, especially for phase transitions driven by BSM thermal effects, where the m/T error in Eq. (5.3.46) can be significant.

---

[4] This inspires the name we use for the standard thermal mass resummation as reviewed in Section 5.2.4. Since it involves computing the mass correction to leading order in high temperature $\Pi \sim T^2$ and substituting $m^2 + \Pi$ into the effective potential, we call it *Truncated Full Dressing*, even though at $\mathcal{O}(T^2)$ there is no actual difference between FD and PD.

5.3.2 A general resummation procedure for BSM theories

We now discuss how to adapt partial dressing for efficient calculation of the phase transition in general BSM theories. We will limit ourselves to phase transitions along the Higgs direction, briefly discussing other cases in the next subsection.

Since partial dressing avoids miscounting of the most important thermal contributions at all orders in the high-T expansion, including the log-term, it can be explicitly applied to the finite-temperature regime. In regions where $\alpha \approx 1$, the high-temperature expansion is valid, and resummation will be properly implemented. This smoothly interpolates to the regime where masses are comparable to temperature, eliminating the separation of scales and making the fixed-order calculation reliable again, with finite-temperature effects decoupling correctly as the mass is increased. Therefore, for a given set of mass corrections δm_i^2 for gauge bosons and scalars i, we define our effective potential along the h-direction by substituting the mass corrections into the first derivative of the loop potential:

$$V_{\text{eff}}^{\text{pd}}(h,T) = V_0 + \sum_i \int dh \left[\frac{\partial V_{\text{CW}}^i}{\partial h}\Big(m_i^2(h) + \delta m_i^2(h,T)\Big) + \frac{\partial V_{\text{th}}^i}{\partial h}\Big(m_i^2(h) + \delta m_i^2(h,T), T\Big)\right] , \tag{5.3.47}$$

Note that V_{th} is not (necessarily) expanded in high- or low-temperature.

Next, how do we obtain the mass corrections δm_i^2? We will concentrate on cases, like our $SM + N_S \times S$ benchmark model, in which the dominant effect of new physics on the phase transition comes from an expanded scalar sector. Therefore, we will retain use of the $\mathcal{O}(T^2)$ gauge boson thermal masses of Eq. (5.2.24), and set

$$\delta m_{GB}^2(h) = \Pi_{GB}(0) \tag{5.3.48}$$

For the scalar mass corrections we numerically solve a set of coupled gap equations at each different value of h and T:

$$\delta m_{\phi_j}^2(h,T) = \sum_i \left[\frac{\partial^2 V_{\text{CW}}^i}{\partial \phi_j^2}\Big(m_i^2(h) + \delta m_i^2(h,T)\Big) + \frac{\partial^2 V_{\text{th}}^i}{\partial \phi_j^2}\Big(m_i^2(h) + \delta m_i^2(h,T), T\Big)\right] \tag{5.3.49}$$

where $\phi_j = h, G_0, S_0$. Since we only consider excursions along the h direction, there are no mixed mass terms, and mass corrections for all singlets and Goldstones respectively are equal.[5]

---

[5] We can also evaluate the potential along the S_0 axis, in which case the mass corrections for S_0 and S_k with $k \geq 1$

Note that while we only numerically solve for the mass corrections of the scalars, these mass corrections will include contributions due to gauge bosons and fermions, which decouple correctly away from the high-temperature limit. We will address some subtleties related to finding consistent numerical solutions to these gap equations, and the effect of derivatives of $\delta m^2_{\phi_j}$, in the next section.

In defining the effective potential Eq. (5.3.47), we are essentially using only the one-loop potential as in Eq. (5.3.35). This represents a great simplification, since calculation of the two-loop lollipop in full generality and at finite temperature [227] may be very onerous in a general BSM theory. Furthermore, implementing the factor-of-$2/3$ "fix" to correctly count sunset contributions may be nontrivial at finite-temperature. Fortunately, we can show that omitting both of these contributions is justified for our cases of interest.

First, the lollipop is suppressed relative to the dominant one-loop resummed potential by factors of N (where N is related to N_S but also the number of Goldstones in the SM) and $\beta < 1$. Even so, it represents our dominant neglected contribution. To explicitly check that it is small, it is sufficient to evaluate the dominant lollipop contributions to the h and S_0 thermal masses in the high-temperature limit. Adapting the loop integral in the high-T limit from [228], this gives

$$\begin{aligned}
\delta m^2_{h,LL}(T) &= \frac{T^2}{16\pi^2}\left[6\lambda^2\left(\log\frac{m_h^2}{T\mu_R}+1.65\right)+N_S\lambda_{HS}^2\left(\log\frac{(m_h+2m_S)^2}{9T\mu_R}+1.65\right)\right] \\
\delta m^2_{S,LL}(T) &= \frac{T^2}{16\pi^2}\left[(N_S+2)\lambda_S^2\left(\log\frac{m_S^2}{T\mu_R}+1.65\right)+4\lambda_{HS}^2\left(\log\frac{(m_S+2m_h)^2}{9T\mu_R}+1.65\right)\right]
\end{aligned} \tag{5.3.50}$$

These diagrams are evaluated with improved propagators. In order for the calculation to be reliable, the ratios of lollipop to resummed one-loop mass corrections must satisfy

$$r^k_{LL} \equiv \frac{1}{\delta m_k^2(h=0,T_c)}\ \delta m^2_{k,LL}(T_c)\big|_{m_h\to\sqrt{m_h^2+\delta m_h^2},m_S\to\sqrt{m_S^2+\delta m_S^2}} \lesssim 0.1\,, \tag{5.3.51}$$

for $k = h, S$ when the high-T approximation is valid at the origin. (As explained in Section 5.2.3, in all operations involving the effective potential or its derivatives, we always only use the real part.)

---

have to be treated separately. Note that Eq. (5.3.49) is also a function of the gauge boson masses and thermal masses, which are set by Eq. (5.3.48), as well as the fermion masses.

Second, the sunset contribution is suppressed relative to the dominant one-loop-resummed potential by factors of h/T, N^2 and $\beta < 1$. More importantly, we expect the most important improvement of our partial dressing computation, compared to the standard truncated full dressing computation, to be the correct inclusion of finite-temperature effects, and the associated decoupling of heavy modes from the plasma away from the origin in field space. This decoupling will dominantly be due to the increased mass of the singlets as h evolves away from the origin, rather than from the two-loop sunset contributions. Since the former is correctly captured by using finite-temperature gap equations and effective potential, the effect of sunsets should be small compared to the lollipop.

Third, we should also ensure that the equivalent of β^3 in our theory is sufficiently small at $T = T_c$. This is very straightforward using Eq. (5.3.41), where δm_1 is the unimproved Higgs or Singlet one-loop thermal mass (using m^2 in propagators), and δm_D^2 is well approximated by the difference between the improved (using M^2) and un-improved thermal mass. Explicitly, we define two parameters:

$$\beta_k \equiv \frac{|\delta m_k^2(0, T_c) - \delta m_k^2(0, T_c)|_{\delta m_i^2 \to 0}\,|}{\delta m_k^2(0, T_c)|_{\delta m_i^2 \to 0}} \tag{5.3.52}$$

for $k = h, S$. β_h^3 and β_S^3 then give the size of the error terms from the most important neglected three-loop diagrams and should be less than ~ 0.1.

Finally, two-loop zero-temperature corrections are small if $N\lambda \ll 4\pi$, which simply restricts the weakly coupled parameter space we can explore. Our PD computation of the phase transition strength v_c/T_c is then robust when all $r_{LL}^{h,S}$ and $\beta_{h,S}^3$ are small.

5.3.3 Future Directions

There are several conceptually straightforward ways to extend the procedure outlined in Section 5.3.2:

1. Even though it cannot be done by simple construction and manipulation of the one-loop effective potential, it would be straightforward to construct the gap equations for the gauge bosons [230] and solve them together with the gap equations for the scalars.

2. With a general finite-temperature expression for the 2-loop lollipop shown in Fig. 5.2, we could evaluate its derivative, substitute $m^2 \to m^2 + \delta m^2$ and by adding it to Eq. (5.3.47) (but not Eq. (5.3.49)) correctly include all lollipop contributions, as in Eq. (5.3.38)

3. In regimes where the gap equation Eq. (5.3.49) can be approximated by a high-temperature expansion, one could implement the $2/3$ factor fix of Eq. (5.3.34) to correctly count sunset graphs at 2- and higher loop order. It is unclear how to implement this fix in the full finite-temperature gap equation, but as we discuss when we introduce *Optimized Partial Dressing* (OPD) in Section 5.4.2, the high-temperature expansion of the gap equation (but not the potential) is sufficient in most BSM calculations.

4. We have applied partial dressing without explicitly checking that fermion and gauge boson effects are correctly accounted for at 2- and higher-loop order. We leave this investigation to future work, but since the dominant BSM effects on the Higgs potential in our models of interest come from the scalar sector, we expect our procedure to be valid.

Note that we explicitly check in our calculation whether the above-mentioned extensions (2) and (3) are numerically significant.

There is also a more involved question, which is how to extend partial dressing for field excursions along several field directions at once, when those field directions cannot be related by a symmetry. The partial dressing procedure unambiguously defines the potential along any one field direction, as long as all other fields are at the origin. In an example with two fields, let us denote as $V_{\text{eff}}^{\text{pd}_\text{i}}(\phi_1, \phi_2)$ the effective resummed one-loop potential obtained by integrating $\partial V_{\text{eff}}/\partial \phi_i$. It is straightforward to show that $V_{\text{eff}}^{\text{pd}_1}(\phi_1, \phi_2) \neq V_{\text{eff}}^{\text{pd}_2}(\phi_1, \phi_2)$, with the difference being of super-daisy order $\mathcal{O}(\beta^2)$. This may not be numerically significant in a given case, but it would be of interest to extend the partial dressing procedure to consistently define

$$V_{\text{eff}}^{\text{pd}}(\phi_1, \phi_2) \, . \tag{5.3.53}$$

Since the above can be evaluated unambigiously diagrammatically, and since the partial dressing procedure was validated in [232] by comparing this to the substitution of M^2 into the first derivative of the potential, there presumably exists a way of generalizing this substitution procedure to obtain a general potential as a function of multiple fields. This is of particular relevance to BSM models where the Higgs mixes with BSM scalars [169, 182, 179], which constitute an important class of models that can give a strong electroweak phase transition.

5.4 Computing the the Strength of the Phase Transition

We now apply the procedure outlined in Section 5.3.2 the the SM + $N_S \times S$ BSM benchmark model with unbroken $O(N_S)$ symmetry in the $T = 0$ ground state.

5.4.1 Zero-Temperature Calculation

The tree-level scalar potential is given by Eqns. (5.2.4) and (5.2.5). All field excursions in the region of parameter space we study (no Higgs-Singlet mixing in the ground state) can be considered without loss of generality to be in either the h or S_0 direction.

For each choice of N_S, there are three Lagrangian BSM parameters, μ_S, λ_{HS} and λ_S. We match these to three physical input parameters which are computed at one-loop level in the $\overline{\text{MS}}$ scheme (in addition to matching the SM Higgs potential parameters λ, μ to m_h and v):

(a) The mass of the singlet in our vacuum

$$m_S^2 = m_S^2(v) = \left.\frac{\partial^2 V_{\text{eff}}^{T=0}}{\partial S_0^2}\right|_{h=v} = \mu_S^2 + \lambda_{HS} v^2 + \ldots \tag{5.4.54}$$

(b) The singlet-Higgs cubic coupling

$$\lambda_{hSS}^{\text{loop}} = \lambda_{hSS}^{\text{loop}}(v) = \frac{1}{2} \left.\frac{\partial^3 V_{\text{eff}}^{T=0}}{\partial S_0^2 \partial h}\right|_{h=v} = \lambda_{HS} v + \ldots \tag{5.4.55}$$

(c) The singlet quartic coupling

$$\lambda_S^{\text{loop}} = \lambda_S^{\text{loop}}(v) = \frac{1}{6} \left.\frac{\partial^4 V_{\text{eff}}^{T=0}}{\partial S_0^4}\right|_{h=v} = \lambda_S + \ldots \tag{5.4.56}$$

The renormalization scale μ_R is set to $m_S(v)$. In all calculations, we vary this scale choice up and down by a factor of 2 in order to estimate the uncertainty due to higher-order zero-temperature corrections. For a given set of input parameters, we compute whether the singlet is stable at the origin when $h = 0$, and if not, the location of the local minimum $(h, S_0) = (0, w)$. When the singlet is unstable at the origin, we impose the vacuum stability condition

$$V_{\text{eff}}^{T=0}(v, 0) < V_{\text{eff}}^{T=0}(0, w) \tag{5.4.57}$$

to ensure the EWSB vacuum is the preferred one for our universe.

The collider phenomenology of the $N_S = 1$ case, with TFD resummation and in the on-shell renormalization scheme, was studied previously in [2]. The following three collider observables are of interest to probe this scenario:[6]

- A measurement of the triple-Higgs coupling with 5% precision at 1σ, which is more pessimistic than recent estimates of the achievable precision [1].
- A search in the VBF jets + MET channel for direct singlet pair production via $h^* \to SS$.
- A measurement of the Zh production cross section deviation from the SM with a 1σ precision of 0.3$\%$ at a TLEP-like lepton collider.

Together, it was found that these measurements provide coverage of the entire parameter space where a strong phase transition is possible.

We analyze the same model as the authors of [2], generalized to $N_S \geq 1$, while comparing standard truncated full dressing to our new partial dressing procedure. We therefore compute the same observables:

(a) The Higgs cubic coupling

$$\lambda_{hhh}^{\text{loop}} = \lambda_{hhh}^{\text{loop}}(v) = \frac{1}{6} \left. \frac{\partial^3 V_{\text{eff}}^{T=0}}{\partial h^3} \right|_{h=v} = \frac{m_h^2}{2v} + \ldots \tag{5.4.58}$$

To obtain the fractional deviation, we compare this to the value of $\lambda_{hhh}^{\text{loop}}$ computed without the S contribution, rematched to the SM parameters with the same choice of renormalization scale as the calculation with the singlet.

---

[6] We assume 3 ab^{-1} of luminosity at 100 TeV throughout.

(b) Singlet pair production cross section at 100 TeV colliders: obtained in MadGraph 5 [85] by using $\lambda_{hSS}^{\text{loop}}$ as the singlet-Higgs tree-level coupling, scaled up by a factor of N_S.

(c) The fractional Zh cross section shift at lepton colliders can be computed using the results in [261, 262]:

$$\delta\sigma_{Zh} = \frac{N_S}{2}\frac{|\lambda_{HS}|^2 v^2}{4\pi^2 m_h^2}\left[1 + F(\tau_\phi)\right] \tag{5.4.59}$$

with the replacement $\lambda_{HS} v \to \lambda_{hSS}^{\text{loop}}$. The loop function $F(\tau)$, with $\tau_\phi = m_h^2/4m_S^2$, is given by

$$F(\tau) = \frac{1}{4\sqrt{\tau(\tau-1)}}\log\left(\frac{1-2\tau-2\sqrt{(\tau(\tau-1))}}{1-2\tau+2\sqrt{(\tau(\tau-1))}}\right). \tag{5.4.60}$$

Note that we estimate changes in cross-sections from the changes in potential couplings. This ignores finite-momentum contributions of new particles in loops to the cross section, but for $m_S \gtrsim m_h$, this is a good approximation.

Note that for these zero-temperature calculations, we do *not* resum mass corrections in the partial dressing scheme. The procedures of Section 5.3.2 can easily be applied to the zero-temperature potential as well, but we have extensively checked that they only have insignificant effects on the matched parameters and corresponding observables. This is expected, since mass resummation at finite temperature is required due to IR-divergent effects which are absent at zero temperature.[7]

5.4.2 Finite-Temperature Calculation

We are interested in finding regions of parameter space where the phase transition is strongly one-step ($v_c/T_c > 0.6$) or two-step.

For each set of input parameters we match the potential, compute zero-temperature observables, and then compute the finite-temperature potential at different temperatures until we find $T = T_c$ where the local minimum at the origin and a local minimum at $v = v_c$ are degenerate. The finite-temperature potential is given by Eq. (5.3.47), where the mass corrections (or thermal

---

[7] Note, however, that in the finite-temperature calculation, the zero-temperature potential gives important contributions beyond T^2 order.

masses) δm_i^2 are computed differently depending on the resummation scheme. If the singlet is unstable at the origin at $T = 0$, we also compute the minimum temperature T_S where thermal effects stabilize the singlet. If $T_S > T_c$, the transition is two-step and we do not analyze it further. In order for our calculation to be reliable, $r_{LL}^{h,S}$ and $\beta_{h,S}$ as defined in Eqns. (5.3.51) and (5.3.52), have to be small.

We compare the three different schemes: Truncated Full Dressing (TFD), Partial Dressing (PD) and Optimized Partial Dressing (OPD). Some of the numerical calculations are performed in Mathematica, and some in a custom-built `c++` framework. For numerical evaluation, `c++` is operation-by-operation $\sim 1000 \times$ faster than Mathematica, but the latter is much more versatile and often preferred for exploring different BSM scenarios. Whenever evaluating the full thermal potential V_{th} or its derivatives without approximations, we use pre-computed lookup tables.

The TFD calculation, which is the standard method for BSM calculations used in [2] and many other analyses, is simple enough that v_c/T_c can be found for a given parameter point using about $\sim \mathcal{O}(1\text{ minute})$ of CPU time in Mathematica. On the other hand, the complete implementation of PD is so numerically intensive that only the `c++` code can be realistically used, and evaluation times for a single parameter point range from 10 seconds to many minutes, indicating that PD is of order 10^4 times more numerically intensive than TFD. Fortunately, a series of carefully chosen approximations allows partial dressing to be implemented in Mathematica, with only $\mathcal{O}(10\%)$ higher CPU cost than TFD, but identical results as PD. This is the OPD scheme, and we hope its ease of implementation and evaluation will be useful for future BSM analyses. We now briefly summarize and contrast the salient features of each resummation implementation.

Truncated Full Dressing (TFD)

This is just the standard thermal mass resummation, using $\delta m_i^2 = \Pi_i \propto T^2$, see Eq. (5.2.24). This thermal mass is substituted into the first derivative of the potential, since there are no differences between full and partial dressing when substituting only the T^2 piece of the thermal mass. The thermal potential derivative V_{th}' is evaluated numerically without any approximations.

The dominant errors in the perturbative expansion arise from neglecting the two-loop lollipop, and miscounting the two-loop daisy. We define the corresponding error term

$$\Delta^{\mathrm{TFD}} \equiv \max(r^h_{LL}, r^S_{LL}, \beta_h, \beta_S) \tag{5.4.61}$$

to perform the perfunctory check that the calculation is reliable. However, is important to note that Δ^{TFD} will greatly underestimate the error of the TFD calculation, since it does not include the $\mathcal{O}(m/T)$ errors in the truncated thermal mass.[8] It is precisely this error that will be explored by comparing the TFD calculation to (O)PD calculation.

Partial Dressing (PD)

This implements the scheme outlined in Section 5.3.2 verbatim. For each temperature T of interest, the algebraic gap equation Eq. (5.3.49) is constructed by substituting $m_i^2 \to m_i^2 + \delta m_i^2$ into the second derivative of the full finite-temperature thermal potential V''_{th} and V''_{CW}. Solutions $\{\delta m_i^2(h)\}$ are obtained numerically for each value of h. The resulting solutions $\delta m_i^2(h, T)$ are substituted into the first derivative of the full effective potential Eq. (5.3.47), again without any approximations. The dominant errors arise from neglected lollipops and three-loop diagrams, and can be estimated with the error term

$$\Delta^{\mathrm{PD}} \equiv \max(r^h_{LL}, r^S_{LL}, \beta_h^3, \beta_S^3) \tag{5.4.62}$$

In practice, considerable complications arise when attempting to solve the gap equation Eq. (5.3.49). We find the best possible solution (whether an exact solution exists or not) by minimizing $|\mathrm{Re}(\mathrm{LHS}) - \mathrm{Re}(\mathrm{RHS})|$ with respect to different choices of $\{\delta m_i^2\}$. A unique solution to the gap equations can always be found at the origin of field space $(h, S) = (0, 0)$. However, sometimes no exact solution $\{\delta m_i^2\}$ can be found. This occurs for values of h where some scalars become tachyonic, which is for example the case across the energy barrier. In that case, we use the closest approximate solution, or discard the solution and interpolate across these pathological values of h. Both methods give very similar results, and in plots we use the former. The approximate solution usually still

---

[8] In particular, the m/T errors are expected to dominate the β-size errors, since the differences between full and partial dressing, which are order β, only show up at subleading order in T.

satisfies the gap equation at the ~ 1 - 10 $\%$ level, which on the face of it appears sufficient for a one-loop exact quantity.

Far more troubling is that for all other non-zero h-values, there exists not one but *many* numerical solutions to the algebraic gap equation. Apart from the computational intensity of PD, this is one of the confusing aspects which prompted us to develop OPD.[9] Physically, one would expect the solution of the gap equation to correspond to the limit of an iteration, whereby propagators in diagrams contributing to the effective potential are recursively dressed with additional one-loop bubbles until their second derivative with respect to the field is consistent with the mass used in the propagators. Therefore, one way we attempt to "find" our way towards the physically relevant gap equation solution is by iteration, where the $n+1$ step is given by

$$\delta m^2_{\phi_j}(h,T)_{n+1} = \sum_i \left[\frac{\partial^2 V^i_{\text{CW}}}{\partial \phi_j^2}\Big(m_i^2(h) + \delta m_i^2(h,T)_n \Big) + \frac{\partial^2 V^i_{\text{th}}}{\partial \phi_j^2}\Big(m_i^2(h) + \delta m_i^2(h,T)_n, T \Big) \right] \tag{5.4.63}$$

for fixed h, T. The iteration starts at $\delta m^2_{\phi_j} = 0$ and continues until the result converges. However, this series does not always converge, instead oscillating between two or more values. This is always the case when there is no exact solution to the gap equation, but can also occur when there are one or more solutions. We numerically circumvent this issue by requiring the solution $\delta m_i^2(h,T)$ to be a set of smooth functions. Therefore, once solutions $\delta m_i^2(h,T)$ are obtained for a grid of h-values and fixed T, we use smoothing to eliminate numerical artifacts (or the jumps due to imperfect or multiple solutions), and interpolate across regions without solutions to obtain a smooth set of functions describing the thermal masses.

Optimized Partial Dressing (OPD)

As we will discuss in Section 5.4.3, the results obtained via PD seem physically reasonable. However, it has two major disadvantages. First, its computational complexity and intensity would likely hamper adoption for other BSM calculations. Second, some of the numerical tricks used to obtain

---

[9] We have checked that our choice of solving a set of coupled gap equations for the scalar thermal masses, while using the analytical approximations for the gauge boson thermal masses Eq. (5.2.24), is not responsible for either the absence or abundance of gap equation solutions at different values of h.

reasonable solutions to the gap equation are slightly unsatisfying. We are therefore motivated to develop the more streamlined OPD resummation scheme that is numerically efficient and does not suffer from either the absence of gap equation solutions for some ranges of h values, nor the preponderance of solutions for all other nonzero h values. Encouragingly, the physical results of this OPD procedure are practically identical to PD.

The first important observation, which is very well-known, is that the high-temperature approximation for the thermal potential, Eq. (5.2.15), has the expected error terms of order $(m/T)^{n+1}$ if truncated at order $(m/T)^n$ (for $n \leq 2$), but is accurate for masses as large as $m \sim (1-3) \times T$ if the log terms are included. This applies both to V_{th} and its derivatives.

Given that the low-temperature approximation Eq. (5.2.16) can easily be expanded to high enough order to be accurate for $m \sim T$, this implies that a piece-wise approximation for the thermal functions $J_{B,F}$ can be used in Eq. (5.3.47) to evaluate the effective potential, as well as its derivatives:

$$\begin{aligned} J_B^{\text{piece}-\text{wise}}(y^2) &= \begin{cases} J_B^{\text{high}-T}(y^2) & \text{for } y^2 \leq 1.22 \\ \tilde{J}_B^{(3)}(y^2) & \text{for } y^2 > 1.22 \end{cases} \\ J_F^{\text{piece}-\text{wise}}(y^2) &= \begin{cases} J_F^{\text{high}-T}(y^2) & \text{for } y^2 \leq 1.29 \\ \tilde{J}_F^{(2)}(y^2) & \text{for } y^2 > 1.29 \end{cases} \end{aligned} \tag{5.4.64}$$

This gives percent-level or better accuracy for J_B and its first two derivatives and J_F and its first derivative, for all positive y^2. For negative y^2 (corresponding to tachyonic masses) the accuracy is $\sim 10\%$ for $m^2 = -10T^2$, but such negative m^2 are rarely encountered after thermal mass corrections are added. Evaluation of this piece-wise approximate form of $J_{B,F}$ is very fast in Mathematica.

This definition of the thermal effective potential V_{th} also allows the algebraic gap equation Eq. (5.3.49) to be defined entirely analytically (as opposed to numerically), even if the ultimate solutions have to be found numerically. This represents a huge simplification and allows Mathematica to find solutions much easier than for the full V_{th} defined via lookup-tables. In its full piece-wise defined form, the thermal functions of Eq. (5.4.64) still allow for the study of e.g. decoupling effects as particles become heavy, which will be important in the future study of EFTs at finite temperature.

However, for the study of strong phase transitions induced by BSM thermal effects, we can make another important simplification. Thermal mass resummation is only needed to obtain accurate results when $m \lesssim T$. Therefore, we are justified in constructing the gap equation Eq. (5.3.49) using *only the high-temperature approximation for the thermal potential* (and the usual V_{CW}). The resulting solutions for the mass corrections $\{\delta m_i^2(h,T)\}$ are practically identical to the solutions obtained with the full finite-temperature potential, except for some modest deviations in regions where $m \gtrsim T$. Even so, the resulting effective potential obtained by integrating Eq. (5.3.47) is practically identical in those regions as well, since thermal effects of the corresponding degrees of freedom are no longer important. Using only $J_{B,F}^{\mathrm{high}-T}$ in the gap equation makes finding solutions so fast that the associated computational cost becomes a subdominant part of the total CPU time required for finding v_c/T_c, making this OPD method only $\mathcal{O}(10\%)$ slower than the standard TFD method (even when the TFD method uses the same piece-wise defined thermal functions in the effective potential).

Alternative formulation of the gap equations

The absence of solutions to the *algebraic* gap equation Eq. (5.3.49) encountered in PD indicate an overconstrained system, meaning there might be missing variables we should also solve for. Furthermore, the numerical tricks utilized in the PD implementation to obtain $\delta m_i^2(h,T)$ solutions for a given T were justified by appealing to the required continuity of the solution (interpolation, smoothing) and the physical interpretation of the gap equation (selecting the correct solution by guiding the numerical root-finding procedure with iteration).

All of these considerations point towards a slightly modified form of the gap equation which appears more consistent with the partial dressing procedure. Recall that the gap equation for both the full and partial dressing procedures, Eq. (5.3.34), was originally defined by substituting $m^2 \to M^2$ in V'' of the ϕ^4 theory:

$$M^2 = m^2 + V_1''|_{m^2 \to M^2} \tag{5.4.65}$$

This yields the gap equation used in the PD procedure Eq. (5.3.49), which is an algebraic equation that is solved for $\{\delta m_i^2\}$, a priori separately for each (h,T). Alternatively, one could define the gap equation by taking the effective potential of partial dressing $V_1'^{pd} = V_1'|_{m^2 \to M^2}$ and differentiating it once more with respect to the field:

$$M^2 = m^2 + [V_1'|_{m^2 \to M^2}]' \tag{5.4.66}$$

In the context of our BSM benchmark model, the corresponding gap equations are

$$\delta m_{\phi_j}^2(h,T) = \sum_i \frac{\partial}{\partial \phi_j}\left[\frac{\partial V_{\rm CW}^i}{\partial \phi_j}\Big(m_i^2(h) + \delta m_i^2(h,T)\Big) + \frac{\partial V_{\rm th}^i}{\partial \phi_j}\Big(m_i^2(h) + \delta m_i^2(h,T), T\Big)\right] \tag{5.4.67}$$

At each point in (h,T) space, these gap equations are algebraic relations of $\{\delta m_i^2\}$ as well as the derivatives at that point $\{\frac{\partial \delta m_i^2}{\partial \phi_j}\}$. The gap equations are now *partial differential equations*: The additional variables (the derivatives of δm_i^2) guarantee that solutions exist at every point[10], while the continuity condition of the PDEs

$$\delta m_i^2(h + \Delta h, T) = \delta m_i^2(h,T) + \Delta h \frac{\delta m_i^2}{\partial h}(h,T) + \mathcal{O}(\Delta h^2) \tag{5.4.68}$$

restricts the number of numerical solutions, selecting the unique physical solution. This eliminates both numerical problems of the original PD procedure.

In practice, constructing Eq. (5.4.67) is very challenging in the full finite-temperature formulation of $V_{\rm th}$, since it involves second derivatives of the thermal functions which are very computationally costly to evaluate. However, in the high-temperature approximation[11] Eq. (5.4.67) becomes a very simple analytical set of equations that Mathematica can easily solve numerically for $\{\delta m_i^2\}$ after eliminating the derivatives $\{\frac{\partial \delta m_i^2}{\partial h}\}$ via the continuity condition Eq. (5.4.68), making the solution at $(h + \Delta h, T)$ dependent on the solution obtained at (h,T). The resulting (h,T)-dependent mass corrections $\delta m_i^2(h,T)$ are well-behaved, defined everywhere, and unique almost everywhere.[12]

---

[10] Symmetry under $\phi_i \to -\phi_i$ implies that $\frac{\partial \delta m_i^2}{\partial \phi_j} = 0$ when $\phi_j = 0$. Since we only consider excursions along the h-direction, only the derivatives with respect to h are ever nonzero. At the origin both kinds of gap equations are the same, but at that point the algebraic gap equation always has a unique solution anyway.

[11] One could also use the piece-wise definition of the thermal functions Eq. (5.4.64), but obtaining a solution takes $\mathcal{O}(10)$ times longer. This can still be useful for studying decoupling effects and matching to EFTs.

[12] In some regions there are multiple near-degenerate solutions, but the ambiguity is not physically significant.

In summary, the OPD method uses the piece-wise defined thermal functions Eq. (5.4.64) in the effective potential Eq. (5.3.47), and the high-temperature approximation in the gap equations Eq. (5.4.67). The gap equations are PDEs instead of simple algebraic relations, which leads to solutions for the mass corrections which are continuous and well-defined for all (h, T) in the regions of interest.

Using gap equation Eq. (5.4.66) instead of Eq. (5.4.65) amounts to treating resummation identically in the effective potential and the gap equation derived from that potential. While this seems reasonable, the important question is whether this particular *algebraic* procedure of constructing a gap equation by manipulating the one-loop potential expressions, and inserting the resulting mass solution back into the potential, is equivalent (up to some order) to the *diagrammatic* procedure of computing various higher-order contributions to the effective potential. As we reviewed in Section 5.3, the authors of [232] showed that using the original gap equation Eq. (5.4.65), this equivalence was accurate up to differences of $\mathcal{O}(\beta^3)$, the neglected two-loop lollipop, and the miscounted two-loop sunset, see Fig. 5.2. We have checked that using the new gap equation Eq. (5.4.66) is equivalent to the same order, the only difference being the precise nature of how the two-loop sunset is miscounted. This means that the $2/3$ correction factor in Eq. (5.3.38) is modified at subleading (i.e. 3-loop sunset) order.

In Section 5.3.2 we argued that the sunset error is subdominant to the $\mathcal{O}(\beta^3)$ and lollipop errors, which we check explicitly are small. We therefore expect the numerical difference between $\delta m_i^2(h, T)$ solutions obtained in the OPD and PD scheme to be even smaller, and as we show below, this is indeed the case. That being said, since the gap equation in the OPD scheme is explicitly written in the high-temperature approximation, inserting the $2/3$ correction factor would be very straightforward.

Finally, one might also worry that the piece-wise defined thermal potential, or the high-temperature approximate gap equation, would be of insufficient accuracy in regions where large cancellations are important, or where masses are very tachyonic and the piecewise approximation is not very accurate. However, thermal resummation prevents masses squared inserted in the thermal potential from being too negative, and in regions where the transition between the high- and low-temperature approximation occurs, the exact solution to the gap equation becomes less numerically relevant

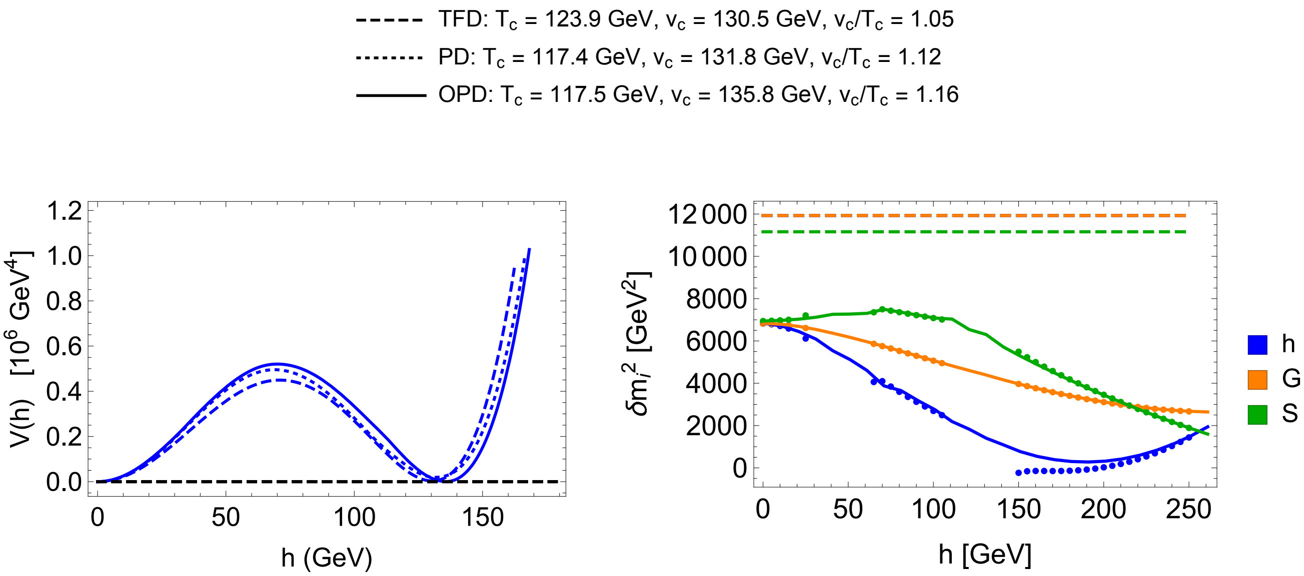

Figure 5.3: Effective Higgs Potential (left) and mass corrections δm_i^2 (right) for the physical Higgs (h), Goldstones (G), and singlets (S) at $T = T_c$ as a function of h. Evaluated in TFD, PD and OPD resummation schemes for $N_S = 3$ and $(m_S, \lambda_{hSS}^{\text{loop}}/v, \lambda_S^{\text{loop}}) = (300\text{GeV}, 1.52, 0.5)$. In the right plot, $\delta m_h^2 = \delta m_G^2$ in the TFD scheme. The dots correspond to δm_i^2 in the PD scheme, with gaps indicating regions of the h-axis where no exact solution to the gap equation can be found, and the $\delta m_i^2(h, T)$ functions used to evaluate the potential are obtained by linearly interpolating between the obtained δm_i^2 solutions as a function of h. This gives nearly the same $V(h, T_c)$ as OPD. Note that the approximate equality of the three (O)PD mass corrections at the origin is a numerical coincidence for this parameter point. Furthermore, the differences in v_c, T_c between TFD and (O)PD are modest here, but for other choices they can be much more pronounced. This is very important when $T_c \sim T_S$ and the predicted nature of the transition can change from one-step to two-step, as we discuss in Section 5.5.

since the calculation reduces to a fixed-order one.

5.4.3 Comparing Resummation Schemes

Here we illustrate the differences between the three resummation schemes for an example point in the parameter space of the SM + $N_S \times S$ model. The differences, in particular of the evaluated thermal mass corrections at $T = T_c$, will inform our discussion of the different physical predictions generated by the new (O)PD vs the standard TFD scheme in the next section. It will also demonstrate that PD and OPD are nearly equivalent.

We focus on regions of parameter space where both TFD and (O)PD produce a sizable first-order one-step phase transition. This allows us to show the resulting Higgs potentials at $T = T_c$ side-by-side, but by necessity restricts our attention to regions of parameter space where all calculation schemes give similar physical predictions. Even so, the differences are very clear in detail and allow us to understand the regions of parameter space where the physical differences are more significant.

Fig. 5.3 shows the effective Higgs potential and mass corrections for the parameter point $(N_S$, m_S, $\lambda_{hSS}^{\text{loop}}/v$, $\lambda_S^{\text{loop}}) = (3, 300\text{GeV}, 1.52, 0.5)$. Immediately we see that PD and OPD give nearly identical functional forms of the mass corrections $\delta m^2_{h,G,S}(h, T_c)$ once OPD solutions are interpolated. As a result, the effective potential and obtained values of v_c and T_c are also nearly identical. We have checked that this holds true across the parameter space. Therefore, the numerically extremely efficient OPD method can be used in place of the numerically costly PD calculation.[13]

The mass corrections obtained with (O)PD behave in a physically reasonable manner, being maximal near the origin and generally decreasing as h increases and the various degrees of freedom acquire more mass, reducing their participation in the thermal plasma. The physical Higgs and Goldstone mass corrections behave differently away from the origin. Compared to the constant TFD prediction, the (O)PD thermal masses are smaller by $\mathcal{O}(40\%)$ or more. This is typical across the whole parameter space, and explains the most important physical difference between the two schemes. The reduced thermal masses in TFD result in higher temperatures T_S where the singlet is stabilized at the origin (if it is unstable at zero temperature). As we show in Section 5.5, this

---

[13] For one-step transitions with very large couplings, where the zero-temperature singlet mass is small near the origin, but significantly larger than the Higgs mass at $h = v$, there are minor $\mathcal{O}(10\%)$ differences between OPD and PD due to the assumed high-T approximation in the gap equation. However, these differences do not significantly affect the physically important boundaries between different phases of the theory, where the PT is strongly first order, with one-step, or two-step transitions.

results in larger regions of parameter space where a two-step transition occurs.

5.5 Physical Consequences

From a formal point of view, development of the (O)PD thermal resummation scheme is most important in the careful study of thermal decoupling effects, especially when spectra change with field excursions. This is necessary for rigorously understanding Effective Field Theories at finite temperature. We are currently pursuing this line of investigation, and will present the results in a future publication. Additionally, compared to TFD calculations, the new (O)PD formalism makes quantitatively different predictions about the regions of parameter space where a one- or two-step phase transition of sufficient strength for EWBG can occur. This in turn affects the predictions of the EWPT (or other phase transitions in the early universe) for cosmological observations and collider experiments which need to be known reliably for planning such experiments. In more realistic extensions of the SM scalar sector, where the individual masses and couplings are not free parameters as in the SM + $N_S \times S$ benchmark model, this could also affect whether a strong phase transition is possible at all.

One way to understand the different predictions of the TFD and (O)PD is to take a slice of parameter space with constant physical singlet mass m_S and singlet quartic λ_S^{loop} in our EWSB vacuum. The strength of the phase transition, v_c/T_c, is shown along with several other important observables and parameters in Fig. 5.4 for $N_S = 6$ and $(m_S, \lambda_S^{\text{loop}}) = (150\text{GeV}, 1.0)$.

We first explain the qualitative features of Fig. 5.4 which are common to both calculations. For very small Higgs portal coupling $\lambda_{HS} \approx \lambda_{hSS}^{\text{loop}}/v$, the singlet sector has no effect on the EWPT, making it weakly first order or second order as in the SM. The singlet mass, which is $m_S^2 = \mu_S^2 + \lambda_{HS} v^2$ at tree-level, is given entirely by the parameter μ_S^2. As λ_{HS} is increased, μ_S^2 decreases and eventually becomes negative to keep m_S fixed. At some point this allows a partial cancellation between μ_S^2 and δm_S^2 along the lines of Eq. (5.2.27) to occur, resulting in a one-step first order phase transition starting around $\lambda_{hSS}^{\text{loop}}/v \approx 0.55$ in Fig. 5.4 (a). This cancellation is only partial, as shown by the plot of total finite-temperature singlet mass at the origin (i). Note from (c) and (d) that T_S, the minimum temperature at which thermal effects stabilize the singlet at the origin, is

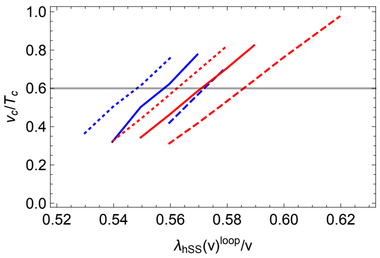

(a) v_c/T_c

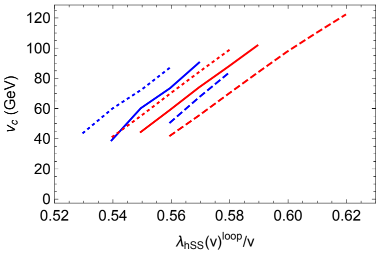

(b) v_c

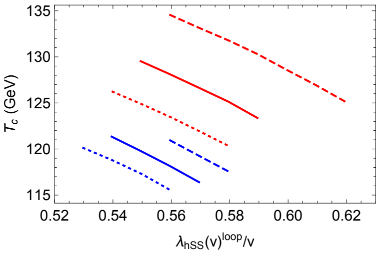

(c) T_c

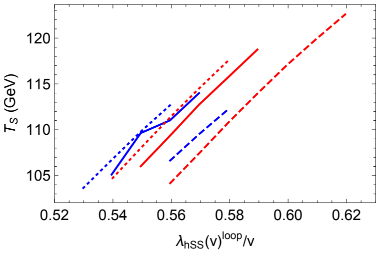

(d) T_S

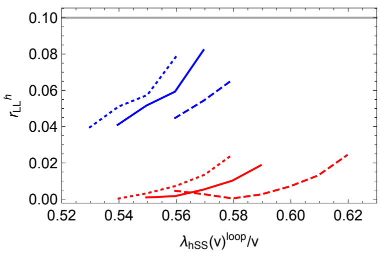

(e) r^h_{LL}

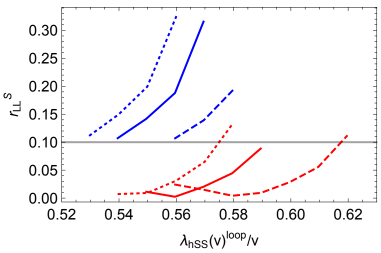

(f) r^S_{LL}

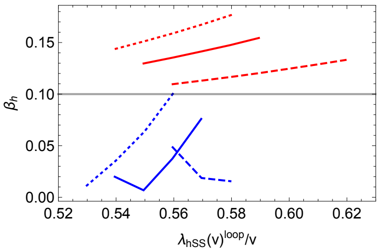

(g) β_h

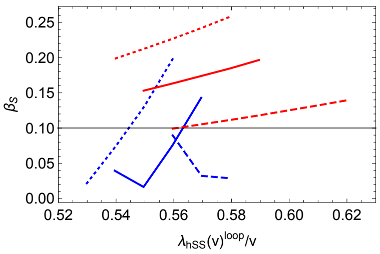

(h) β_S

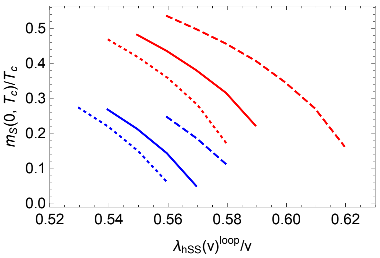

(i) m_S at origin

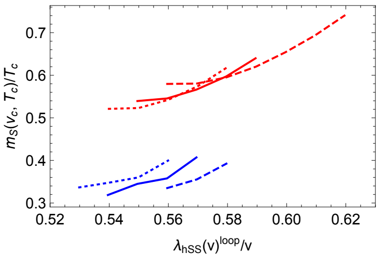

(j) m_S at v_c

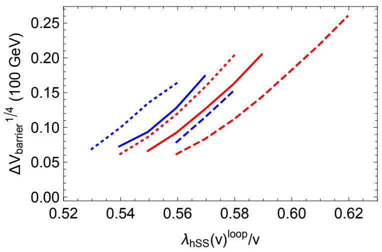

(k) potential barrier

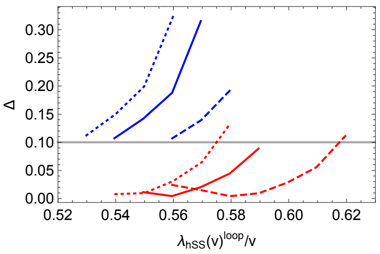

(l) Largest error term $\Delta^{\rm TFD,PD}$

Figure 5.4: Comparison of one-step phase transition in the new PD (blue) vs the standard TFD (red) calculation, for $N_S = 6$ and $(m_S, \lambda_S^{\rm loop}) = (150{\rm GeV}, 1.0)$. The renormalization scale is set to $\mu_R = m_S$ (solid lines). Dashed (dotted) lines correspond to $mu_R = 2m_S$ $(m_S/2)$ to demonstrate the effect of scale variation. To the left of the curves, the PT is one-step and weakly first order or second order. To the right of the curves, $T_S > T_c$ and the transition is two-step for $\lambda_{hSS}(v)^{\rm loop} < \lambda_{hSS}^{\rm max}$. This upper bound is is set by the condition that EWSB vacuum is preferred and depends on $N_S, m_S, \lambda_S^{\rm loop}, \mu_R$ but not the choice of thermal resummation scheme.

lower than T_c, as required for the singlet to be stable when the Higgs undergoes its one-step phase transition. Increasing the Higgs portal coupling drastically increases v_c and hence the strength of the phase transition, see (a) and (b), since it enhances the negative "cubic term" of Eq. (5.2.27) (from the tree-level Higgs dependence of the singlet mass) while also increasing the singlet thermal mass and therefore enhancing the cancellation of μ_S^2 and δm_S^2, see (i). For $\delta m_{h,S}^2 \sim \lambda_{HS} T^2$, both T_c and T_S can be schematically understood as the solution to the equations $\mu^2 = \lambda_{HS} T^2$ and $-\mu_S^2 = \lambda_{HS} T^2$ (neglecting numerical prefactors). This explains why T_c decreases with increasing Higgs portal coupling, but is insufficient to understand why T_S increases, since both μ_S^2 and δm_S^2 depend linearly on λ_{HS} at leading order in temperature for fixed physical singlet mass m_S. Solving for T_S with the full high-temperature expansion of the thermal potential reproduces the behavior shown in (d). As the Higgs portal coupling is further increased, T_S becomes larger than T_c, which occurs around $\lambda_{hSS}^{\text{loop}}/v \approx 0.6$ in Fig. 5.4. This means the phase transition is now two-step: as the universe cools it falls first into the $(h, S) = (0, w)$ vacuum before transitioning to the $(v, 0)$ vacuum. Increasing λ_{HS} decreases the potential difference $V_{\text{eff}}^{T=0}(v, 0) - V_{\text{eff}}^{T=0}(0, w)$, which delays the second transition, and by lowering T_c enhances v_c/T_c. Two-step phase transitions can therefore be very strong, since they can rely on supercooling the universe. Finally, as λ_{HS} is increased further still the $(h, S) = (0, w)$ vacuum becomes preferred to our vacuum at zero temperature, and the model is not compatible with our universe.

With this understanding, we can now interpret the differences between the standard TFD and the new (O)PD calculation in detail:

- (O)PD and TFD predict different parameter regions where the one-step phase transition is strongly first order. This arises due to three effects: in (O)PD, v_c is larger, T_c is smaller, and T_S is larger than in TFD. The first and second effect make the PT stronger at a given parameter point, but the second and third effect lead to a lower Higgs portal coupling at which the switch from one-step to two-step PT occurs.

  The third effect can be traced back to the smaller thermal mass corrections obtained in (O)PD, while the first two effects are also connected to the h-dependence of the mass correction (see Fig. 5.3).

As a result, the region of parameter space in which (O)PD predicts a strong first order one-step PT with $v_c/T_c > 0.6$ is much smaller than in TFD, and shifted to smaller Higgs portal couplings. By the same token, the region of parameter space where the PT is two-step (to the right of the curves in Fig. 5.4) is larger in (O)PD.

- The finite temperature singlet mass at the origin and at v_c, shown in Fig. 5.4 (i) and (j), shows that the high-temperature approximation is fairly reliable in its untruncated form (since $m/T \lesssim 1$), but the truncated high-T approximation assumed in the TFD thermal mass calculation makes errors of $m/T \sim$ 30 - 70$\%$ depending on h, which is consistent with Fig. 5.3 (right).
- The Higgs portal dependent curves of (b) v_c and (k) potential barrier height of the (O)PD calculation are very similar to TFD curves that are shifted to lower couplings. The same holds for v_c/T_c, which is controlled by the rapidly-varying v_c. Therefore, we expect the ratio T_n/T_c of the nucleation temperature, when the bubbles of true vacuum actually form, to the critical temperature to be similar in the two calculation.
- The absolute value of the critical temperature T_c for a given strength of phase transition v_c/T_c is $\sim 10\%$ lower than predicted by the TFD calculation. If a one-step transition could be strong enough to be detected by gravitational wave observations, this would effect the frequency spectrum of the stochastic gravitational wave signal.
- In the example of Fig. 5.4, the overall error term (l) $\Delta^{TFD,PD}$ is dominated by the singlet lollipop ratio (f) r^S_{LL}. The error term is much larger in the new (O)PD calculation than the standard TFD. Since the latter underestimates the error, we expect Δ^{PD} to give a much better representation of the calculation's reliability, which is breaking down near the switch from one-step to two-step phase transitions (larger $\lambda_{hSS}^{\text{loop}}/v$).

  For other slices of parameter space, the β-errors can dominate, in which case the (O)PD calculation can be much more reliable, since the first neglected contributions are $\mathcal{O}(\beta^3)$.

It is now straightforward to interpret Fig. 5.5, which shows the regions of the $\lambda_{hSS}^{\text{loop}} - \lambda_S^{\text{loop}}$ coupling plane that give a strong one- or two-step first order EWPT in the TFD and (O)PD calculations

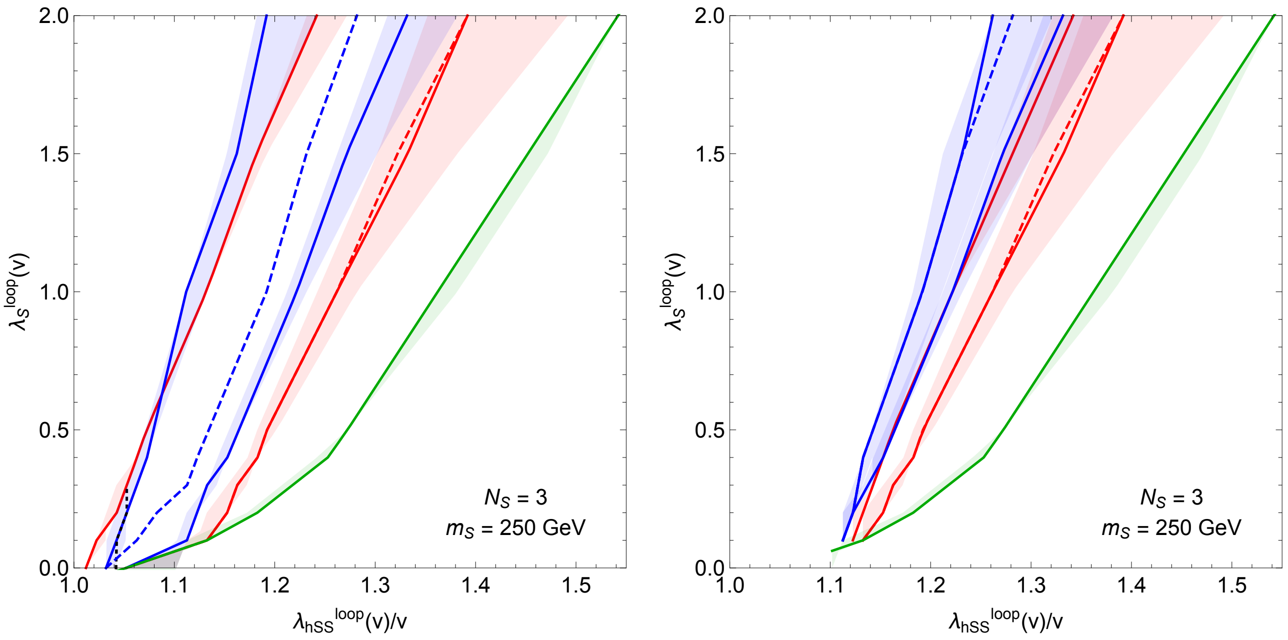

Figure 5.5: SM + $N_S \times S$ parameter space with a strong EWPT for $N_S = 3$ and $m_S = 250\text{GeV}$. Region between solid red (blue) lines: regions with strong one-step PT satisfying $v_c/T_c > 0.6$ for the standard TFD (new PD) calculation on the *left*, and $v_c/T_c > 1.0$ on the *right*. To the left of these lines, the PT is weakly first order or second order. Between the red (blue) lines and the green line, the PT is two-step in TFD (PD) calculation. To the right of the green line, the EWSB vacuum is not preferred at zero temperature (this does not depend on the thermal mass resummation scheme). Varying μ_R between 0.5 and 2 m_S gives the variation indicated by the red/blue/green shading. To the right of the red (blue) dashed lines, Δ^{TFD} (Δ^{PD}) > 0.1 for $\mu_R = m_S$. To the left of the black dotted line, the singlet is stable at the origin at zero temperature for $\mu_R = 1$.

for $N_S = 3$ and $m_S = 250\text{GeV}$. In the left plot, a strong one-step transition is defined with the maximally permissive criterion $v_c/T_c > 0.6$. In the right plot, the criterion is slightly tightened, to the usual $v_c/T_c > 1.0$. In the more correct (O)PD calculation, the region allowing for a strong one-step transition (between blue lines) is smaller than in TFD (red lines), while the region with a strong two-step transition (between the blue/red lines and the green line) is larger in (O)PD. This is especially pronounced when v_c/T_c is required to be larger than 1, in which case there is almost no overlap between the two region with a strong one-step phase transition.

For the specific SM + $N_S \times S$ benchmark model, the collider phenomenology depends almost exclusively on the Higgs portal coupling and the singlet mass. Fig. 5.6 shows the parameter regions where, for some choices of the Singlet quartic λ_S, the one- or two-step EWPT can be strong enough for EWBG. This generalizes the results of [2] to $N_S \geq 1$ and makes clear that future colliders will be able to probe the entire parameter space of this representative class of models for arbitrary number of singlets.

In this particular benchmark model, the singlet quartic and the Higgs portal coupling are free parameters, and the lack of mixing with the Higgs makes the physical effects of the singlet quartic very hard to observe at colliders. Therefore, the old TFD and more correct (O)PD calculations give very similar predictions for the collider phenomenology of EWBG. However, as discussed above, the situation would be very different in more complete theories, especially if a full calculation of the baryon asymmetry reveals that v_c/T_c has to be larger than 0.6. Furthermore, even in the SM + $N_S \times S$ benchmark model, there is an important difference: the minimum singlet mass required for a strong one-step PT is *higher* in (O)PD than in TFD. This means that for light singlet masses, the only possibility for EWBG is via a two-step transition. As discussed in [256], these transitions can form runaway bubbles of true vacuum, which do not permit successful baryon number generation, and further study could reveal very strong additional constraints on the parameter space actually compatible with complete EWBG. Furthermore, the stochastic gravitational wave background generated by a strong two-step transition, but *not* a moderately strong one-step transition, could be detected by gravitational wave observatories [251]. The (O)PD calculation reveals this exciting possibility to be more likely for light singlet masses than previously assumed.

5.6 Conclusions

In this paper we developed the *Partial Dressing* and *Optimized Partial Dressing* schemes for computation and resummation of thermal masses beyond the high-temperature approximation in general BSM scenarios. This allows for the strength of Phase Transitions to be determined to much greater accuracy than the standard Truncated Full Dressing scheme, which only resums hard ther-

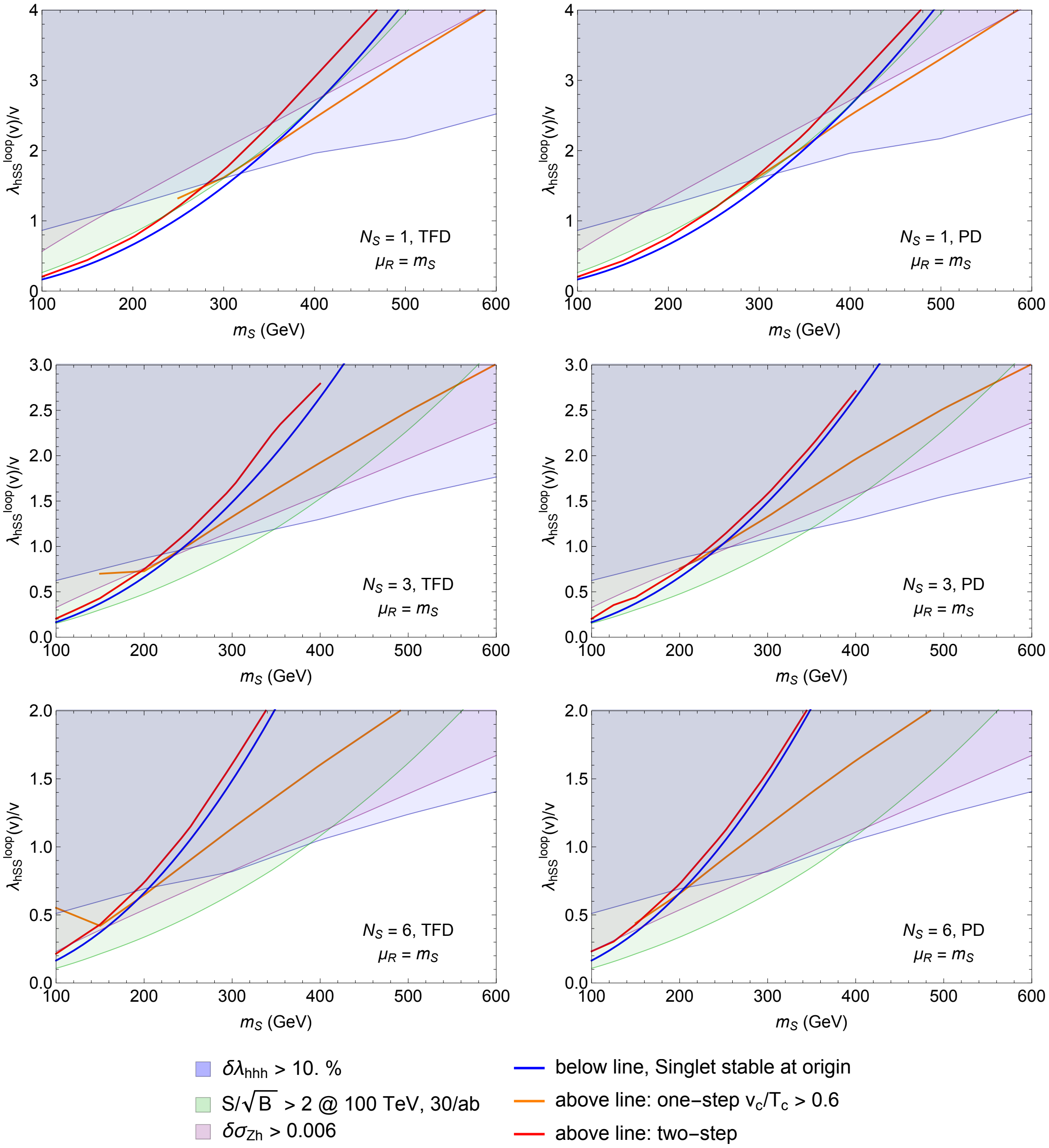

Figure 5.6: Phenomenological parameter space of the SM + $N_S \times S$ benchmark model of EWBG, for $N_S = 1, 3, 6$, computed in the TFD or PD thermal resummation scheme. The physical singlet mass in our EWSB vacuum is on the horizontal axis, the higgs-singlet cubic coupling is on the vertical axis. This determines most collider observables. The Higgs cubic coupling deviation Eq. (5.4.58) is bigger than 10% in the *blue shaded region*, to which a 100 TeV collider with 30 ab^{-1} has more than 2σ sensitivity [1]. For the same luminosity, a direct VBF + MET search for invisible singlet pair production can exclude the *green shaded region* [2]. In the *purple shaded region*, a TLEP-like lepton collider can probe the Zh cross section deviation, see Eq. (5.4.59), at the 2σ level. Below the *blue line*, the singlet is stable at the origin. Above the *orange or red solid lines*, a one-step or two-step phase transition strong enough for EWBG can occur ($\mu_R = m_S$). In this projected-down parameter space, the effect of scale variation is minor.

mal loops by inserting $\Pi_i \sim T^2$ into the effective potential.

Our phenomenological analysis of the EWPT in the SM + $N_S \times S$ benchmark model generalizes the results of [2], and shows that EWBG in singlet extensions without Higgs mixing is guaranteed to be discovered at future 100 TeV and lepton colliders. Given that more general models with Higgs mixing generate additional signatures which are expected to be detectable at a future 100 TeV collider [255], the outlook for a general phenomenological no-lose theorem is optimistic, though more work is needed to make this conclusion completely robust.

The (O)PD calculation shows two-step phase transitions are more prevalent than previously assumed from TFD calculations. This is encouraging, as strong two-step transitions can generate observable gravity wave signals [251]. They are also more constrained, since runaway bubbles are incompatible with baryon number generation [256]. Further analysis is needed to determine whether this translates to additional constraints on the SM + $N_S \times S$ benchmark model.

The OPD scheme represents a simple extension on the standard TFD calculation, takes only slightly more CPU time to solve for the strength of the phase transition, and is easy to implement in Mathematica. We supply a condensed instruction manual in Appendix A. We hope that the OPD calculation will be useful in the future study of other BSM scenarios. This is particularly motivated, since for more complete theories with additional correlations amongst the low-energy parameters than in our benchmark model, the OPD calculation makes significantly different predictions for the EWBG-viable parameter space, and hence the associated collider and cosmological observables. In some cases, scenarios which were thought to be viable may now be excluded.

Developing the (O)PD thermal resummation scheme is a necessary ingredient for the careful study of EFTs at higher temperature, which in turn would represent a great leap in our model-independent understanding of EWBG. We are currently conducting such an analysis, and will present the results in a future publication.

Chapter 6

Higgs Precision Constraints on Colored Naturalness

6.1 Introduction

The discovery of a Higgs-like particle at Run I of the LHC [10, 11] without any accompanying Beyond the Standard Model (BSM) particles has brought into sharp focus the hierarchy problem and the naturalness of the Weak scale. A minimal ingredient of any natural model is a mechanism to soften the quadratic divergences of the Higgs mass-squared parameter, m_h^2, that appear when computing quantum corrections in the Standard Model (SM). Since models of naturalness characteristically predict additional particles near the Weak scale, an urgent question is how these particles could have escaped detection at the LHC. Various possibilities exist, ranging from particle spectra that are hidden from direct searches to models of “neutral" naturalness [263, 264].

Currently, two symmetry mechanisms are known that can account for a light Higgs naturally and satisfy experimental constraints — supersymmetry (SUSY) and having the Higgs arise as a pseudo-Nambu-Goldstone boson (PNGB) of a larger global symmetry.[1] Models of naturalness contain new BSM “partner” states, which are related to the SM particles by these symmetries.

---

[1] Conformal symmetry could yield a light scalar [265], but we will not consider this further, since no complete model exists.

While the partner states cancel the quadratic divergence of m_h^2, the Higgs mass is now quadratically dependent on the mass scale of the partner states. A natural theory thus requires that these states be near the Weak scale. Moreover, the largest contribution to m_h^2 in the SM comes from the top quark, t, since it has the largest coupling to the Higgs. This implies that the largest correction among partner particles comes from the partner of the top quark, motivating searches for top partners.

The partner particles affect the rates for producing the Higgs boson at colliders as well as the decay rates of Higgs bosons to SM states. Precision measurements of Higgs properties can thus constrain the partner particles. In this paper, we focus solely on the impact of top-partners on Higgs precision physics. To carry out this program we have to choose first whether the symmetry that relates the top partners to the top itself commutes with $SU(3)$-color of the SM. In addition, the spin of the top partner dictates the symmetry structure that is needed to cancel the quadratic divergences. In this paper, we choose to focus on colored top partners of spin-0, 1/2, and 1, which represents all models of naturalness other than those that fall under the rubric of “neutral naturalness". This is a sensible choice, since the top is colored and color does not play a priori a central role in naturalness. Moreover, current Higgs precision measurements, which are the focus of this paper, are not the best probe of “neutral naturalness" [262, 266].

The generic predictions of colored top partners from naturalness have been studied in many contexts. In particular, both indirect searches and more model-dependent direct searches for colored top partners have been proposed and undertaken at the LHC. Direct searches can offer a powerful way to search for particular top partners, but specific partner-mass spectra [267, 37] or additional BSM physics can easily hide the top-partner signal from specific searches without affecting the “naturalness” of the model. For example, in the context of SUSY, direct production bounds on the colored top partners (“stops”) can be as high as $m_{\tilde{t}} \gtrsim \mathcal{O}(800)$ GeV [268, 269, 270, 271, 272], but assume that the stops decay to energetic SM final states and missing transverse energy. Instead, if the stop decays to a top quark and neutralino, $\tilde{\chi}_1^0$, with $m_{\tilde{t}} - m_{\tilde{\chi}_1^0} \approx m_t$, the searches become much more challenging. In this “compressed” region, the top quark and neutralino are collinear in the lab frame; the stop-pair production will thus be similar to the top-pair production, and no significant missing transverse energy is observed [273, 274, 275, 276]. Similar difficult regions emerge when $m_{\tilde{t}} - m_{\tilde{\chi}_1^0} \approx m_W$ or $m_{\tilde{t}} - m_{\tilde{\chi}_1^0} \approx 0$. Direct searches can be complicated further by additions to the Minimal Supersymmetric Standard Model (MSSM) such as Stealth SUSY [267, 277]. As such, although direct searches are powerful there still is room for colored top partners to evade these searches, which argues for employing also alternative search methods.

Indirect searches for top partners from Higgs precision measurements have been carried out, for example, in the context of SUSY, see e.g. [278, 279, 280, 281, 282, 283, 284, 285, 286] and references therein. Since the stops couple to the Higgs, they can significantly affect the loop-induced Higgs-gluon-gluon (hgg) and Higgs-photon-photon ($h\gamma\gamma$) couplings. Higgs precision data can thus constrain low-mass stops independent of their production or decay modes, although heavier stops remain unconstrained as they decouple from the hgg and $h\gamma\gamma$ loops as $\mathcal{O}(1/m_{\tilde{t}}^2)$. For example, the earliest Higgs data constrained models of electroweak baryogenesis in the Minimal Supersymmetric Standard Model (MSSM), which require a light stop (independent of naturalness) [206, 287, 207, 288]. Direct and indirect searches are thus complementary.

In this paper, we update the bounds on colored top partners using the latest available Higgs precision data, including data up to EPS 2017 [289]. We also provide projections for expected future data from the LHC Run 3 (300 fb^{-1}) and LHC Run 4 (3 ab^{-1}), as well as from possible future colliders, namely the Future Circular Collider (FCC-ee and FCC-hh), Circular Electron Positron Collider (CEPC), and the International Linear Collider (ILC). This updates and extends related previous work on spin-0 (SUSY) [278, 279, 280, 281, 282, 283, 284, 285, 286], spin-1/2 [290, 291, 292, 293], and spin-1 [294].

We also investigate the robustness of the current and projected indirect constraints by allowing for non-SM Higgs couplings, invisible Higgs decays, and exotic Higgs decays. We describe which of these possibilities are best at hiding the effects of top partners and weakening the constraints on their masses. We discuss briefly how these additional deviations could be implemented in realistic models, which allows for further work that focuses on the most “natural" models that explain electroweak symmetry breaking (EWSB). In principle there will also be bounds from direct constraints or other precision tests of colored top partners, which are often complementary. However, as we show, there are remarkably powerful statements that can be made through Higgs precision measurements alone.

The rest of the paper is organized as follows. In Section 6.2, we review the interplay between fine-tuning and the masses of the colored top partners. In Section 6.3, we discuss the methodology for setting constraints on top partners, as well as how to reduce the sensitivity of Higgs precision data to colored top partners through modifications that affect the Higgs cross sections and decay rates. Section 6.4 describes the Higgs data that we use to calculate our constraints and projections, and also details our analysis method. Section 6.5 discusses canonical top partner models and some extensions. In Section 6.6, we present our results, before concluding in Section 6.7. In Appendix B, we review how Higgs precision measurements, only relevant at future colliders, such as the $e^+e^- \to Zh$ cross section or $pp \to hh$ production can provide complementary probes. Appendices C, D, and E contain additional information, including the detailed data sets used in our paper, as well as a validation cross-check of our results.

6.2 Naturalness and Higgs Couplings

To understand the hierarchy problem and possible symmetry-based solutions, we utilize the one-loop Coleman-Weinberg (CW) potential with a hard UV cutoff, Λ, and examine the contributions to the Higgs-mass term in the potential in the mass eigenbasis. The form of the Coleman-Weinberg potential for the Higgs is [281]

$$V_{\text{CW}} = \frac{1}{64\pi^2}\sum_i (-1)^{F_i} N_{f,i}\left(2M_i^2\Lambda^2 + M_i^4 \log\frac{M_i^2}{\Lambda^2}\right) , \tag{6.2.1}$$

where i runs over all particles in the Higgs loop diagrams, $N_{f,i}$ is the number of flavors of particle i, F_i is the fermion number, and M_i is the field-dependent mass taking the form

$$M_i^2 = \mu_i^2 + a_i h^2 , \tag{6.2.2}$$

where a_i is given by the particle's effective coupling to the Higgs, and μ_i represents a possible bare mass for the particle whose origin is not from the Higgs mechanism. The origin of the hierarchy problem comes from quadratic divergences that appear when computing the shift in the Higgs mass at one-loop,

$$\delta m_h^2 = \frac{d^2V_{\text{CW}}}{dh^2} \simeq \frac{1}{32\pi^2}\sum_i (-1)^{F_i} N_{f,i}\left(a_i\Lambda^2 + 2\mu_i^2 a_i \ln\frac{\Lambda^2}{M_i^2}\right) . \tag{6.2.3}$$

A necessary condition to "solve" the hierarchy problem is then given by

$$\sum_i (-1)^{F_i} N_{f,i} a_i = 0\,. \tag{6.2.4}$$

This imposes certain relationships among the Higgs couplings that must be preserved by a symmetry. If the particles responsible for the cancellation are charged under the SM gauge symmetries, as in our case, this immediately has implications for Higgs precision physics, since their couplings to the Higgs are related to SM couplings of the Higgs through Eq. (6.2.3).

To predict the impact of the new physics on Higgs phenomenology, we also need its overall mass scale. This is dictated by the sub-leading terms in Eq. (6.2.3), since cancellation of the quadratic divergences do not automatically eliminate $\log \Lambda$ divergences as well.[2] This results in the usual logarithmic dependence on the cutoff in theories that solve the hierarchy problem, and a quadratic sensitivity to the mass of the BSM states

$$\delta m_h^2 \simeq \frac{1}{16\pi^2} \sum_i (-1)^{F_i} N_{f,i} \mu_i^2 a_i \ln \frac{\Lambda^2}{M_i^2}\,. \tag{6.2.5}$$

Since the top has by far the largest SM coupling to the Higgs, the top-partner mass scale is the most critical among the BSM masses. For a natural theory, all μ_i for the top partners should be $\mathcal{O}(m_{\text{weak}})$, and masses heavier than this require tuning for successful EWSB.

On the other hand, lowering top-partner masses as required by fine-tuning considerations increases the visibility of the partners at colliders. Top partners that share the top's color and electrical charge affect the loop-induced hgg and $h\gamma\gamma$ couplings. The qualitative behavior can be immediately understood by considering the low-energy Higgs theorem [295, 296] , which relates the mass of charged particles to their contribution to these couplings. For a heavy particle that receives some or all of its mass from the Higgs mechanism, the effective coupling is proportional to

$$\frac{v^2}{M_{\hat{t}}^2} \frac{\partial M_{\hat{t}}^2}{\partial v^2} \frac{h}{v} G^{\mu\nu} G_{\mu\nu}\,, \tag{6.2.6}$$

where $v \simeq 246$ GeV is the Higgs vacuum expectation value (VEV), $M_{\hat{t}}^2$ is the appropriately evaluated mass-squared matrix for the top partner, and $G^{\mu\nu}$ is the gluon field strength; a simi-

---

[2] Note that even if one eliminates the $\log \Lambda$ divergences, which could be done with, for example, a conformal symmetry, there would likely be problems with achieving electroweak symmetry breaking.

lar equation holds for the electromagnetic field-strength. When the partial derivative is an $\mathcal{O}(1)$ constant, we can see the $\propto 1/M_{\hat{t}}^2$ dependence drives the phenomenology. Therefore in a natural theory the largest contributions to Higgs observables arise from colored top partners. We shall also encounter cases where, due to fortuitous cancellations, the partial derivative evaluates to a very small number. However the colored top partners still contribute to Higgs wave-function renormalization (WFR), which leads to deviations from the SM prediction for Higgs associated production. Broadly, improving Higgs precision measurements without seeing deviations from the SM expectations results in a more fine-tuned theory, since it requires larger top-partner masses. Thus Higgs phenomenology and naturalness are inexorably tied together for colored top partners, and it provides an important constraint independent of direct searches.

6.3 Higgs Precision Constraints & Colored Top Partners

In this section, we describe our formalism and strategy to constrain colored top-partner models through Higgs precision physics. We discuss the generic features of these models that are most constrained by current data. Moreover, we identify those model features that are best at hiding top partners from current Higgs precision data alone, thereby reducing tension with naturalness. Finally, we describe how upcoming data from the LHC, future proton-proton, and future precision electron-positron colliders will affect these model features.

Higgs precision data can constrain BSM models mainly if these models modify the coupling of the Higgs to SM particles or contain new decay modes for the Higgs. Modifications to the Higgs couplings can affect the Higgs partial widths and production modes, while new decay modes affect only the partial widths. In our attempt to be model-agnostic, we do not investigate off-shell decays of the Higgs to top partners, but we do include the contributions to the Higgs partial width of on-shell decays for $M_{\hat{t}} < m_h/2$. This provides an important constraint at low masses. We will also consider the possibility that new decay modes can help hide colored top partners from Higgs precision measurements.

6.3.1 Definitions for non-Standard Model Higgs couplings

As we have emphasized in the introduction, a generic prediction of colored top partners is a modification of a certain set of Higgs couplings. Since the SM Higgs fits the data well, we parameterize modifications to the most important tree-level SM Higgs couplings as

$$r_j = c_{hjj}/c_{hjj}^{\mathrm{SM}}\,, \tag{6.3.7}$$

where $j = t$, b, V, or τ, c_{hjj} is the coupling of the Higgs to the state j, and c_{hjj}^{SM} is the coupling of the SM Higgs to the state j; the SM value is $r_j^{\mathrm{SM}} = 1$.[3]

However, this definition is not sufficient for BSM particles, since c_{hjj}^{SM} is not defined. We present a more general definition that works for both SM and BSM particles, which is derived directly from the mass M_j for a mass-eigenstate j . The 125 GeV Higgs, h, can in principle be a linear combination of Higgses H_i with vacuum expectation values (VEVs), v_i, that supply some or all of the mass to j.[4] The ratio of the hjj coupling to its SM value is then given by

$$r_j = \sum_i \langle h|H_i\rangle \frac{v}{v_i}\frac{\mathrm{d}\log[M_j^2]}{\mathrm{d}\log[v_i^2]}\,. \tag{6.3.8}$$

In the SM there is only a single Higgs and therefore this reduces to $r_j = 1$ as desired. Note that this is similar to the "κ framework" in [297] and in practice they are the same except for how new contributions are included in the Higgs width. Here we use the precise definition given in Eq. (6.3.8).

Apart from BSM physics affecting tree-level couplings, the loop-induced couplings hgg and $h\gamma\gamma$ play a particularly important role in constraining colored and electrically charged top partners. These partners appear at the same order in perturbation theory as SM processes. Moreover, the hgg coupling controls the dominant production mechanism in the SM, and the $h\gamma\gamma$ coupling controls one of the most sensitive decay channels. When these loop particles are heavy and can be integrated out, the effective vertex is given by the low-energy Higgs theorems [295, 296]. The one-loop result

---

[3] For simplicity, we assume that the Higgs boson couples equally to the W- and Z-bosons, i.e. $r_V \equiv r_W = r_Z$, as otherwise electroweak precision tests would be far more constraining than Higgs precision data for the foreseeable future.

[4] $h = \sum_i R_i H_i$ such that $\langle h|H_i\rangle = R_i$.

for the hgg coupling, including finite mass effects, is given by

$$\mathcal{L} \supset -\frac{1}{4} c_G \frac{h}{v} G^a_{\mu\nu} G^{\mu\nu a} \,, \tag{6.3.9}$$

where

$$c_G = \frac{\alpha_s}{12\pi} \sum_j N_{c,j} C_2(R) r_j \mathcal{A}_j(\tau_j) \,. \tag{6.3.10}$$

Here $N_{c,j}$ is the number of colors, $C_2(R)$ is the quadratic Casimir, and $\mathcal{A}_j \equiv \mathcal{A}^{s_j}(\tau_j)$ are the loop functions defined in Appendix C, which depend on the spin s_j and $\tau_j \equiv m_h^2/4m_j^2$, where m_j are the eigenvalues of M_j. For electrically charged states, a similar operator with the electromagnetic field strength replacing the gluon field strength can be used to calculate the Higgs coupling to two photons.

These definitions allow us to express the modifications to the effective hgg coupling from a colored top-partner, $\hat{t}$, and any accompanying BSM physics that affects the tree-level couplings r_j as

$$r_G \equiv \frac{c_G}{c_G^{\text{SM}}} = \frac{r_t \mathcal{A}_t + r_b \mathcal{A}_b + r_{\hat{t}} \mathcal{A}_{\hat{t}} + \delta r_G}{\mathcal{A}_t + \mathcal{A}_b} \,, \tag{6.3.11}$$

where δr_G captures the presence of other colored BSM (non-top-partner) particles. For modifications to the effective $h\gamma\gamma$ coupling, we have

$$r_\gamma \equiv \frac{c_\gamma}{c_\gamma^{\text{SM}}} = \frac{\sum_{j=W,t,b,\tau} r_j Q_j^2 \mathcal{A}_j + r_{\hat{t}} Q_{\hat{t}}^2 \mathcal{A}_{\hat{t}} + \delta r_\gamma}{\sum_{j=W,t,b,\tau} Q_j^2 \mathcal{A}_j} \,, \tag{6.3.12}$$

where δr_γ captures other (non-top-partner) particles carrying electrical charge.

It is now useful to define a new variable $\mathcal{N}_{\hat{t}}$ such that

$$\mathcal{N}_{\hat{t}} \equiv \frac{r_{\hat{t}} \mathcal{A}_{\hat{t}}}{r_t \mathcal{A}_t} \,. \tag{6.3.13}$$

This serves also to eliminate the $\langle h | H_i \rangle$ dependence of the top-partner contribution, as it is common to both the top-quark and top partner. We can then re-express r_G as

$$r_G = \frac{r_t \mathcal{A}_t (1 + \mathcal{N}_{\hat{t}}) + r_b \mathcal{A}_b + \delta r_G}{\mathcal{A}_t + \mathcal{A}_b} \,. \tag{6.3.14}$$

Finally, changing the couplings of the Higgs to SM particles affects the partial widths and hence the total width possibly as well. To parametrize the effects of this shift we define

$$r_h \equiv 1 + \sum_{j=G,\gamma,V,b,\tau} (|r_j|^2 - 1) B^{\text{SM}}_{h\to jj} \,, \tag{6.3.15}$$

where the SM branching ratios are given in e.g. [298]. While this is a redundant definition, it is useful, because in addition to colored top partners there may also be new decay modes for the Higgs, which would either be a contribution to the invisible width of the Higgs or an exotic decay channel. The difference between invisible and exotic decays will occur only whether we include direct searches for invisible Higgs decays. In particular, it is much easier to constrain an invisible decay rather than an arbitrary exotic decay. We also explicitly include the partial width into the top partners, which is nonzero only for low top-partner masses. We do not specify how the top partners decay, so this possibility is only constrained by how it affects the Higgs branching fractions of the other states. The total decay width of the Higgs, Γ_{tot}, is then given by

$$\Gamma_{\text{tot}} = r_h \Gamma_{\text{tot}}^{\text{SM}} + \Gamma_{\text{exo}} + \Gamma_{\text{inv}} + \Gamma_{\hat{t}\hat{t}}\, \Theta(m_h/2 - m_{\hat{t}})\,, \tag{6.3.16}$$

where $\Gamma_{\text{tot}}^{\text{SM}}$, Γ_{exo}, Γ_{inv}, and $\Gamma_{\hat{t}\hat{t}}$ are decay widths of the Higgs to SM particles, exotic final states, invisible final states, and top partner(s), respectively. This relation can be re-parameterized as

$$r_{\text{exo}} \equiv \frac{\Gamma_{\text{exo}}}{\Gamma_{\text{tot}}^{\text{SM}}} = \frac{r_h B_{\text{exo}}}{1 - B_{\text{exo}} - B_{\text{inv}} - B_{\hat{t}\hat{t}}\, \Theta(m_h/2 - m_{\hat{t}})}\,, \tag{6.3.17}$$

$$r_{\text{inv}} \equiv \frac{\Gamma_{\text{inv}}}{\Gamma_{\text{tot}}^{\text{SM}}} = \frac{r_h B_{\text{inv}}}{1 - B_{\text{exo}} - B_{\text{inv}} - B_{\hat{t}\hat{t}}\, \Theta(m_h/2 - m_{\hat{t}})}\,, \tag{6.3.18}$$

where the branching ratios are defined as $B_{\text{inv}} \equiv \Gamma_{\text{inv}}/\Gamma_{\text{tot}}$, $B_{\text{exo}} \equiv \Gamma_{\text{exo}}/\Gamma_{\text{tot}}$ and $B_{\hat{t}\hat{t}} \equiv \Gamma_{\hat{t}\hat{t}}/\Gamma_{\text{tot}}$.

6.3.2 How to Constrain and Hide Top Partners

With the definitions given in the previous sub-section, it is straightforward to understand where the strongest constraints on top partners come from. To constrain top partners, we use, for example, the signal strengths reported by ATLAS and CMS for particular final states of the Higgs. These are given by

$$\mu_f \equiv \frac{\sigma_{\text{prod}}^{\text{BSM}} \times B_{h\to ff}^{\text{BSM}}}{\sigma_{\text{prod}}^{\text{SM}} \times B_{h\to ff}^{\text{SM}}}\,, \qquad \mu_{\text{inv}} \equiv \frac{\sigma_{\text{prod}}^{\text{BSM}} \times B_{h\to \text{inv}}^{\text{BSM}}}{\sigma_{\text{prod}}^{\text{SM}}}\,, \tag{6.3.19}$$

where for the SM $\mu_f^{\text{SM}} = 1$ and $\mu_{\text{inv}}^{\text{SM}} = 0$. Given that a particular final state may come from a variety of different production modes, we must also take into account the weighting of the production modes, $\xi_{G,V,T}$, which give the relative strength of contributions to Higgs production from gluon fusion (ggF), vector-boson fusion plus Higgs associated production (VBF+VH), and top-quark-pair production in association with a Higgs (ttH), respectively. Similarly, for a particular production channel with multiple final states, we weight the decay modes (see Appendix E for more details).

In the limit that all SM particles couple to the Higgs with their SM tree-level values ($r_j = 1$), and assuming there are no exotic/invisible Higgs decays, the largest shift to Higgs phenomenology appears in r_G (see Eq. (6.3.14)),

$$r_G \sim (1 + \mathcal{N}_{\hat{t}}) \,. \tag{6.3.20}$$

In this limit,

$$\mu_f \sim \left(|r_G|^2 \xi_G + \xi_V + \xi_t\right) \frac{1}{1 + (|r_G|^2 - 1) B^{\text{SM}}_{h\to gg} + \cdots} \,, \tag{6.3.21}$$

which will give $\mu_f \gg 1$ for many channels if they have a large contribution from gluon fusion. This then implies a bound on $\mathcal{N}_{\hat{t}}$, which can be translated into a bound on the mass of the top-partner and a constraint on naturalness. However, many models have modified Higgs-SM couplings from an extended Higgs sector or from non-renormalizable contributions, so that other shifts, r_j, must be taken into account, especially for larger top-partner masses when $\mathcal{N}_{\hat{t}}$ becomes small. In models with multiple top partners, the contribution to r_G from the different top partners can cancel amongst themselves, a possibility we will investigate in Section 6.5.

Ignoring the possibility of multiple top partners for now, it is useful to see how best to alleviate a shift in r_G from its SM value. From Eq. (6.3.11), naively the simplest way to return r_G to its SM value would be by appropriately adding an equal and opposite contribution of δr_G from some new physics contribution. For instance in SUSY, one could add vector-like matter with a large bare mass, and interactions with the Higgs that could give the requisite δr_G to offset the stop contribution. Because of the large bare mass, they would not be seen in direct searches nor in other Higgs precision observables. Nevertheless we will not investigate this option further as it requires additional fine tuning for the new sector to cancel the inherent change in r_G without a symmetry, and additionally the extra sector would also contribute more significantly to the naturalness problem throughout most of its parameter space.

Next, we investigate how to alleviate changes in r_G through other coupling changes for the Higgs. If gluon fusion was the *only* way the LHC produced the Higgs, it would be straightforward to change the total width of the Higgs to offset this with a $r_{\text{exo/inv}}$ contribution to attempt to hide this shift. However, since gluon fusion is not the only production channel, this will not reduce the constraints significantly, as there are currently strong constraints on all production mechanisms except for ttH. Instead, a shift in one or more SM couplings is needed to offset the contribution of a colored top partner to r_G.

From Eq. (6.3.14), in the limit that the top quark and top partner dominate the contributions to r_G, we have

$$r_G \sim r_t(1+\mathcal{N}_{\hat{t}})\,. \tag{6.3.22}$$

We thus see that a natural way to hide the shift from $\mathcal{N}_{\hat{t}}$ is by adjusting r_t. While other coupling modifications are possible, they would require a parametrically larger shift from their SM values than a shift in $ht\bar{t}$ coupling, which is the largest and among the least-constrained couplings. In particular, r_t is currently only constrained independently from measurements where ttH is the dominant production mode. Whether r_t can be modified from its SM value, is a model-dependent question. In particular, the spin of the top partner is correlated with the sign of $\mathcal{N}_{\hat{t}}$. For spin-0 partners, $\mathcal{N}_{\hat{t}}$ is positive, which implies that r_t must be smaller than 1. For spin-1/2 partners, $\mathcal{N}_{\hat{t}}$ is negative, implying that $r_t > 1$ is desired; however, in models it is usual to have $r_t < 1$. We will comment more on particular model building aspects in future sections.

Adjusting r_t is currently the best mechanism for hiding the effects of a colored top partner and only measurements of the ttH coupling at the ILC and FCC-hh will constrain r_t at a percent level. This points to this channel as the best possible mode for indirect hints of top partners. However, it also implies that other mechanisms are needed to avoid Higgs precision constraints on top partners if no deviations are found. After r_t, changing r_b is most promising, since it also enters into the loop functions. As stated earlier, r_{inv} can offset some of the increase from r_G but only at the expense of affecting other channels as well. With this in mind, we will investigate the correlations of each possible shift in correlation with $\mathcal{N}_{\hat{t}}$ to determine the best mechanism for hiding top partners in current and in future datasets. We will also investigate whether existing models like the MSSM can be effective in hiding top partners from Higgs precision data, or if further model building is needed.

6.4 Data Sets and Fitting Procedure

6.4.1 Current and future proton collider data

Here we review the Higgs-signal-strength data sets used in our analyses. Explicit values and detailed references are included in Appendix E. Note that the constraints on $h \to \mathrm{invisible}$ requires special treatment for the current and projected data, as we discuss below.

1. **Current Limits**: This data set consists of existing Higgs measurements from ATLAS and CMS Run 1 (7 and 8 TeV), Run 2 (13 TeV), and the Tevatron (which is only marginally relevant for the $b\bar{b}$-channel). It includes data up to EPS 2017 [289]. We denote the observed signal strength as μ, and 1σ upper and lower error bars as σ^{up} and σ^{down} respectively.

2. **Current Expected Sensitivities**: Several existing measurements of the Higgs-signal-strengths differ slightly from their SM values. This is expected from statistical fluctuations, but could also be a sign of new physics. It is thus useful to compare the current constraints on top partners with the expected constraints assuming the existing measurements would have been in perfect agreement with the SM values. Moreover, the expected constraints provide a good benchmark with which to compare the projected sensitivities from future Run 3 and Run 4 data sets (see below).

   We construct the current expected sensitivities from the same Higgs measurements as used to derive the "Current Limits" above, but with the signal strengths set to their SM values, $\mu^{\mathrm{obs}}_{\mathrm{exp}} = \mu^{\mathrm{SM}}$ ($\mu^{\mathrm{SM}}_{f} = 1$, $\mu^{\mathrm{SM}}_{\mathrm{inv}} = 0$). We take the 1σ error bar to be the average of the original asymmetric 1σ error bars, i.e. $\sigma^{\mathrm{up/down}}_{\mathrm{exp}} = (\sigma^{\mathrm{up}} + \sigma^{\mathrm{down}})/2$.

3. **LHC Run 3 Data (projected, 300 fb^{-1})**: To derive the prospective constraints on top partners by the end of the LHC Run 3, we use the projected sensitivities on the Higgs signal strengths for ATLAS Run 3 from [3]. The projections are based on simulations of various search channels and assume a center-of-mass energy of 14 TeV and an integrated luminosity of 300 fb^{-1}. The theoretical uncertainties are assumed to be the same as today. CMS also has several projections [299], but for simplicity, we assume that they will analyze the same

search channels as ATLAS and obtain identical results as in [3]. We thus calculate projected sensitivities for the combined ATLAS+CMS data set (referred to as "LHC Run 3"), which consists of 600 fb^{-1}. We take the production-channel weights from [4]. Note that current LHC Run 2 measurement have already included several search channels that are not listed in [3], such as measuring $hb\bar{b}$ through ttH [300, 301]. Our projections are thus conservative.

4. **LHC Run 4 Data (HL-LHC) (projected, 3 ab^{-1})**: We also derive prospective constraints on top partners by the end of the LHC Run 4 (high-luminosity run), again using the ATLAS prescription and the same caveats discussed above for Run 3 [3]. This data set is similar to the LHC Run 3 data, but the integrated luminosity is set instead to 3 ab^{-1} for each experiment (i.e. for a total of 6 ab^{-1}). We assume that the theoretical systematic uncertainties remain unchanged as the integrated luminosity grows from 300 fb^{-1} to 3 ab^{-1} in [3] (i.e. they are assumed to be the same as today). This is likely a pessimistic assumption, but it is conservative.

5. **Proton-proton beams at the Future Circular Collider (FCC-hh)**: We project sensitivities for FCC-hh (100 TeV, 30 ab^{-1}) based on the Higgs-coupling data from FCC-ee (see Sec. 6.4.2 below) but assuming a measurement of the $ht\bar{t}$ coupling, r_t. This coupling is expected to be measured at a statistical limited level of 1% [8], an improvement compared to the expected FCC-ee measurement of 13% (see Table E.5).

Current and projected $h \to \text{invisible}$ search data is treated differently in our analysis compared to the other data, as we now describe. Most of the published LHC results only show upper limits for $\mu_{\text{inv}} \equiv \sigma_{\text{prod}} \times B_{\text{inv}}/\sigma^{\text{SM}}_{\text{prod}}$ at 95% confidence level (CL) (denoted as $\sigma^{95\%}_{\text{inv}}$) rather than a likelihood scan with respect to μ. In the absence of the likelihood curve, we do not know the best-fit and 1σ values. In these cases, we set the "observed" μ to be 0 and translate the 95% CL upper limit into 1σ CL uncertainty ($\sigma^{\text{up/down}}_{\text{inv}} = \sigma^{95\%}_{\text{inv}}/\sqrt{3.84}$). For our prospective constraints, we use projected VBF $\to h \to$ invisible data from [302], which is based on $\sqrt{s} = 13$ TeV with up to 3 ab^{-1} of data (similar projections are also found in [303]). We choose the scenario in [302] in which the experimental systematic uncertainties and the theoretical systematic uncertainties stay the same as the integrated luminosity increases. This projects $\sigma_{\text{inv}}^{95\%} = 21\%$ for LHC Run 3 Data and $\sigma_{\text{inv}}^{95\%} = 20\%$ for LHC Run 4 Data.

The Higgs may also have exotic decays [304], distinct from purely invisible decays. Exotic decays of the Higgs are an important window to new physics and several searches have been conducted by ATLAS and CMS [305, 306, 307, 308, 309, 310, 311, 312, 313, 314, 315, 316, 317, 318, 319]. However, many possibilities exist, which have not yet all been constrained. The bound on the total Higgs width [320, 321] from direct measurements does not provide a strong constraint on arbitrary exotic Higgs decays. Instead, as discussed in Sec. 6.3.2, exotic-decay modes are constrained as they would also modify the signal strengths. As we will see, while they can help to hide spin-0 top partners, they do not help in hiding spin-1/2 and spin-1 top partners.

We construct the overall χ^2 fitting function of all the search channels as

$$\chi^2 = \sum_{f,\text{inv}} \frac{(\mu_f - \mu_f^{\text{obs}})^2}{\sigma_f^2} \quad \text{with} \quad \sigma_f = \begin{cases} \sigma_f^{\text{up}}, & \mu_f \geq \mu_f^{\text{obs}} \\ \sigma_f^{\text{down}}, & \mu_f < \mu_f^{\text{obs}} \end{cases}, \tag{6.4.23}$$

where f (inv) runs over all the (invisible) search channels. In Appendix D, we show good agreement between our results, obtained using the above χ^2, and the results obtained using the more involved method adopted by `HiggsSignals` [322].

6.4.2 Future lepton collider data

Future lepton colliders provide new opportunities to constrain the Higgs sector. Here we focus on three proposed projects and compare their reaches to those of the current and future proton colliders (see Table E.5 for the expected precision on the Higgs couplings):

1. **International Linear Collider (ILC)** [22]. Projected Higgs-signal-strengths on individual search channels for ILC do not exist yet. However, there are combined Higgs-coupling fits to the 11-parameter set consisting of r_W, r_Z, r_b, r_G, r_γ, r_τ, r_c, r_μ, r_t, Γ_{tot}, and B_{inv} [5]. We choose the sensitivities of the “Full Data Set" of ILC (250 GeV, 2 ab^{-1} $\oplus$ 350 GeV, 200 fb^{-1} $\oplus$ 550 GeV, 4 ab^{-1}) for our projections.

2. **Circular Electron Positron Collider (CEPC)** [6]. Similar to ILC, there are only sensitivities from combined Higgs-coupling fits to the 10-parameter set: r_W, r_Z, r_b, r_G, r_γ, r_τ, r_c,

r_μ, Γ_{tot}, and B_{inv} [6]. We use the CEPC (240 GeV, 10 ab^{-1}) expected sensitivities to derive our projections.

3. **Electron-positron beams at the Future Circular Collider (FCC-ee)** [24]. FCC-ee also only provides sensitivities from combined Higgs-coupling fits, to the following 11-parameters: r_W, r_Z, r_b, r_G, r_γ, r_τ, r_c, r_μ, r_t, Γ_{tot}, and B_{inv} [24, 8]. Although FCC-ee, running at 350 GeV, cannot directly measure r_t like ILC, it could constrain r_t indirectly in the $e^+e^- \to t\bar{t}$ channel through virtual Higgs-exchange. We use the FCC-ee (240 GeV, 10 ab^{-1} $\oplus$ 350 GeV, 2.6 ab^{-1}) expected sensitivities to derive our projections. The improvements in the sensitivities of FCC-ee compared to the ILC and CEPC are due to the increased integrated luminosity, more interaction points, and a better electron beam energy resolution [24].

Other future lepton colliders, such as the Compact Linear Collider [23], yield similar constraints on colored top partners. We do not include them below.

We interpret the projected sensitivities in Table E.5 as 1σ-error bars for a particular coupling, σ_{r_i}, and construct a χ^2-function as

$$\chi^2 = \sum_{i=W,Z,b,G,\gamma,\tau,c,\mu,t} \frac{(r_i-1)^2}{\sigma_{r_i}^2} + \frac{(r_h + r_{\text{inv}} + r_{\text{exo}} - 1)^2}{\sigma_{\Gamma_{\text{tot}}}^2} + \frac{(r_{\text{inv}} - 0)^2}{\sigma_{r_{\text{inv}}}^2}, \tag{6.4.24}$$

where r_h, r_{inv}, and r_{exo} are given by Eq. (6.3.15) and Eq. (6.3.17), respectively. Since we focus only on the parameters most relevant for deriving the constraints on top partners, we set $r_W = r_Z = r_V$ and $r_\mu = r_\tau$, and construct r_G and r_γ from r_t,[5] r_b, r_V, r_τ, and $r_{\hat{t}}$ according to Eqs. (6.3.11) and (6.3.12), respectively. In many cases discussed below, we set $r_c = 1$, since it is not relevant for constraining top partners. However, in some cases (e.g., in the MSSM or in 2HDM models), we set $r_c = r_t$, and thus a precise measurement of r_c will allow strong constraints to be set on top-partner models in which r_t is affected. For invisible decays, we use Eq. (6.3.17) and translate $\sigma_{B_{\text{inv}}}$ from the 95% CL upper limit given in Tab. E.5 using the relation $\sigma_{B_{\text{inv}}} = \sigma_{B_{\text{inv}}}^{95\%}/\sqrt{3.84}$.

---

[5] For CEPC, we set $r_t = 1$ in Eqs. (6.3.11), (6.3.12), and (6.4.24).

6.5 Canonical Top Partner Models and Extensions

We outline now the models of three specific classes of colored top partners – spin-0, 1/2, and 1 – that we study. The symmetries that enforce the cancellation of quadratic divergences, see Eq. (6.2.4), will be different in the various cases, and therefore the basic moving parts of a model and their predictions for Higgs phenomenology are different. We briefly comment on their generic prediction for $\mathcal{N}_{\hat{t}}$ defined by Eq. (6.3.13) and the extensions that can reduce the overall contribution to r_G.

6.5.1 Spin-0

For spin-0 colored top partners (without loss of generality we will refer to them as stops), enforcing Eq. (6.2.4) requires a symmetry between the fermionic tops of the SM and scalar particles. Supersymmetry is the only known symmetry that can have such a relation, and in the minimal incarnations that can incorporate the SM there will be two stops, a partner for the right-handed and left-handed top quarks. Moreover, since the top-quark is part of an $SU(2)$ doublet with the bottom-quark, SUSY will also require a left-handed bottom-partner. We assume that other partner particles are heavy, which in any case does not spoil naturalness.

In this limit we have the equality $a_{\tilde{t}} = a_t = \lambda_t^2$ in Eq. (6.2.2), and due to scalars and fermions contributing with opposite signs to the Higgs-loop integrals, Eq. (6.2.4) is automatically satisfied. The usual diagrammatic presentation of the cancellation of quadratic divergences is shown in Fig. 6.1.

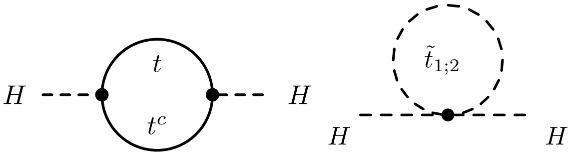

Figure 6.1: Diagrams relevant to the cancellation of the top loop with spin-0 partners: the one-loop diagram for the SM top (left) and the two stops (right).

Even though Eq. (6.2.4) is satisfied for a natural theory, the precise structure of the model and the Higgs sector is model-dependent. In the case of SUSY, the Higgs sector must be enlarged at least to a two-Higgs-doublet model (2HDM) because of the symmetry that enforces Eq. (6.2.4). This has implications for the Higgs phenomenology, since the Higgs observed at the LHC must then be a linear combination of the fields within the 2HDM (or additional Higgs states if there are more). For simplicity, we will start with the minimal 2HDM required for stops, which is a type-II model as in the MSSM, and take the decoupling limit. In the decoupling limit, the Higgs couples to the SM fields as the SM Higgs (i.e., r_t and the other Higgs-SM couplings are 1). We will comment below in Sections 6.5.1 and 6.5.1 on changes that occur from extended Higgs sectors.

We now first review the structure of the stop masses and their couplings to the Higgs, and then explain how Higgs precision measurements constrain the stops. We then discuss how the stop constraints are affected when including the left-handed sbottom.

After EWSB the stop-mass matrix is given by

$$\begin{pmatrix} m_{Q_3}^2 + m_t^2 + D_L^t & m_t X_t \\ m_t X_t^* & m_{U_3}^2 + m_t^2 + D_R^t \end{pmatrix}, \tag{6.5.25}$$

where m_{Q_3} and m_{U_3} are the soft SUSY breaking masses of the left- and right-handed stops, respectively.[6] D_L^t and D_R^t are D-terms

$$D_L^t = \left(\frac{1}{2} - \frac{2}{3}\sin^2\theta_W\right) m_Z^2 \cos 2\beta, \quad D_R^t = \frac{2}{3}\sin^2\theta_W m_Z^2 \cos 2\beta\,, \tag{6.5.26}$$

where θ_W is the Weinberg angle and $\tan\beta \equiv v_2/v_1$ is the ratio of the two Higgs VEVs. The stop matrix has two eigenvalues, $m_{\tilde{t}_1}$ and $m_{\tilde{t}_2}$. We order the eigenvalues such that $m_{\tilde{t}_1}$ contains mostly m_{Q_3} and $m_{\tilde{t}_2}$ contains mostly m_{U_3}. The eigenvalues $m_{\tilde{t}_1}$ and $m_{\tilde{t}_2}$ satisfy the relation

$$|m_{\tilde{t}_1}^2 - m_{\tilde{t}_2}^2| = \sqrt{(m_{Q_3}^2 - m_{U_3}^2 + D_L^t - D_R^t)^2 + 4m_t^2 X_t^2}\,. \tag{6.5.27}$$

Since m_{Q_3}, m_{U_3}, D_L^t, and D_R^t are real, the maximum value for X_t is given by

$$|X_t^{\max}| = \frac{|m_{\tilde{t}_1}^2 - m_{\tilde{t}_2}^2|}{2m_t}\,. \tag{6.5.28}$$

---

[6] In the MSSM, the off-diagonal mixing parameter can be written as $X_t = A_t - \mu\cot\beta$, where A_t is a soft-SUSY breaking parameter and μ is a supersymmetric mass term for the Higgs doublets; for a review see [323].

To calculate the effect of the stops on Higgs-precision measurement, we need to know the couplings between the Higgs, $\tilde{t}_1$, and $\tilde{t}_2$. In the decoupling limit, these are given by

$$g_{h\tilde{t}_1\tilde{t}_1} = \frac{2}{v}\left(m_t^2 - \frac{m_t^2 X_t^2}{m_{\tilde{t}_2}^2 - m_{\tilde{t}_1}^2} + D_{11}\right) , \tag{6.5.29}$$

$$g_{h\tilde{t}_2\tilde{t}_2} = \frac{2}{v}\left(m_t^2 + \frac{m_t^2 X_t^2}{m_{\tilde{t}_2}^2 - m_{\tilde{t}_1}^2} + D_{22}\right) , \tag{6.5.30}$$

$$g_{h\tilde{t}_1\tilde{t}_2} = \frac{m_t}{v} X_t \left(\cos 2\theta_t + D_{12}\right) , \tag{6.5.31}$$

where

$$D_{11} = \cos 2\beta m_Z^2 \left[\frac{1}{4} + c_{2\theta_t}\left(\frac{1}{4} - \frac{2}{3}\sin^2\theta_W\right)\right] , \tag{6.5.32}$$

$$D_{22} = \cos 2\beta m_Z^2 \left[\frac{1}{4} - c_{2\theta_t}\left(\frac{1}{4} + \frac{2}{3}\sin^2\theta_W\right)\right] , \tag{6.5.33}$$

$$D_{12} = -\frac{4}{m_{\tilde{t}_2}^2 - m_{\tilde{t}_1}^2} m_Z^2 \cos 2\beta \left(\frac{2}{3}\sin\theta_W^2 - \frac{1}{4}\right) , \tag{6.5.34}$$

$$\cos 2\theta_t = \sqrt{1 - \left(\frac{2 m_t X_t}{m_{\tilde{t}_2}^2 - m_{\tilde{t}_1}^2}\right)^2} . \tag{6.5.35}$$

We can now discuss how the stops affect Higgs precision measurements. First, the stops can contribute to the hgg coupling, $\mathcal{N}_{\tilde{t}}$ (see Eq. (6.3.13)) as

$$\mathcal{N}_{\tilde{t}} = \frac{\mathcal{A}^{\mathrm{s}=0}(m_h^2/4m_{\tilde{t}_1}^2)}{\mathcal{A}^{\mathrm{s}=1/2}(m_h^2/4m_t^2)} \frac{g_{h\tilde{t}_1\tilde{t}_1}}{m_{\tilde{t}_1}^2}\frac{v}{2} + \frac{\mathcal{A}^{\mathrm{s}=0}(m_h^2/4m_{\tilde{t}_2}^2)}{\mathcal{A}^{\mathrm{s}=1/2}(m_h^2/4m_t^2)} \frac{g_{h\tilde{t}_2\tilde{t}_2}}{m_{\tilde{t}_2}^2}\frac{v}{2} . \tag{6.5.36}$$

Second, stops with mass below $m_h/2$ do not only appear in such loop processes, but also provide an exotic decay-channel for the Higgs, contributing to the total Higgs width (recall that we do not specify the stop decay channels or investigate off-shell decays in this paper). The tree-level Higgs-decay width to two stops is given by

$$\Gamma(h \to \tilde{t}_i\tilde{t}_j) = \frac{3}{16\pi m_h} g_{h\tilde{t}_i\tilde{t}_j}^2 \left[1 - \frac{2(m_{\tilde{t}_i}^2 + m_{\tilde{t}_j}^2)}{m_h^2} - \frac{(m_{\tilde{t}_i}^2 - m_{\tilde{t}_j}^2)^2}{m_h^4}\right]^{1/2} \Theta\left(m_h - m_{\tilde{t}_i} - m_{\tilde{t}_j}\right) , \tag{6.5.37}$$

so that the total width for the Higgs decays into stops is

$$\Gamma_{\text{tot}}(h \to \tilde{t}\tilde{t}) \equiv \Gamma(h \to \tilde{t}_1\tilde{t}_1) + \Gamma(h \to \tilde{t}_2\tilde{t}_2) + \Gamma(h \to \tilde{t}_1\tilde{t}_2) . \tag{6.5.38}$$

In Section 6.6, we will present the explicit exclusions from all the various contributions. However it is useful, as in Section 6.3.2, to develop an intuition for the shape of the exclusion curves. Given that the two main sources are contributions to $\mathcal{N}_{\tilde{t}}$ and the width, it is helpful to look at their approximate expressions and understand where their contributions are extremized. In the limit $m_{\tilde{t}_{1,2}} \gg m_h/2$, we get

$$\mathcal{N}_{\tilde{t}} \approx \frac{v}{8}\left(\frac{g_{h\tilde{t}_1\tilde{t}_1}}{m_{\tilde{t}_1}^2} + \frac{g_{h\tilde{t}_2\tilde{t}_2}}{m_{\tilde{t}_2}^2}\right). \tag{6.5.39}$$

It is a good approximation to neglect the D-terms, so that $\mathcal{N}_{\tilde{t}}$ becomes

$$\mathcal{N}_{\tilde{t}} \approx \frac{1}{4}\left(\frac{m_t^2}{m_{\tilde{t}_1}^2} + \frac{m_t^2}{m_{\tilde{t}_2}^2} - \frac{m_t^2 X_t^2}{m_{\tilde{t}_1}^2 m_{\tilde{t}_2}^2}\right). \tag{6.5.40}$$

(We note that this expression can be also obtained from the low-energy Higgs theorem discussed in Section 2 [295, 296, 324, 280, 325, 282].) Eq. (6.5.40) depends only on the stop masses and the mixing. Moreover, $m_{\tilde{t}_1}$ and $m_{\tilde{t}_2}$ have symmetric contribution to Higgs precision measurements.[7] The lowest allowed value for X_t from Eq. (6.5.40) is given by

$$|X_t^{\text{min}}|^2 \approx \frac{m_t^2\left(m_{\tilde{t}_1}^2 + m_{\tilde{t}_2}^2\right) - 4m_{\tilde{t}_1}^2 m_{\tilde{t}_2}^2 (\mathcal{N}_{\tilde{t}})^{\text{fit;max}}}{m_t^2}, \tag{6.5.41}$$

where $(\mathcal{N}_{\tilde{t}})^{\text{fit;max}}$ is the upper limit allowed from Higgs precision data. Combined with Eq. (6.5.28), a given set of $m_{\tilde{t}_1}$ and $m_{\tilde{t}_2}$ are ruled out if $|X_t^{\text{min}}| > |X_t^{\text{max}}|$. The resulting constraints are strongest in the degenerate limit ($m_{\tilde{t}_1} = m_{\tilde{t}_2} \equiv m_{\tilde{t}}$); from Eq. (6.5.40), the constraint is given by

$$m_{\tilde{t}} \geq \frac{m_t}{\sqrt{2\,(\mathcal{N}_{\tilde{t}})^{\text{fit;max}}}}. \tag{6.5.42}$$

As a result, smaller $(\mathcal{N}_{\tilde{t}})^{\text{fit;max}}$ leads to stronger constraints on $m_{\tilde{t}}$, while $(\mathcal{N}_{\tilde{t}})^{\text{fit;max}} < 0$ completely rules out the degenerate direction.

The non-degenerate direction is less constrained. X_t^{max} increases as the difference between $m_{\tilde{t}_1}$ and $m_{\tilde{t}_2}$ increases, see Eq. (6.5.28), and it becomes easier to find specific values of $X_t = X_t^{\text{blind}}$ that allow $\mathcal{N}_{\tilde{t}}$ to vanish (this was referred to as the stop blind-spot in [283]). X_t^{blind} is given by

$$X_t^{\text{blind}} = (m_{\tilde{t}_1}^2 + m_{\tilde{t}_2}^2)^{1/2}. \tag{6.5.43}$$

---

[7] In Appendix B, we discuss how stops are constrained from the future Higgs precision probe $e^+e^- \to Zh$; we will see that $\tilde{t}_1$ and $\tilde{t}_2$ contribute differently to this process.

For $m_{\tilde{t}_1} \to 0$, one finds that $m_{\tilde{t}_2} = |X_t^{\text{min}}| \leq |X_t^{\text{max}}| = m_{\tilde{t}_2}^2/(2m_t)$ is always satisfied for $m_{\tilde{t}_2} \gtrsim 2m_t$ (similarly for $m_{\tilde{t}_2} \to 0$). This means that Higgs precision measurements that constrain only $\mathcal{N}_{\tilde{t}}$ are not sufficient to probe this region.

Back to the full expression, the vanishing of $\mathcal{N}_{\tilde{t}}$ in the non-degenerate direction occurs since $g_{h\tilde{t}_1\tilde{t}_1}/m_{\tilde{t}_1}^2 = -g_{h\tilde{t}_2\tilde{t}_2}/m_{\tilde{t}_2}^2$, see Eq. (6.5.39). However, in this limit, at least for $m_{\tilde{t}_1} < m_h/2$ and/or $m_{\tilde{t}_2} < m_h/2$, the Higgs can also decay to the stops. The Higgs decay width to stops does not vanish for the same choice of parameters as does $\mathcal{N}_{\tilde{t}}$, and one might naively conclude that any stop lighter than $m_h/2$ will be ruled out. However, in the limit that the other stop is sufficiently heavy, the coupling of the lighter stop to the Higgs becomes small. We can see this by integrating out the heavy stop [283] to obtain the following effective lighter stop-Higgs coupling:

$$\mathcal{L} = \frac{2m_t^2}{v^2}\left(1 - \frac{X_t^2}{m_{\tilde{t}_h}^2 - m_{\tilde{t}_l}^2}\right)|H_u|^2|\tilde{t}_l|^2 \,. \tag{6.5.44}$$

where H_u represents a up-type Higgs doublet, $\tilde{t}_h$ and $\tilde{t}_l$ stands for the heavier and lighter stops respectively. This vanishes for $X_t = X_t^{\text{blind}}$ in the non-degenerate limit. In this case, the lighter stop only couples very weakly to the Higgs, while the heavier stop is too heavy to affect the Higgs precision measurements. Higgs precision measurements thus cannot alone rule out the possibility of a very light stop entirely (see also Section 6.6 and Fig. 6.3).

In the particular limit we are studying here, there also will be a left-handed sbottom in the spectrum. In the full MSSM there is a right-handed sbottom and the full couplings of the sbottom will resemble those of Eqns. (6.5.29)–(6.5.31). We leave a full accounting of third-generation squarks to future work, and focus instead on the natural SUSY limit in which the right-handed sbottom is decoupled. The sbottom-eigenstate mass can be written in terms of the stop parameters as

$$m_{\tilde{b}_1}^2 = \frac{1}{2}\left(1 + \cos 2\theta_t\right) m_{\tilde{t}_1}^2 + \frac{1}{2}\left(1 - \cos 2\theta_t\right) m_{\tilde{t}_2}^2 - m_t^2 - m_W^2 \cos 2\beta + m_b^2 \,. \tag{6.5.45}$$

The Higgs-sbottom-sbottom coupling is given by

$$g_{h\tilde{b}_1\tilde{b}_1} \approx \frac{2}{v}\left\{m_b^2 + m_Z^2 \cos 2\beta \left[-\frac{1}{2} + \frac{2}{3}\sin^2\theta_W\right]\right\} \,. \tag{6.5.46}$$

The sbottom can contribute to both $\mathcal{N}_{\tilde{b}}$ and $\Gamma(h \to \tilde{b}_1 \tilde{b}_1)$, with expressions similar to the ones given for the stops above. From Eq. (6.5.46), we see that there are two contributions to $g_{h\tilde{b}_1\tilde{b}_1}$: the first is suppressed by the small bottom quark mass, while the D-term contribution generically gives a large coupling of $\mathcal{O}(v)$. We thus see that it is useful to investigate two limits: one in which the sbottoms do not contribute at all and one in which the sbottoms contribute with a large coupling given by the D-term. Below, we will investigate these two cases with the following specific parameter choices:

$$\tan\beta \simeq 1 \quad \Longrightarrow \quad g_{h\tilde{b}_1\tilde{b}_1} = 0\,, \tag{6.5.47}$$

$$\text{large } \tan\beta \quad \Longrightarrow \quad g_{h\tilde{b}_1\tilde{b}_1} \simeq \frac{m_Z^2}{v}\left(1 - \frac{2}{3}\,\sin^2\theta_W\right)\,. \tag{6.5.48}$$

We will show the results for these two cases in Section 6.6 (see Fig. 6.3). Note that we also ensure that $m_{\tilde{b}_1}$ in Eq. (6.5.45) is real for all viable choices of $m_{\tilde{t}_1}$, $m_{\tilde{t}_2}$, and X_t when we calculate the current constraints and projected sensitivities in Section 6.6.

Finally, we note that the process $e^+e^- \to Zh$ will also generically be affected by stops [326], and could avoid some of the blind spots of the other measures. However, since it is only relevant for a future high-precision e^+e^- collider, we defer its discussion to Appendix B.

Our discussion thus far is sufficient to talk about the bounds on stops in any model. However, as mentioned above, there are at least two Higgs doublets instead of a single doublet as in the SM, which can impact the phenomenology. Furthermore, in a concrete model such as the MSSM, there will be a number of relationships that relate the top-sector with other sectors through the particular structure of EWSB. We next discuss how the relations imposed by concrete models affect their ability to accommodate light stops. We then outline the most promising model building directions to hide spin-0 colored top partners.

Concrete model: MSSM

In this subsection, we restrict ourselves to the EWSB structure of the MSSM. After EWSB, there are two CP-even Higgs bosons, and we identify the lightest of these as the 125 GeV SM-like Higgs boson for the rest of our discussion. The Higgs couplings in a MSSM(-like) model are described by two parameters: the rotation angle of the Higgs mass matrix, α,[8] and the ratio of the two Higgs VEVs, $\tan\beta$. The modifications of tree-level Higgs couplings are

$$r_c = r_t = \frac{\cos\alpha}{\sin\beta}, \quad r_b = r_\tau = -\frac{\sin\alpha}{\cos\beta}, \quad r_V = \sin(\beta-\alpha), \tag{6.5.49}$$

which can be recast into a more convenient form in terms of r_t and $\tan\beta$

$$r_c = r_t, \quad r_b = r_\tau = \sqrt{1+(1-r_t^2)\tan^2\beta}, \quad r_V = \frac{r_t\tan^2\beta + \sqrt{1+(1-r_t^2)\tan^2\beta}}{1+\tan^2\beta}\,. \tag{6.5.50}$$

As discussed in Section 6.3, the most powerful way to hide top partners is to modify r_t directly. The 2HDM naturally allows for modifications of top Yukawa to non-SM values, and to hide stops, we would require $r_t < 1$ given $\mathcal{N}_{\tilde{t}} > 1$. However, in the MSSM, Eq. (6.5.50) indicates that r_b and r_V depends on r_t, which is not well constrained by current data. The $\tan\beta \to 0$ limit however removes the r_t dependence of r_b and r_V, and fixes them to 1 allowing lower values of r_t without changing other Higgs observables. There is a lower limit of $\tan\beta = 2.2$ (obtained at one-loop, ignoring threshold corrections) in order to retain perturbativity of Yukawa couplings at the GUT scale. Smaller values of $\tan\beta$ would necessarily require new physics below the GUT scale but even $\tan\beta < 1$ is in principle possible. Requiring the top Yukawa to be smaller than 4π at 10 TeV (100 TeV) leads to $\tan\beta \geq 0.63\ (0.8)$. In the opposite limit of large $\tan\beta$, $r_t, r_V \to 1$, independent of $\tan\beta$. We also emphasize that the equality $r_c = r_t$ still holds in all these limits. Precise measurement of r_c at future lepton colliders will therefore indirectly constrain r_t.

Extended Higgs sectors

The restrictive relation Eq. (6.5.50) could in principle be eased by extending the MSSM Higgs sector. The simplest extension is to add a new scalar singlet as in the Next-to-Minimal Supersymmetric Standard Model (NMSSM). However this yields a uniform reduction in all the couplings [327, 328]. This is not sufficient for hiding top partners because the tradeoff for reducing the contribution to r_G reduces also all other SM Higgs couplings, in particular r_V. Introducing additional Higgs doublets could break the relationship of r_V with other couplings and could thus

---

[8] In MSSM models $-\pi/2 \leq \alpha \leq 0$ while in a general type-II 2HDM $-\pi/2 \leq \alpha < \pi$.

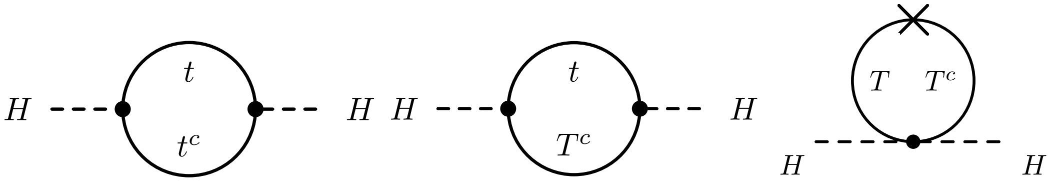

Figure 6.2: Diagrams involved in the cancellation of top loop in a spin 1/2 top partner model. The original one-loop diagram of SM top (left), the one-loop diagram with HTt^c interaction (middle), and the one-loop diagram with a dimension-five h^2TT^c coupling and a T mass insertion (right).

better hide top partners from Higgs precision measurements. Additional modifications to the Higgs sector that break the $r_c = r_t$ relation while avoiding flavor constraints is another interesting direction to pursue. We leave a detailed investigation to future work.

6.5.2 Spin-1/2

Spin-1/2 top partners appear in Little Higgs (LH) theories (see e.g. [329, 330, 331, 332]) and Composite Higgs (CH) models (for recent reviews see e.g. [333, 334]). In these theories, the Higgs is a pseudo-Nambu-Goldstone-boson (PNGB) of a larger symmetry that is collectively broken, ensuring the cancellation of one-loop quadratic divergences. This is a different symmetry realization than spin-0 that ensures the cancellation in Eq. (6.2.4), and thus the diagrammatic cancelation also is different in the low-energy effective field theory (EFT). For fermionic top partners, the cancelation occurs because of a higher-dimension interaction between the top-partner and Higgs, unlike the spin-statistics cancellation with renormalizable terms for spin-0. For instance, if the fermionic top partner, T, is a singlet under $SU(2)$, one can add a dimension-five operator h^2TT^c in addition to the allowed renormalizable interactions. Diagramatically a cancellation can occur as shown in Fig. 6.2. The collective symmetry breaking ensures the couplings of the various terms are appropriately related to preserve the cancelation. Since the Higgs is realized as a PNGB it can be parametrized by an EFT expansion with the Higgs field residing in a nonlinear-sigma-model (NLSM) field and an expansion scale f with cutoff $\Lambda \sim 4\pi f$.

Rather than investigating a complete model, we focus on the physics of the fermionic top partner's cancellation of quadratic divergences. We start with the simplest spin-1/2 top partner extension, a singlet fermionic top partner, T under the EW gauge group. The Lagrangian of the top sector takes the form,

$$\mathcal{L}_{\text{top}} = (T, t)\, M \begin{pmatrix} T^c \\ t^c \end{pmatrix} + \text{h.c.}\,, \tag{6.5.51}$$

where M is a 2×2 mixing matrix of the top/top-partner, and t^c and T^c are the right-handed top/top-partner conjugates. We assign t and t^c with $SU(2)_L$ charge $(t, t^c) = (\mathbf{2}, \mathbf{1})$ as in the SM. The top Lagrangian, before EWSB, in the mass eigenbasis up to $\mathcal{O}(1/f^2)$ is then restricted to be

$$\mathcal{L}_{\text{top}} = (T, t) \begin{pmatrix} M_1 - aH^2/f & -bH^2/f \\ c\,(H - c'H^2/f^2) & dH\,(1 - d'H^2/f^2) \end{pmatrix} \begin{pmatrix} T^c \\ t^c \end{pmatrix} + \text{h.c.}\,, \tag{6.5.52}$$

where $\{a, b, c, d, c', d'\}$ are dimensionless real coefficients obtained from the expansion of a NLSM field and M_1 is a bare mass that can exist for singlets. H^2 is the shorthand notation for $H^\dagger H$. The mass matrix given in Eq. (6.5.52) shows that T is massive and t remains massless before EWSB. The cancellation of diagrams in Fig. 6.2 requires the following relationship to be satisfied

$$2aM_1/f = c^2 + d^2\,. \tag{6.5.53}$$

After EWSB, H gets a VEV, which generates additional mixing in the top/top-partner sector, requiring further rotation to switch to the mass eigenbasis. This gives electroweak-scale masses to the top partner and top of

$$m_T = M_1 \left[1 - \frac{v^2}{f^2}\left(\frac{f^2}{M_1^2}\right)\frac{d^2}{2} + \mathcal{O}\left(\frac{v^4}{f^4}\right)\right], \quad m_t = vd\left[1 + \frac{v^2}{f^2}\frac{\epsilon_t}{2} + \mathcal{O}\left(\frac{v^4}{f^4}\right)\right] \tag{6.5.54}$$

with $\epsilon_t = \left[-4a^2c^2d + 4abc(c^2 + d^2) + 2d^2d'(c^2 + d^2)^2\right]/(c^2+d^2)^2$. In the limit of a heavy top/top-partner, $\mathcal{N}_T$ defined in Eq. (6.3.13) is given by

$$\mathcal{N}_T = -\frac{m_t^2}{m_T^2}\,, \tag{6.5.55}$$

up to $\mathcal{O}(v^2/f^2)$ corrections. The relation is very similar to the degenerate stop case in Eq. (6.5.42). Furthermore this is a negative-definite quantity. Given a lower limit on $\mathcal{N}_T$ ($-1 < \mathcal{N}_T < 0$) from Higgs precision measurements, we can use Eq. (6.5.55) to constrain m_T.

Concrete models: Little Higgs models with one Higgs doublet

Two classes of concrete LH models exist in literature: the Simplest Little Higgs (SLH) models [331, 335, 332] and the Littlest Little Higgs (LLH) models [329, 330]. In the $SU(3)$ SLH and the $SU(5)$ LLH, there is only a single Higgs doublet. A generic feature of these models is that $r_t \leq 1$. Since we need to have $r_t > 1$ to compensate for the negative definite $\mathcal{N}_T$, constraints on top partners from Higgs precision data cannot be weakened by adjusting r_t.

Concrete models: Little Higgs models with two Higgs doublets

If the Higgs sector is extended to a 2HDM, as in the $SU(4)$ SLH model, then $r_t > 1$ is possible. In contrast to the MSSM case, we can explore also other types of 2HDM, but these cannot weaken appreciably constraints on top partners. For type-III (lepton-specific), this limitation is due to the restriction $r_t = r_b$, so that a precise measurement of $hb\bar{b}$, which restricts r_b, also indirectly constrains r_t. For type-IV (flipped), a similar limitation arises from $r_t = r_\tau$. For type-I, both limitations exist. For type-II models, there is no restriction between r_t and r_b or r_τ. It can be tuned independently and hence is helpful to hide the top partner. In all these cases, it is important to note that $r_t = r_c$, which results in competitive indirect constraints on r_t through a precise measurement of r_c at future lepton colliders. In the sections below, we will focus on LH with type-II 2HDM.

Top-partners with additional resonances

The generic prediction of $r_t < 1$ is tied to the NLSM nature of the Higgs fields, however this is just a low-energy EFT description. In principle one could imagine that a strongly coupled UV complete description of the theory contained additional resonances similar to QCD where the Higgs as “pions" would come along with the ρ mesons and other resonances. The Yukawa coupling of the top-quark to the Higgs in this low-energy EFT theory should then be thought of as an effective form factor. Similar to QCD if these additional resonances were introduced they could come with different signs and change the generic relation of $r_t < 1$. However, this is not a standard prediction of the low-energy theory and would require a more complete model [336] to investigate the constraints. Nevertheless, this is an interesting model building direction for the near future given it is the strongest avenue for maintaining naturalness in the basic top-partner sector.

Extended fermionic top partners sectors

Another promising direction for naturalness in fermionic top partner models is to extend this sector itself with additional top partners. The Lagrangian in Eq. (6.5.51) can be extended trivially to multiple top partners with degenerate top-partner masses and couplings.[9] We investigate now the effects of non-degeneracy in masses and couplings in the case of two spin-1/2 top partners. For this case, we consider the mass matrix to the same order in $1/f$ given by

$$M = \begin{pmatrix} M_1 - a_{11}H^2/f & 0 & 0 \\ 0 & M_2 - a_{22}H^2/f & 0 \\ 0 & 0 & a_{33}H \end{pmatrix} , \tag{6.5.56}$$

where again the a's are dimensionless coefficients from a NLSM field expansion as before. In general off-diagonal terms would also be present and require a symmetry to be forbidden. This generality would cause increased mixing between the SM top and top-partners making our choice more conservative.

The cancellation of Higgs mass loops requires the relation

$$2(M_1 a_{11} + M_2 a_{22}) = f a_{33}^2 , \tag{6.5.57}$$

and consequently the total contribution from top partners to hgg is given by

$$\mathcal{N}_T = -m_t^2 \left(\frac{\rho}{m_{T_1}^2} + \frac{1-\rho}{m_{T_2}^2} \right) , \tag{6.5.58}$$

where

$$\rho \equiv \frac{2M_1 a_{11}}{f a_{33}^2} \tag{6.5.59}$$

defines the “fraction" of the cancellation coming from the T_1 loop. It is interesting to note that for $\rho > 1$, T_2 and the SM t yield the same-sign contribution to the quadratic divergence of Higgs mass,

---

[9] If N top partners have identical masses and Higgs couplings, g_{hTT}, the product $N g_{hTT}$ needs to be kept invariant to cancel the Higgs mass loop. The same factor occurs inside the gluon fusion loop and therefore all our arguments in the previous section remain valid.

which is cancelled entirely by T_1. This scenario, if realizable in a complete model, would allow for tuning r_G to the SM value without affecting other Higgs precision data. This happens when

$$\frac{\rho}{m_{T_1}^2} = -\frac{1-\rho}{m_{T_2}^2}, \tag{6.5.60}$$

for ρ in Eq. (6.5.58). This allows for a stealth region to avoid Higgs precision measurement, which is unavailable with a single spin-1/2 top partner, and is reminiscent of the stop blind spot. However, unlike the stop blind spot, the parameter space that is open at low masses for spin-1/2 top partners is very small (see Section 6.6.3). We thus do not explicitly investigate if Higgs decays to spin-1/2 top partners can constrain it further. Instead, we investigate in Appendix B how future precision measurements of the Zh cross section can probe the stealth region.

6.5.3 Spin-1

For a spin-1 top partner, the cancellation between the top and its partner again relies on the two being in the same multiplet of a larger symmetry. As in the case of the spin-0 top partner, the only symmetry that can do this is SUSY [337]. However, this immediately presents a challenge: the top lives in a vector multiplet as a “gaugino", which should be in a real representations of a gauge symmtetry. Ref. [338] proposes a way around: the gauge symmetry is enlarged beyond the SM and broken in a way such that the heavy gauge bosons transform in other representations of the residual unbroken SM symmetries. The original Cai-Cheng-Terning (CCT) model [338] includes a breaking of $SU(5) \to SU(3) \times SU(2) \times U(1)$.[10] This generates massive X, Y gauge bosons that can be identified as the spin-1 partners of the left-handed top.[11] This in turn requires the left-handed top to be a gaugino of the enlarged gauge symmetry.

The structure of a spin-1 top partner makes the connection between Higgs precision and colored naturalness more tenuous because many other particles must be introduced to generate the correct

---

[10] Not to be confused with the SM symmetries, which result from a subsequent symmetry breaking step when mixed with other gauge groups.

[11] The usual problems of X, Y gauge bosons are avoided because this model is not solely an $SU(5)$ and the gauge symmetry has to be enlarged.

interactions. For instance, the $ht\bar{t}$ interaction must arise from a gaugino interaction of the form

$$g\lambda^a \phi^* T^a \psi \,. \tag{6.5.61}$$

This in turn requires: (1) the Higgs must be inside a representation of the larger gauge symmetry and (2) the Higgsino needs to be identified as the right-handed top to generate a Yukawa type SM interaction. This then dictates that the gauge coupling of the enlarged gauge symmetry is identified with the top Yukawa coupling. Those requirements necessarily introduce other interactions that contribute to the Higgs mass tuning. In [338], the Higgsino partners in the multiplet of the top-quark and the gauge bosons of the $SU(2)$ give a quadratic contribution to the Higgs potential proportional to the top Yukawa and their masses.

Nevertheless, it is still meaningful to ask what is the correction to the Higgs couplings from a spin-1 top partner alone, as for instance in [294]. Determining this will give us a conservative lower estimate on tuning as there is necessarily additional large tuning coming from the same interaction term but with particles not included here.[12] Keeping this in mind, we investigate a particular implementation, the CCT model [338, 294]. In this model, the symmetry group in the UV is $SU(5) \times SU(3) \times SU(2) \times U(1)_H \times U(1)_V$. We refer the detailed description of the field content to [338]. The relevant terms in the Lagrangian that lead to Higgs coupling are,

$$\mathcal{L} \supset |D_\mu \bar{H}|^2 + \sqrt{2}\hat{g}_5 \bar{H}^* T^a \lambda_a \widetilde{\bar{H}} \,, \tag{6.5.62}$$

where $D_\mu = d_\mu - i\hat{g}_5 A^a_\mu T_a$, $\bar{H} = (t_R, H_d)$, $\tilde{H} = (\tilde{t}_R, \tilde{H}_d)^T$, and λ^a are gauginos corresponding to the broken $SU(5)$. After the UV symmetry group breaks to the SM gauge groups, we are left with multiple heavy gauge bosons (and gauginos), which consist of heavy gluons G', $\vec{Q}$ are top-partners transforming like the SM left-handed top, heavy $SU(2)$ gauge boson W', and $U(1)$ gauge bosons, B' and B''. For Higgs precision studies, it turns out that *only* $\vec{Q}$ and W' are relevant. Their color and electrical charge are $(N_{c,\vec{Q}}, Q_{\vec{Q}}) = (3, 2/3)$ and $(N_{c,W'}, Q_{W'}) = (1, 1)$. After EWSB, we get the Higgs from $H_d = (0, (v_d + h)/\sqrt{2})^T$ (note that it is a down-type Higgs doublet H_d, not a

---

[12] This can be contrasted to the spin-0 or spin-1/2 scenarios, where additional tunings to the Higgs mass exist other than from the top partners, but they are controlled by other interactions.

up-type Higgs doublet H_u as in a spin-0 model). The relevant Lagrangian is

$$\mathcal{L} \supset \frac{1}{2}\hat{g}_5^2 h^2 \vec{Q}^2 + \frac{1}{2}\hat{g}_5^2 h^2 W'^{+} W'^{-} + \hat{g}_5 h t_R t_R^* + \text{h.c.}\,, \tag{6.5.63}$$

where $\hat{g}_5 h t_R t_R^*$ is identified with the top Yukawa, and hence $r_t = \hat{g}_5 \approx \sqrt{1+\tan^2\beta} > 1$. The $h^2\vec{Q}^2$ interaction modifies both hgg and $h\gamma\gamma$ couplings, while $h^2 W'^{+} W'^{-}$ affects only the latter. In principle, $m_{\vec{Q}}$ and $m_{W'}$ are uncorrelated. However, they should be around the same energy scale due to the their common origin. For simplicity, we enforce $m_{\vec{Q}} = m_{W'}$ in our fits. For $\mathcal{N}_{\vec{Q}}$ in Eq. (6.3.13), we obtain

$$\mathcal{N}_{\vec{Q}} = -\frac{1}{\cos\beta}\frac{21}{4}\frac{m_t^2}{m_Q^2}\,, \tag{6.5.64}$$

where $\tan\beta$ is the usual MSSM VEV ratio. The large $21/4$ prefactor in Eq. (6.5.64) comes from the spin-1 loop function, see Appendix C. Therefore, there are stricter limits on vector top partners compared to other top partners. While novel, this model requires a plethora of additional particles resulting in tuning penalties as well as large deviations in Higgs phenomenology. For this reason, we do not investigate further extensions.

6.6 Results and Discussions

In this section, we present the exclusion limits for various top-partner scenarios and their extensions. We derive current and projected bounds on top-partner masses by first considering the minimal case in which all Higgs-couplings are SM-like except that the top partners (and bottom partners, if present) can contribute to the hgg and $h\gamma\gamma$ loops, i.e. they affect r_G and r_γ; moreover, we include Higgs decays to top partners (and bottom partners) when allowed. We then additionally modify other Higgs couplings from their SM values, and numerically evaluate which modifications are most effective at hiding the top partners from Higgs precision studies. Finally, we consider constraints and projections for canonical models (like the MSSM) and extensions.

As discussed in Section 6.4, we use the existing results from the LHC and Tevatron to derive the current constraints, and we derive projected sensitivities based on projected Higgs coupling measurements at the future LHC Runs 3 and 4, the proposed electron-positron colliders ILC, CEPC, and FCC-ee, and the proposed proton-proton collider FCC-hh.

6.6.1 Constraints on top partners that only affect $hgg, h\gamma\gamma$ loops

Spin-0

We begin with the spin-0 scenario discussed in Section 6.5.1. Recall that we assume that there are two spin-0 particles, which we call stops, $\tilde{t}_1$ and $\tilde{t}_2$ and a light left-handed sbottom $\tilde{b}_1$; any other partner particles have been decoupled. (This limit is similar to the natural SUSY limit, although we do not include Higgsinos.) The stop mass eigenstate $\tilde{t}_1$ is mostly left-handed (i.e., $m_{\tilde{t}_1}$ contains mostly m_{Q_3}), while $\tilde{t}_2$ is mostly right-handed (i.e., $m_{\tilde{t}_2}$ contains mostly m_{U_3}).

We first assume that the top partners are the only BSM contributions to the Higgs couplings r_G and r_γ, and can contribute to r_{exo} through possible exotic Higgs decay to stops and sbottoms. The other Higgs couplings are fixed to their SM values, i.e., $r_t = r_b = r_\tau = r_V = 1$ and $r_{\text{inv}} = \delta r_\gamma = \delta r_G = 0$. The χ^2-function in Eq. (6.4.23) is then only a function of $\mathcal{N}_{\hat{t}}$ (Eq. (6.3.13) or Eq. (6.5.36)), $\Gamma_{\text{tot}}(h \to \tilde{t}\tilde{t})$ (Eq. (6.5.38)), and, possibly, $\Gamma(h \to \tilde{b}_1\tilde{b}_1)$. To calculate the excluded parameter space in the $m_{\tilde{t}_2}$ versus $m_{\tilde{t}_1}$ plane, we proceed as follows. First, we fix $\tan\beta$. Then for a given value of $m_{\tilde{t}_1}$ and $m_{\tilde{t}_2}$, we let X_t take on values from 0 up to $X_t^{\max}$ in Eq. (6.5.28). For each value of X_t, we calculate $g_{h\tilde{t}_1\tilde{t}_1}$, $g_{h\tilde{t}_1\tilde{t}_2}$, $g_{h\tilde{t}_2\tilde{t}_2}$, $g_{h\tilde{b}_1\tilde{b}_1}$, $m_{\tilde{b}_1}$, with which we then calculate $\mathcal{N}_{\tilde{t}}$, $\mathcal{N}_{\tilde{b}}$, $\Gamma_{\text{tot}}(h \to \tilde{t}\tilde{t})$, $\Gamma(h \to \tilde{b}_1\tilde{b}_1)$, and check that $m_{\tilde{b}_1}$ is real. This determines r_G, r_γ, and r_{exo}, which are used, together with the Higgs precision data described in Section 6.4, as inputs to the χ^2-fitting procedure. If no value of X_t can be found for which the χ^2 is satisfactory, the chosen $m_{\tilde{t}_1}$ and $m_{\tilde{t}_2}$ values are disfavored.

In Fig. 6.3 we show the resulting excluded parameter space (dark gray region) from current LHC and Tevatron data. The expected sensitivity from the current data is shown in light gray, while the expected sensitivities from future collider data is shown in various colors. We consider two choices for $\tan\beta$ that are representative of the possible range for the phenomenology: Fig. 6.3 (left) shows the constraints without any sbottom contribution (i.e. $\tan\beta \simeq 1$, $g_{h\tilde{b}_1\tilde{b}_1} = 0$, Eq. (6.5.47)), while Fig. 6.3 (right) shows the constraints when sbottom contributions are included (i.e. large $\tan\beta$, with $g_{h\tilde{b}_1\tilde{b}_1}$ given by the D-term contribution, Eq. (6.5.48)). Note that even for the left plot, although we set $g_{h\tilde{b}_1\tilde{b}_1} = 0$, we require that the choice of stop-sector masses and mixing allow the left-handed sbottom to be real, see Eq. (6.5.45).

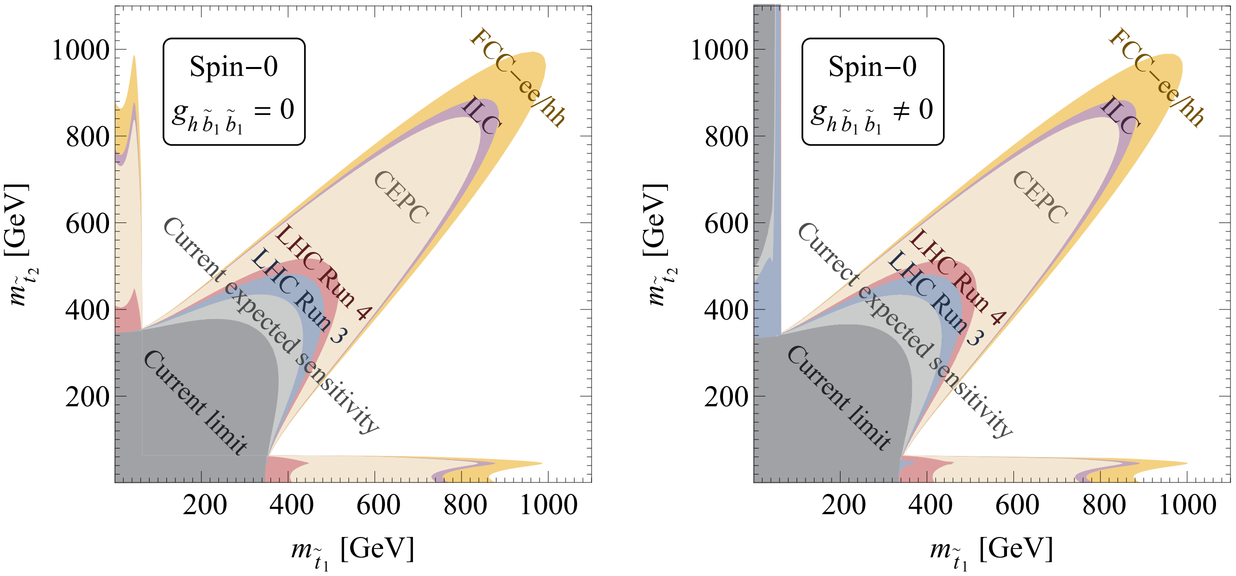

Figure 6.3: Excluded parameter space and expected sensitivities at the 2σ CL of current (gray) and future data (various colors) for spin-0 top-partners in the $m_{\tilde{t}_2}$ versus $m_{\tilde{t}_1}$ plane. In the *left* plot, we assume $\tan\beta \simeq 1$ and $h\tilde{b}_1\tilde{b}_1$ coupling vanishes (Eq. (6.5.47)), while in the *right* plot, $\tan\beta$ is large to maximize the D-term contributions in the stop and sbottom sector (Eq. (6.5.48)). We assume that top partners are the only BSM contributions to the Higgs couplings and can contribute to exotic Higgs decay through $h \to \tilde{t}\tilde{t}$ and, possibly, $h \to \tilde{b}_1\tilde{b}_1$. The other Higgs couplings are fixed to their SM values. For both plots, we require $m_{\tilde{b}_1}$ to be real in the allowed region.

As anticipated in Section 6.5.1, the lower bounds on the masses are strongest for $m_{\tilde{t}_1} = m_{\tilde{t}_2}$ and weaker for split masses. The constraints and projections along the degenerate direction for high masses arise dominantly from the presence of the two stops in the hgg and $h\gamma\gamma$ loops. Comparing the two plots in this region, we see that the D-term contribution in the stop mass matrix Eq. (6.5.25) and in the Higgs-stop-stop couplings Eqs. (6.5.29)–(6.5.31), as well as including the sbottom contribution, only slightly extends the constraints and projections at the $\mathcal{O}(1\%)$ level. When one of the stops becomes lighter than half the Higgs mass, constraints arise from $h \to \tilde{t}\tilde{t}$ (left plot) and from $h \to \tilde{t}\tilde{t}$ and $h \to \tilde{b}_1\tilde{b}_1$ (right plot). If one of the stops becomes heavy, the coupling of the Higgs to the lighter stop with mass below $m_h/2$ becomes small and the Higgs decay to the lighter stop vanishes. However, in the presence of a light left-handed sbottom (corresponding to a light

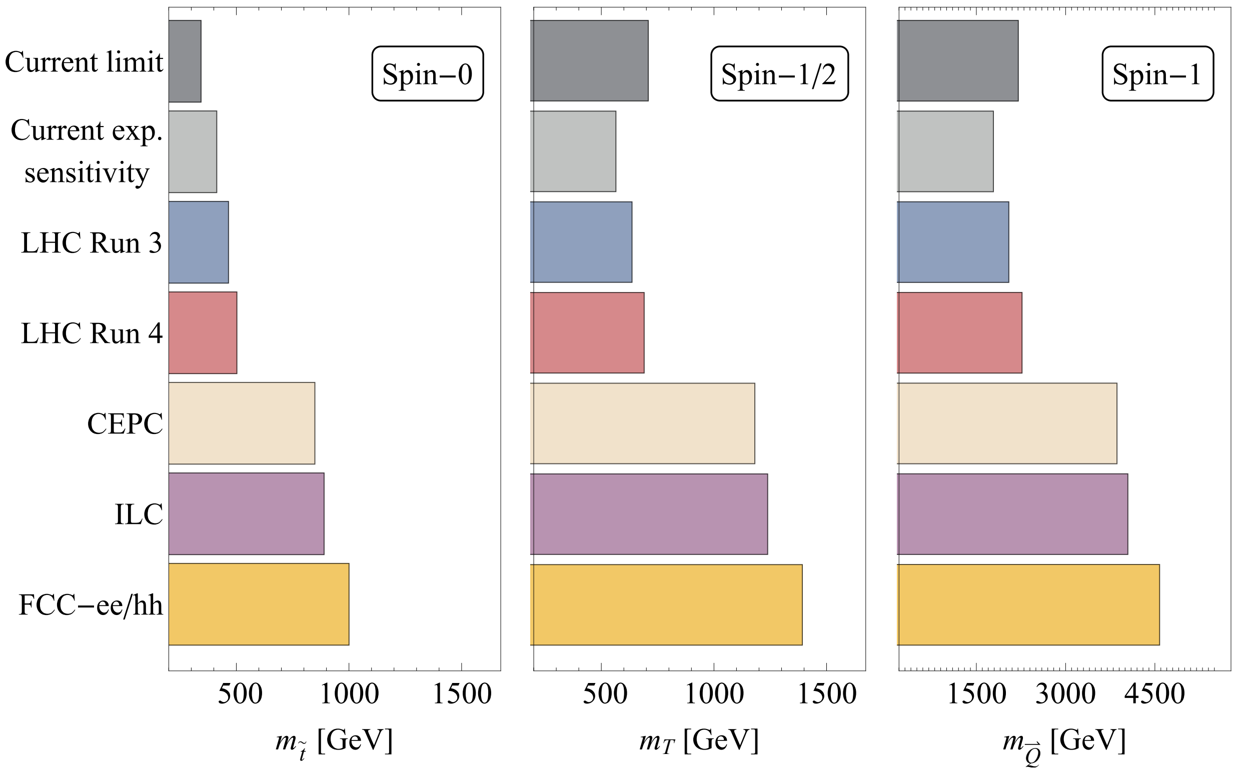

Figure 6.4: Excluded parameter space and expected sensitivities at the 2σ CL of current and future data for spin-0 (left), spin-1/2 (middle), and spin-1 (right) top-partners. We assume that the two spin-0 top partners are degenerate in mass, $m_{\tilde{t}_1} = m_{\tilde{t}_2} \equiv m_{\tilde{t}}$. We assume that top partners contribute only in the hgg and $h\gamma\gamma$ loops, there are no modifications of the Higgs couplings to other SM particles, and there are no exotic or invisible Higgs decays. The parameter space excluded by current LHC and Tevatron data is shown in dark gray, while the expected sensitivity of the current data is shown in light gray. Future LHC runs and the proposed future colliders (ILC, CEPC, and FCC-ee/hh) are shown in various colors.

left-handed stop, $\tilde{t}_1$), the Higgs decay width to sbottoms is large; while the current data is unable to rule out the $m_{\tilde{t}_2} < m_h/2$ region entirely, future LHC Run 3 data can sufficiently constrain exotic Higgs decays to probe this region completely.

Comparison of Constraints between Spin-0, Spin-1/2, and Spin-1

To compare constraints on spin-0 particles with constraints on spin-1/2 and spin-1, we focus on the degenerate direction for spin-0 ($m_{\tilde{t}_1} = m_{\tilde{t}_2}$), because our canonical spin-1/2 and spin-1 models only have a single top partner. Recall that along the high-mass spin-0 degenerate direction, the contributions from the left-handed sbottom and from stop D-terms only matter at a few-percent level. For the remainder of Section 6, we set $g_{h\tilde{b}_1\tilde{b}_1} = 0$, but require that the choice of stop-sector masses and mixing allow the left-handed sbottom to be real, see Section 6.5.1 (note that we include D-term contributions in the stop-sector, i.e., large $\tan\beta$).

In Fig. 6.4 we show the current constraints and expected sensitivities for degenerate spin-0 (left), spin-1/2 (middle), and spin-1 (right) top-partners. The current constraints from Tevatron and LHC data for these different spin-states are about 350 GeV, 700 GeV, and 2.2 TeV, respectively. The LHC Run 4 is expected to improve on these by a few hundred GeV, while the possible future ILC, CEPC, and FCC-ee/hh are expected to improve by another few hundred GeV for spin-1/2 and by almost 2 TeV for spin-1. These projected sensitivities probe similar parameter space to current direct searches, but of course with fewer model assumptions. Due to the current data preferring $r_G > 1$, the current constraints are weaker (stronger) for spin-0 (spin-$\frac{1}{2}$ and spin-1) models compared to their expected sensitivities.

The constraints on spin-1 top partners are much stronger than for spin-0 and spin-1/2 states. The tuning from the spin-1 state alone is already significant given that the current limit on the top-partner mass is already approaching 2 TeV. Moreover, as discussed in Section 6.5.3, a contribution to the tuning should be included from the other scalars and vectors that are required in spin-1 top-partner models. We will thus not consider spin-1 top partners further, focusing instead on how best to hide spin-0 and spin-1/2 partners from Higgs precision measurements.

6.6.2 Constraints on top-partners with modified SM Higgs couplings

In addition to the top-partners contributing to the hgg and $h\gamma\gamma$ loops, the Higgs couplings to SM particles could also be modified from their SM values. In this section, we numerically quantify which modifications are most efficient at absorbing the top-partner-loop contributions. We allow

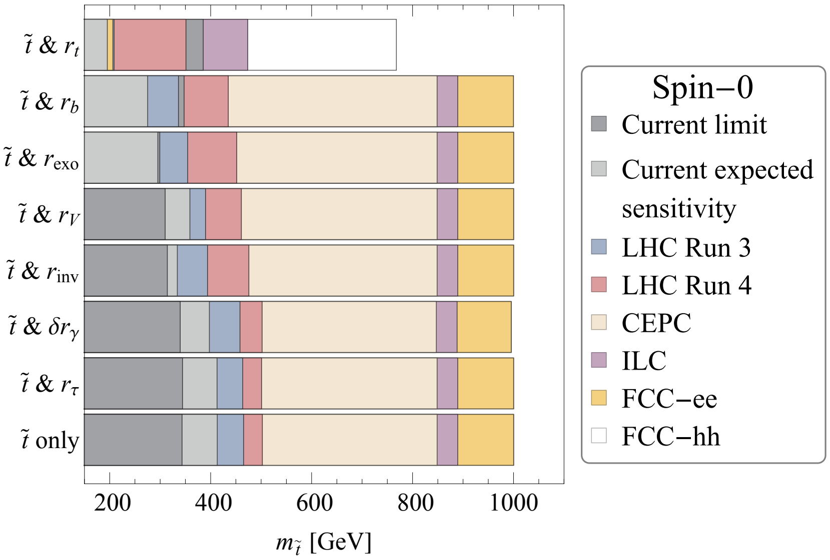

Figure 6.5: Excluded parameter space and expected sensitivities at the 2σ C.L. on degenerate spin-0 top partner masses, $m_{\tilde{t}_1} = m_{\tilde{t}_2} \equiv m_{\tilde{t}}$, from various joint-fits of current and future data. We assume here that in addition to top partners contributing in the hgg and $h\gamma\gamma$ loops, there is one additional modification to the couplings as indicated by the description on the left axis; for example, for "$\tilde{t}$ & r_t", the top-partner contributes to the hgg and $h\gamma\gamma$ loops and r_t is allowed to vary from its SM value, while all other r_j are fixed to their SM value. Note that the current limit shaded in dark gray is naively stronger for "$\tilde{t}$ & r_t" and "$\tilde{t}$ & r_b" than the expected sensitivity of the future LHC Run 3 and/or Run 4 data (see text for details).

for one Higgs coupling, $r_i \in \{r_t, r_b, r_\tau, r_V, r_{\text{exo}}, r_{\text{inv}}, \delta r_\gamma\}$, to differ from its SM value, while fixing all other couplings to their SM values. To obtain the 2σ CL regions for the top-partner masses, we adjust their masses, while marginalizing over r_i, until their contributions to hgg and $h\gamma\gamma$ expressed in terms of the variable $\mathcal{N}_{\hat{t}}$ in Eq. (6.3.13) gives the appropriate $\Delta\chi^2$.

The results for spin-0 and spin-1/2 scenarios are shown in Fig. 6.5 and Fig. 6.6, respectively. Not surprisingly, the additional degree of freedom helps in reducing the current top-partner bounds and projected sensitivities. As anticipated in Section 6.3, allowing for a non-SM $ht\bar{t}$ coupling is currently the best way to hide a top partner. Future LHC, ILC, and FCC-hh data will measure $ht\bar{t}$ production precisely improve constraints on top parters.

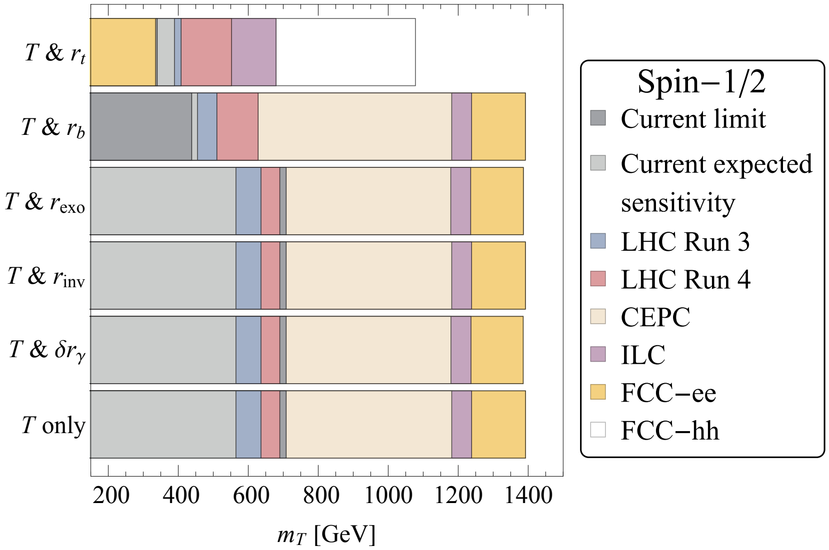

Figure 6.6: Similar to Fig. 6.5, but here showing excluded parameter space and expected sensitivities at the 2σ C.L. on spin-1/2 top partner mass, m_T, from various joint-fits of current and future data.

For the spin-0 "$\tilde{t}$ & r_t" and "$\tilde{t}$ & r_b" scenario (see Fig. 6.5), the current data naively excludes larger degenerate stop masses than the expected sensitivity of the data from the LHC Run 3 and Run 4. This is because some of the current Higgs data prefers $r_t = 1.18$ and $r_b = 0.89$ that are far away from 1. Given Eq. (6.3.14), i.e.,

$$r_G = 1.05 r_t (1 + \mathcal{N}_{\tilde{t}}) + (-0.05 + 0.07i) r_b, \tag{6.6.65}$$

a negative $(\mathcal{N}_{\tilde{t}})^{\rm fit}$ is favored to remove $r_t > 1$ or $r_b < 1$. We find that the 2σ CL upper limit, $(\mathcal{N}_{\tilde{t}})^{\rm fit;max}$, while not negative, is a small positive number. This leads to a relatively large bound on degenerate stop mass compared to the LHC Run 4 and Run 4 expected sensitivities, which, by definition, assume a measured $r_t = r_b = 1$. It is thus better to compare future expected sensitivities to the current expected sensitivity indicated by the light-gray shaded region. We note that the current limit is weaker than the current expected sensitivity for the spin-1/2 "T & r_t" scenario. This is because $\mathcal{N}_T$ is negative-definite from LH theories ($\mathcal{N}_T = -m_t^2/m_T^2$), and a smaller m_T is preferred to cancel $r_t > 1$ or $r_b < 1$.

Besides varying the $ht\bar{t}$ coupling, varying the $hb\bar{b}$ coupling is the second most effective way to hide both spin-0 and spin-1/2 top partners. Exotic Higgs decays, invisible Higgs decays, and hVV also help to hide top-partners for the spin-0 scenario, although to a lesser extent than varying either r_t or r_b. For the spin-1/2 scenario, exotic or invisible decays do not help. The reason is that spin-1/2 top partners can only suppress the hgg coupling, with exotic or invisible decays suppressing the signal strength further. For spin-0 partners, the hgg coupling can also be enhanced, in which case additional non-standard Higgs decay modes help hide the partners. Finally particles contributing to $h\gamma\gamma$, or non-SM $h\tau^+\tau^-$ decays, barely help to hide the spin-0 top partners.

Nevertheless, as seen in Fig. 6.5 and Fig. 6.6, those hiding methods are no longer effective for future colliders. Generally speaking, future colliders can measure precisely the $hb\bar{b}$ and hVV couplings as well as the invisible and exotic Higgs-decay width. Therefore the modifications to SM Higgs couplings are very constrained, and the exclusion limits on top-partner masses are almost identical to the top-partner only cases.

Allowing several Higgs couplings to vary simultaneously would further weaken current constraints, but the effect would still be dominated by r_t. We thus consider concrete models next.

6.6.3 Constraints on canonical models and extensions

Spin-0 top partners in the MSSM

We consider now constraints on stops in the context of the MSSM. We have seen that allowing $r_t < 1$, i.e. lowering the $ht\bar{t}$-coupling, currently provides the best way to hide spin-0 top partners. In the MSSM, we can lower r_t by lowering $\tan\beta$. However, this forces r_b, r_τ, and r_V to vary in a correlated way, see Eq. (6.5.50). Since these parameters are well-constrained by current and expected future data, it is more difficult to hide stops in the MSSM than in models in which only r_t is being varied. We also note that we set $r_t = r_c$, so that future measurements of r_c indirectly constrain r_t.

We show in Fig. 6.7 the constraints on the two stop-mass eigenstates in the MSSM, setting $\tan\beta = 10$. We see again that the constraint is much stronger for degenerate stop masses compared to the case with large stop mixing, and more generally is very similar to the case in which only the top-partner contributions to the hgg and $h\gamma\gamma$ loops are included, see Fig. 6.3 (left). Note that like

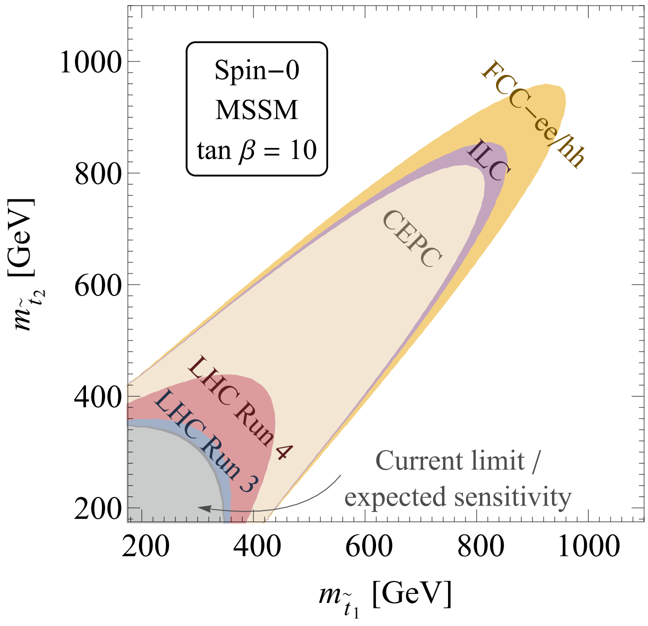

Figure 6.7: Excluded parameter space and projected expected sensitivities at the 2σ C.L. of current and future data, respectively, for stops in the MSSM in the $m_{\tilde{t}_2}$ versus $m_{\tilde{t}_1}$ plane. The parameter space formally excluded by current LHC and Tevatron data is shown in dark gray. It mostly overlaps with the current expected sensitivity in light gray. Future LHC runs and the proposed future colliders (ILC, CEPC, and FCC-ee/hh) are shown in various colors.

in Fig. 6.3 (left), we set the sbottom-sbottom-Higgs coupling to zero, but ensure that the sbottom mass is real. The anomalously strong current limits (dark gray) are due to the current data favoring a minimum with $r_b < 1$; this is for the same reason as discussed in Section 6.6.2 and seen in Fig. 6.5.

In Fig. 6.8, we show current constraints and projected sensitivities on stops in the MSSM for various $\tan\beta$. Note that the constraints are significantly stronger compared to “$\tilde{t}$ & r_t" mostly due to the $r_t = r_c$ relation in the MSSM. Furthermore, we clearly see that lower values of $\tan\beta$ provide weaker projected sensitivities. This is because for small $\tan\beta$ we can vary r_t without affecting r_b or r_V, which are measured very well. We cannot lower $\tan\beta$ too much without the top Yukawa reaching a Landau pole near the weak scale.

It is worth comparing the MSSM scenario with $\tan\beta = 10$ in Fig. 6.8 and the “$\tilde{t}$ & r_b" scenario

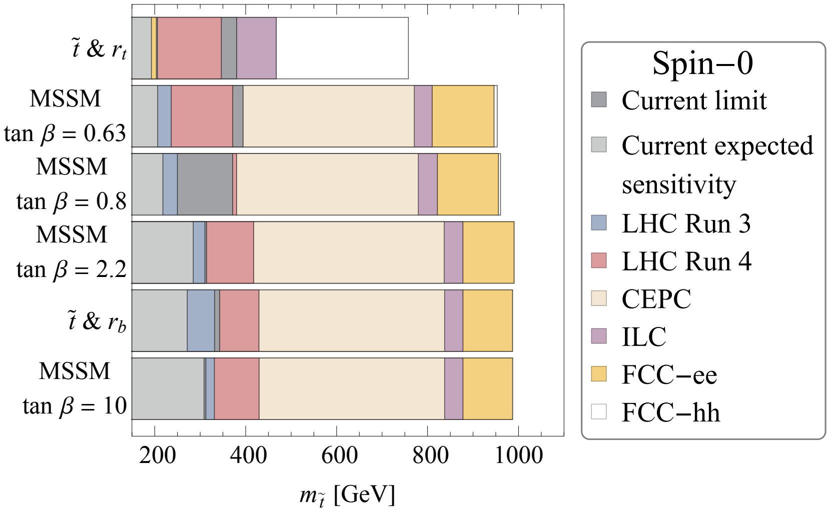

Figure 6.8: Excluded parameter space and expected sensitivities at 2σ C.L. on degenerate spin-0 top partner mass, $m_{\tilde{t}_1} = m_{\tilde{t}_2} \equiv m_{\tilde{t}}$, in the MSSM with various $\tan\beta$ of current and future data. In the plots, we again show the (non-MSSM) "$\tilde{t}$ & r_t" and "$\tilde{t}$ & r_b" results from Fig. 6.5 as a reference. Note that the anomalously strong limits in the "current data" fit (dark gray) are due to the current data favoring a minimum with $r_t > 1$ and $r_b < 1$.

from Fig. 6.5 and repeated in Fig. 6.8. Naively they are very similar given that $\tan\beta$ is large, which fixes $r_t = r_V = 1$, but leaves r_b as free parameter. In the "$\tilde{t}$ & r_b" scenario, r_b is constrained by $hb\bar{b}$ only. In the MSSM scenario, it is additionally restricted by $h\tau^+\tau^-$ measurements due to the type-II 2HDM structure that restricts $r_b = r_\tau$. The current data prefers $r_b < 1$, but the additional restriction $r_b = r_\tau$ together with the current data preferring a value for r_τ just slightly above 1, forces r_b to be closer to 1. This results in weaker exclusions in the MSSM scenario on $m_{\tilde{t}}$. When $r_b = 1$ (as is assumed when calculating the current and future projected sensitivities), the additional restriction is less important when comparing the two scenarios.

Spin-1/2 top partners with one Higgs doublet

In LH models with only a single Higgs doublet, such as the $SU(3)$ SLH and $SU(5)$ LLH models, we have $r_t \leq 1$. As discussed in Section 6.5.2, since $\mathcal{N}_T$ is negative-definite, $r_t < 1$ does not help to hide the top partner compared to what is shown in Fig. 6.6, which marginalizes over all values

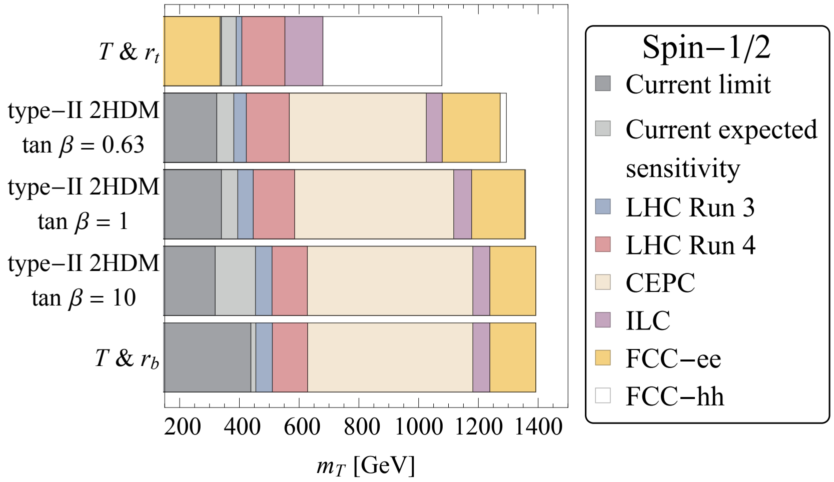

Figure 6.9: Excluded parameter space at 2σ C.L. on spin-1/2 top-partner mass, m_T, in type-II 2HDM with various $\tan\beta$ of current and future data (various colors). In the plots, we again show the (non-2HDM) "T & r_t" and "T & r_b" scenarios from Fig. 6.6 for ease of comparison.

of r_t. These theories thus prefer $r_t = 1$, and Fig. 6.4 shows the resulting constraints on the mass of the top partners up to 1.4 TeV at FCC-ee/hh.

Spin-1/2 top partners in type-II 2HDM

Similarly to the MSSM case in Section 6.6.3, we can now consider spin-1/2 top partners with a Higgs sector given by a 2HDM model (such as the $SU(4)$ SLH). We focus on a 2HDM type-II model, since this allows for the weakest constraints on top partners as discussed in Section 6.5.2. The results are given in Fig. 6.9 for various values of $\tan\beta$. To simplify comparisons with the cases in Section 6.6.2, we again show the results for "T & r_b" and "T & r_t". As for the MSSM case, we see that lower values of $\tan\beta$ help in hiding the spin-1/2 top partners.

Extended spin-1/2 top partner sectors

While the 2HDM presents one concrete way to reduce the sensitivity to spin-1/2 partners from Higgs precision measurements, we can study further improvements by introducing multiple top partners, as discussed in Section 6.5.2. When $\rho \leq 1$ in Eq. (6.5.58), the sensitivity to top partners remains unchanged, see Fig. 6.10 (left), but there is an extra fine-tuning penalty for moving away from the diagonal degenerate region as measured by

$$\delta m_h^2 = \frac{3}{8\pi^2}\left[|\rho| m_{T_1}^2 \log\left(\frac{\Lambda_{\text{Strong}}^2}{m_{T_1}^2}\right) + |1-\rho| m_{T_2}^2 \log\left(\frac{\Lambda_{\text{Strong}}^2}{m_{T_2}^2}\right)\right] . \tag{6.6.66}$$

However, $\rho \geq 1$ allows for a “stealth” scenario, as shown by the gray dashed line in Fig. 6.10 (right) for a fixed choice of ρ. In this case, there is an accidental cancellation to the hgg and $h\gamma\gamma$ loop from the two top partners, which is not constrained by the Higgs precision observables under consideration. However, it is probed by a complementary Higgs precision measurement – the Zh cross section – at future lepton colliders, as we discuss in Appendix A. Nevertheless, the current bounds on this scenario are weak and could thus provide a promising direction for model building, perhaps one in which a symmetry allows for the presence of the “stealth" region with minimal fine-tuning.

6.7 Conclusions

In this paper, we performed a model-agnostic investigation of the limits from Higgs-precision data alone to probe naturalness from the presence of colored top partners. There are many other complementary probes of naturalness, such as direct collider searches, electroweak precision constraints and rare decays. However, while any given test may be avoided in principle through model-building tricks that allow for a “natural" model, it is useful to understand how well any given probe can test colored naturalness. Higgs precision tests are quite robust even on their own, since the couplings involved are inherently tied to the very question of naturalness itself.

We find that with Higgs precision measurements alone, the HL-LHC can constrain spin-0 and spin-1/2 top partners almost to $\mathcal{O}(500)$ GeV in theories where there is only one spin-1/2 top partner or there is minimal mixing between the states. With proposed future lepton and hadron colliders this can be extended to the TeV scale. Spin-1 top partners are generically excluded to the multi-TeV regime. However, we have also identified a number of “blind-spots" where top partners can still be light even if future colliders are realized. In particular, if there is a hierarchy between multiple top partners from mixing of the states, the standard probe using gluon-fusion can be avoided. However,

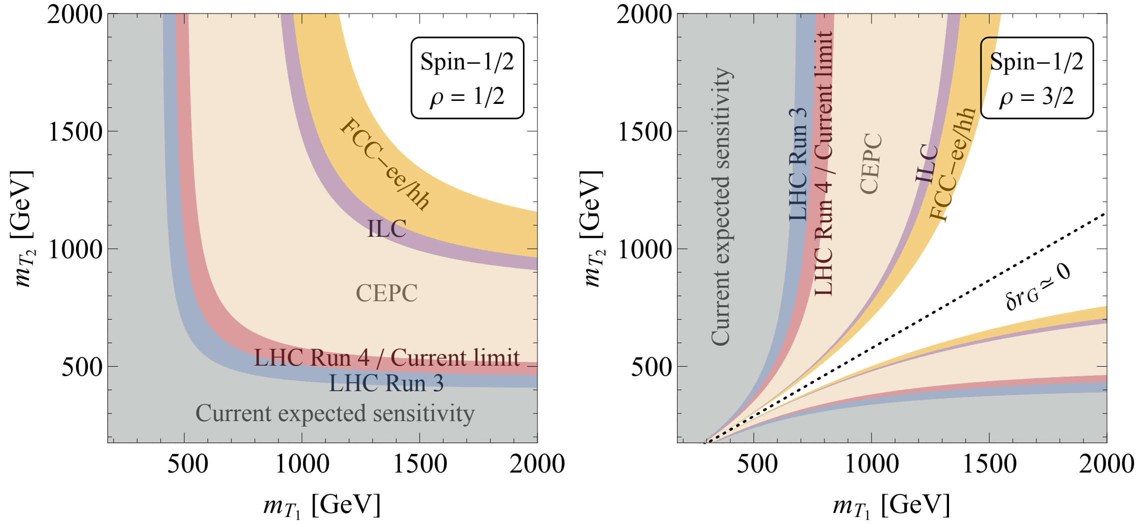

Figure 6.10: Excluded parameter space and expected sensitivities at the 2σ C.L. of current and future data (various colors) for two spin-1/2 top partners in the m_{T_2} versus m_{T_1} plane. The left plot shows the case in which both spin-1/2 top partners contribute equally to canceling the Higgs-mass contribution of the top-quark loop, i.e. $\rho = 1/2$, where ρ is defined in Eq. (6.5.58). In the right plot, T_2 contributes with the same sign as the top-quark to the Higgs mass, but both contributions are cancelled by T_1, $\rho = 3/2$. The latter allows for a "stealth" limit (black dotted line), in which Higgs precision measurements are not sensitive to the presence of spin-1/2 top-partners.

there are still bounds from Higgs precision measurements that are complementary to what is probed by gluon fusion. For instance, in the case of spin-0 top partners, in the extreme limit where one eigenvalue becomes lighter than $m_h/2$, constraints from gluon-fusion Higgs production can still be avoided but there are strong bounds instead from the new contribution to the total width of the Higgs. Nevertheless, there still exist particular points in parameter space that can avoid all Higgs precision measurements, similar to the light-sbottom window [339, 340]. While these blind-spots were known for spin-0 cases, we have extended them to lower masses and included decays, and demonstrated that they can also occur in fermionic top partner models as well. This provides an interesting model building direction, since minimal fermionic top-partner models, such as in Little Higgs theories, are generically in more tension with Higgs precision constraints than their spin-0 counterparts. There are other orthogonal probes that are only relevant in the future, such as radiative shifts in the Zh cross-section, which we discuss in Appendix A. It would also be interesting for very light masses to study the interplay between contributions to the well-measured Z-boson-width and the Higgs properties. We leave this for future work.

Another potential avenue for light colored top partners comes from changes in the couplings of other SM particles or the introduction of new states that couple to the Higgs and affect its width. We have categorized different changes to find what is the best way to still have light colored top partners in light of the current and future data. We find that the most promising direction to relax current constraints through the modification of SM-Higgs couplings is to modify the $ht\bar{t}$ coupling, which can be done in models with extended Higgs sectors. However, the upcoming LHC Runs 3 and 4 and the proposed ILC and FCC-hh projects, which can measure the $ht\bar{t}$ coupling down to 1% level, will extensively probe this possibility.

It remains unclear whether the EW scale is natural. We have shown that future colliders will allow for a robust probe of the parameter space of natural models using Higgs properties alone.

Appendices

Appendix A

Instruction Manual for Optimized Partial Dressing Calculation of Phase Transition

Here we summarize the detailed procedure for obtaining the effective finite-temperature potential $V_{\text{eff}}^{\text{pd}}(h, T)$ as a function of h for a given temperature T in the Optimized Partial Dressing (OPD) scheme. This will be familiar to anyone studying the EWPT in BSM theories, and implementing the OPD calculation in Mathematica is very similar to the familiar TFD calculation, and only $\sim \mathcal{O}(10\%)$ more CPU intensive. We explain this procedure in the context of the SM + $N_S \times S$ benchmark model, but it generalizes easily to other theories with one-step phase transitions. At every point, only use the real parts of various potential contributions or their derivatives. Note that we do not perform this resummation for zero temperature matching and other calculations, since the effect is small.

For a given temperature, we first have to find the thermal mass corrections $\delta m_i^2(h, T)$. For gauge bosons, use the standard $\delta m_i^2 = \Pi_i \sim T^2$, see e.g. Eq. (5.2.24) for the SM contributions. For scalars we have to solve a set of coupled gap equations:

$$\delta m_{\phi_j}^2(h, T) = \sum_i \frac{\partial}{\partial \phi_j} \left[\frac{\partial V_{\text{CW}}^i}{\partial \phi_j} \Big(m_i^2(h) + \delta m_i^2(h, T) \Big) + \frac{\partial V_{\text{th}}^i}{\partial \phi_j} \Big(m_i^2(h) + \delta m_i^2(h, T), T \Big) \right] \tag{A.0.1}$$

See Eqns. (5.2.8) and (5.2.13) for definitions of the Coleman-Weinberg and finite-temperature potential. For the latter, use the high-temperature expansion to log-order in the gap equation, see

Eq. (5.2.15). Note that this makes the RHS a set of fully analytical expressions that can be easily manipulated in Mathematica.

In our specific benchmark model, there are three gap equations: for $j = h, G_0, S_0$. Since we are interested in excursions along the h-axis, all Goldstone thermal masses are the same but different from the physical Higgs mass, and all scalar thermal masses are the same.[1] Note that the sum i also runs over all particles, including fermions and gauge bosons.

We numerically solve this set of gap equations by essentially treating it as a set of partial differential equations. Specifically, set up a coarse grid[2] along the Higgs axis $h = \{0, 10, 20, \ldots, 250\}$. The RHS of the gap equation is a function of thermal masses and their derivatives. Expanding the mass correction around $h = h_a$:

$$\delta m_j^2(h, T) \approx \delta m_{j(a)}^2 + (h - h_a) \frac{\partial \delta m_{j(a)}^2}{\partial h} \tag{A.0.2}$$

and substituting this form of $\delta m_{h,G_0,S}^2$ (as well as the h-independent gauge boson thermal masses) into the RHS yields three gap equations that depend on six parameters: the value of the scalar thermal masses $\delta m_{h(a)}^2, \delta m_{G_0(a)}^2, \delta m_{S(a)}^2$ and their first derivatives $\partial \delta m_{h(a)}^2/\partial h, \partial \delta m_{G_0(a)}^2/\partial h, \partial \delta m_{S(a)}^2/\partial h$.

At the origin, the derivatives are zero, and solving for just the three thermal masses yields a numerically unique set of solutions. Then we work our way away from the origin. The solution at $h = h_a$ can be obtained by first eliminating either the derivatives or the actual thermal masses from the gap equation using the continuity condition

$$\delta m_{j(a-1)}^2 \approx \delta m_{j(a)}^2 + (h_{a-1} - h_a) \frac{\partial \delta m_{j(a)}^2}{\partial h} \tag{A.0.3}$$

given the known solution at $h = h_{a-1}$. We found in practice that eliminating the $\delta m_{j(a)}^2$ and solving for the three derivatives $\partial \delta m_{j(a)}^2/\partial h$ was more reliable. If the solution fails the resolution of the grid may have to be increased, but we found a coarse grid with 10 GeV spacing to be sufficient.[3]

---

[1] If we solved for excursions along the S_0 direction, we would have to treat S_0 and $S_{k>0}$ differently but could treat all Higgs degrees of freedom the same.

[2] To avoid singularities the origin can be defined to be a very small positive displacement instead of identically zero.

[3] The automatic Mathematica functions for differential equation solving failed with these gap equations, possibly by over-interpreting unphysical local singularities or numerical noise. We found our manual implementation to be very simple, fast and reliable.

Once a grid of solutions is obtained, the continuous functions $\delta m_j^2(h,T)$ are defined by linear interpolation. The thermal potential is then defined by

$$V_{\rm eff}^{\rm pd}(h,T) = V_0 + \sum_i \int dh \left[\frac{\partial V_{\rm CW}^i}{\partial h}\Big(m_i^2(h) + \delta m_i^2(h,T)\Big) + \frac{\partial V_{\rm th}^i}{\partial h}\Big(m_i^2(h) + \delta m_i^2(h,T), T\Big)\right] , \tag{A.0.4}$$

where i runs over all scalars, gauge bosons and fermions (with zero thermal mass for the latter). Importantly, in this effective potential, use the piece-wise defined thermal functions

$$\begin{aligned} J_B^{\rm piece-wise}(y^2) &= \begin{cases} J_B^{\rm high-T}(y^2) & \text{for } y^2 \leq 1.22 \\ \tilde{J}_B^{(3)}(y^2) & \text{for } y^2 > 1.22 \end{cases} \\ J_F^{\rm piece-wise}(y^2) &= \begin{cases} J_F^{\rm high-T}(y^2) & \text{for } y^2 \leq 1.29 \\ \tilde{J}_F^{(2)}(y^2) & \text{for } y^2 > 1.29 \end{cases} \end{aligned} \tag{A.0.5}$$

See Eqns. (5.2.15) and (5.2.16) for the definition of the approximate thermal functions. The integrand can then be defined as an analytical function in Mathematica, which can be evaluated on a grid of Higgs values $h = \{0, 5, 10, \ldots, 250\text{GeV}\}$ and interpolated to efficiently perform the integral at arbitrary values of $h < 250\text{GeV}$.

Appendix B

Future Complementary Higgs Precision Probes

In this appendix, we explore two complementary Higgs precision probes, $\sigma(e^+e^- \to Zh)$ and (briefly) $gg \to hh$. These will only be measured with sufficiency precision at future colliders, but could potentially probe different regions of parameter space than $\mathcal{N}_{\hat{t}}$ and $\Gamma_{\hat{t}\hat{t}}$. As was noted in earlier sections, the typically dominant effect on Higgs precision from colored top partners, $\mathcal{N}_{\hat{t}}$, can have “blind spots" if there is more than one top partner. These “blind-spots" have been noticed before, for instance in [326, 283] with reference to colored stops in the natural SUSY paradigm.

The inherent reason for the blind spots comes from the linear dependence on couplings in $\mathcal{N}_{\hat{t}}$, and occurs when

$$\frac{g_{h\tilde{t}_1\tilde{t}_1}}{m^2_{\tilde{t}_1}} = -\frac{g_{h\tilde{t}_2\tilde{t}_2}}{m^2_{\tilde{t}_2}} \tag{B.0.1}$$

for stops and

$$\frac{\rho}{m^2_{T_1}} = -\frac{1-\rho}{m^2_{T_2}} \tag{B.0.2}$$

for multiple fermionic top partners. In both cases, there is a destructive interference between the top-partner loops arising from the relative negative sign between the couplings of the top partners to the Higgs.

Processes that depend quadratically on the Higgs coupling can potentially avoid this blind spot. For instance the contribution to $\Gamma_{\hat{t}\hat{t}}$ for stops discussed in Section 6.5.1 excludes a different region of parameter space than the “blind-spot". However, as we discussed, $\Gamma_{\hat{t}\hat{t}}$ vanishes if one stop is sufficiently heavy, which leads to a new blind-spot. Nevertheless, there are other processes that depend quadraticallly on multiple Higgs couplings and thereby can fill in the $\mathcal{N}_{\hat{t}}$ “blind-spot" more robustly if sufficient precision is achieved. One such example is Higgs WFR [326] from BSM states that cause deviations in tree-level Higgs couplings after canonical normalization. These loop corrections to tree-level couplings are hard to measure, and the first opportunity to detect such deviations would be at future lepton colliders where the Zh coupling can be measured with great precision. The inclusive Higgstrahlung cross section $\sigma(e^+e^- \to Zh)$ can itself be precisely measured to $< 1\%$ level [7, 341], and as a result the Zh coupling can be measured to an order of magnitude better than other Higgs couplings.

The quadratic dependence on Higgs couplings is straightforward to see. For stops in natural SUSY the full WFR including stop-mixing was discussed in [283]. The deviation in the Zh coupling from WFR contributions is

$$\delta\sigma_{\mathrm{Zh}}[\mathrm{WFR}] = \frac{3}{16\pi^2}(g_{h_{11}}^2 + g_{h_{22}}^2 + 2g_{h_{12}}^2) I(m_h^2, m_{\tilde{t}_1}^2, m_{\tilde{t}_2}^2)\,, \tag{B.0.3}$$

where I is the loop function defined in [283], potentially covering the $\mathcal{N}_{\hat{t}}$ “blind-spot". However, in [326] it was pointed out that the WFR contribution can dramatically mis-estimate $\delta\sigma_{Zh}$ and that a full one-loop calculation is instead required. Since other one-loop diagrams contain only one stop-Higgs vertex ($h\tilde{t}_1\tilde{t}_1$ or $h\tilde{t}_2\tilde{t}_2$, but not $h\tilde{t}_1\tilde{t}_2$), there is destructive interference for particular choices of parameters. In particular, [326] considered degenerate soft masses and observed that Higgstrahlung limits overlapped with $gg \to h$ limits.

Here we explore Higgstrahlung probes in the most general stop mass plane (without restricting to degenerate soft masses). We follow the treatment of [326] to calculate $\sigma(e^+e^- \to Zh)$ to include complete one-loop corrections using the `FeynArts 3.9` – `FormCalc 9.4` – `LoopTools 2.13` suite [342].[1] We fix the $\sqrt{s} = 240\mathrm{GeV}$ for all the results displayed here to match with the CEPC/FCC-ee setting. We also test the result with various center-of-mass energies, $\sqrt{s} = 240\mathrm{GeV}$, $250\mathrm{GeV}$, $350\mathrm{GeV}$, and $500\mathrm{GeV}$, and find that the resulting excluded region is the same at the level of a few percent.

---

[1] We thank Matthew McCullough for providing his implementation of Natural SUSY in the FeynArts suite.

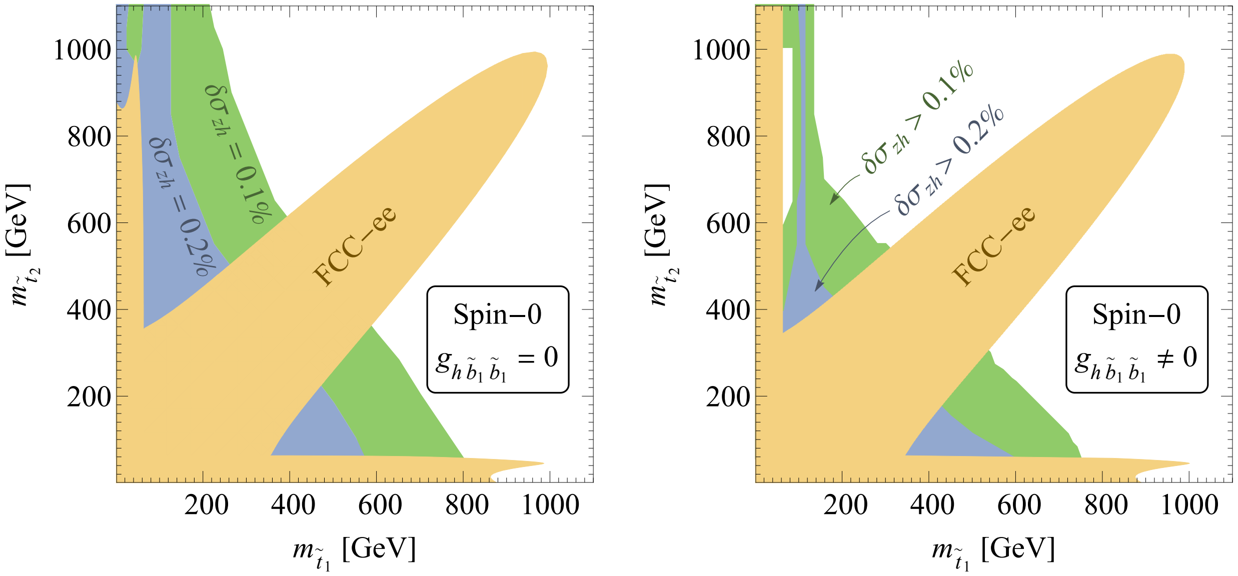

Figure B.1: Expected sensitivities at the 2σ C.L. of FCC-ee for spin-0 models with additional constraints from $\delta\sigma_{Zh}$. In the *left* plot, we assume $\tan\beta \simeq 1$ and $h\tilde{b}_1\tilde{b}_1$ coupling vanishes (Eq. (6.5.47)), while in the *right* plot, $\tan\beta$ is large to maximize the D-term contributions in the stop and sbottom sector (Eq. (6.5.48)).

In Fig. B.1, we show the additional constraints obtained from $\delta\sigma_{Zh}$ compared to the Higgs precision probes included in Fig. 6.3. We find that with $\delta\sigma_{Zh} \geq 0.2\%$ (projected for ILC, CEPC and FCC-ee [5, 7, 6]), we observe additional constraints in the non-degenerate region when $\tan\beta \to 1$. As seen in Fig. B.1, less additional parameter space is constrained when $\tan\beta$ is large. If we were to increase the statistics of the future lepton colliders and improve the measurement on $\delta\sigma_{Zh}$ to 0.1%, we start to probe more of the non-degenerate region in both cases. With 0.1% of data, we can also robustly rule out $m_{\tilde{t}_1} \leq 150\text{GeV}$ in both cases. However, one should note that this is tied to the ansatz that $\tilde{t}_1$ is mostly left-handed in our setup, which fixes the $\tilde{b}_1$ mass. This is also the reason why the limits are not symmetric under the interchange of $\tilde{t}_1$ and $\tilde{t}_2$. It would be interesting to study fully the large-mixing region of small stop- and sbottom-masses in the MSSM to find robust lower bounds.

For fermionic top partners, which we consider to be part of an EFT, we do not implement a full one-loop analysis, as there can be additional dimension-six operators generated at the UV

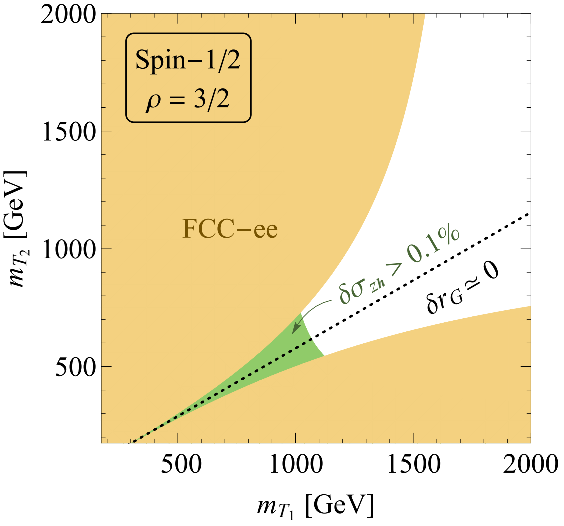

Figure B.2: Expected sensitivities at the 2σ C.L. of FCC-ee for two spin-1/2 top-partner model with additional constraints from $\delta\sigma_{Zh}$. The projected sensitivity from FCC-ee is taken from Fig. 6.10.

scale that could also contribute to the Higgstrahlung cross-section. However, we can still make a conservative estimate of the contribution to the Zh cross section from the top-partners using WFR in the EFT with the assumption that there are no large cancellations between the loop-effects and higher-dimension operators. With this assumption, the deviation in the Zh cross-section, from the the finite contributions to Higgs WFR in the multiple fermionic top partner model in Section 6.5.2, is given by,

$$\delta\sigma_{Zh} = -\frac{m_t^2}{8\pi^2}\left[\frac{\rho^2}{m_{T_1}^2} + \frac{(1-\rho)^2}{m_{T_2}^2}\right]. \tag{B.0.4}$$

We find that the stealth region in the right panel of Fig. 6.10 can be covered to the TeV scale by the measurement of $\delta\sigma_{Zh}$ from future lepton colliders as shown in Fig. B.2. This is a conservative estimate, and the effects would in general be larger unless there was a symmetry or additional tuning of different contributions at the UV scale.

Finally, we briefly comment on di-Higgs production, which also is quadratically sensitive to the Higgs-top-partner coupling. Similar to $gg \to h$, colored top partners contribute to the double Higgs production process, $gg \to hh$, at the loop-level[343]. It contains two Higgs vertices, which can spoil this cancellation, and naively we would expect some coverage of the “blind-spots" by measuring the deviation of $\sigma(gg \to hh)$ from its SM prediction. However, even at future colliders, the total cross section for double-Higgs production is much smaller than single-Higgs production making this a difficult measurement without much discriminating power.

At a 100 TeV hadron collider, with 30 ab^{-1} of data, we can measure this cross section to 1.6% accuracy [1]. However, even so, it is notoriously hard to differentiate between new colored particles in the loop and a change in the triple Higgs coupling [344]. We leave for future work a calculation of the constraints that includes a shape analysis of the m_{hh}^2 spectrum near the light top-partner mass threshold.

Appendix C

Loop-induced Higgs Couplings

The loop functions introduced in Section 6.3 depend on the spin s of the particle and are given by

$$\mathcal{A}^{\mathrm{s}=0}(\tau) = \frac{3}{4}\frac{1}{\tau^2}\left[-\tau + f(\tau)\right], \tag{C.0.1}$$

$$\mathcal{A}^{\mathrm{s}=1/2}(\tau) = \frac{3}{2}\frac{1}{\tau^2}\left[\tau + (\tau-1)f(\tau)\right], \tag{C.0.2}$$

$$\mathcal{A}^{\mathrm{s}=1}(\tau) = \frac{3}{4}\frac{1}{\tau^2}\left[-2\tau^2 - 3\tau + 3\left(1-2\tau\right)f(\tau)\right], \tag{C.0.3}$$

where $\tau = m_h^2/4m_i^2$, and m_i is the mass of loop particles. $f(\tau)$ is given by

$$f(\tau) = \begin{cases} \left(\sin^{-1}\sqrt{\tau}\right)^2 & \text{if } \tau \leq 1 \\ -\frac{1}{4}\left[\ln\frac{1+\sqrt{1-\tau^{-1}}}{1-\sqrt{1-\tau^{-1}}} - i\pi\right]^2 & \text{if } \tau > 1\,. \end{cases} \tag{C.0.4}$$

When $m_i \to \infty$,

$$\mathcal{A}^{\mathrm{s}=0}(\tau \to 0) = \frac{1}{4}, \tag{C.0.5}$$

$$\mathcal{A}^{\mathrm{s}=1/2}(\tau \to 0) = 1, \tag{C.0.6}$$

$$\mathcal{A}^{\mathrm{s}=1}(\tau \to 0) = -\frac{21}{4}\,. \tag{C.0.7}$$

The loop functions become complex when $m_i < m_h/2$. In Fig. C.1, we take $\mathcal{A}^{\mathrm{s}=0}$ as an example and show its real and imaginary parts as a function of $m_{\tilde{t}}$. $\mathcal{A}^{\mathrm{s}=1/2}$ and $\mathcal{A}^{\mathrm{s}=1}$ have similar behaviors as $\mathcal{A}^{\mathrm{s}=0}$.

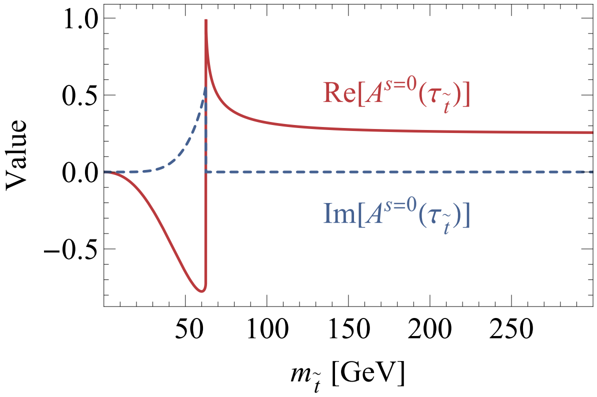

Figure C.1: The real and imaginary part of the pre-factor of $\mathcal{A}^{\mathrm{s}=0}(\tau_{\tilde{t}})$.

Appendix D

Cross-check with HiggsSignals

We use `HiggsSignals 1.4.0` to cross-check the results from our fitting method described in Sec. 6.4.[1] `HiggsSignals 1.4.0` contains the available data up to the summer of 2015. To make the comparison, we use the data sets with a single decay channel that are included in the `HiggsSignals 1.4.0` package. We choose to compare the constraints on $\{r_\gamma, r_G\}$, setting all other couplings to be their SM values.

We show a comparison between our method and the `HiggsSignals` fit in Fig. D.1, finding reasonable agreement, especially for the 2σ-CL exclusion contours. The main difference between the two methods is that `HiggsSignals` correlates the theoretical uncertainties in the SM production cross sections and branching ratios, and also correlates the error on the individual production and decay with the BSM modifications to the couplings. If we set the theoretical uncertainties of SM cross sections and branching ratios to zero, our results agree with `HiggsSignals`. We note, however, that `HiggsSignals` also does not capture the correlations among the systematic uncertainties in the data, which is not public information.

---

[1] We thank Tim Stefaniak for help in setting up `HiggsSignals`.

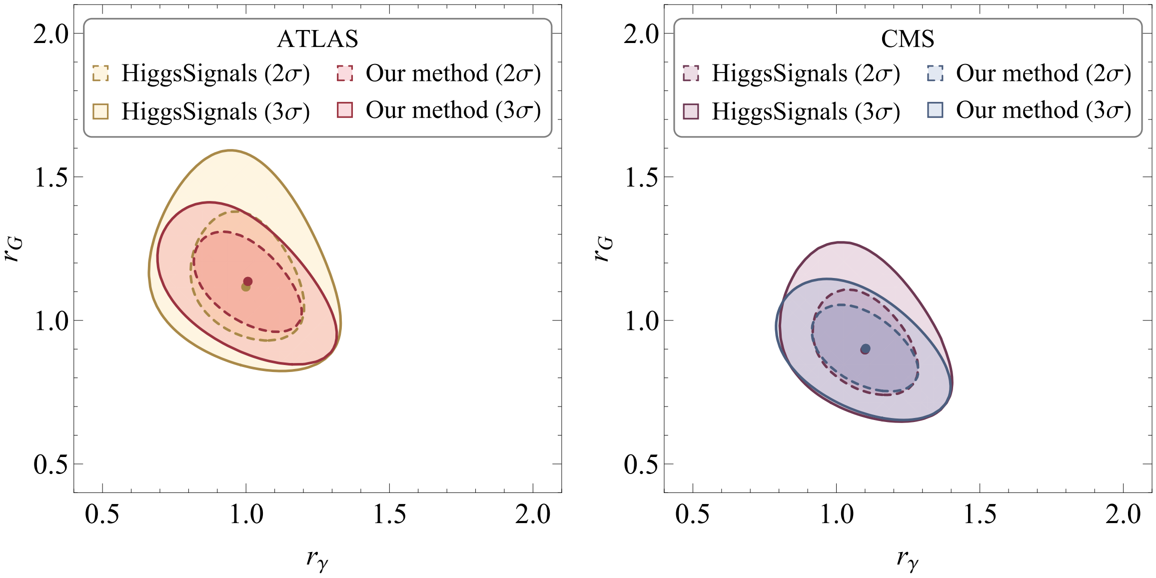

Figure D.1: A comparison of $r_G - r_\gamma$ joint fits from HiggsSignals and our fitting method described in Sec. 6.4 for ATLAS (left) and CMS (right) data (see text for more details).

Appendix E

Data Tables

We here provide tables of the current and future Higgs-precision data used in our analyses. Current data for LHC and Tevatron are listed in Tab. E.1, Tab. E.2, and Tab. E.3. The signal strength (the fourth column) is expressed in the format $\mu^{+\sigma_{\text{up}}}_{-\sigma_{\text{down}}}$, where σ_{up} and σ_{down} are the (asymmetric) 1σ-error bars of the observed signal strength μ. Tab. E.1 lists all searches with single decay and multiple productions. The signal strength Eq. (6.3.19) can be expressed as

$$\mu_f = \left(|r_G|^2\xi_G + |r_V|^2\xi_V + |r_t|^2\xi_t\right)\frac{|r_f|^2}{r_h + r_{\text{inv}}}\,, \tag{E.0.1}$$

where ξ_G, ξ_V, and ξ_t are the weights in the Higgs production for gluon fusion, vector-boson fusion plus associated production, and associated production with tops, respectively. The signal strength and weights given in Tab. E.3 are defined in a similar manner,

$$\mu_{\text{inv}} = \left(|r_G|^2\xi_G + |r_V|^2\xi_V + |r_t|^2\xi_t\right)\frac{r_{\text{inv}}}{r_h + r_{\text{inv}}}\,. \tag{E.0.2}$$

Tab. E.2 lists all searches with multiple decays and single production. The signal strength Eq. (6.3.19) is instead expressed as

$$\mu_f = \frac{|r_t^2|}{r_h + r_{\text{inv}}}\left(|r_V^2|\zeta_{VV} + |r_b^2|\zeta_{bb} + |r_\tau|^2\zeta_{\tau\tau}\right)\,, \tag{E.0.3}$$

where ζ_{VV}, ζ_{bb}, and $\zeta_{\tau\tau}$ stand for weights in the Higgs decays into WW plus ZZ, bb, and $\tau^+\tau^-$, respectively.

Future ATLAS Run 3 and Run 4 data are listed in Tab. E.4. We assume CMS will perform identical searches and effectively double the data listed in Tab. E.4 for our projections. Sensitivities for ILC (250 GeV, 2 ab^{-1} $\oplus$ 350 GeV, 200 fb^{-1} $\oplus$ 550 GeV, 4 ab^{-1}), CEPC (240 GeV, 10 ab^{-1}), FCC-ee (240 GeV, 10 ab^{-1} $\oplus$ 350 GeV, 2.6 ab^{-1}), and FCC-hh (100 TeV, 30 ab^{-1}) are listed in Tab. E.5.

Channel	Analysis	$\sqrt{s}$	L	μ	ξ_G	ξ_V	ξ_t	Ref.
		(TeV)	(fb^{-1})		(%)	(%)	(%)	
$\gamma\gamma$ (ttH; multijet)	CMS	8	full	$1.24^{+4.24}_{-2.70}$	3	3	94	[345]
$\gamma\gamma$ (ttH; lepton)	CMS	8	full	$3.52^{+3.89}_{-2.45}$	0	4	96	[345]
$\gamma\gamma$ (ttH)	CMS	7	full	$0.71^{+6.20}_{-3.56}$	3	5	92	[345]
$\gamma\gamma$ (untagged 0)	CMS	7	full	$1.97^{+1.50}_{-1.25}$	80	19	1	[345]
$\gamma\gamma$ (untagged 0)	CMS	8	full	$0.13^{+1.09}_{-0.74}$	71	27	2	[345]
$\gamma\gamma$ (untagged 1)	CMS	7	full	$1.23^{+0.98}_{-0.88}$	92	8	0	[345]
$\gamma\gamma$ (untagged 1)	CMS	8	full	$0.92^{+0.57}_{-0.49}$	82	18	1	[345]
$\gamma\gamma$ (untagged 2)	CMS	7	full	$1.60^{+1.25}_{-1.17}$	92	8	0	[345]
$\gamma\gamma$ (untagged 2)	CMS	8	full	$1.10^{+0.48}_{-0.44}$	89	11	0	[345]
$\gamma\gamma$ (untagged 3)	CMS	7	full	$2.61^{+1.74}_{-1.65}$	92	8	0	[345]
$\gamma\gamma$ (untagged 3)	CMS	8	full	$0.65^{+0.65}_{-0.89}$	89	10	0	[345]
$\gamma\gamma$ (untagged 4)	CMS	8	full	$1.46^{+1.29}_{-1.24}$	91	8	0	[345]
$\gamma\gamma$ (VBF; dijet 0)	CMS	7	full	$4.85^{+2.17}_{-1.76}$	19	81	0	[345]
$\gamma\gamma$ (VBF; dijet 0)	CMS	8	full	$0.82^{+0.75}_{-0.58}$	14	85	0	[345]
$\gamma\gamma$ (VBF; dijet 1)	CMS	7	full	$2.60^{+2.16}_{-1.76}$	38	61	0	[345]
$\gamma\gamma$ (VBF; dijet 1)	CMS	8	full	$-0.21^{+0.75}_{-0.69}$	24	76	0	[345]
$\gamma\gamma$ (VBF; dijet 2)	CMS	8	full	$2.60^{+1.33}_{-0.99}$	38	61	1	[345]
$\gamma\gamma$ (VH; dijet)	CMS	7	full	$7.86^{+8.86}_{-6.40}$	27	71	2	[345]
$\gamma\gamma$ (VH; dijet)	CMS	8	full	$0.39^{+2.16}_{-1.48}$	25	72	3	[345]
$\gamma\gamma$ (VH; MET)	CMS	7	full	$4.32^{+6.72}_{-4.15}$	5	87	8	[345]
$\gamma\gamma$ (VH; MET)	CMS	8	full	$0.08^{+1.86}_{-1.28}$	13	75	12	[345]

$\gamma\gamma$ (VH; loose)	CMS	7	full	$3.10^{+8.29}_{-5.34}$	4	95	1	[345]
$\gamma\gamma$ (VH; loose)	CMS	8	full	$1.24^{+3.69}_{-2.62}$	2	96	2	[345]
$\gamma\gamma$ (VH; tight)	CMS	8	full	$-0.34^{+1.30}_{-0.63}$	0	96	4	[345]
WW ($3l3\nu$)	CMS	7+8	full	$0.56^{+1.27}_{-0.95}$	0	100	0	[31]
WW (0/1j)	CMS	7+8	full	$0.74^{+0.22}_{-0.20}$	82	18	0	[31]
WW (VBF; 2j)	CMS	7+8	full	$0.60^{+0.57}_{-0.46}$	20	80	0	[31]
WW (VH; $2l2\nu$)	CMS	7+8	full	$0.39^{+1.97}_{-1.87}$	54	46	0	[31]
ZZ (0/1j)	CMS	7+8	full	$0.88^{+0.34}_{-0.27}$	90	10	0	[346]
ZZ (2j)	CMS	7+8	full	$1.55^{+0.95}_{-0.66}$	58	42	0	[346]
bb (VBF)	CMS	7+8	full	$2.80^{+1.60}_{-1.40}$	0	100	0	[347]
bb (VH)	CMS	7+8	full	$0.89^{+0.43}_{-0.43}$	0	100	0	[347]
bb (ttH)	CMS	7+8	full	$0.70^{+1.80}_{-1.80}$	0	0	100	[347]
$\tau\tau$ (ttH)	CMS	7+8	full	$-1.30^{+6.30}_{-5.50}$	0	0	100	[348]
$\tau\tau$ (0j)	CMS	7+8	full	$0.34^{+1.09}_{-1.09}$	98	2	0	[349]
$\tau\tau$ (1j)	CMS	7+8	full	$1.07^{+0.46}_{-0.46}$	77	23	0	[349]
$\tau\tau$ (VBF; 2j)	CMS	7+8	full	$0.94^{+0.41}_{-0.41}$	19	81	0	[349]
$\tau\tau$ (VH)	CMS	7+8	full	$-0.33^{+1.02}_{-1.02}$	0	100	0	[349]
$\gamma\gamma$ (central low p_{T_t})	ATLAS	7+8	full	$0.62^{+0.42}_{-0.40}$	91	8	0	[350]
$\gamma\gamma$ (central high p_{T_t})	ATLAS	7+8	full	$1.62^{+1.00}_{-0.83}$	67	31	2	[350]
$\gamma\gamma$ (forward low p_{T_t})	ATLAS	7+8	full	$2.03^{+0.57}_{-0.53}$	91	9	0	[350]
$\gamma\gamma$ (forward high p_{T_t})	ATLAS	7+8	full	$1.73^{+1.34}_{-1.18}$	66	33	1	[350]
$\gamma\gamma$ (VBF; loose)	ATLAS	7+8	full	$1.33^{+0.92}_{-0.77}$	33	67	0	[350]
$\gamma\gamma$ (VBF; tight)	ATLAS	7+8	full	$0.68^{+0.67}_{-0.51}$	15	85	0	[350]
$\gamma\gamma$ (VH; di-jet)	ATLAS	7+8	full	$0.23^{+1.67}_{-1.39}$	39	61	0	[350]
$\gamma\gamma$ (VH; MET)	ATLAS	7+8	full	$3.51^{+3.31}_{-2.42}$	7	86	7	[350]
$\gamma\gamma$ (VH; 1l)	ATLAS	7+8	full	$0.41^{+1.43}_{-1.06}$	0	98	2	[350]
$\gamma\gamma$ (ttH; hadronic)	ATLAS	7+8	full	$-0.84^{+3.23}_{-1.25}$	12	4	84	[350]
$\gamma\gamma$ (ttH; leptonic)	ATLAS	7+8	full	$2.42^{+3.21}_{-2.07}$	7	19	74	[350]

WW ($e\mu$,$l_2 = \mu$,$n_j = 0$)	ATLAS	7+8	full	$1.08^{+0.41}_{-0.36}$	98	2	0	[351]
WW ($e\mu$,$l_2 = e$,$n_j = 0$)	ATLAS	7+8	full	$1.40^{+0.49}_{-0.44}$	98	2	0	[351]
WW ($ee\mu\mu$,$n_j = 0$)	ATLAS	7+8	full	$0.47^{+0.74}_{-0.70}$	97	3	0	[351]
WW ($e\mu$,$n_j = 1$)	ATLAS	7+8	full	$1.16^{+0.51}_{-0.42}$	85	15	0	[351]
WW ($ee\mu\mu$,n_j=1)	ATLAS	7+8	full	$0.19^{+1.12}_{-0.98}$	85	15	0	[351]
WW (ggF; $e\mu$,$n_j \geq 2$)	ATLAS	7+8	full	$1.20^{+0.96}_{-0.83}$	74	26	0	[351]
WW (VBF; $e\mu$,$n_j \geq 2$)	ATLAS	7+8	full	$0.98^{+0.48}_{-0.40}$	27	73	0	[351]
WW(VBF; $ee\mu\mu$,$n_j \geq 2$)	ATLAS	7+8	full	$1.98^{+0.84}_{-0.67}$	25	75	0	[351]
WW(VH; 4l,2SFOS)	ATLAS	7+8	full	$-5.9^{+6.8}_{-4.1}$	0	100	0	[352]
WW(VH; 4l,1SFOS)	ATLAS	7+8	full	$9.6^{+8.1}_{-5.4}$	0	100	0	[352]
WW(VH; 3l,1SFOS/3SF)	ATLAS	7+8	full	$-2.9^{+2.7}_{-2.1}$	6	94	0	[352]
WW(VH; 3l,0SFOS)	ATLAS	7+8	full	$1.7^{+1.9}_{-1.4}$	0	100	0	[352]
WW(VH; 2l,DFOS)	ATLAS	7+8	full	$2.2^{+2.0}_{-1.9}$	51	49	0	[352]
WW(VH; 2l,SS2jet)	ATLAS	7+8	full	$7.6^{+6.0}_{-5.4}$	0	100	0	[352]
WW(VH; 2l,SS1jet)	ATLAS	7+8	full	$8.4^{+4.3}_{-3.8}$	0	100	0	[352]
ZZ (ggF+ttH)	ATLAS	7+8	full	$1.66^{+0.51}_{-0.44}$	89	10	0	[353]
ZZ (VBF+VH)	ATLAS	7+8	full	$0.26^{+1.64}_{-0.94}$	32	68	0	[353]
bb (VH; 0l)	ATLAS	8	full	$-0.35^{+0.55}_{-0.52}$	0	100	0	[354]
bb (VH; 1l)	ATLAS	8	full	$1.17^{+0.66}_{-0.60}$	0	100	0	[354]
bb (VH; 2l)	ATLAS	8	full	$0.94^{+0.88}_{-0.79}$	0	100	0	[354]
bb (VBF; 2j)	ATLAS	8	full	$-0.80^{+2.30}_{-2.30}$	28	72	0	[355]
bb (ttH; 2l)	ATLAS	8	full	$2.80^{+2.00}_{-2.00}$	0	0	100	[356]
bb (ttH; lepton+jets)	ATLAS	8	full	$1.20^{+1.30}_{-1.30}$	0	0	100	[356]
bb (ttH; hadronic)	ATLAS	8	full	$1.60^{+2.60}_{-2.60}$	0	0	100	[357]
$\tau_l\tau_l$ (VBF)	ATLAS	7+8	full	$1.70^{+1.00}_{-0.90}$	42	58	0	[358]
$\tau_l\tau_l$ (boosted)	ATLAS	7+8	full	$3.00^{+2.00}_{-1.70}$	65	35	0	[358]
$\tau_l\tau_h$ (VBF)	ATLAS	7+8	full	$1.00^{+0.60}_{-0.50}$	34	66	0	[358]
$\tau_l\tau_h$ (boosted)	ATLAS	7+8	full	$0.90^{+1.00}_{-0.90}$	67	33	0	[358]

$\tau_h\tau_h$ (VBF)	ATLAS	7+8	full	$1.40^{+0.90}_{-0.70}$	39	61	0	[358]
$\tau_h\tau_h$ (boosted)	ATLAS	7+8	full	$3.60^{+2.00}_{-1.60}$	62	38	0	[358]
$\tau_h\tau_h$ (ZH)	ATLAS	8	full	$4.60^{+3.20}_{-3.20}$	0	100	0	[359]
$\tau_l\tau_h$ (ZH)	ATLAS	8	full	$1.00^{+3.50}_{-3.50}$	0	100	0	[359]
$\tau_h\tau_h$ (WH)	ATLAS	8	full	$1.80^{+3.10}_{-3.10}$	0	100	0	[359]
$\tau_l\tau_h$ (WH)	ATLAS	8	full	$1.30^{+2.80}_{-2.80}$	0	100	0	[359]
$\gamma\gamma$ (ggF)	CMS	13	35.9	$1.11^{+0.19}_{-1.18}$	100	0	0	[360]
$\gamma\gamma$ (VBF)	CMS	13	35.9	$0.5^{+0.6}_{-0.5}$	0	100	0	[360]
$\gamma\gamma$ (ttH)	CMS	13	35.9	$2.2^{+0.9}_{-0.8}$	0	0	100	[360]
$\gamma\gamma$ (VH)	CMS	13	35.9	$2.3^{+1.1}_{-1.0}$	0	100	0	[360]
WW ($0j$)	CMS	13	15.2	$0.9^{+0.4}_{-0.3}$	97	3	0	[361]
WW ($1j$)	CMS	13	15.2	$1.1^{+0.4}_{-0.4}$	85	15	0	[361]
WW ($2j$)	CMS	13	15.2	$1.3^{+1.0}_{-1.0}$	74	26	0	[361]
WW (VBF; $2j$)	CMS	13	15.2	$1.4^{+0.8}_{-0.8}$	38	62	0	[361]
WW (VH; $2j$)	CMS	13	15.2	$2.1^{+2.3}_{-2.2}$	54	46	0	[361]
WW (WH; $3l$)	CMS	13	15.2	$-1.4^{+1.5}_{-1.5}$	4	96	0	[361]
ZZ (untagged)	CMS	13	35.9	$1.17^{+0.23}_{-0.21}$	95	5	0	[362]
ZZ (VBF; $1j$)	CMS	13	35.9	$0.97^{+0.40}_{-0.32}$	86	14	0	[362]
ZZ (VBF; $2j$)	CMS	13	35.9	$0.63^{+0.51}_{-0.34}$	46	54	0	[362]
ZZ (VH; hadronic)	CMS	13	35.9	$0.76^{+0.78}_{-0.48}$	68	30	2	[362]
bb (ttH; lepton+jets)	CMS	13	12.9	$-0.43^{+1.02}_{-1.02}$	0	0	100	[300]
bb (ttH; $2l$)	CMS	13	12.9	$-0.04^{+1.50}_{-1.39}$	0	0	100	[300]
bb (VBF)	CMS	13	2.3	$-3.70^{+2.40}_{-2.50}$	28	72	0	[363]
bb (boosted)	CMS	13	35.9	$2.30^{+1.80}_{-1.60}$	54	31	15	[364]
$\tau\tau$ ($e\mu$)	CMS	13	35.9	$0.66^{+0.61}_{-0.59}$	17	83	0	[365]
$\tau\tau$ ($e\tau_h$)	CMS	13	35.9	$0.56^{+0.58}_{-0.56}$	48	52	0	[365]
$\tau\tau$ ($\mu\tau_h$)	CMS	13	35.9	$1.09^{+0.41}_{-0.41}$	32	68	0	[365]
$\tau\tau$ ($\tau_h\tau_h$)	CMS	13	35.9	$1.30^{+0.37}_{-0.33}$	59	41	0	[365]

$\gamma\gamma$ (ggF)	ATLAS	13	36.1	$0.8^{+0.19}_{-0.18}$	93	7	0	[366]
$\gamma\gamma$ (VBF)	ATLAS	13	36.1	$2.1^{+0.60}_{-0.60}$	42	58	0	[366]
$\gamma\gamma$ (VH)	ATLAS	13	36.1	$0.7^{+0.9}_{-0.8}$	53	44	3	[366]
$\gamma\gamma$ (ttH)	ATLAS	13	36.1	$0.5^{+0.6}_{-0.6}$	11	7	82	[366]
WW (VBF; $e\mu$,$n_j \geq 2$)	ATLAS	13	5.8	$1.70^{+1.10}_{-0.90}$	38	62	0	[367]
WW (WH; $3l$+MET)	ATLAS	13	5.8	$3.20^{+4.40}_{-4.20}$	4	96	0	[367]
ZZ (ggF; $0j$)	ATLAS	13	36.1	$1.22^{+0.34}_{-0.29}$	98	2	0	[368]
ZZ (ggF;$1j$;p_T^H low)	ATLAS	13	36.1	$0.5^{+0.85}_{-0.76}$	92	8	0	[368]
ZZ (ggF;$1j$;p_T^H med)	ATLAS	13	36.1	$1.3^{+0.98}_{-0.73}$	84	16	0	[368]
ZZ (ggF;$1j$;p_T^H high)	ATLAS	13	36.1	$1.3^{+2.4}_{-1.7}$	75	25	0	[368]
ZZ (ggF;$2j$)	ATLAS	13	36.1	$1.5^{+1.4}_{-1.0}$	69.5	29.5	1	[368]
ZZ (VBF;p_T^j low)	ATLAS	13	36.1	$2.9^{+2.0}_{-1.6}$	62	37	1	[368]
ZZ (VBF;p_T^j high)	ATLAS	13	36.1	$13^{+12.0}_{-8.0}$	57	40	3	[368]
bb (VH; $2l$)	ATLAS	13	36.1	$1.9^{+0.78}_{-0.64}$	0	100	0	[369]
bb (VH; $1l$)	ATLAS	13	36.1	$1.43^{+0.69}_{-0.59}$	0	100	0	[369]
bb (VH; $0l$)	ATLAS	13	36.1	$0.45^{+0.53}_{-0.51}$	0	100	0	[369]
bb (VBF; $2j$+γ)	ATLAS	13	12.6	$-3.90^{+2.80}_{-2.70}$	0	100	0	[370]
bb (ttH; $2l$)	ATLAS	13	13.2	$4.60^{+2.90}_{-2.30}$	0	0	100	[301]
bb (ttH; $1l$)	ATLAS	13	13.2	$1.60^{+1.10}_{-1.10}$	0	0	100	[301]
$\gamma\gamma$	Tevatron	1.96	full	$5.79^{+3.39}_{-3.12}$	78	22	0	[371]
WW	Tevatron	1.96	full	$0.94^{+0.85}_{-0.83}$	78	22	0	[371]
bb	Tevatron	1.96	full	$1.59^{+0.69}_{-0.72}$	0	100	0	[371]
$\tau\tau$	Tevatron	1.96	full	$1.68^{+2.28}_{-1.68}$	50	50	0	[371]

Table E.1: Signal strength μ_f for current LHC and Tevatron data. The central value, sup-script and subscript for μ represents observed signal strength, 1σ upper error bar, and 1σ down error bar respectively. ξ_G, ξ_V, and ξ_t indicate for weights in the Higgs production for gluon fusion, vector boson fusion plus associated production, and associated production with tops, respectively. Official values for weights are used when available, otherwise estimates are made.

Channel	Analysis	$\sqrt{s}$ (TeV)	L (fb^{-1})	μ	ζ_{VV} (%)	ζ_{bb} (%)	$\zeta_{\tau\tau}$ (%)	Ref.
ttH ($4l$)	CMS	8	full	$-4.70^{+5.00}_{-1.30}$	72	0	28	[348]
ttH ($3l$)	CMS	8	full	$3.10^{+2.40}_{-2.00}$	77	0	23	[348]
ttH ($2l_{ss}$)	CMS	8	full	$5.30^{+2.10}_{-1.80}$	77	0	23	[348]
ttH ($1l2\tau_h$)	CMS	13	35.9	$-1.20^{+1.50}_{-1.47}$	3	0	97	[372]
ttH ($2l_{ss}1\tau_h$)	CMS	13	35.9	$0.86^{+0.79}_{-0.66}$	42	0	58	[372]
ttH ($3l1\tau_h$)	CMS	13	35.9	$1.22^{+1.34}_{-1.00}$	43	0	57	[372]
ttH ($4l$)	CMS	13	35.9	$0.90^{+2.30}_{-1.60}$	72	0	28	[373]
ttH ($3l$)	CMS	13	35.9	$1.00^{+0.80}_{-0.70}$	79	0	21	[373]
ttH ($2l_{ss}$)	CMS	13	35.9	$1.70^{+0.60}_{-0.50}$	80	0	20	[373]
ttH ($4l$)	ATLAS	8	full	$1.80^{+6.90}_{-6.90}$	82	4	14	[374]
ttH ($3l$)	ATLAS	8	full	$2.80^{+2.20}_{-1.80}$	81	4	15	[374]
ttH ($2l1\tau_h$)	ATLAS	8	full	$-0.90^{+3.10}_{-2.00}$	37	1	62	[374]
ttH ($2l0\tau_h$)	ATLAS	8	full	$2.80^{+2.10}_{-1.90}$	83	2	15	[374]
ttH ($1l2\tau_h$)	ATLAS	8	full	$-9.60^{+9.60}_{-9.70}$	4	3	93	[374]
ttH ($3l$)	ATLAS	13	13.2	$0.50^{+1.70}_{-1.60}$	78	2	20	[375]
ttH ($2l0\tau_h$)	ATLAS	13	13.2	$4.00^{+2.10}_{-1.70}$	80	3	17	[375]
ttH ($2l1\tau_h$)	ATLAS	13	13.2	$6.20^{+3.60}_{-2.70}$	48	1	51	[375]

Table E.2: Signal strength for ttH multi-lepton searches μ_f for current LHC data. ζ_{VV}, ζ_{bb}, and $\zeta_{\tau\tau}$ indicate weights in the Higgs decays into WW plus ZZ, $b\bar{b}$, and $\tau^+\tau^-$, respectively. Official values for weights are used when given. “$2l_{ss}$" stands for two same-sign di-leptons.

Channel	Analysis	$\sqrt{s}$ (TeV)	L (fb^{-1})	μ	ξ_G (%)	ξ_V (%)	ξ_t (%)	Ref.
Invisible (VBF)	CMS	7+8 +13	full 2.3	$0.16^{+0.15}_{-0.15}$	9	91	0	[376]
Invisible (VH)	CMS	7+8 +13	full 2.3	$0.00^{+0.12}_{-0.12}$	0	100	0	[376]
Invisible (ggF)	CMS	7+8 +13	full 2.3	$0.00^{+0.27}_{-0.27}$	70	30	0	[376]
Invisible (VH; mono-j)	CMS	13	35.9	$0.00^{+0.38}_{-0.38}$	73	27	0	[377]
Invisible (VH; mono-V)	CMS	13	35.9	$0.00^{+0.25}_{-0.25}$	39	61	0	[377]
Invisible (ZH)	CMS	13	35.9	$0.00^{+0.20}_{-0.20}$	0	100	0	[378]
Invisible (ZH)	ATLAS	7+8	full	$0.00^{+0.38}_{-0.38}$	0	100	0	[379]
Invisible (VBF)	ATLAS	8	full	$0.00^{+0.14}_{-0.14}$	6	94	0	[311]
Invisible (VH)	ATLAS	8	full	$0.00^{+0.40}_{-0.40}$	39	61	0	[380]
Invisible ($1j$+MET)	ATLAS	8	full	$0.00^{+0.81}_{-0.81}$	52	48	0	[381]
Invisible (ZH; ee)	ATLAS	13	36.1	$0.00^{+0.31}_{-0.31}$	0	100	0	[382]
Invisible (ZH; $\mu\mu$)	ATLAS	13	36.1	$0.00^{+0.50}_{-0.50}$	0	100	0	[382]

Table E.3: Signal strengths for Higgs invisible searches μ_{inv} for current LHC data. Official signal strengths and 1σ error bars are used if the likelihood curve is provided. Otherwise we assume the observed signal strength is 0 and translate the 95% upper limits on signal strength, $\sigma_{\text{inv}}^{95\%}$, into 1σ error bars ($\sigma_{\text{inv}}^{\text{up/down}} = \sigma_{\text{inv}}^{95\%}/\sqrt{3.84}$). Official values for weights are used when given.

L	Channel	μ	ξ_G (%)	ξ_V (%)	ξ_t (%)	Ref.
300 fb^{-1}	$\gamma\gamma$ ($0j$)	$1.0^{+0.19}_{-0.19}$	92	8	0	[3]
	$\gamma\gamma$ ($1j$)	$1.0^{+0.27}_{-0.27}$	82	18	0	[3]
	$\gamma\gamma$ (VBF)	$1.0^{+0.47}_{-0.47}$	39	61	0	[3]
	$\gamma\gamma$ (WH-like)	$1.0^{+0.48}_{-0.48}$	2	79	19	[3]
	$\gamma\gamma$ (ZH-like)	$1.0^{+0.85}_{-0.85}$	2	79	19	[3]
	$\gamma\gamma$ (ttH-like)	$1.0^{+0.38}_{-0.38}$	0	0	100	[3]
	WW ($0j$)	$1.0^{+0.18}_{-0.18}$	98	2	0	[3]
	WW ($1j$)	$1.0^{+0.30}_{-0.30}$	88	12	0	[3]
	WW (VBF-like)	$1.0^{+0.21}_{-0.21}$	8	92	0	[3]
	ZZ (VH-like)	$1.0^{+0.35}_{-0.35}$	30	56	14	[3]
	ZZ (ttH-like)	$1.0^{+0.49}_{-0.49}$	9	6	85	[3]
	ZZ (VBF-like)	$1.0^{+0.36}_{-0.36}$	45	54	1	[3]
	ZZ (ggF-like)	$1.0^{+0.12}_{-0.12}$	89	10	1	[3]
	bb (WH)	$1.0^{+0.57}_{-0.57}$	0	100	0	[3]
	bb (ZH)	$1.0^{+0.29}_{-0.29}$	0	100	0	[3]
	$\tau\tau$ (VBF-like)	$1.0^{+0.21}_{-0.21}$	20	80	0	[3]
	Invisible (VBF)	$0.0^{+0.11}_{-0.11}$	0	100	0	[302]
3 ab^{-1}	$\gamma\gamma$ ($0j$)	$1.0^{+0.16}_{-0.16}$	92	8	0	[3]
	$\gamma\gamma$ ($1j$)	$1.0^{+0.23}_{-0.23}$	82	18	0	[3]
	$\gamma\gamma$ (VBF)	$1.0^{+0.22}_{-0.22}$	39	61	0	[3]
	$\gamma\gamma$ (WH-like)	$1.0^{+0.19}_{-0.19}$	2	79	19	[3]
	$\gamma\gamma$ (ZH-like)	$1.0^{+0.28}_{-0.28}$	2	79	19	[3]
	$\gamma\gamma$ (ttH-like)	$1.0^{+0.17}_{-0.17}$	0	0	100	[3]
	WW ($0j$)	$1.0^{+0.16}_{-0.16}$	98	2	0	[3]
	WW ($1j$)	$1.0^{+0.26}_{-0.26}$	88	12	0	[3]
	WW (VBF-like)	$1.0^{+0.15}_{-0.15}$	8	92	0	[3]
	ZZ (VH-like)	$1.0^{+0.13}_{-0.13}$	30	56	14	[3]
	ZZ (ttH-like)	$1.0^{+0.20}_{-0.20}$	9	6	85	[3]
	ZZ (VBF-like)	$1.0^{+0.21}_{-0.21}$	45	54	1	[3]
	ZZ (ggF-like)	$1.0^{+0.11}_{-0.11}$	89	10	1	[3]
	bb (WH)	$1.0^{+0.37}_{-0.37}$	0	100	0	[3]
	bb (ZH)	$1.0^{+0.14}_{-0.14}$	0	100	0	[3]

	ILC	CEPC	FCC-ee	FCC-hh
σ_{Γ_h}	1.8%	1.9%	1%	–
σ_{r_b}	0.7%	0.92%	0.42%	–
σ_{r_c}	1.2 %	1.2%	0.71%	–
σ_{r_G}	1%	1.1%	0.8%	–
σ_{r_W}	0.42%	0.87%	0.19%	–
σ_{r_τ}	0.9%	1%	0.54%	–
σ_{r_Z}	0.32%	0.18%	0.15%	–
σ_{r_γ}	3.4%	3.3%	1.5%	–
σ_{r_μ}	9.2%	6.1%	6.2%	–
σ_{r_t}	3%	–	13%	1%
B_{inv}	0.29%	0.2%	0.19%	–

Table E.5: Constraints on sensitivities for ILC (250 GeV, 2 ab^{-1} $\oplus$ 350 GeV, 200 fb^{-1} $\oplus$ 550 GeV, 4 ab^{-1}) [5], CEPC (240 GeV, 10 ab^{-1}) [6], FCC-ee (240 GeV, 10 ab^{-1} $\oplus$ 350 GeV, 2.6 ab^{-1}) from [7, 8], and FCC-hh (100 TeV, 30 ab^{-1}) [8]. Note that since most of sensitivities of FCC-hh are still under study (except for r_t) [8], we use the corresponding values from FCC-ee for our projections. B_{inv} in the last row are the upper limits with 95% CL.

Bibliography

[1] R. Contino et al. Physics at a 100 TeV pp collider: Higgs and EW symmetry breaking studies. 2016.

[2] David Curtin, Patrick Meade, and Chiu-Tien Yu. Testing Electroweak Baryogenesis with Future Colliders. *JHEP*, 11:127, 2014.

[3] ATLAS Collaboration et al. Projections for measurements of higgs boson signal strengths and coupling parameters with the atlas detector at a hl-lhc. Technical report, LHC/ATLAS Experiment, 2014.

[4] Philip Bechtle, Sven Heinemeyer, Oscar Stål, Tim Stefaniak, and Georg Weiglein. Probing the Standard Model with Higgs signal rates from the Tevatron, the LHC and a future ILC. *JHEP*, 11:039, 2014.

[5] Keisuke Fujii et al. Physics Case for the International Linear Collider. 2015.

[6] CEPC-SPPC Study Group. CEPC-SPPC Preliminary Conceptual Design Report. 1. Physics and Detector. 2015.

[7] Sally Dawson et al. Working Group Report: Higgs Boson. In *Community Summer Study 2013: Snowmass on the Mississippi (CSS2013) Minneapolis, MN, USA, July 29-August 6, 2013*, 2013.

[8] Michelangelo L. Mangano. Fcc ee/hh and high energy lhc. The Fifth Annual Large Hadron Collider Physics conference, 2017.

[9] Abdelhak Djouadi. The Anatomy of electro-weak symmetry breaking. I: The Higgs boson in the standard model. *Phys. Rept.*, 457:1–216, 2008.

[10] Georges Aad et al. Observation of a new particle in the search for the Standard Model Higgs boson with the ATLAS detector at the LHC. *Phys. Lett.*, B716:1–29, 2012.

[11] Serguei Chatrchyan et al. Observation of a new boson at a mass of 125 GeV with the CMS experiment at the LHC. *Phys. Lett.*, B716:30–61, 2012.

[12] Steven Weinberg. *Cosmology*. 2008.

[13] Steven Weinberg. Anthropic Bound on the Cosmological Constant. *Phys. Rev. Lett.*, 59:2607, 1987.

[14] Mariangela Lisanti. Lectures on Dark Matter Physics. In *Proceedings, Theoretical Advanced Study Institute in Elementary Particle Physics: New Frontiers in Fields and Strings (TASI 2015): Boulder, CO, USA, June 1-26, 2015*, pages 399–446, 2017.

[15] S. F. King. Neutrino mass models. *Rept. Prog. Phys.*, 67:107–158, 2004.

[16] Antonio Riotto. Theories of baryogenesis. In *Proceedings, Summer School in High-energy physics and cosmology: Trieste, Italy, June 29-July 17, 1998*, pages 326–436, 1998.

[17] Michael Dine. TASI lectures on the strong CP problem. In *Flavor physics for the millennium. Proceedings, Theoretical Advanced Study Institute in elementary particle physics, TASI 2000, Boulder, USA, June 4-30, 2000*, pages 349–369, 2000.

[18] R. N. Mohapatra. Supersymmetric grand unification. In *Supersymmetry, supergravity and supercolliders. Proceedings, Theoretical Advanced Study Institute in elementary particle physics, TASI'97, Boulder, USA, June 2-27, 1997*, pages 601–657, 1997.

[19] Gian Francesco Giudice. Naturally Speaking: The Naturalness Criterion and Physics at the LHC. 2008.

[20] The T. E. V. N. P. H..Working Group. Combined CDF and D0 Upper Limits on Standard Model Higgs-Boson Production with up to 6.7 fb^{-1} of Data. In *Proceedings, 35th International Conference on High energy physics (ICHEP 2010): Paris, France, July 22-28, 2010*, 2010.

[21] Lisa Randall and Raman Sundrum. A Large mass hierarchy from a small extra dimension. *Phys. Rev. Lett.*, 83:3370–3373, 1999.

[22] Ties Behnke, James E. Brau, Brian Foster, Juan Fuster, Mike Harrison, James McEwan Paterson, Michael Peskin, Marcel Stanitzki, Nicholas Walker, and Hitoshi Yamamoto. The International Linear Collider Technical Design Report - Volume 1: Executive Summary. 2013.

[23] Strahinja Lukić. Higgs physics at CLIC. In *38th International Conference on High Energy Physics (ICHEP 2016) Chicago, IL, USA, August 03-10, 2016*, 2016.

[24] David d'Enterria. Physics at the FCC-ee. In *17th Lomonosov Conference on Elementary Particle Physics Moscow, Russia, August 20-26, 2015*, 2016.

[25] Georges Aad et al. Measurement of W^+W^- production in pp collisions at $\sqrt{s}$=7??TeV with the ATLAS detector and limits on anomalous WWZ and WW? couplings. *Phys. Rev.*, D87(11):112001, 2013. [Erratum: Phys. Rev.D88,no.7,079906(2013)].

[26] The ATLAS collaboration. Measurement of the W^+W^- production cross section in proton-proton collisions at $\sqrt{s} = 8$ TeV with the ATLAS detector. 2014.

[27] Serguei Chatrchyan et al. Measurement of the W^+W^- Cross section in pp Collisions at $\sqrt{s} = 7$ TeV and Limits on Anomalous $WW\gamma$ and WWZ couplings. *Eur. Phys. J.*, C73(10):2610, 2013.

[28] Serguei Chatrchyan et al. Measurement of W+W- and ZZ production cross sections in pp collisions at sqrt(s) = 8 TeV. *Phys. Lett.*, B721:190–211, 2013.

[29] Stefano Frixione. A Next-to-leading order calculation of the cross-section for the production of W+ W- pairs in hadronic collisions. *Nucl. Phys.*, B410:280–324, 1993.

[30] J. Ohnemus. An Order α^-s calculation of hadronic W^-W^+ production. *Phys. Rev.*, D44:1403–1414, 1991.

[31] Serguei Chatrchyan et al. Measurement of Higgs boson production and properties in the WW decay channel with leptonic final states. *JHEP*, 01:096, 2014.

[32] Georges Aad et al. Measurements of Higgs boson production and couplings in diboson final states with the ATLAS detector at the LHC. *Phys. Lett.*, B726:88–119, 2013. [Erratum: Phys. Lett.B734,406(2014)].

[33] G. Davatz, G. Dissertori, M. Dittmar, M. Grazzini, and F. Pauss. Effective K factors for gg —> H —> WW —> l nu l nu at the LHC. *JHEP*, 05:009, 2004.

[34] David Curtin, Prerit Jaiswal, and Patrick Meade. Charginos Hiding In Plain Sight. *Phys. Rev.*, D87(3):031701, 2013.

[35] David Curtin, Prerit Jaiswal, Patrick Meade, and Pin-Ju Tien. Casting Light on BSM Physics with SM Standard Candles. *JHEP*, 08:068, 2013.

[36] Krzysztof Rolbiecki and Kazuki Sakurai. Light stops emerging in WW cross section measurements? *JHEP*, 09:004, 2013.

[37] David Curtin, Patrick Meade, and Pin-Ju Tien. Natural SUSY in Plain Sight. *Phys. Rev.*, D90(11):115012, 2014.

[38] Jong Soo Kim, Krzysztof Rolbiecki, Kazuki Sakurai, and Jamie Tattersall. 'Stop' that ambulance! New physics at the LHC? *JHEP*, 12:010, 2014.

[39] Prerit Jaiswal, Karoline Kopp, and Takemichi Okui. Higgs Production Amidst the LHC Detector. *Phys. Rev.*, D87(11):115017, 2013.

[40] Nikolas Kauer and Giampiero Passarino. Inadequacy of zero-width approximation for a light Higgs boson signal. *JHEP*, 08:116, 2012.

[41] Nikolas Kauer. Interference effects for H → WW/ZZ → $\ell\bar{\nu}_\ell\bar{\ell}\nu_\ell$ searches in gluon fusion at the LHC. *JHEP*, 12:082, 2013.

[42] Francisco Campanario, Michael Rauch, and Sebastian Sapeta. W^+W^- production at high transverse momenta beyond NLO. *Nucl. Phys.*, B879:65–79, 2014.

[43] Francisco Campanario and Sebastian Sapeta. WZ production beyond NLO for high-pT observables. *Phys. Lett.*, B718:100–104, 2012.

[44] F. Cascioli, S. Höche, F. Krauss, P. Maierhöfer, S. Pozzorini, and F. Siegert. Precise Higgs-background predictions: merging NLO QCD and squared quark-loop corrections to four-lepton + 0,1 jet production. *JHEP*, 01:046, 2014.

[45] Marco Bonvini, Fabrizio Caola, Stefano Forte, Kirill Melnikov, and Giovanni Ridolfi. Signal-background interference effects for $gg?H?W^+W^-$ beyond leading order. *Phys. Rev.*, D88(3):034032, 2013.

[46] F. Cascioli, T. Gehrmann, M. Grazzini, S. Kallweit, P. Maierhöfer, A. von Manteuffel, S. Pozzorini, D. Rathlev, L. Tancredi, and E. Weihs. ZZ production at hadron colliders in NNLO QCD. *Phys. Lett.*, B735:311–313, 2014.

[47] S. Dawson, Ian M. Lewis, and Mao Zeng. Threshold resummed and approximate next-to-next-to-leading order results for W^+W^- pair production at the LHC. *Phys. Rev.*, D88(5):054028, 2013.

[48] Lorenzo Magnea and George F. Sterman. Analytic continuation of the Sudakov form-factor in QCD. *Phys. Rev.*, D42:4222–4227, 1990.

[49] Valentin Ahrens, Thomas Becher, Matthias Neubert, and Li Lin Yang. Origin of the Large Perturbative Corrections to Higgs Production at Hadron Colliders. *Phys. Rev.*, D79:033013, 2009.

[50] Valentin Ahrens, Thomas Becher, Matthias Neubert, and Li Lin Yang. Renormalization-Group Improved Prediction for Higgs Production at Hadron Colliders. *Eur. Phys. J.*, C62:333–353, 2009.

[51] M. Grazzini. Soft-gluon effects in WW production at hadron colliders. *JHEP*, 01:095, 2006.

[52] Yan Wang, Chong Sheng Li, Ze Long Liu, Ding Yu Shao, and Hai Tao Li. Transverse-Momentum Resummation for Gauge Boson Pair Production at the Hadron Collider. *Phys. Rev.*, D88:114017, 2013.

[53] Victor Mukhamedovich Abazov et al. Measurement of the W boson mass with the D0 detector. *Phys. Rev.*, D89(1):012005, 2014.

[54] Daniel de Florian, Giancarlo Ferrera, Massimiliano Grazzini, and Damiano Tommasini. Transverse-momentum resummation: Higgs boson production at the Tevatron and the LHC. *JHEP*, 11:064, 2011.

[55] Andrea Banfi, Gavin P. Salam, and Giulia Zanderighi. NLL+NNLO predictions for jet-veto efficiencies in Higgs-boson and Drell-Yan production. *JHEP*, 06:159, 2012.

[56] Andrea Banfi, Pier Francesco Monni, Gavin P. Salam, and Giulia Zanderighi. Higgs and Z-boson production with a jet veto. *Phys. Rev. Lett.*, 109:202001, 2012.

[57] Carola F. Berger, Claudio Marcantonini, Iain W. Stewart, Frank J. Tackmann, and Wouter J. Waalewijn. Higgs Production with a Central Jet Veto at NNLL+NNLO. *JHEP*, 04:092, 2011.

[58] Frank J. Tackmann, Jonathan R. Walsh, and Saba Zuberi. Resummation Properties of Jet Vetoes at the LHC. *Phys. Rev.*, D86:053011, 2012.

[59] Iain W. Stewart, Frank J. Tackmann, Jonathan R. Walsh, and Saba Zuberi. Jet p_T resummation in Higgs production at $NNLL' + NNLO$. *Phys. Rev.*, D89(5):054001, 2014.

[60] Thomas Becher and Matthias Neubert. Factorization and NNLL Resummation for Higgs Production with a Jet Veto. *JHEP*, 07:108, 2012.

[61] Thomas Becher, Matthias Neubert, and Lorena Rothen. Factorization and N^3LL_p+NNLO predictions for the Higgs cross section with a jet veto. *JHEP*, 10:125, 2013.

[62] Ian Moult and Iain W. Stewart. Jet Vetoes interfering with $H \to WW$. *JHEP*, 09:129, 2014.

[63] Yuri L. Dokshitzer, Dmitri Diakonov, and S. I. Troian. On the Transverse Momentum Distribution of Massive Lepton Pairs. *Phys. Lett.*, B79:269–272, 1978.

[64] G. Parisi and R. Petronzio. Small Transverse Momentum Distributions in Hard Processes. *Nucl. Phys.*, B154:427–440, 1979.

[65] G. Curci, Mario Greco, and Y. Srivastava. QCD Jets From Coherent States. *Nucl. Phys.*, B159:451–468, 1979.

[66] John C. Collins and Davison E. Soper. Back-To-Back Jets in QCD. *Nucl. Phys.*, B193:381, 1981. [Erratum: Nucl. Phys.B213,545(1983)].

[67] John C. Collins and Davison E. Soper. Back-To-Back Jets: Fourier Transform from B to K-Transverse. *Nucl. Phys.*, B197:446–476, 1982.

[68] Jiro Kodaira and Luca Trentadue. Summing Soft Emission in QCD. *Phys. Lett.*, B112:66, 1982.

[69] Jiro Kodaira and Luca Trentadue. Single Logarithm Effects in electron-Positron Annihilation. *Phys. Lett.*, B123:335–338, 1983.

[70] Guido Altarelli, R. Keith Ellis, Mario Greco, and G. Martinelli. Vector Boson Production at Colliders: A Theoretical Reappraisal. *Nucl. Phys.*, B246:12–44, 1984.

[71] John C. Collins, Davison E. Soper, and George F. Sterman. Transverse Momentum Distribution in Drell-Yan Pair and W and Z Boson Production. *Nucl. Phys.*, B250:199–224, 1985.

[72] Stefano Catani, Daniel de Florian, and Massimiliano Grazzini. Universality of nonleading logarithmic contributions in transverse momentum distributions. *Nucl. Phys.*, B596:299–312, 2001.

[73] Giuseppe Bozzi, Stefano Catani, Daniel de Florian, and Massimiliano Grazzini. Transverse-momentum resummation and the spectrum of the Higgs boson at the LHC. *Nucl. Phys.*, B737:73–120, 2006.

[74] Giuseppe Bozzi, Stefano Catani, Giancarlo Ferrera, Daniel de Florian, and Massimiliano Grazzini. Production of Drell-Yan lepton pairs in hadron collisions: Transverse-momentum resummation at next-to-next-to-leading logarithmic accuracy. *Phys. Lett.*, B696:207–213, 2011.

[75] Daniel de Florian and Jose Zurita. Soft-gluon resummation for pseudoscalar Higgs boson production at hadron colliders. *Phys. Lett.*, B659:813–820, 2008.

[76] Stefano Catani, Daniel de Florian, Massimiliano Grazzini, and Paolo Nason. Soft gluon resummation for Higgs boson production at hadron colliders. *JHEP*, 07:028, 2003.

[77] Thomas Becher and Matthias Neubert. Drell-Yan Production at Small q_T, Transverse Parton Distributions and the Collinear Anomaly. *Eur. Phys. J.*, C71:1665, 2011.

[78] A. Vogt. Efficient evolution of unpolarized and polarized parton distributions with QCD-PEGASUS. *Comput. Phys. Commun.*, 170:65–92, 2005.

[79] A. D. Martin, W. J. Stirling, R. S. Thorne, and G. Watt. Parton distributions for the LHC. *Eur. Phys. J.*, C63:189–285, 2009.

[80] Eric Laenen, George F. Sterman, and Werner Vogelsang. Higher order QCD corrections in prompt photon production. *Phys. Rev. Lett.*, 84:4296–4299, 2000.

[81] G. Bozzi, S. Catani, D. de Florian, and M. Grazzini. The q(T) spectrum of the Higgs boson at the LHC in QCD perturbation theory. *Phys. Lett.*, B564:65–72, 2003.

[82] Paolo Nason. A New method for combining NLO QCD with shower Monte Carlo algorithms. *JHEP*, 11:040, 2004.

[83] Stefano Frixione, Paolo Nason, and Carlo Oleari. Matching NLO QCD computations with Parton Shower simulations: the POWHEG method. *JHEP*, 11:070, 2007.

[84] Simone Alioli, Paolo Nason, Carlo Oleari, and Emanuele Re. A general framework for implementing NLO calculations in shower Monte Carlo programs: the POWHEG BOX. *JHEP*, 06:043, 2010.

[85] J. Alwall, R. Frederix, S. Frixione, V. Hirschi, F. Maltoni, O. Mattelaer, H. S. Shao, T. Stelzer, P. Torrielli, and M. Zaro. The automated computation of tree-level and next-to-leading order differential cross sections, and their matching to parton shower simulations. *JHEP*, 07:079, 2014.

[86] M. Bahr et al. Herwig++ Physics and Manual. *Eur. Phys. J.*, C58:639–707, 2008.

[87] Torbjorn Sjostrand, Stephen Mrenna, and Peter Z. Skands. PYTHIA 6.4 Physics and Manual. *JHEP*, 0605:026, 2006.

[88] J. Pumplin, D.R. Stump, J. Huston, H.L. Lai, Pavel M. Nadolsky, et al. New generation of parton distributions with uncertainties from global QCD analysis. *JHEP*, 0207:012, 2002.

[89] J. de Favereau et al. DELPHES 3, A modular framework for fast simulation of a generic collider experiment. *JHEP*, 1402:057, 2014.

[90] Stefano Frixione and Bryan R. Webber. Matching NLO QCD computations and parton shower simulations. *JHEP*, 06:029, 2002.

[91] Giuseppe Bozzi, Stefano Catani, Giancarlo Ferrera, Daniel de Florian, and Massimiliano Grazzini. Transverse-momentum resummation: A Perturbative study of Z production at the Tevatron. *Nucl. Phys.*, B815:174–197, 2009.

[92] Vardan Khachatryan et al. Measurement of the $pp \to ZZ$ production cross section and constraints on anomalous triple gauge couplings in four-lepton final states at $\sqrt{s}$ =8 TeV. *Phys. Lett.*, B740:250–272, 2015. [erratum: Phys. Lett.B757,569(2016)].

[93] Michal Czakon, Alexander Mitov, Michele Papucci, Joshua T. Ruderman, and Andreas Weiler. Closing the stop gap. *Phys. Rev. Lett.*, 113(20):201803, 2014.

[94] T. Gehrmann, M. Grazzini, S. Kallweit, P. Maierhöfer, A. von Manteuffel, S. Pozzorini, D. Rathlev, and L. Tancredi. W^+W^- Production at Hadron Colliders in Next to Next to Leading Order QCD. *Phys. Rev. Lett.*, 113(21):212001, 2014.

[95] Thomas Gehrmann, Andreas von Manteuffel, and Lorenzo Tancredi. The two-loop helicity amplitudes for $q\overline{q}' \to V_1V_2 \to 4$ leptons. *JHEP*, 09:128, 2015.

[96] Lorenzo Tancredi, Thomas Gehrmann, and Andreas von Manteuffel. Two-loop QCD corrections to vector boson pair production at the LHC. *PoS*, RADCOR2015:025, 2016.

[97] Radovan Dermisek, Enrico Lunghi, and Seodong Shin. Contributions of flavor violating couplings of a Higgs boson to $pp \to WW$. *JHEP*, 08:126, 2015.

[98] Radovan Dermisek, Enrico Lunghi, and Seodong Shin. Two Higgs doublet model with vectorlike leptons and contributions to $pp \to WW$ and $H \to WW$. *JHEP*, 02:119, 2016.

[99] Prerit Jaiswal and Takemichi Okui. Explanation of the WW excess at the LHC by jet-veto resummation. *Phys. Rev.*, D90(7):073009, 2014.

[100] Patrick Meade, Harikrishnan Ramani, and Mao Zeng. Transverse momentum resummation effects in W^+W^- measurements. *Phys. Rev.*, D90(11):114006, 2014.

[101] Vardan Khachatryan et al. Measurement of the $\mathrm{W}^+\mathrm{W}^-$ cross section in pp collisions at $\sqrt{s} = 8$ TeV and limits on anomalous gauge couplings. *Eur. Phys. J.*, C76(7):401, 2016.

[102] Pier Francesco Monni and Giulia Zanderighi. On the excess in the inclusive $W^+W^- \to l^+l^-\nu\overline{\nu}$ cross section. *JHEP*, 05:013, 2015.

[103] Thomas Becher, Rikkert Frederix, Matthias Neubert, and Lorena Rothen. Automated NNLL $+$ NLO resummation for jet-veto cross sections. *Eur. Phys. J.*, C75(4):154, 2015.

[104] Prerit Jaiswal. A New Perspective on Scale Uncertainties for Diboson Processes. 2014.

[105] Prerit Jaiswal and Takemichi Okui. Reemergence of rapidity-scale uncertainty in soft-collinear effective theory. *Phys. Rev.*, D92(7):074035, 2015.

[106] Massimiliano Grazzini, Stefan Kallweit, Dirk Rathlev, and Marius Wiesemann. Transverse-momentum resummation for vector-boson pair production at NNLL+NNLO. *JHEP*, 08:154, 2015.

[107] Thomas Becher and Guido Bell. Enhanced nonperturbative effects through the collinear anomaly. *Phys. Rev. Lett.*, 112(18):182002, 2014.

[108] CMS Collaboration. Measurement of the W^+W^- cross section in pp collisions at sqrt(s) = 8 TeV and limits on anomalous gauge couplings. 2015.

[109] Massimiliano Procura, Wouter J. Waalewijn, and Lisa Zeune. Resummation of Double-Differential Cross Sections and Fully-Unintegrated Parton Distribution Functions. *JHEP*, 02:117, 2015.

[110] Measurement of WW production rate. *CMS-PAS-SMP-12-005*, 2012.

[111] Measurement of WW production rate. *CMS-PAS-SMP-12-013*, 2012.

[112] Massimiliano Grazzini, Stefan Kallweit, Stefano Pozzorini, Dirk Rathlev, and Marius Wiesemann. W^+W^- production at the LHC: fiducial cross sections and distributions in NNLO QCD. 2016.

[113] Stefano Catani, Leandro Cieri, Giancarlo Ferrera, Daniel de Florian, and Massimiliano Grazzini. Vector boson production at hadron colliders: a fully exclusive QCD calculation at NNLO. *Phys. Rev. Lett.*, 103:082001, 2009.

[114] John M. Campbell, R. Keith Ellis, and Ciaran Williams. Vector boson pair production at the LHC. *JHEP*, 07:018, 2011.

[115] Prerit Jaiswal, Patrick Meade, and Harikrishnan Ramani. Precision diboson measurements and the interplay of pT and jet-veto resummations. 2015.

[116] Harikrishnan Ramani. The WW story. *PoS*, DIS2015:118, 2015.

[117] Georges Aad et al. Measurement of total and differential W^+W^- production cross sections in proton-proton collisions at $\sqrt{s} = 8$ TeV with the ATLAS detector and limits on anomalous triple-gauge-boson couplings. 2016.

[118] Fabrizio Caola, Johannes M. Henn, Kirill Melnikov, Alexander V. Smirnov, and Vladimir A. Smirnov. Two-loop helicity amplitudes for the production of two off-shell electroweak bosons in gluon fusion. *JHEP*, 06:129, 2015.

[119] Christian W. Bauer, Sean Fleming, and Michael E. Luke. Summing Sudakov logarithms in B —> X(s gamma) in effective field theory. *Phys. Rev.*, D63:014006, 2000.

[120] Christian W. Bauer, Sean Fleming, Dan Pirjol, and Iain W. Stewart. An Effective field theory for collinear and soft gluons: Heavy to light decays. *Phys. Rev.*, D63:114020, 2001.

[121] Christian W. Bauer and Iain W. Stewart. Invariant operators in collinear effective theory. *Phys. Lett.*, B516:134–142, 2001.

[122] Christian W. Bauer, Dan Pirjol, and Iain W. Stewart. Soft collinear factorization in effective field theory. *Phys. Rev.*, D65:054022, 2002.

[123] M. Beneke, A. P. Chapovsky, M. Diehl, and T. Feldmann. Soft collinear effective theory and heavy to light currents beyond leading power. *Nucl. Phys.*, B643:431–476, 2002.

[124] M. Beneke and T. Feldmann. Multipole expanded soft collinear effective theory with non-Abelian gauge symmetry. *Phys. Lett.*, B553:267–276, 2003.

[125] Richard J. Hill and Matthias Neubert. Spectator interactions in soft collinear effective theory. *Nucl. Phys.*, B657:229–256, 2003.

[126] T. Gleisberg, Stefan. Hoeche, F. Krauss, M. Schonherr, S. Schumann, F. Siegert, and J. Winter. Event generation with SHERPA 1.1. *JHEP*, 02:007, 2009.

[127] Stefano Catani and Massimiliano Grazzini. An NNLO subtraction formalism in hadron collisions and its application to Higgs boson production at the LHC. *Phys. Rev. Lett.*, 98:222002, 2007.

[128] F. Krauss, R. Kuhn, and G. Soff. AMEGIC++ 1.0: A Matrix element generator in C++. *JHEP*, 02:044, 2002.

[129] Tanju Gleisberg and Stefan Hoeche. Comix, a new matrix element generator. *JHEP*, 12:039, 2008.

[130] Thomas Gehrmann, Thomas Luebbert, and Li Lin Yang. Calculation of the transverse parton distribution functions at next-to-next-to-leading order. *JHEP*, 06:155, 2014.

[131] S. Dittmaier, S. Kallweit, and P. Uwer. NLO QCD corrections to WW+jet production at hadron colliders. *Phys. Rev. Lett.*, 100:062003, 2008.

[132] Tom Melia, Kirill Melnikov, Raoul Rontsch, Markus Schulze, and Giulia Zanderighi. Gluon fusion contribution to W+W- + jet production. *JHEP*, 08:115, 2012.

[133] John M. Campbell, David J. Miller, and Tania Robens. Next-to-Leading Order Predictions for WW+Jet Production. *Phys. Rev.*, D92(1):014033, 2015.

[134] S. Catani and M. H. Seymour. A General algorithm for calculating jet cross-sections in NLO QCD. *Nucl. Phys.*, B485:291–419, 1997. [Erratum: Nucl. Phys.B510,503(1998)].

[135] Fabio Cascioli, Philipp Maierhofer, and Stefano Pozzorini. Scattering Amplitudes with Open Loops. *Phys. Rev. Lett.*, 108:111601, 2012.

[136] Stefano Catani, Leandro Cieri, Daniel de Florian, Giancarlo Ferrera, and Massimiliano Grazzini. Universality of transverse-momentum resummation and hard factors at the NNLO. *Nucl. Phys.*, B881:414–443, 2014.

[137] Charalampos Anastasiou, Lance J. Dixon, Kirill Melnikov, and Frank Petriello. Dilepton rapidity distribution in the Drell-Yan process at NNLO in QCD. *Phys. Rev. Lett.*, 91:182002, 2003.

[138] C. Anastasiou, E. W. Nigel Glover, and M. E. Tejeda-Yeomans. Two loop QED and QCD corrections to massless fermion boson scattering. *Nucl. Phys.*, B629:255–289, 2002.

[139] A. D. Martin, W. J. Stirling, R. S. Thorne, and G. Watt. Heavy-quark mass dependence in global PDF analyses and 3- and 4-flavour parton distributions. *Eur. Phys. J.*, C70:51–72, 2010.

[140] Jonathan R. Gaunt. Glauber Gluons and Multiple Parton Interactions. *JHEP*, 07:110, 2014.

[141] Mao Zeng. Drell-Yan process with jet vetoes: breaking of generalized factorization. *JHEP*, 10:189, 2015.

[142] Ira Z. Rothstein and Iain W. Stewart. An Effective Field Theory for Forward Scattering and Factorization Violation. 2016.

[143] Thomas Becher, Matthias Neubert, and Gang Xu. Dynamical Threshold Enhancement and Resummation in Drell-Yan Production. *JHEP*, 07:030, 2008.

[144] Ye Li and Xiaohui Liu. High precision predictions for exclusive VH production at the LHC. *JHEP*, 06:028, 2014.

[145] Mrinal Dasgupta, Frédéric Dreyer, Gavin P. Salam, and Gregory Soyez. Small-radius jets to all orders in QCD. *JHEP*, 04:039, 2015.

[146] Andrea Banfi, Fabrizio Caola, Frédéric A. Dreyer, Pier F. Monni, Gavin P. Salam, Giulia Zanderighi, and Falko Dulat. Jet-vetoed Higgs cross section in gluon fusion at N^{3}LO+NNLL with small-R resummation. *JHEP*, 04:049, 2016.

[147] Jui-yu Chiu, Ambar Jain, Duff Neill, and Ira Z. Rothstein. The Rapidity Renormalization Group. *Phys. Rev. Lett.*, 108:151601, 2012.

[148] Jui-Yu Chiu, Ambar Jain, Duff Neill, and Ira Z. Rothstein. A Formalism for the Systematic Treatment of Rapidity Logarithms in Quantum Field Theory. *JHEP*, 05:084, 2012.

[149] Yasuyuki Akiba et al. The Hot QCD White Paper: Exploring the Phases of QCD at RHIC and the LHC. 2015.

[150] P. A. R. Ade et al. Planck 2015 results. XIII. Cosmological parameters. *Astron. Astrophys.*, 594:A13, 2016.

[151] Edward W. Kolb and Michael S. Turner. The Early Universe. *Front.Phys.*, 69:1–547, 1990.

[152] A. D. Sakharov. Violation of CP Invariance, c Asymmetry, and Baryon Asymmetry of the Universe. *Pisma Zh. Eksp. Teor. Fiz.*, 5:32–35, 1967. [Usp. Fiz. Nauk161,61(1991)].

[153] V.A. Kuzmin, V.A. Rubakov, and M.E. Shaposhnikov. On the Anomalous Electroweak Baryon Number Nonconservation in the Early Universe. *Phys.Lett.*, B155:36, 1985.

[154] Frans R. Klinkhamer and N.S. Manton. A Saddle Point Solution in the Weinberg-Salam Theory. *Phys.Rev.*, D30:2212, 1984.

[155] M. E. Shaposhnikov. Possible Appearance of the Baryon Asymmetry of the Universe in an Electroweak Theory. *JETP Lett.*, 44:465–468, 1986. [Pisma Zh. Eksp. Teor. Fiz.44,364(1986)].

[156] M. E. Shaposhnikov. Baryon Asymmetry of the Universe in Standard Electroweak Theory. *Nucl. Phys.*, B287:757–775, 1987.

[157] Peter Brockway Arnold and Larry D. McLerran. Sphalerons, Small Fluctuations and Baryon Number Violation in Electroweak Theory. *Phys.Rev.*, D36:581, 1987.

[158] Peter Brockway Arnold and Larry D. McLerran. The Sphaleron Strikes Back. *Phys.Rev.*, D37:1020, 1988.

[159] S. Yu. Khlebnikov and M.E. Shaposhnikov. The Statistical Theory of Anomalous Fermion Number Nonconservation. *Nucl.Phys.*, B308:885–912, 1988.

[160] James M. Cline. Baryogenesis. 2006.

[161] Mark Trodden. Electroweak baryogenesis. *Rev.Mod.Phys.*, 71:1463–1500, 1999.

[162] Antonio Riotto and Mark Trodden. Recent progress in baryogenesis. *Ann.Rev.Nucl.Part.Sci.*, 49:35–75, 1999.

[163] Mariano Quiros. Finite temperature field theory and phase transitions. pages 187–259, 1999.

[164] David E. Morrissey and Michael J. Ramsey-Musolf. Electroweak baryogenesis. *New J.Phys.*, 14:125003, 2012.

[165] L. Dolan and R. Jackiw. Symmetry Behavior at Finite Temperature. *Phys. Rev.*, D9:3320–3341, 1974.

[166] Steven Weinberg. Gauge and Global Symmetries at High Temperature. *Phys.Rev.*, D9:3357–3378, 1974.

[167] A. I. Bochkarev and M. E. Shaposhnikov. Electroweak Production of Baryon Asymmetry and Upper Bounds on the Higgs and Top Masses. *Mod. Phys. Lett.*, A2:417, 1987.

[168] K. Kajantie, M. Laine, K. Rummukainen, and Mikhail E. Shaposhnikov. The Electroweak phase transition: A Nonperturbative analysis. *Nucl. Phys.*, B466:189–258, 1996.

[169] Stefano Profumo, Michael J. Ramsey-Musolf, and Gabe Shaughnessy. Singlet Higgs phenomenology and the electroweak phase transition. *JHEP*, 0708:010, 2007.

[170] A. Ashoorioon and T. Konstandin. Strong electroweak phase transitions without collider traces. *JHEP*, 0907:086, 2009.

[171] Poul H. Damgaard, Donal O'Connell, Troels C. Petersen, and Anders Tranberg. Constraints on New Physics from Baryogenesis and Large Hadron Collider Data. *Phys.Rev.Lett.*, 111(22):221804, 2013.

[172] Vernon Barger, Paul Langacker, Mathew McCaskey, Michael J. Ramsey-Musolf, and Gabe Shaughnessy. LHC Phenomenology of an Extended Standard Model with a Real Scalar Singlet. *Phys.Rev.*, D77:035005, 2008.

[173] Jose R. Espinosa, Thomas Konstandin, and Francesco Riva. Strong Electroweak Phase Transitions in the Standard Model with a Singlet. *Nucl.Phys.*, B854:592–630, 2012.

[174] Andrew Noble and Maxim Perelstein. Higgs self-coupling as a probe of electroweak phase transition. *Phys.Rev.*, D78:063518, 2008.

[175] James M. Cline and Kimmo Kainulainen. Electroweak baryogenesis and dark matter from a singlet Higgs. *JCAP*, 1301:012, 2013.

[176] James M. Cline, Kimmo Kainulainen, Pat Scott, and Christoph Weniger. Update on scalar singlet dark matter. *Phys.Rev.*, D88:055025, 2013.

[177] Tommi Alanne, Kimmo Tuominen, and Ville Vaskonen. Strong phase transition, dark matter and vacuum stability from simple hidden sectors. 2014.

[178] Jose Ramon Espinosa and Mariano Quiros. Novel Effects in Electroweak Breaking from a Hidden Sector. *Phys.Rev.*, D76:076004, 2007.

[179] Stefano Profumo, Michael J. Ramsey-Musolf, Carroll L. Wainwright, and Peter Winslow. Singlet-Catalyzed Electroweak Phase Transitions and Precision Higgs Studies. 2014.

[180] Kaori Fuyuto and Eibun Senaha. Improved sphaleron decoupling condition and the Higgs coupling constants in the real singlet-extended SM. *Phys.Rev.*, D90:015015, 2014.

[181] Malcolm Fairbairn and Robert Hogan. Singlet Fermionic Dark Matter and the Electroweak Phase Transition. *JHEP*, 1309:022, 2013.

[182] Minyuan Jiang, Ligong Bian, Weicong Huang, and Jing Shu. Impact of a complex singlet: Electroweak baryogenesis and dark matter. *Phys. Rev.*, D93(6):065032, 2016.

[183] Massimo Pietroni. The Electroweak phase transition in a nonminimal supersymmetric model. *Nucl.Phys.*, B402:27–45, 1993.

[184] A.T. Davies, C.D. Froggatt, and R.G. Moorhouse. Electroweak baryogenesis in the next-to-minimal supersymmetric model. *Phys.Lett.*, B372:88–94, 1996.

[185] Stephan J. Huber, Thomas Konstandin, Tomislav Prokopec, and Michael G. Schmidt. Electroweak Phase Transition and Baryogenesis in the nMSSM. *Nucl.Phys.*, B757:172–196, 2006.

[186] A. Menon, D.E. Morrissey, and C.E.M. Wagner. Electroweak baryogenesis and dark matter in the nMSSM. *Phys.Rev.*, D70:035005, 2004.

[187] Stephan J. Huber, Thomas Konstandin, Tomislav Prokopec, and Michael G. Schmidt. Baryogenesis in the MSSM, nMSSM and NMSSM. *Nucl.Phys.*, A785:206–209, 2007.

[188] Weicong Huang, Zhaofeng Kang, Jing Shu, Peiwen Wu, and Jin Min Yang. New Insights of Electroweak Phase Transition in NMSSM. 2014.

[189] Jonathan Kozaczuk, Stefano Profumo, Laurel Stephenson Haskins, and Carroll L. Wainwright. Cosmological Phase Transitions and their Properties in the NMSSM. 2014.

[190] G. C. Dorsch, S. J. Huber, and J. M. No. A strong electroweak phase transition in the 2HDM after LHC8. *JHEP*, 10:029, 2013.

[191] G. C. Dorsch, S. J. Huber, K. Mimasu, and J. M. No. Echoes of the Electroweak Phase Transition: Discovering a second Higgs doublet through $A_0 \to ZH_0$. *Phys. Rev. Lett.*, 113(21):211802, 2014.

[192] Hiren H. Patel and Michael J. Ramsey-Musolf. Stepping Into Electroweak Symmetry Breaking: Phase Transitions and Higgs Phenomenology. *Phys. Rev.*, D88:035013, 2013.

[193] Nikita Blinov, Jonathan Kozaczuk, David E. Morrissey, and Carlos Tamarit. Electroweak Baryogenesis from Exotic Electroweak Symmetry Breaking. *Phys. Rev.*, D92(3):035012, 2015.

[194] Satoru Inoue, Grigory Ovanesyan, and Michael J. Ramsey-Musolf. Two-Step Electroweak Baryogenesis. *Phys. Rev.*, D93:015013, 2016.

[195] Marcela S. Carena, M. Quiros, and C.E.M. Wagner. Opening the window for electroweak baryogenesis. *Phys.Lett.*, B380:81–91, 1996.

[196] M. Laine and K. Rummukainen. The MSSM electroweak phase transition on the lattice. *Nucl.Phys.*, B535:423–457, 1998.

[197] J.R. Espinosa. Dominant two loop corrections to the MSSM finite temperature effective potential. *Nucl.Phys.*, B475:273–292, 1996.

[198] D. Delepine, J.M. Gerard, R. Gonzalez Felipe, and J. Weyers. A Light stop and electroweak baryogenesis. *Phys.Lett.*, B386:183–188, 1996.

[199] Marcela S. Carena, M. Quiros, and C.E.M. Wagner. Electroweak baryogenesis and Higgs and stop searches at LEP and the Tevatron. *Nucl.Phys.*, B524:3–22, 1998.

[200] S.J. Huber, P. John, and M.G. Schmidt. Bubble walls, CP violation and electroweak baryogenesis in the MSSM. *Eur.Phys.J.*, C20:695–711, 2001.

[201] Marcela S. Carena, M. Quiros, M. Seco, and C.E.M. Wagner. Improved results in supersymmetric electroweak baryogenesis. *Nucl.Phys.*, B650:24–42, 2003.

[202] Christopher Lee, Vincenzo Cirigliano, and Michael J. Ramsey-Musolf. Resonant relaxation in electroweak baryogenesis. *Phys.Rev.*, D71:075010, 2005.

[203] Marcela Carena, Germano Nardini, Mariano Quiros, and Carlos E.M. Wagner. The Effective Theory of the Light Stop Scenario. *JHEP*, 0810:062, 2008.

[204] M. Carena, Germano Nardini, M. Quiros, and C.E.M. Wagner. The Baryogenesis Window in the MSSM. *Nucl.Phys.*, B812:243–263, 2009.

[205] Vincenzo Cirigliano, Yingchuan Li, Stefano Profumo, and Michael J. Ramsey-Musolf. MSSM Baryogenesis and Electric Dipole Moments: An Update on the Phenomenology. *JHEP*, 1001:002, 2010.

[206] David Curtin, Prerit Jaiswal, and Patrick Meade. Excluding Electroweak Baryogenesis in the MSSM. *JHEP*, 08:005, 2012.

[207] Timothy Cohen, David E. Morrissey, and Aaron Pierce. Electroweak Baryogenesis and Higgs Signatures. *Phys. Rev.*, D86:013009, 2012.

[208] Andrey Katz and Maxim Perelstein. Higgs Couplings and Electroweak Phase Transition. 2014.

[209] Andrey Katz, Maxim Perelstein, Michael J. Ramsey-Musolf, and Peter Winslow. Stop-Catalyzed Baryogenesis Beyond the MSSM. *Phys. Rev.*, D92(9):095019, 2015.

[210] James M. Cline and Kimmo Kainulainen. A New source for electroweak baryogenesis in the MSSM. *Phys.Rev.Lett.*, 85:5519–5522, 2000.

[211] Guy D. Moore. Electroweak bubble wall friction: Analytic results. *JHEP*, 0003:006, 2000.

[212] P. John and M.G. Schmidt. Do stops slow down electroweak bubble walls? *Nucl.Phys.*, B598:291–305, 2001.

[213] P. John and M.G. Schmidt. Bubble wall velocity in the MSSM. pages 284–288, 2000.

[214] Ariel Megevand and Alejandro D. Sanchez. Velocity of electroweak bubble walls. *Nucl.Phys.*, B825:151–176, 2010.

[215] J.M. Moreno, M. Quiros, and M. Seco. Bubbles in the supersymmetric standard model. *Nucl.Phys.*, B526:489–500, 1998.

[216] A. Riotto. The More relaxed supersymmetric electroweak baryogenesis. *Phys.Rev.*, D58:095009, 1998.

[217] Vincenzo Cirigliano, Michael J. Ramsey-Musolf, Sean Tulin, and Christopher Lee. Yukawa and tri-scalar processes in electroweak baryogenesis. *Phys.Rev.*, D73:115009, 2006.

[218] Daniel J.H. Chung, Bjorn Garbrecht, Michael J. Ramsey-Musolf, and Sean Tulin. Yukawa Interactions and Supersymmetric Electroweak Baryogenesis. *Phys.Rev.Lett.*, 102:061301, 2009.

[219] Yingchuan Li, Stefano Profumo, and Michael Ramsey-Musolf. Bino-driven Electroweak Baryogenesis with highly suppressed Electric Dipole Moments. *Phys.Lett.*, B673:95–100, 2009.

[220] James M. Cline, Michael Joyce, and Kimmo Kainulainen. Supersymmetric electroweak baryogenesis in the WKB approximation. *Phys.Lett.*, B417:79–86, 1998.

[221] James M. Cline, Michael Joyce, and Kimmo Kainulainen. Supersymmetric electroweak baryogenesis. *JHEP*, 0007:018, 2000.

[222] Thomas Konstandin, Tomislav Prokopec, and Michael G. Schmidt. Kinetic description of fermion flavor mixing and CP-violating sources for baryogenesis. *Nucl.Phys.*, B716:373–400, 2005.

[223] Thomas Konstandin, Tomislav Prokopec, and Michael G. Schmidt. Axial currents from CKM matrix CP violation and electroweak baryogenesis. *Nucl.Phys.*, B679:246–260, 2004.

[224] Jonathan Kozaczuk, Stefano Profumo, Michael J. Ramsey-Musolf, and Carroll L. Wainwright. Supersymmetric Electroweak Baryogenesis Via Resonant Sfermion Sources. *Phys.Rev.*, D86:096001, 2012.

[225] Hiren H. Patel and Michael J. Ramsey-Musolf. Baryon Washout, Electroweak Phase Transition, and Perturbation Theory. *JHEP*, 1107:029, 2011.

[226] David J. Gross, Robert D. Pisarski, and Laurence G. Yaffe. QCD and Instantons at Finite Temperature. *Rev. Mod. Phys.*, 53:43, 1981.

[227] Rajesh R. Parwani. Resummation in a hot scalar field theory. *Phys. Rev.*, D45:4695, 1992. [Erratum: Phys. Rev.D48,5965(1993)].

[228] Peter Brockway Arnold and Olivier Espinosa. The Effective potential and first order phase transitions: Beyond leading-order. *Phys. Rev.*, D47:3546, 1993. [Erratum: Phys. Rev.D50,6662(1994)].

[229] J. R. Espinosa, M. Quiros, and F. Zwirner. On the phase transition in the scalar theory. *Phys. Lett.*, B291:115–124, 1992.

[230] J. R. Espinosa, M. Quiros, and F. Zwirner. On the nature of the electroweak phase transition. *Phys. Lett.*, B314:206–216, 1993.

[231] Mariano Quiros. On daisy and superdaisy resummation of the effective potential at finite temperature. In *Elementary particle physics. Proceedings, 4th Hellenic School, Corfu, Greece, September 2-20, 1992. 1&2*, pages 502–511, 1992.

[232] C. Glenn Boyd, David E. Brahm, and Stephen D. H. Hsu. Resummation methods at finite temperature: The Tadpole way. *Phys. Rev.*, D48:4963–4973, 1993.

[233] Michael Dine, Robert G. Leigh, Patrick Y. Huet, Andrei D. Linde, and Dmitri A. Linde. Towards the theory of the electroweak phase transition. *Phys. Rev.*, D46:550–571, 1992.

[234] C. Glenn Boyd, David E. Brahm, and Stephen D. H. Hsu. Corrections to the electroweak effective action at finite temperature. *Phys. Rev.*, D48:4952–4962, 1993.

[235] Christophe Grojean, Geraldine Servant, and James D. Wells. First-order electroweak phase transition in the standard model with a low cutoff. *Phys.Rev.*, D71:036001, 2005.

[236] Dietrich Bodeker, Lars Fromme, Stephan J. Huber, and Michael Seniuch. The Baryon asymmetry in the standard model with a low cut-off. *JHEP*, 02:026, 2005.

[237] Cedric Delaunay, Christophe Grojean, and James D. Wells. Dynamics of Non-renormalizable Electroweak Symmetry Breaking. *JHEP*, 0804:029, 2008.

[238] Benjamin Grinstein and Michael Trott. Electroweak Baryogenesis with a Pseudo-Goldstone Higgs. *Phys. Rev.*, D78:075022, 2008.

[239] D.M. Asner, T. Barklow, C. Calancha, K. Fujii, N. Graf, et al. ILC Higgs White Paper. 2013.

[240] Junping Tian and Keisuke Fujii. Measurement of Higgs couplings and self-coupling at the ILC. *PoS*, EPS-HEP2013:316, 2013.

[241] Jingyu Tang et al. Concept for a Future Super Proton-Proton Collider. 2015.

[242] Alan J. Barr, Matthew J. Dolan, Christoph Englert, Danilo Enoque Ferreira de Lima, and Michael Spannowsky. Higgs Self-Coupling Measurements at a 100 TeV Hadron Collider. *JHEP*, 02:016, 2015.

[243] ATLAS-PHYS-PUB-2013-001, 2013.

[244] J. Baglio, A. Djouadi, R. Gröber, M.M. Mühlleitner, J. Quevillon, et al. The measurement of the Higgs self-coupling at the LHC: theoretical status. *JHEP*, 1304:151, 2013.

[245] Florian Goertz, Andreas Papaefstathiou, Li Lin Yang, and Jose Zurita. Higgs Boson self-coupling measurements using ratios of cross sections. *JHEP*, 1306:016, 2013.

[246] Vernon Barger, Lisa L. Everett, C.B. Jackson, and Gabe Shaughnessy. Higgs-Pair Production and Measurement of the Triscalar Coupling at LHC(8,14). *Phys.Lett.*, B728:433–436, 2014.

[247] Weiming Yao. Studies of measuring Higgs self-coupling with $HH \to b\bar{b}\gamma\gamma$ at the future hadron colliders. 2013.

[248] Matthew J. Dolan, Christoph Englert, and Michael Spannowsky. Higgs self-coupling measurements at the LHC. *JHEP*, 10:112, 2012.

[249] Peisi Huang, Aniket Joglekar, Bing Li, and Carlos E. M. Wagner. Probing the Electroweak Phase Transition at the LHC. *Phys. Rev.*, D93(5):055049, 2016.

[250] Marc Kamionkowski, Arthur Kosowsky, and Michael S. Turner. Gravitational radiation from first order phase transitions. *Phys. Rev.*, D49:2837–2851, 1994.

[251] Christophe Grojean and Geraldine Servant. Gravitational Waves from Phase Transitions at the Electroweak Scale and Beyond. *Phys. Rev.*, D75:043507, 2007.

[252] Sidney R. Coleman and Erick J. Weinberg. Radiative Corrections as the Origin of Spontaneous Symmetry Breaking. *Phys. Rev.*, D7:1888–1910, 1973.

[253] Daniel J.H. Chung, Andrew J. Long, and Lian-Tao Wang. The 125 GeV Higgs and Electroweak Phase Transition Model Classes. *Phys.Rev.*, D87:023509, 2013.

[254] Michel Le Bellac. *Thermal Field Theory*. Cambridge University Press, 2011.

[255] Ashutosh V. Kotwal, Michael J. Ramsey-Musolf, Jose Miguel No, and Peter Winslow. Singlet-catalyzed electroweak phase transitions in the 100 TeV frontier. *Phys. Rev.*, D94(3):035022, 2016.

[256] Jonathan Kozaczuk. Bubble Expansion and the Viability of Singlet-Driven Electroweak Baryogenesis. *JHEP*, 10:135, 2015.

[257] P. H. Damgaard, A. Haarr, D. O'Connell, and A. Tranberg. Effective Field Theory and Electroweak Baryogenesis in the Singlet-Extended Standard Model. *JHEP*, 02:107, 2016.

[258] Stephen P. Martin. Taming the Goldstone contributions to the effective potential. 2014.

[259] J. Elias-Miro, J. R. Espinosa, and T. Konstandin. Taming Infrared Divergences in the Effective Potential. *JHEP*, 08:034, 2014.

[260] M. E. Carrington. The Effective potential at finite temperature in the Standard Model. *Phys. Rev.*, D45:2933–2944, 1992.

[261] Christoph Englert and Matthew McCullough. Modified Higgs Sectors and NLO Associated Production. *JHEP*, 1307:168, 2013.

[262] Nathaniel Craig, Christoph Englert, and Matthew McCullough. New Probe of Naturalness. *Phys. Rev. Lett.*, 111(12):121803, 2013.

[263] Z. Chacko, Hock-Seng Goh, and Roni Harnik. The Twin Higgs: Natural electroweak breaking from mirror symmetry. *Phys. Rev. Lett.*, 96:231802, 2006.

[264] Gustavo Burdman, Z. Chacko, Hock-Seng Goh, and Roni Harnik. Folded supersymmetry and the LEP paradox. *JHEP*, 02:009, 2007.

[265] William A. Bardeen. On naturalness in the standard model. In *Ontake Summer Institute on Particle Physics Ontake Mountain, Japan, August 27-September 2, 1995*, 1995.

[266] David Curtin and Prashant Saraswat. Towards a No-Lose Theorem for Naturalness. *Phys. Rev.*, D93(5):055044, 2016.

[267] JiJi Fan, Matthew Reece, and Joshua T. Ruderman. Stealth Supersymmetry. *JHEP*, 11:012, 2011.

[268] The ATLAS collaboration. Search for the Supersymmetric Partner of the Top Quark in the Jets+Emiss Final State at sqrt(s) = 13 TeV. 2016.

[269] The ATLAS collaboration. Further searches for squarks and gluinos in final states with jets and missing transverse momentum at $\sqrt{s}$ =13 TeV with the ATLAS detector. 2016.

[270] CMS Collaboration. Search for supersymmetry in events with jets and missing transverse momentum in proton-proton collisions at 13 TeV. 2016.

[271] CMS Collaboration. Search for new physics in the all-hadronic final state with the MT2 variable. 2016.

[272] An inclusive search for new phenomena in final states with one or more jets and missing transverse momentum at 13 TeV with the AlphaT variable. Technical Report CMS-PAS-SUS-16-016, CERN, Geneva, 2016.

[273] Zhenyu Han, Andrey Katz, David Krohn, and Matthew Reece. (Light) Stop Signs. *JHEP*, 08:083, 2012.

[274] Kaoru Hagiwara and Toshifumi Yamada. Equal-velocity scenario for hiding dark matter at the LHC. *Phys. Rev.*, D91(9):094007, 2015.

[275] Haipeng An and Lian-Tao Wang. Opening up the compressed region of top squark searches at 13 TeV LHC. *Phys. Rev. Lett.*, 115:181602, 2015.

[276] Hsin-Chia Cheng, Christina Gao, Lingfeng Li, and Nicolas A. Neill. Stop Search in the Compressed Region via Semileptonic Decays. *JHEP*, 05:036, 2016.

[277] JiJi Fan, Matthew Reece, and Joshua T. Ruderman. A Stealth Supersymmetry Sampler. *JHEP*, 07:196, 2012.

[278] Asimina Arvanitaki and Giovanni Villadoro. A Non Standard Model Higgs at the LHC as a Sign of Naturalness. *JHEP*, 02:144, 2012.

[279] Dean Carmi, Adam Falkowski, Eric Kuflik, and Tomer Volansky. Interpreting LHC Higgs Results from Natural New Physics Perspective. *JHEP*, 07:136, 2012.

[280] Kfir Blum, Raffaele Tito D'Agnolo, and JiJi Fan. Natural SUSY Predicts: Higgs Couplings. *JHEP*, 01:057, 2013.

[281] Marco Farina, Maxim Perelstein, and Nicolas Rey-Le Lorier. Higgs Couplings and Naturalness. *Phys. Rev.*, D90(1):015014, 2014.

[282] JiJi Fan and Matthew Reece. A New Look at Higgs Constraints on Stops. *JHEP*, 06:031, 2014.

[283] JiJi Fan, Matthew Reece, and Lian-Tao Wang. Precision Natural SUSY at CEPC, FCC-ee, and ILC. *JHEP*, 08:152, 2015.

[284] C. Englert, A. Freitas, M. M. Mühlleitner, T. Plehn, M. Rauch, M. Spira, and K. Walz. Precision Measurements of Higgs Couplings: Implications for New Physics Scales. *J. Phys.*, G41:113001, 2014.

[285] Brian Henning, Xiaochuan Lu, and Hitoshi Murayama. What do precision Higgs measurements buy us? 2014.

[286] Kyu Jung Bae, Howard Baer, Natsumi Nagata, and Hasan Serce. Prospects for Higgs coupling measurements in SUSY with radiatively-driven naturalness. *Phys. Rev.*, D92(3):035006, 2015.

[287] Timothy Cohen and Aaron Pierce. Electroweak Baryogenesis and Colored Scalars. *Phys. Rev.*, D85:033006, 2012.

[288] Marcela Carena, Germano Nardini, Mariano Quiros, and Carlos E. M. Wagner. MSSM Electroweak Baryogenesis and LHC Data. *JHEP*, 02:001, 2013.

[289] EPS 2017: `http://eps-hep2017.eu`.

[290] J. Reuter and M. Tonini. Can the 125 GeV Higgs be the Little Higgs? *JHEP*, 02:077, 2013.

[291] Joshua Berger, Jay Hubisz, and Maxim Perelstein. A Fermionic Top Partner: Naturalness and the LHC. *JHEP*, 07:016, 2012.

[292] Bingfang Yang, Guofa Mi, and Ning Liu. Higgs couplings and Naturalness in the littlest Higgs model with T-parity at the LHC and TLEP. *JHEP*, 10:047, 2014.

[293] Chengcheng Han, Archil Kobakhidze, Ning Liu, Lei Wu, and Bingfang Yang. Constraining Top partner and Naturalness at the LHC and TLEP. *Nucl. Phys.*, B890:388–399, 2014.

[294] Jack H. Collins, Bithika Jain, Maxim Perelstein, and Nicolas Rey-Le Lorier. Spin-One Top Partner: Phenomenology. *JHEP*, 08:022, 2014.

[295] John R. Ellis, Mary K. Gaillard, and Dimitri V. Nanopoulos. A Phenomenological Profile of the Higgs Boson. *Nucl. Phys.*, B106:292, 1976.

[296] Mikhail A. Shifman, A. I. Vainshtein, M. B. Voloshin, and Valentin I. Zakharov. Low-Energy Theorems for Higgs Boson Couplings to Photons. *Sov. J. Nucl. Phys.*, 30:711–716, 1979. [Yad. Fiz.30,1368(1979)].

[297] J R Andersen et al. Handbook of LHC Higgs Cross Sections: 3. Higgs Properties. 2013.

[298] Higgs Working Group. *Branching ratio for the SM Higgs*. `https://twiki.cern.ch/twiki/bin/view/LHCPhysics/CrossSections#Higgs_cross_sections_and_decay_b`.

[299] Talk by A. de Wit at EPS 2017: "Higgs measurements at the HL-LHC with CMS".

[300] CMS Collaboration. Search for $\mathrm{t\bar{t}H}$ production in the $\mathrm{H} \to \mathrm{b\bar{b}}$ decay channel with 2016 pp collision data at $\sqrt{s} = 13\ \mathrm{TeV}$. 2016.

[301] The ATLAS collaboration. Search for the Standard Model Higgs boson produced in association with top quarks and decaying into $b\bar{b}$ in pp collisions at $\sqrt{s}$ = 13 TeV with the ATLAS detector. 2016.

[302] Updates on Projections of Physics Reach with the Upgraded CMS Detector for High Luminosity LHC. Oct 2016.

[303] James Brooke, Matthew R. Buckley, Patrick Dunne, Bjoern Penning, John Tamanas, and Miha Zgubic. Vector Boson Fusion Searches for Dark Matter at the LHC. 2016.

[304] David Curtin et al. Exotic decays of the 125 GeV Higgs boson. *Phys. Rev.*, D90(7):075004, 2014.

[305] The ATLAS collaboration. Search for exotic Higgs-boson decays in events with at least one photon, missing transverse momentum, and two forward jets produced in $\sqrt{s}$ = 8 TeV $\boldsymbol{pp}$ collisions with the ATLAS detector. 2015.

[306] The ATLAS collaboration. Search for new light gauge bosons in Higgs boson decays to four-lepton final states in pp collisions at $\sqrt{s} = 8$ TeV with the ATLAS detector at the LHC. 2015.

[307] Georges Aad et al. Search for long-lived, weakly interacting particles that decay to displaced hadronic jets in proton-proton collisions at $\sqrt{s} = 8$ TeV with the ATLAS detector. *Phys. Rev.*, D92(1):012010, 2015.

[308] Georges Aad et al. Search for Higgs bosons decaying to aa in the $\mu\mu\tau\tau$ final state in pp collisions at $\sqrt{s} = 8$ TeV with the ATLAS experiment. *Phys. Rev.*, D92(5):052002, 2015.

[309] Georges Aad et al. Search for new light gauge bosons in Higgs boson decays to four-lepton final states in pp collisions at $\sqrt{s} = 8$ TeV with the ATLAS detector at the LHC. *Phys. Rev.*, D92(9):092001, 2015.

[310] Vardan Khachatryan et al. Search for exotic decays of a Higgs boson into undetectable particles and one or more photons. *Phys. Lett.*, B753:363–388, 2016.

[311] Georges Aad et al. Search for invisible decays of a Higgs boson using vector-boson fusion in pp collisions at $\sqrt{s} = 8$ TeV with the ATLAS detector. *JHEP*, 01:172, 2016.

[312] Georges Aad et al. Constraints on new phenomena via Higgs boson couplings and invisible decays with the ATLAS detector. *JHEP*, 11:206, 2015.

[313] Georges Aad et al. Search for new phenomena in events with at least three photons collected in pp collisions at $\sqrt{s}$ = 8 TeV with the ATLAS detector. *Eur. Phys. J.*, C76(4):210, 2016.

[314] CMS Collaboration. Search for Higgs Decays to New Light Bosons in Boosted Tau Final States. 2015.

[315] Vardan Khachatryan et al. Search for a very light NMSSM Higgs boson produced in decays of the 125 GeV scalar boson and decaying into τ leptons in pp collisions at $\sqrt{s} = 8$ TeV. *JHEP*, 01:079, 2016.

[316] Toyoko Orimoto. Search for new physics in the low MET monophoton channel with the CMS Detector. In *Proceedings, Meeting of the APS Division of Particles and Fields (DPF 2015): Ann Arbor, Michigan, USA, 4-8 Aug 2015*, 2015.

[317] CMS Collaboration. Search for the Exotic Decay of the Higgs Boson to Two Light Pseudoscalar Bosons with Two Taus and Two Muons in the Final State at $\sqrt{s} = 8$ TeV. 2016.

[318] CMS Collaboration. Search for exotic decays of the Higgs boson to a pair of new light bosons with two muon and two b jets in final states. 2016.

[319] Morad Aaboud et al. Search for the Higgs boson produced in association with a W boson and decaying to four b-quarks via two spin-zero particles in pp collisions at 13 TeV with the ATLAS detector. *Eur. Phys. J.*, C76(11):605, 2016.

[320] Fabrizio Caola and Kirill Melnikov. Constraining the Higgs boson width with ZZ production at the LHC. *Phys. Rev.*, D88:054024, 2013.

[321] Lance J. Dixon and Ye Li. Bounding the Higgs Boson Width Through Interferometry. *Phys. Rev. Lett.*, 111:111802, 2013.

[322] Philip Bechtle, Sven Heinemeyer, Oscar Stål, Tim Stefaniak, and Georg Weiglein. $HiggsSignals$: Confronting arbitrary Higgs sectors with measurements at the Tevatron and the LHC. *Eur. Phys. J.*, C74(2):2711, 2014.

[323] Stephen P. Martin. A Supersymmetry primer. 1997. [Adv. Ser. Direct. High Energy Phys.18,1(1998)].

[324] Radovan Dermisek and Ian Low. Probing the Stop Sector and the Sanity of the MSSM with the Higgs Boson at the LHC. *Phys. Rev.*, D77:035012, 2008.

[325] Dean Carmi, Adam Falkowski, Eric Kuflik, Tomer Volansky, and Jure Zupan. Higgs After the Discovery: A Status Report. *JHEP*, 10:196, 2012.

[326] Nathaniel Craig, Marco Farina, Matthew McCullough, and Maxim Perelstein. Precision Higgsstrahlung as a Probe of New Physics. *JHEP*, 03:146, 2015.

[327] Ulrich Ellwanger, Cyril Hugonie, and Ana M. Teixeira. The Next-to-Minimal Supersymmetric Standard Model. *Phys. Rept.*, 496:1–77, 2010.

[328] M. Maniatis. The Next-to-Minimal Supersymmetric extension of the Standard Model reviewed. *Int. J. Mod. Phys.*, A25:3505–3602, 2010.

[329] N. Arkani-Hamed, A. G. Cohen, E. Katz, A. E. Nelson, T. Gregoire, and Jay G. Wacker. The Minimal moose for a little Higgs. *JHEP*, 08:021, 2002.

[330] N. Arkani-Hamed, A. G. Cohen, E. Katz, and A. E. Nelson. The Littlest Higgs. *JHEP*, 07:034, 2002.

[331] David E. Kaplan and Martin Schmaltz. The Little Higgs from a simple group. *JHEP*, 10:039, 2003.

[332] Martin Schmaltz, Daniel Stolarski, and Jesse Thaler. The Bestest Little Higgs. *JHEP*, 09:018, 2010.

[333] Brando Bellazzini, Csaba Csáki, and Javi Serra. Composite Higgses. *Eur. Phys. J.*, C74(5):2766, 2014.

[334] Csaba Csaki, Christophe Grojean, and John Terning. Alternatives to an Elementary Higgs. 2015.

[335] Martin Schmaltz. The Simplest little Higgs. *JHEP*, 08:056, 2004.

[336] Michael Peskin. *to appear*.

[337] Rudolf Haag, Jan T. Lopuszanski, and Martin Sohnius. All Possible Generators of Supersymmetries of the s Matrix. *Nucl. Phys.*, B88:257, 1975.

[338] Haiying Cai, Hsin-Chia Cheng, and John Terning. A Spin-1 Top Quark Superpartner. *Phys. Rev. Lett.*, 101:171805, 2008.

[339] Patrick Janot. Closing the light sbottom mass window from a compilation of $e^+e^- \to$ hadron data. *Phys. Lett.*, B594:23–34, 2004.

[340] Brian Batell, Carlos E. M. Wagner, and Lian-Tao Wang. Constraints on a Very Light Sbottom. *JHEP*, 05:002, 2014.

[341] Michael E. Peskin. Comparison of LHC and ILC Capabilities for Higgs Boson Coupling Measurements. 2012.

[342] Thomas Hahn. Generating Feynman diagrams and amplitudes with FeynArts 3. *Comput. Phys. Commun.*, 140:418–431, 2001.

[343] Brian Batell, Matthew McCullough, Daniel Stolarski, and Christopher B. Verhaaren. Putting a Stop to di-Higgs Modifications. *JHEP*, 09:216, 2015.

[344] S. Dawson, A. Ismail, and Ian Low. What?s in the loop? The anatomy of double Higgs production. *Phys. Rev.*, D91(11):115008, 2015.

[345] Vardan Khachatryan et al. Observation of the diphoton decay of the Higgs boson and measurement of its properties. *Eur. Phys. J.*, C74(10):3076, 2014.

[346] Serguei Chatrchyan et al. Measurement of the properties of a Higgs boson in the four-lepton final state. *Phys. Rev.*, D89(9):092007, 2014.

[347] Vardan Khachatryan et al. Search for the standard model Higgs boson produced through vector boson fusion and decaying to $b\bar{b}$. *Phys. Rev.*, D92(3):032008, 2015.

[348] Vardan Khachatryan et al. Search for the associated production of the Higgs boson with a top-quark pair. *JHEP*, 09:087, 2014. [Erratum: JHEP10,106(2014)].

[349] Serguei Chatrchyan et al. Evidence for the 125 GeV Higgs boson decaying to a pair of τ leptons. *JHEP*, 05:104, 2014.

[350] Georges Aad et al. Measurement of Higgs boson production in the diphoton decay channel in pp collisions at center-of-mass energies of 7 and 8 TeV with the ATLAS detector. *Phys. Rev.*, D90(11):112015, 2014.

[351] Georges Aad et al. Observation and measurement of Higgs boson decays to WW* with the ATLAS detector. *Phys. Rev.*, D92(1):012006, 2015.

[352] Georges Aad et al. Study of (W/Z)H production and Higgs boson couplings using $H \to WW^*$ decays with the ATLAS detector. *JHEP*, 08:137, 2015.

[353] Georges Aad et al. Measurements of Higgs boson production and couplings in the four-lepton channel in pp collisions at center-of-mass energies of 7 and 8 TeV with the ATLAS detector. *Phys. Rev.*, D91(1):012006, 2015.

[354] Georges Aad et al. Search for the $b\bar{b}$ decay of the Standard Model Higgs boson in associated $(W/Z)H$ production with the ATLAS detector. *JHEP*, 01:069, 2015.

[355] Morad Aaboud et al. Search for the Standard Model Higgs boson produced by vector-boson fusion in 8 TeV pp collisions and decaying to bottom quarks with the ATLAS detector. 2016.

[356] Georges Aad et al. Search for the Standard Model Higgs boson produced in association with top quarks and decaying into $b\bar{b}$ in pp collisions at $\sqrt{s}$ = 8 TeV with the ATLAS detector. *Eur. Phys. J.*, C75(7):349, 2015.

[357] Georges Aad et al. Search for the Standard Model Higgs boson decaying into $b\bar{b}$ produced in association with top quarks decaying hadronically in pp collisions at $\sqrt{s} = 8$ TeV with the ATLAS detector. *JHEP*, 05:160, 2016.

[358] Georges Aad et al. Evidence for the Higgs-boson Yukawa coupling to tau leptons with the ATLAS detector. *JHEP*, 04:117, 2015.

[359] Georges Aad et al. Search for the Standard Model Higgs boson produced in association with a vector boson and decaying into a tau pair in pp collisions at $\sqrt{s} = 8$ TeV with the ATLAS detector. *Phys. Rev.*, D93(9):092005, 2016.

[360] CMS Collaboration. Measurements of properties of the Higgs boson in the diphoton decay channel with the full 2016 data set. 2017.

[361] Higgs to WW measurements with $15.2\ \mathrm{fb}^{-1}$ of 13 TeV proton-proton collisions. Technical Report CMS-PAS-HIG-16-021, CERN, Geneva, 2017.

[362] CMS Collaboration. Measurements of properties of the Higgs boson decaying into four leptons in pp collisions at sqrts = 13 TeV. 2017.

[363] CMS Collaboration. VBF H to bb using the 2015 data sample. 2016.

[364] Inclusive search for the standard model Higgs boson produced in pp collisions at $\sqrt{s} = 13$ TeV using H$\to$ $\mathrm{b\bar{b}}$ decays. Technical Report CMS-PAS-HIG-17-010, CERN, Geneva, 2017.

[365] CMS Collaboration. Observation of the SM scalar boson decaying to a pair of τ leptons with the CMS experiment at the LHC. 2017.

[366] The ATLAS collaboration. Measurements of Higgs boson properties in the diphoton decay channel with $36.1\ \mathrm{fb}^{-1}$ pp collision data at the center-of-mass energy of 13 TeV with the ATLAS detector. 2017.

[367] The ATLAS collaboration. Measurements of the Higgs boson production cross section via Vector Boson Fusion and associated WH production in the $WW^* \to \ell\nu\ell\nu$ decay mode with the ATLAS detector at $\sqrt{s}$ = 13 TeV. 2016.

[368] The ATLAS collaboration. Measurement of the Higgs boson coupling properties in the H $\to$ ZZ $\to$ 4l decay channel at $\sqrt{s} = 13$ TeV with the ATLAS detector. 2017.

[369] The ATLAS collaboration. Evidence for the H $\to$ $b\bar{b}$ decay with the ATLAS detector. 2017.

[370] The ATLAS collaboration. Search for Higgs boson production via weak boson fusion and decaying to $b\bar{b}$ in association with a high-energy photon in the ATLAS detector. 2016.

[371] T. Aaltonen et al. Higgs Boson Studies at the Tevatron. *Phys. Rev.*, D88(5):052014, 2013.

[372] CMS Collaboration. Search for the associated production of a Higgs boson with a top quark pair in final states with a τ lepton at $\sqrt{s} = 13$ TeV. 2017.

[373] Search for Higgs boson production in association with top quarks in multilepton final states at $\sqrt{s} = 13$ TeV. Technical Report CMS-PAS-HIG-17-004, CERN, Geneva, 2017.

[374] The ATLAS collaboration. Search for the associated production of the Higgs boson with a top quark pair in multi-lepton final states with the ATLAS detector. 2015.

[375] The ATLAS collaboration. Search for the Associated Production of a Higgs Boson and a Top Quark Pair in Multilepton Final States with the ATLAS Detector. 2016.

[376] CMS Collaboration. Searches for invisible Higgs boson decays with the CMS detector. 2016.

[377] CMS Collaboration. Search for new physics in final states with an energetic jet or a hadronically decaying W or Z boson using $35.9\ \mathrm{fb}^{-1}$ of data at $\sqrt{s} = 13$ TeV. 2017.

[378] CMS Collaboration. Search for dark matter, invisible Higgs boson decays, and large extra dimensions in the $\ell\ell + E_{\mathrm{T}}^{\mathrm{miss}}$ final state using 2016 data. 2017.

[379] Serguei Chatrchyan et al. Search for invisible decays of Higgs bosons in the vector boson fusion and associated ZH production modes. *Eur. Phys. J.*, C74:2980, 2014.

[380] Georges Aad et al. Search for invisible decays of the Higgs boson produced in association with a hadronically decaying vector boson in pp collisions at $\sqrt{s}$ = 8 TeV with the ATLAS detector. *Eur. Phys. J.*, C75(7):337, 2015.

[381] Georges Aad et al. Search for new phenomena in final states with an energetic jet and large missing transverse momentum in pp collisions at $\sqrt{s}$ =8 TeV with the ATLAS detector. *Eur. Phys. J.*, C75(7):299, 2015. [Erratum: Eur. Phys. J.C75,no.9,408(2015)].

[382] The ATLAS collaboration. Search for an invisibly decaying Higgs boson or dark matter candidates produced in association with a Z boson in pp collisions at $\sqrt{s} = 13$ TeV with the ATLAS detector. 2017.